Characterisation Of The Blazhko Effect In RR Lyrae Stars Using SuperWASP Data

Thesis

Characterisation of the Blazhko effect in RR Lyrae stars using SuperWASP data.

Thesis submitted for the degree of Doctor of Philosophy.

Physical Science

Paul Greer

December 2017

Abstract

This thesis investigates the characteristics of the Blazhko effect using data from the SuperWASP archive. The SuperWASP instrument combines wide–field coverage with a short cadence, providing time–series analysis on a range of timescales for a large number of stars. The Blazhko effect is the amplitude and frequency modulation of RR Lyrae variable pulsating stars. Its physical causes are still unexplained by stellar structure and evolution models. The stellar pulsation mechanism and modulation are introduced before comparing the WASP project to other wide–field surveys.

The aim of this research is to identify correlations between the basic pulsation and Blazhko effect characteristics that may provide clues to its origins. To accomplish this, the Blazhko effect is investigated in temporal, frequency and phase spaces.

A catalogue of 4963 RRab class RR Lyrae objects was created through the classification of phase–folded light curves. Blazhko periods were calculated for 18 out of 20 highly modulated objects by phase–folding the amplitude modulation induced upper envelope function of their light curves.

983 Blazhko objects have been identified using coincident low frequency peaks and sidebands, or equidistant sidepeaks, in frequency spectra created using the CLEAN algorithm. Analysis of pulsation and Blazhko attributes within this large sample shows no correlation between them.

140 Blazhko candidates were also identified by short–term periodic trends in their O–C diagrams. This phase domain analysis also led to the identification of 17 candidates for rare binary objects, due to their sinusoidal O–C curves. 73 objects had quadratic O–C curves, suggesting binary candidates with periods longer than the duration of SuperWASP observations.

The classification and investigation of Blazhko effect and binary candidates contained

herein provide the opportunity for further study with both existing, and future, ground– and space–based missions such as Gaia, the LSST and PLATO.

Acknowledgements

This work would not have been possible without the guidance, support and encouragement of my primary supervisor Andrew Norton. I hope I have adequately rewarded his patience! Andrew's calm and friendly approach has made the past three and a bit years of work easily the most enjoyable of my professional and academical career.

If Andrew was my strategist, then Marcus Lohr was my tactician, without whose lengthy discussions on time–series analysis techniques I would not have achieved the level of clarity I have managed. Marcus is a first rate mentor and I would recommend him to any aspiring scientist.

Of course, my immense personal gratitude goes to my wife, Jackie, whose ability to pretend to be listening to my ramblings has kept me relatively sane throughout both good times and the not so good. Jackie's support and positivity has been truly incredible.

Contents

List of Tables

List of Figures

List of publications

Parts of Chapters 3 and 4 have been published in Astronomy & Astrophysics: Greer P. A., Payne S. G., Norton A. J., Maxted P. F. L., Smalley B., et al. 2017. *A&A*. **607**:A11. DOI: 10.1051/0004-6361/201630296

Preliminary results from Chapter 5 are included in conference proceedings to be published by the Proceedings of the Polish Astronomical Society, edited by Radek Smolec, Karen Kinemuchi and Richard Anderson.

Items not bound with thesis

The complete tables of results described in Appendices A, C and D are available in electronic format on DVD supplied with this thesis.

Introduction

This thesis is a study into the characteristics of the Blazhko effect using data from the SuperWASP archive. The Blazhko effect is the amplitude and frequency modulation of the pulsations of a type of classical pulsating stars called RR Lyrae, after the prototype object, RR Lyra. The RR nomenclature simply denotes that this is the 10th brightest variable object in the Lyra constellation. These pulsating variable stars are the subject of the first chapter of this work.

The second chapter describes the WASP project and compares it to other wide–field surveys. SuperWASP has wide–field coverage of a large proportion of the night sky with a short cadence that allows time–series analysis on a wide range of timescales. The large coverage provides a large number of field stars of a given type allowing the analysis of trends and correlations within a statistically significant population. Such large coverage also allows the investigation of rare objects such as binary systems containing post–main sequence pulsators. The short cadence of SuperWASP allows several observations of an object within each night. This is crucial for the measurement of changes in both amplitude and timings of pulsations through the fitting of templates to measurements from individual nights.

This thesis then continues with an investigation of the Blazhko effect using selected objects from the SuperWASP archive. An explanation of the mysterious Blazhko effect is a challenge to models of stellar pulsations. Current stellar models struggle to replicate all the features of the pulsation modulation, never mind explain the physical causes of it. Since it affects stellar pulsations, it is therefore important when modelling both stellar structure and evolution because such models must be able to recreate the conditions required to instigate and maintain these pulsations within the correct temperature ranges and ages of stars. This chapter also offers the opportunity to discuss the findings of space–based missions and how

they have furthered our knowledge of pulsating variable stars and the Blazhko effect.

This study investigates the characteristics of the Blazhko effect across three closely related domains: time, frequency and phase. Since a pulsation is the change in brightness of each star over time, confirmation of the RRab sub–classification of the objects using the shape of their pulsations is the first area of focus in the time domain analysis chapter. The outcome of this analysis is the production of a catalogue of SuperWASP RRab objects. The first aspect of the Blazhko effect to be investigated in this thesis is the change in amplitude of the pulsations over the duration of observations, known as amplitude modulation, requiring further time domain analysis.

The pulsations of RR Lyrae are can be broken up into several harmonic components if the the pulsations are converted into frequency spectra. Investigation of the second aspect of the Blazhko effect, the frequency modulation of pulsations, requires this frequency–space analysis in order to detect the effects that the modulation has on these individual components. The result of this stage of investigation is a catalogue of SuperWASP Blazhko candidates.

The frequency modulation can be seen over time as a change in the phase of the pulsations, or phase modulation. Whereas the time domain chapter investigated the change in amplitude of pulsations caused by amplitude modulation, the phase domain chapter analyses the change in the timings of pulsations. Periodic changes in timings can be caused by the phase modulation aspect of the Blazhko effect. Alternatively, similar modulation can be caused by the effects of the pulsating star orbiting another stellar object in a binary system. Binaries containing a middle–aged, post red giant branch pulsating object are extremely rare and worthy of research using the large SuperWASP archive. The outcomes of this phase domain analysis are a second, further list of Blazhko candidates, and a short list of exciting binary candidates.

This thesis now continues with a chapter on pulsating variable objects, and the methods of analysing these pulsations.

Chapter 1

Pulsating Variable Stars

1.1 Introduction

Most stars vary in brightness to some degree. Sometimes this is an extrinsic effect due to other stellar bodies around it, and sometimes this is due to intrinsic processes physically changing the size, shape and flux output of the star. Those stars that periodically change in brightness due to these intrinsic processes are known as pulsating variables. Several classes of pulsating variable stars are defined due to the size, period and shape of these pulsations, although it is possible that all stars pulsate, or at least oscillate, to a greater or lesser degree, including our very own Sun.

This thesis concerns a particular type of pulsating variable star known as the RR Lyrae type and the mysterious Blazhko effect that they exhibit. A theory of why stars pulsate is relatively new, only having been proposed in the 1950's, even though by this time we already had seen exceptions to the rule in the form of stars that refused to maintain a constant period or amplitude of pulsations. The Blazhko effect, which is the amplitude modulation and frequency modulation of the pulsations of the RR Lyrae class of variable horizontal branch stars, was named after it was discovered in the analysis of RR Dra by Sergey Blazhko in 1907 (Blažko, 1907). Despite modern computational modelling techniques coupled with large datasets and detailed information from space based surveys, the physical causes of this modulation of the pulsations of RR Lyrae stars are still a mystery. Understanding stellar pulsations is important because they provide an insight into the structure of stars which in turn provides clues about how the different layers interact and evolve, an integral part of

modelling stellar structure and mid– to late–stage stellar evolution. Also, RR Lyrae stars are valuable as distance markers and age indicators for globular clusters and stellar populations and therefore anything that affects their physical properties should be investigated.

This chapter continues with the following sections: section 1.2 provides information into RR Lyrae as pulsating horizontal branch stars, the defining characteristics of RR Lyrae stars and their uses in astronomy; the pulsations of RR Lyrae are discussed in section 1.3; techniques commonly used to describe regular pulsations are demonstrated in 1.4; amplitude and frequency modulation and how they appear in these techniques is explained in 1.5; section 1.6 describes the Blazhko effect; the various models that attempt to explain it are set out in 1.7; discussions on the current and future studies of RR Lyrae and the Blazhko effect are presented in section 1.8 along with conclusions to this chapter.

1.2 RR Lyrae Stars

Generally, stars are spectrally classified based on the strength of absorption lines in their spectra, which in turn depends on their mass, age and evolutionary stage. Within groups of stars there may be sub-groups and sub–classifications until a single group contains no more than a handful of very distinctive objects. This distinction could be peculiarly strong emission lines or the fact that they vary in flux over observable time–scales, i.e. variable stars. Usually these stars are named after the prototype, the first one to be discovered to have that sort of pulsation. One such object is the pulsating variable star type RR Lyrae, named after the prototype RR Lyr, the tenth variable star in the constellation Lyra, discovered in 1908 by Henrietta Leavitt (Catelan, Márcio and Smith, Horace A., 2014). The following section describes where RR Lyrae can be found in the Herzsprung–Russell diagram (HRD) in relation to other types of stars, and what makes them both unique and useful among variable objects in the night sky.

1.2.1 Evolutionary phase

RR Lyrae are pulsating stars in the horizontal branch (HB) of the colour–magnitude diagram (CMD), the empirical version of the HRD, as shown in Fig. 1.1. They have evolved off the main sequence (MS), past the red giant branch (RGB) and have commenced helium

burning in their cores having reached a core temperature of 0.1 – 0.4 GK (1GK = 10^9 K). By this evolutionary stage they are 0.6 – 0.8 solar masses ($M_\odot$), have absolute magnitudes of approximately 32 times solar luminosity ($L_\odot$), radii that vary from 5.1 to 5.6 solar radii ($R_\odot$) during their pulsation (Kolenberg et al., 2010b), and are approximately 10 Gyr (10 billion years) old (Fiorentino et al., 2012) – a considerable fraction of the age of the universe. Their ages from initial models were questioned when these early models calculated the age of clusters to be greater than the age of the Universe derived from cosmological models. Their effective (observable photospheric surface) temperature T_{eff} is approximately 7000 K. Since $\log(T_{RR}) = 3.85$, '3.85' will appear as a superscript in equations from Caputo (1998) below, to highlight that those equations specifically relate to RR Lyrae and the middle of the Instability Strip. Spectroscopic studies have shown that RR Lyrae rotate relatively slowly between 50 and 100 km s^{-1} (Strugnell et al., 1986).

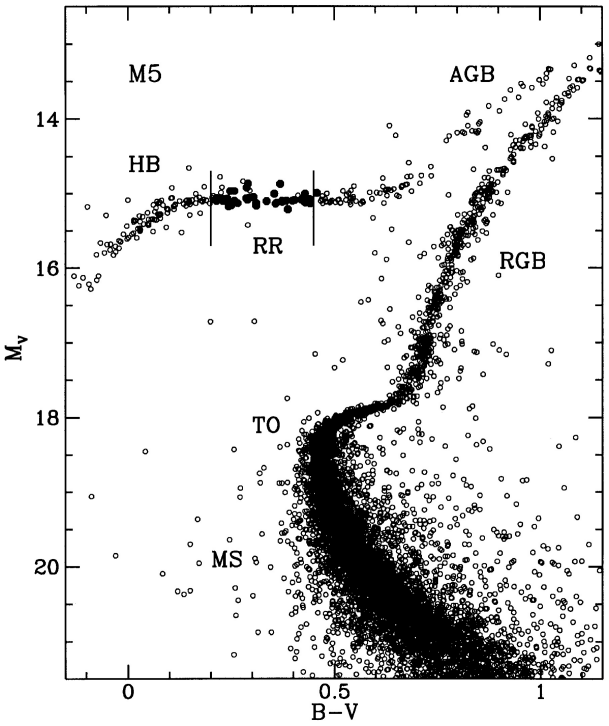

Figure 1.1: A colour–magnitude diagram showing the stars of a single globular cluster, the M5 cluster, at their various evolutionary stages. The x–axis labelled B–V refers to the colour from blue on the left to red on the right so temperature increases to the left. The vertical axis is magnitude in the V band. TO refers to the main sequence Turn Off stage also called the MSTO in the main text. The shape of the CMD, specifically the position of the TO and the HB are used in the age dating process. (Reproduced from Caputo, 1998, Fig. 2, p. 37)

1.2.2 The Horizontal Branch

The horizontal branch (HB) in the HRD represents stars of varying metallicity at different temperatures but only within a narrow range of luminosities around 1.6 $L_{\odot}$. RR Lyrae spend the majority of their time within a small range of luminosities of only $\Delta \log L \sim 0.04$ (Caputo, 1998). This narrow range of luminosity is because they are all burning helium in the triple–α process in a core of roughly the same size of 0.5 $M_{\odot}$. The wide range in observed temperatures is because the different opacities and thicknesses of their envelopes leave the hotter core closer to or further from the surface (Gallart et al., 2005), making the star appear more blue or red, respectively. The different envelope masses are due to different rates of mass loss on the earlier RGB stage.

1.2.3 Metallicity and stellar populations

The metallicity of a star refers to its proportion of elements heavier than helium. It is sometimes labelled as Z in the context of mass proportions (where hydrogen is labelled X, and helium as Y). In the context of relationships between stellar properties such as age, distance or pulsation period, it is normally given as the ratio of iron to hydrogen compared to that of the Sun,

$$\left[\frac{Fe}{H}\right] = \log_{10}\left(\frac{Fe}{H}\right)_{*} - \log_{10}\left(\frac{Fe}{H}\right)_{\odot} \tag{1.1}$$

and given the unit of 'dex'. In sources where metallicity is given as Z it is possible to convert from Z using $\log_{10} Z = [Fe/H] - 1.73$ (Caputo, 1998).

Population II stars are described by Caputo (1998, p. 34) as 'mild' metal deficient stars with $Z \sim 10^{-4}$ to 10^{-3} and tend to be found in the galactic halo rather than the disc. They are less than 2 solar masses and at least 1 Gyr old. Younger stars such as our Sun are designated 'Population I', whereas the first, extremely low–metal generation of stars are called 'Population III' and are yet to be observed. Caputo (1998) recommends that the definition should relate to chemical composition since satellite dwarf galaxies can be of intermediate age but still be metal poor.

Metallicity can be related to both luminosity and the periods of RR Lyrae, as described in sections 1.2.5 and 1.3.5 below.

1.2.4 RR Lyrae in Globular clusters

Globular clusters (GC) are densely packed, gravitationally bound, spherical groups of 10^4 – 10^6 Population II stars of various masses that are thought to have formed at the same time, although second and third generations are possible (Jurcsik et al., 2014). Since stars evolve at different speeds depending on their mass, an HRD of an old globular cluster can represent stars at almost every stage of their lives. Fig. 1.1 shows a CMD of the GC M5 with the evolutionary stages labelled, including the horizontal branch (HB) and the position of RR Lyrae stars (RR) within it. More stars can be found in the slowly evolving stages, whereas the short–lived stages contain fewer stars.

RR Lyrae are so common in globular clusters that they were known as "cluster variables" until the 1950's (Smith et al., 2009) although they can also exist in the outer regions of galaxies in galactic halos as field stars. RR Lyrae are important in the context of GC as standard candles, or distance markers, and age indicators because their pulsations make them easy to identify.

1.2.5 RR Lyrae in distance calculations

Since the intensity of the light follows an inverse square law as it travels outwards from a star, the distance to the stars can be calculated using Eq. 1.2 below:

$$S = \frac{L}{4\pi R^2} \tag{1.2}$$

where L is the intrinsic luminosity of the star, S is its observed flux (brightness), and r is the distance between observer and star. Therefore, the simplest way to gauge the distance of a star of observed brightness is when the intrinsic brightness of the star is already known. Such stellar objects are known as 'standard candles'. The intrinsic luminosities of RR Lyrae are so well defined because the narrow range of core masses on the HB produces such a narrow range of luminosities. This makes calculating distances to GC that contain the easily recognisable RR Lyrae class of stars a far simpler task.

Unlike Cepheids, RR Lyrae have a range of periods with little discernible difference in luminosity (Ngeow et al., 2013). The equation below from Bono et al. (1997) is more

applicable when looking at other pulsating stars within the instability strip, such as Cepheids.

$$\log P = 11.627 + 0.823 \log\left(\frac{L}{L_\odot}\right) - 0.582 \log\left(\frac{M}{M_\odot}\right) - 3.506 \log T_e \tag{1.3}$$

The luminosity of RR Lyrae stars, however, can vary slightly with metallicity. The metallicity-luminosity relation is given by Gratton et al. (1997) in terms of visible magnitude M_V:

$$M_V^{3.85} = 0.82 + 0.22\left[\frac{Fe}{H}\right] \tag{1.4}$$

specifically for RR Lyrae as indicated by the '3.85' superscript. There are also quadratic versions such as:

$$M_V^{3.85} = 0.991 - 0.460\left[\frac{Fe}{H}\right] + 0.087\left[\frac{Fe}{H}\right]^2 \tag{1.5}$$

cited in Caputo (1998).

Feast et al. (2008) state that there is a period–luminosity (PL) relation for RR Lyrae in the near–infrared K band, which also includes a term in metallicity that they consider to be negligible:

$$M_{K_s} = -2.38\,(\pm 0.04) \log P + 0.08\,(\pm 0.11)\left[\frac{Fe}{H}\right] - 1.05\,(\pm 0.13) \tag{1.6}$$

where M_{K_s} is the magnitude in the K band. They confirmed that the PL relation for RR Lyrae is an extrapolation of the corresponding Cepheid relation. During the mapping of the Galactic halo by Sesar et al. (2017) in visible and infrared bands, the following PL relation was derived:

$$M_{iP1} = -1.77 \log_{10}(P/0.6) + 0.46 \tag{1.7}$$

where $iP1$ refers to the Pan–STARRS1 (PS1) i–band (see Sect. 2.3.4). The dependency on metallicity was removed by assuming a galactic halo metallicity centred on −1.5 dex, and it used a reference period of 0.6 d. PL relationships have been published by Braga et al. (2015) for RR Lyrae in the red and near infrared wavelength ranges based on studies of globular cluster M4. These are shown graphically in Fig. 1.2. The cyan and red indicate different pulsation modes which will be described in more detail in subsection 1.3.2. The relation increases in steepness when moving from the red band to the infrared showing that

the relation is clearer in infrared, and, conversely, demonstrating how the relation becomes negligible in visible bands. The vertical bars show that the standard deviation decreases when moving from the optical to the infrared wavelengths.

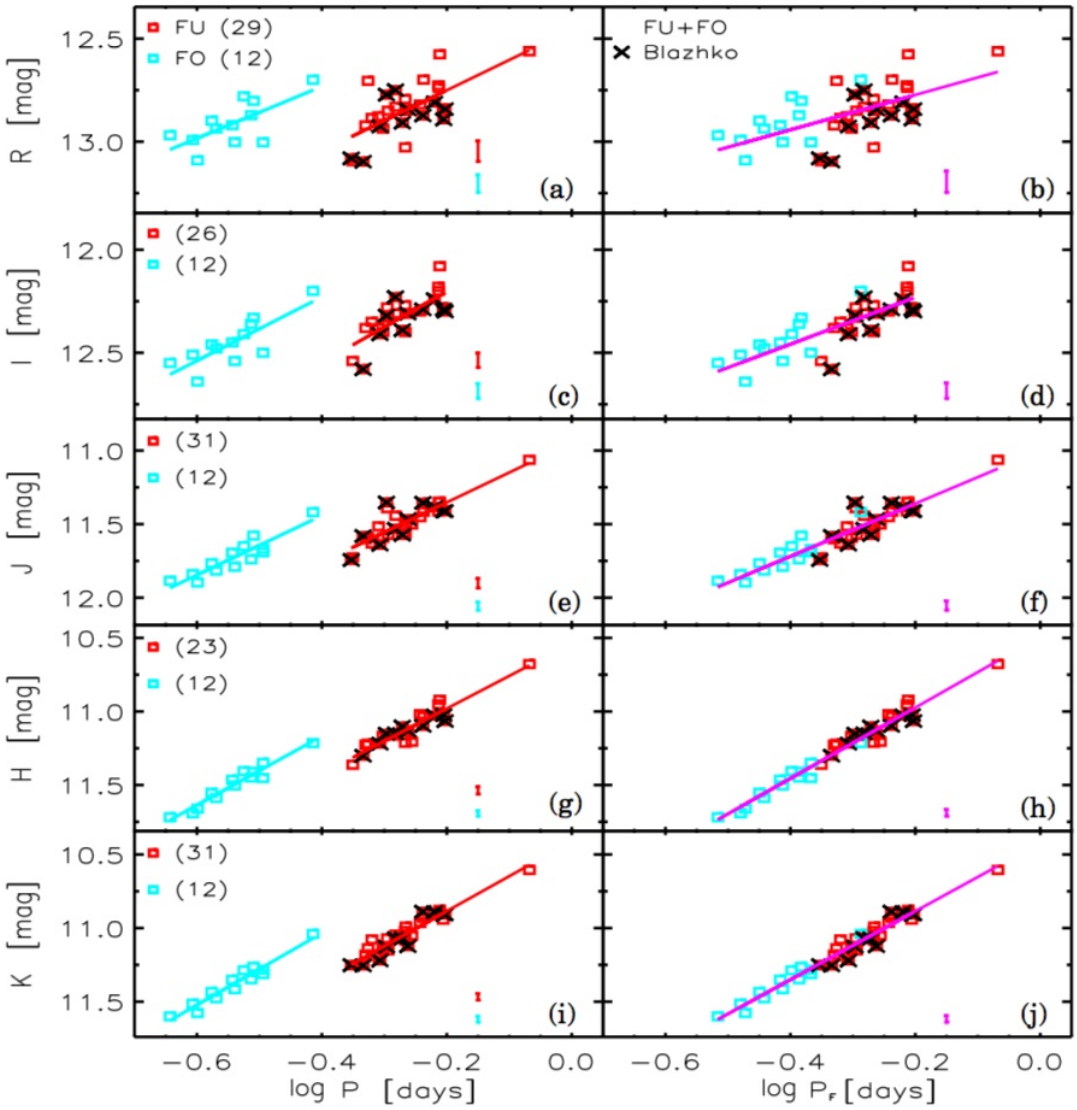

Figure 1.2: Period–luminosity relations for RR Lyrae in GC M4. Different pulsation modes are marked in cyan and red, with black crosses indicating Blazhko objects. The letters on the vertical axis refer to the waveband. (Reproduced from Braga et al., 2015, Fig. 5, p. 1)

The slope and zero point of period–luminosity relationships need to be calibrated, which is possible using parallax measurements of nearby clusters by missions such as HIPPARCOS (Benedict et al., 2011; Feast et al., 2008) and in future with the Gaia mission.

1.2.6 Estimating GC ages

Since a globular cluster mostly contains stars of the same age, the CMD for a GC can be matched against stellar evolutionary models to estimate its age. The models can be used to produce isochrones which are lines joining stars of the same age but different stellar evolutionary phase due to their different masses and metallicity.

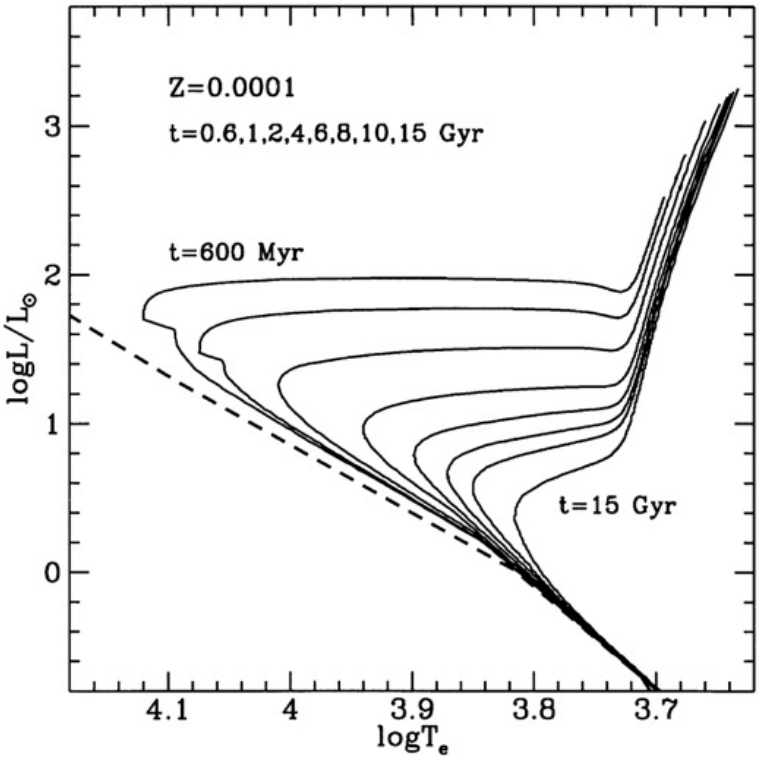

Figure 1.3: Isochrones showing how loci for stars of different masses, but the same age and metallicity, can be connected (on an HRD in this case). These lines highlight the stellar phase from the main sequence, through the MSTO (or just TO), across the subgiant branch and up the red giant branch (RGB). Notice how the MSTO curves upwards first which has consequences for age estimation as described in this section. (Reproduced from Caputo, 1998, Fig. 6, p. 42)

The age of GC can be estimated using the main sequence turn off point (MSTO) (see the area marked "TO" in Fig. 1.1) since the MSTO becomes fainter and redder for older stellar systems; imagine stars "peeling off" the main sequence from the top left to bottom right as the cluster ages, as shown in Fig. 1.3 above by the different isochrones leaving the zero age main sequence at lower points for clusters of higher ages (Caputo, 1998). The MSTO can also be compared to the HB, which can be clearly identified using the distinctive pulsations of RR Lyrae stars, called the ΔV technique (Caputo, 1998). The advantage of using the HB is that it has a narrow range of luminosities whereas the vertical section of the curved MSTO makes it difficult to define a precise MSTO luminosity (Caputo, 1998). However,

using the difference between these two points within the same cluster removes uncertainties due to distance and the change of colour of observed stars (due to dust between them and the observer). The extreme age of GC make them important as a lower limit on the age of the Universe (Caputo, 1998).

However, the metallicity of a GC can vary depending on its age. This can then create a range of possible calculated ages for an observed cluster because metallicity is a parameter in the theoretical models used to create the isochrones that GC are measured against.

Although RR Lyrae are complex, their use as standard candles and globular cluster markers make them extremely useful for further research into generations of stars within single GC (Jurcsik et al., 2014), while their pulsations further our understanding of both stellar interiors and evolution.

1.3 Pulsations of stars in the Instability Strip

As the previous section described, RR Lyrae are defined by their pulsations. These pulsations physically alter the size, luminosity, and in the case of non-radial pulsations described later, the shape of these stars. They are maintained until long–term evolutionary effects either change the mode of pulsation or the star evolves out of the small temperature range causing the pulsation mechanism. Pulsations and oscillations allow an insight into the interiors of stars through asteroseismology. In the following section these pulsations are described in more detail, explaining how they are created and maintained within such large stars. Subclasses of RR Lyrae, due to subtle differences in these pulsations, are described. Then, how these provide clues about the interior of RR Lyrae and help to define populations of stars within dense globular clusters is explained.

1.3.1 The Instability strip and pulsation mechanism

As HB stars evolve they pass through the intersection of the instability strip (IS) and HB, where helium burning stars undergo thermal pulsations. This is understood to be due to the Kappa–mechanism which cycles through the following stages.

Initially, a layer of partially ionised helium collapses under gravity, but at about 4×10^4 K the potential energy released is used to ionise the helium further rather than raising

the temperature, so the layer continues to collapse, falling beyond the point of hydrostatic equilibrium. Normally the increase in density would result in an increase in temperature thereby reducing opacity according to Kramer's law:

$$\kappa \propto \frac{\rho}{T^{3.5}} \tag{1.8}$$

where κ, 'kappa', represents how opaque the material is to photons. However the opacity by this stage is dominated by electron scattering which is independent of temperature. The density of the layer increases due to the collapse, but since the temperature remains roughly constant, the opacity increases. This increased opacity effectively traps heat in the layers underneath which are now becoming more compressed and they heat up accordingly, increasing pressure. Eventually this pressure acts as a piston, pushing the He^+ layer outwards, past its equilibrium position. As it rises the partially ionised helium layer cools, leading to the recombination of the free electrons with the helium ions. This reduces the opacity of the helium but also releases chemical potential energy. The layer starts to fall inwards again, increasing the temperature and re–ionising the helium to start the pulsation cycle over again. Normally the star will be most luminous when the radius is at a minimum, but the time it takes to push the helium layer back to the surface delays the peak brightness slightly (Fossati et al., 2014).

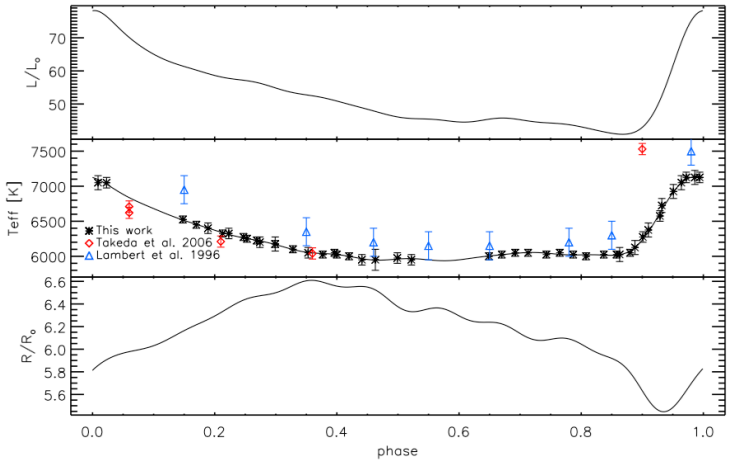

Figure 1.4: The variation in luminosity, effective temperature and radius across the pulsation period of an RR Lyrae star. Notice how the luminosity increases rapidly shortly after minimum radius before decreasing steadily throughout the rest of the cycle. (Reproduced from Fossati et al., 2014, Fig. 4, p. 6)

In all cases there has to be enough stellar material above the He^+ layer to provide the

required restoring force to make the pulsations self–sustaining. The effectiveness of convection at transporting heat away means that stars below $T_{\rm eff} \approx 5500$ K are unable to pulsate, whereas those above a $T_{\rm eff}$ of 7500 K do not have enough material above their ionisation zones to pulsate. This leads to a small range of temperatures of varying luminosity where pulsations are self sustaining: the instability strip. The core is thought to remain unaffected by pulsations as the pulsating RR Lyrae stars have the same mean temperature and luminosity as other non–pulsating HB stars (Caputo, 1998).

Nemec et al. (2011) and Caputo (1998) both cite von Ritter's 1879 equation as the original stellar pulsation equation:

$$P\sqrt{\rho} = Q \tag{1.9}$$

where ρ is the mean stellar density and Q is known as the pulsation constant.

Bono et al. (1997) points out that pulsation periods can be derived using a linear approach thanks to this von Ritter equation but the calculation of pulsation amplitudes require a more complex nonlinear approach. Such nonlinear convective envelope models were used by Bono et al. (1997) to calculate the blue and red edges of the instability strip for RR Lyrae with a range of typical masses of 0.58, 0.65 and 0.75 $M_\odot$. For a fixed mass of 0.58 $M_\odot$, the temperatures range from 7250 K for the blue edge of a first overtone pulsator with a luminosity of 41 $L_\odot$ to 5750 K for the red edge of a fundamental mode pulsator with 65 $L_\odot$. These fundamental and first overtone modes are the subject of the following subsection.

1.3.2 Pulsation modes

There are two main sources of pulsations in stars, see Kurtz (2006) for a review: pressure (p–modes), where the restoring force is the vertical gas pressure; and gravity (g–modes), where the source is a horizontal buoyancy restoring force. The p–mode waves, which are also known as acoustic waves, can be directly observed as they produce an anti–node at the surface of the star. The g–mode waves tend to be trapped under the convective layer and are refracted around the denser core of the star. They have not been directly observed but are thought to be present in the Sun (García et al., 2008; Cunha et al., 2007). They are also present in several other classes of stars including δ Scuti and their more massive counterparts β Cephei stars. Also, g–modes are the primary pulsation mode in γ Doradus

and slowly pulsating B stars Cunha et al. (2007).

Pulsations can also be radial or non–radial. Radial pulsations are the product of pressure modes and are radially symmetric so the size of the whole star changes. In non–radial pulsations the star changes shape but not size. Non–radial modes are the products of p– and g–modes and are described by spherical harmonics using a combination of a main order number n, the harmonic degree number l, and the azimuthal number m. The order number describes the number of nodes (parts of the star where motion is cancelled out), which are spherical in the case of radial modes, but are flat surfaces in the case of non–radial modes as shown below in Fig. 1.5. Non–radial modes with $m > 0$ lose their degeneracy when rotation is included, as some pulsations will appear prograde while others appear retrograde.

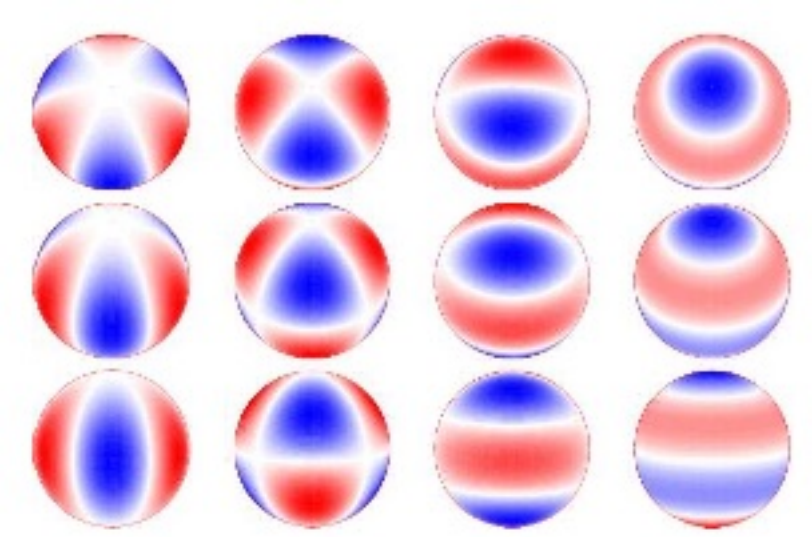

Figure 1.5: Non–radial pulsation modes with the order $l = 0$ on the left to $l = 3$ on the right. The rows represent 3 views taken at 30°, 60° and 90° from the pole. The columns show the azimuthal number m for $m = 3$ on the left to $m = 0$ on the right. Red represents areas that are moving in and blue means outwards. The white lines represent the nodes where no net movement occurs. These can be visualised as plane surfaces dissecting the star. (Reproduced from Kurtz, 2006, Fig. 4, p. 112)

1.3.3 Overtones

In stellar pulsations the term ‘overtone’ refers to a separate pulsation mode at specific ratio of the fundamental pulsation mode. Due to the temperature and density gradient across the interior of the star overtone frequencies are not at integer multiples of the fundamental frequency, therefore the terms overtone and harmonic are not synonymous. For instance, in RR Lyrae stars the first overtone is approximately 0.70 times the fundamental frequency (Percy, 2007). First overtones have been observed at 0.731, 0.753 and 0.721 times the fun-

damental frequency for stars in the Kepler field (Jurcsik et al., 2014, and references therein). Similarly, Cepheids have a 0.71 ratio between their fundamental and first overtone pulsation modes (Kurtz, 2006).

As in musical instruments, harmonic frequencies are integer mulitples ($2f, 3f$, etc.) of the fundamental frequency and are therefore resonant. Fig. 1.6 shows this for an open ended instrument, an organ pipe for example, with an anti–node at one end. In RR Lyrae each pulsation mode consists of several harmonic frequencies, in the same way that a musical chord consists of several harmonious notes. Since these are at whole integer multiples of the pulsation mode (or root note in our chord analogy), they can be easily identified in Fourier analysis of pulsations and separated out from overtone pulsation modes described above.

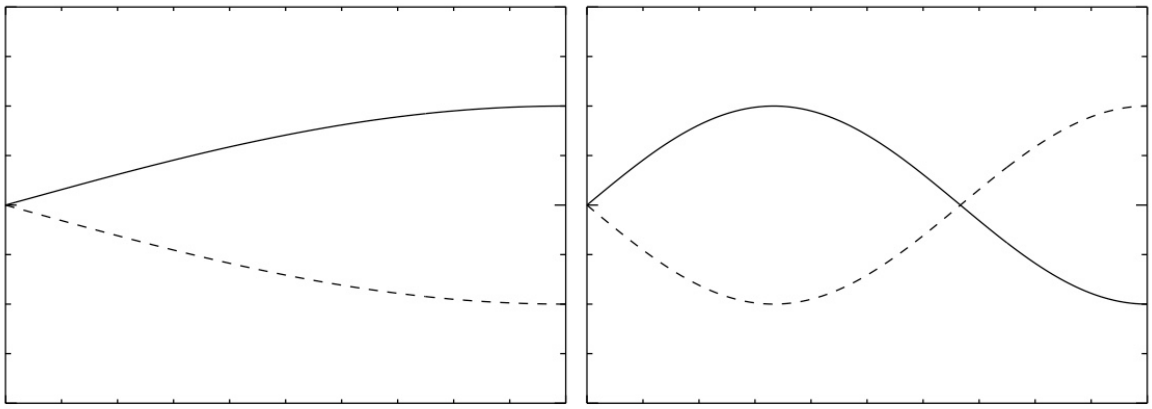

Figure 1.6: The fundamental mode and first harmonic of an open–ended instrument such as an organ pipe. The right side forms an anti–node so the fundamental mode (note) is at $1f/4$ and harmonics are at $3f/4$ (shown), $5f/4$, etc. (Reproduced from Kurtz, 2006, Fig. 2, p. 107)

1.3.4 Bailey classification

Bailey (1902) classified the RR Lyrae of the GC ω Centauri depending on the shape of their folded light curves (the process of creating a light curve is described in section 1.4.1). RRa

had moderately long periods, large amplitude pulsations, with a highly asymmetric curve; RRb had a longer period but smaller pulsation amplitudes but still had a highly asymmetric curve. The original RRa and RRb Bailey classifications have been combined into RRab (Gillet, 2013) because it has since been discovered that there is a continuum of light curve shapes rather than two discrete populations. RRc have short period, small pulsation, slightly asymmetric sinusoidal curves (Percy, 2007). This small amount of asymmetry is useful in distinguishing between RRc stars and close binary systems (Drake et al., 2014; Soszyński et al., 2014) which also tend to have shorter periods of less than 5.5 hours. RRc make up about 5% of the RR Lyrae population. Examples of the two main types of light curve, RRab and RRc, are shown below in Fig. 1.7. The different light curve shapes are a result of the combination of different harmonic frequencies as described in Sect. 1.4.3.

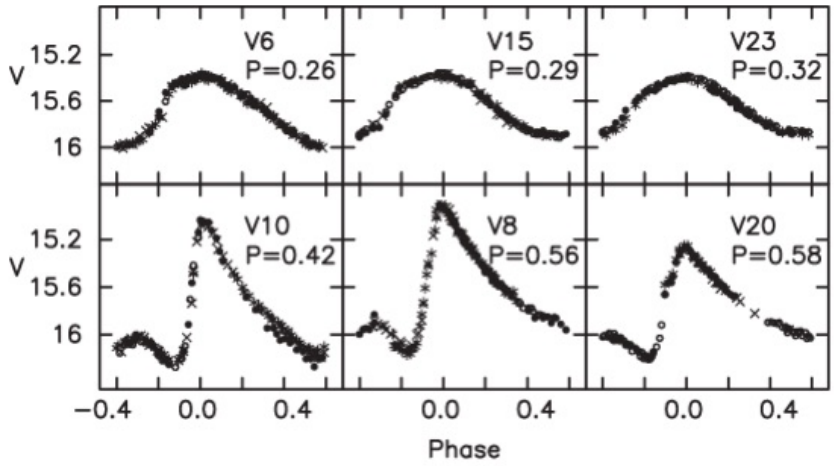

Figure 1.7: Phase folded lightcurves for RRc (top row) and RRab (bottom row) variable stars from the GC M107 (NGC 6171). (Reproduced from Percy, 2007, Fig. 6.19, p. 175)

The difference between RRab and RRc pulsations can be explained in terms of the dominant pulsation mode: RRab are fundamental mode pulsators, RRc are first overtone (1O) mode pulsators, and when the object pulsates in both fundamental and first overtone modes they are classified as RRd for double–mode. Petersen diagrams plot the period ratio against the log of the period, showing a ratio of about 0.7 between the fundamental mode and first overtone RRc stars. An example of a Petersen diagram is shown below in Fig. 1.8.

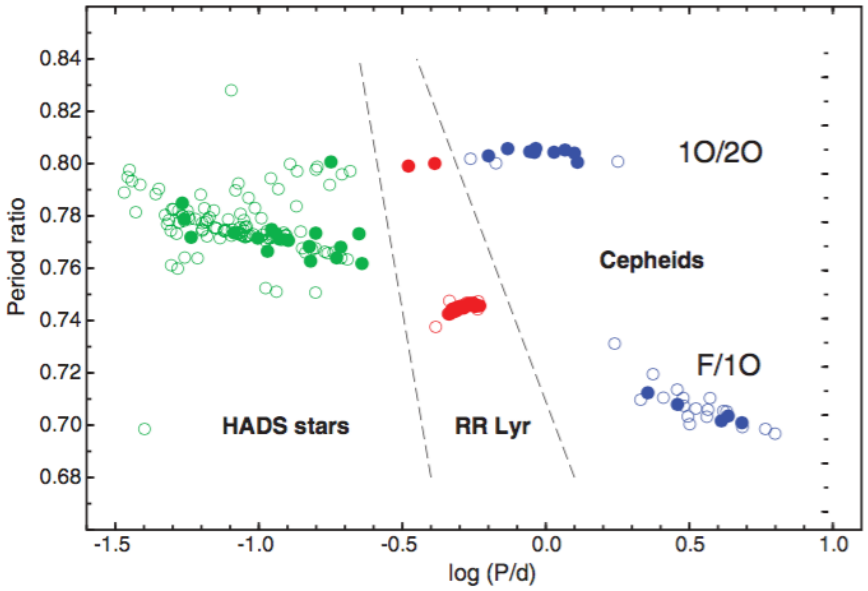

Figure 1.8: Petersen diagram showing the period ratios for different types of pulsating stars taken during the All Sky Automated Survey (ASAS). RR Lyrae are shown in red with the larger clump demonstrating that the ratio of fundamental (F) to first overtone (1O) is around 0.74. The two higher RR Lyr points represent two rarer stars found using ASAS that pulsate in the first and second (2O) overtones. HADS refers to high–amplitude delta scuti stars, whereas Cepheids are brighter pulsators found higher in the instability strip. (Reproduced from Pigulski, 2013, Fig. 3, p. 36)

The ratios between periods are useful in determining the mass, radius (Percy, 2007) and metallicity (Smolec et al., 2015b) of the star using stellar models: see (Nemec et al., 2011) for examples involving KIC 7021124 and V350 Lyr.

Szabó et al. (2004) explains how the current pulsation mode of RR Lyrae stars depends on their evolutionary progression along the HB as a form of hysteresis. RR Lyrae stars could start their evolution blueward along the HB with the fundamental mode dominant (RRab), before returning redward to the cooler side of the IS with the first overtone mode dominant (RRc). Furthermore, there is a small range of metallicities and solar masses that allow for double–mode (RRd) pulsations as part of their evolutionary journey. The RRd region of the IS could therefore be expected to lie between the fundamental and first overtone regions. However, there is an overlap between the fundamental and first overtone regions, and that the RRd region is populated by objects with higher masses than their fundamental–or–overtone cousins.

Additional mode combinations continue to be discovered, complicating the classification of RR Lyrae, but perhaps also providing clues to the physical models of stellar pulsations. RRe are RR Lyrae that pulsate in the second radial overtone (Gavrilchenko et al., 2014), for

instance. An additional pulsation mode at 0.61 times the frequency of the first overtone (f_1) has been discovered using data from the OGLE ground–based survey (Netzel et al., 2015; Smolec et al., 2015a). Despite being close to the frequencies of radial overtones this mode does not match any theoretical radial mode so the likely cause is a non–radial mode. It only appears in RRc or double–mode RRd stars, thereby creating radial–non–radial combinations.

1.3.5 The Bailey diagram and the Oosterhoff dichotomy

A Bailey diagram plots the log of period against visible V band pulsation amplitude, and can be used to show the two Oosterhoff groups. The Oosterhoff dichotomy is the appearance of two separate types of globular clusters defined by the average RRab pulsation periods of 0.55 d as Oosterhoff group I (OoI) and 0.65 d as Oosterhoff group II (OoII) (Caputo, 2012). Fig. 1.9 below shows this using GC M3 and ω Cen. Even though OoII clusters have been found to contain a larger proportion of RRc stars, because the RRc stars in OoII clusters also have longer periods than those in OoI clusters, the average period of OoII clusters remains longer than that of OoI (Smith et al., 2009).

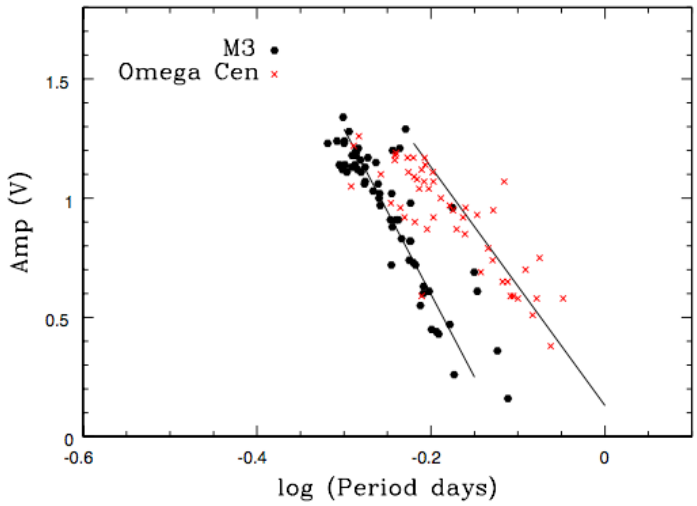

Figure 1.9: The Bailey diagram of RRab stars in the M3 and ω Cen clusters. Although there is some crossover between the two types M3 is categorised as an Oosterhoff type I (OoI) cluster, and ω Cen is defined as OoII. (Reproduced from Smith et al., 2011, Fig. 3, p. 4)

The Oosterhoff dichotomy also appears when comparing the metallicity and average RRab periods: the cluster population with a shorter period has a higher metallicity, and the other has longer periods with relatively low metallicities as shown in Fig. 1.10. However, Sandage (1993) shows several clusters where a population gap between -1.7 and -1.9 dex

gives the appearance of a gap in periodicity (the 'Oosterhoff gap') despite period varying continuously with metallicity. There are two Oosterhoff populations in GC M3 (Caputo, 2012) with RRc on the left ($\log P = -0.6$ to -0.45), and RRab on the right (-0.3 to -0.15) leaving a gap of about $\log -0.15$, i.e. just under 0.71 days.

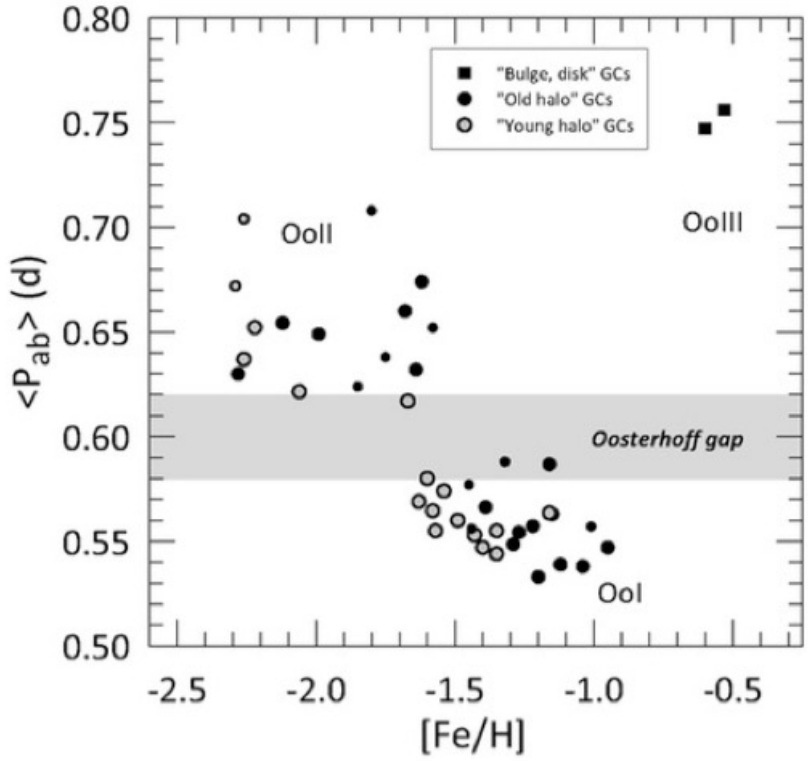

Figure 1.10: The two main Oosterhoff groups also appear when the average periods of RR Lyrae pulsations are plotted against the metallicity of globular clusters [Fe/H]. The main text explains how the metallicity is calculated but the diagram clearly shows the two populations centred around –2.0 dex and –1.25 dex. The legend gives the rough location or type of cluster. 'OoIII' represents outlier clusters NGC 6388 and NGC 6441 with both high metallicity and long periods. (Reproduced from Smith et al., 2011, Fig. 2, p. 3)

This has repercussions firstly for stellar evolution: based on work by Jurcsik et al. (2003), Marconi et al. (2003), and Clement & Shelton (1999), Nemec et al. (2011) conclude that the Oosterhoff dichotomy is actually an evolutionary effect – zero age horizontal branch (ZAHB) stars are OoI, whereas brighter, later stage stars are OoII. If globular clusters are comprised of a single generation of stars, the cluster would appear as a single Oosterhoff type. However, some stars evolve more quickly, and there could be more than a single generation of stars in a single cluster. As the range of periods in ω Cen in Fig. 1.9 shows, OoII clusters appear more evolved by the progression of part of the population from OoI to OoII. This theory is then reiterated in Jurcsik et al. (2014) where a second generation of RRc objects is proposed

to exist in the GC M3.

The Oosterhoff groups also have interesting implications for galaxy evolution. The Milky Way halo RR Lyrae stars are predominantly OoI and the galactic plane is more OoII. When the dwarf galaxies surrounding the Milky Way were analysed they fell into the Oosterhoff gap which contradicts the theory that the halo is created from historical mergers with dwarf galaxies (Smith et al., 2009). They can also map out the dwarf galaxy populations; for example, finding 128 RR Lyrae stars helped to map out M54 (part of the Sagittarius Dwarf Spheroidal Galaxy (Sgr dSph) behind the galactic bulge. A separate population of stars in a stellar stream cutting vertically through the bulge were identified that could be part of a disrupted GC or dwarf galaxy (Soszyński et al., 2014).

1.3.6 Period doubling

An interesting feature that has recently been observed in Kepler data is 'period doubling' (Szabó et al., 2010). With period doubling, light curve peaks appear to alternate in amplitude giving the appearance that there are two pulsation modes with slightly different amplitudes, beating together in resonance but out of phase by half a period. Therefore the period of each pulsation mode is actually twice the main pulsation period. Even more interesting is that this feature only appears in Blazhko RR Lyrae stars, including RR Lyr itself, V360 Lyr (part of which is shown below in Fig. 1.11), and V460 Lyr. Realistic models of the Blazhko effect must be able to replicate this recently discovered feature, as well as amplitude modulation and frequency modulation. This feature was not observed by ground based telescopes, due to the near half–day periods of RR Lyrae, and has emerged from analysis of data from the space bound Kepler telescope. Moskalik et al. (2015) has also detected period doubling in RRc objects where it appeared in frequency spectra (see Sect. 1.4.3 below) at 1/2 and 3/2 times the recently discovered additional $0.61 \times f_1$ mode.

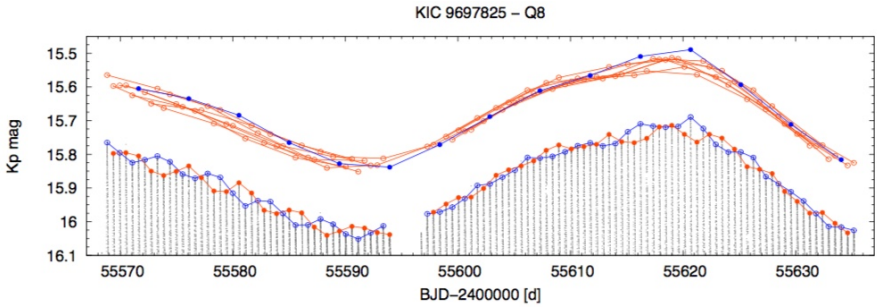

Figure 1.11: Lightcurve of V360 Cyg. The lower part shows alternating pulsation peaks in red and blue to help identify the two separate pulsation modes that are combined to produce the overall light curve. This combination of two apparent pulsations is known as period doubling. The lines in the upper section of the diagram are drawn across every eigth peak to highlight what appears to be an overall period consisting of 8 shorter beats resulting from overtone resonances. The figures at the bottom of the diagram refer to days after the barycentric julian date (BJD) 2400000 and the vertical axis is labelled in Kepler magnitudes. (Reproduced from Molnár et al., 2014, Fig. 1, p. 2)

In summary, stars can pulsate in several ways and it is these pulsations that define the fundamental mode RRab class of RR Lyrae pulsating variables. Before being able to investigate the Blazhko Effect, the methods of analysing pulsations from photometric data such as that from SuperWASP observations are described in the following section.

1.4 Data Analysis

This section explains some of the methods used when analysing periodic signals in astronomy as applied to RR Lyrae stars. Results from non–modulated pulsation signals are explained first; how modulation can be found in these signals using these techniques is explained later in the Modulation section. These methods cover, firstly, investigating the pulsations using the more intuitive time domain analysis; then investigating the phase domain using O–C techniques is briefly described; before finally moving onto the frequency domain with spectral analysis.

1.4.1 Phase folding

Phase folding involves finding the period of a light curve, and repetitively overlaying segments of the light curve divided by this period. The phase is the fraction of the cycle, from zero to one whole period. The horizontal axis represents the phase of the cycle, and periodic features such as peaks and dips will appear at the same phase point along the horizontal

axis if the correct period is used. Since it may only be possible to observe parts of individual cycles during individual observing sessions, a more complete picture can be built up by overlaying multiple cycles of the light curve. Phase folding larger numbers of segments of the light curve increases the precision of the calculated period because the higher number of observed data points will contribute to a better quality light curve, and the effect of outliers due to bad observation conditions ('seeing') is reduced.

A typical method of folding the light curve involves Phase Dispersion Minimisation (Norton et al., 2007; Stellingwerf, 1984). This involves folding the light curve by a trial period, binning the data points and totalling the scatter (or dispersion) across all bins. With a poor trial period, the light curve will be featureless and the scatter in each bin will be large. The mean flux of each bin will also be close to the mean level for the whole light curve and the total of the differences will give a low result. For the trial period closest to the true period, the total dispersion in each bin will be minimised, while the difference between the mean values in each bin and the mean level of the whole light curve will be maximised. The dispersion can be measured using a least squares fit, such as a χ^2 fit. The process can be made more robust by finding periods where a low bin dispersion figure coincides with a large light curve dispersion result. However, phase folding is susceptible to aliasing where longer false periods are created by daily duty cycles, or yearly observational patterns. In such cases the light curve will not have a realistic shape, which can be verified by visually checking (or 'eyeballing').

1.4.2 O–C diagrams

Analysis in the phase domain can be performed using observed–minus–calculated (O–C) diagrams where long–term deviations from a light curve with constant period are plotted against time. As the name suggests O–C diagrams measures this difference between the calculated or modelled (C) phase and the observed (O) phase. Calculating accurate residuals therefore requires accurate periods. In the case of pulsating stars, the ephemeris of the peak (maxima) may be used, but sometimes the entire phase folded light curve is modelled and compared with the observed light curve (Hajdu et al., 2015) because of the difficulty in matching quadratic (parabolic shaped) models to the maxima of RRab light curve. In other objects such as eclipsing binaries, the ephemerides of minima are routinely used (Lohr et al.,

2012), although, again, better results are achieved by modelling the entire folded light curve (Lohr et al., 2013).

1.4.3 Fourier transforms and power spectra

Fourier decomposition is the breaking down of complex waveforms (the shapes of signals) into simpler sine and cosine components each with their own frequency, amplitude and phase. These components can then be seen when plotted against a range of frequencies, thereby changing the time domain to the frequency domain (or frequency space). Performing a discrete Fourier transform:

$$\mathrm{FT}_X(\omega) = \sum_{j=1}^{N_0} X(t_j) \exp(-i\omega t_j) \tag{1.10}$$

on a sample of data $\{X(t_i), i = 1, 2, ..., N_0\}$ (hence the reason for the *discrete* Fourier transform) causes the components at specific frequencies (ω) to be left while other frequencies cancel out. The equation above expresses the power spectrum as a normalised sum of the combination of the data X at times t_j and a second function dependent on the frequency and the timings t_j themselves. This second function is the spectral window function which represents the normalised sampling regime of the observations, but is independent of the data itself. In the time domain it consists of delta functions at each time of observation, forming a function known as a Dirac comb. In the frequency domain, as the number of observations $N_0 \to \infty$ each observing frequency can also be represented by a delta function $\delta_j(\omega)$ at each sampling frequency, (ω), forming a Dirac comb, but where the spacing becomes $1/T$ for regularly sampled data. The spectral window is therefore

$$\delta_j(\omega) = \sum_{j=1}^{j=N_0} \exp(-i\omega j) \tag{1.11}$$

Since $\delta_j(0) = N_0$ for both regular and irregular sampling, the spectral window function is normalised by N_0^{-1} so that $\gamma_j(0) = 1$. The spectral window function is now defined as $\gamma_j(\omega) = N_0^{-1}\delta_j(\omega)$. The observed Fourier transform is the convolution of the raw data $F(\omega)$

with the spectral window function:

$$N_0^{-1} P_X(\omega) = X_j(\omega) * \gamma_j(\omega) \tag{1.12}$$

In the case of real observations with complex irregular sampling regimes, and a finite number of observations over a finite time, the spacing between each delta function $\delta_j(\omega)$ is no longer regular and the spectral window function therefore becomes more complicated due to interference between the peaks in the function, as shown in the Fig. 1.12. Recovery of the original signal is no longer a trivial deconvolution exercise, and requires more advanced techniques such as the CLEAN algorithm which is described in more detail in Chapter 4. The recovery of the actual signal involves reversing the effect the window function has had on that original signal. To do this reversal, the convolution of each component part of the signal with the window function needs to be removed from the observed raw power spectrum. Normally each component can be identified by their relatively high intensity in the power spectrum. Since the window function depends only on the timing of the samples and not on the data, it is possible to recreate the window function for each object purely from the timings of the observations. Each identified component can thereby be convolved with the correct window function and the result removed while retaining the location and power of the component in order to recreate the power spectrum of the original signal.

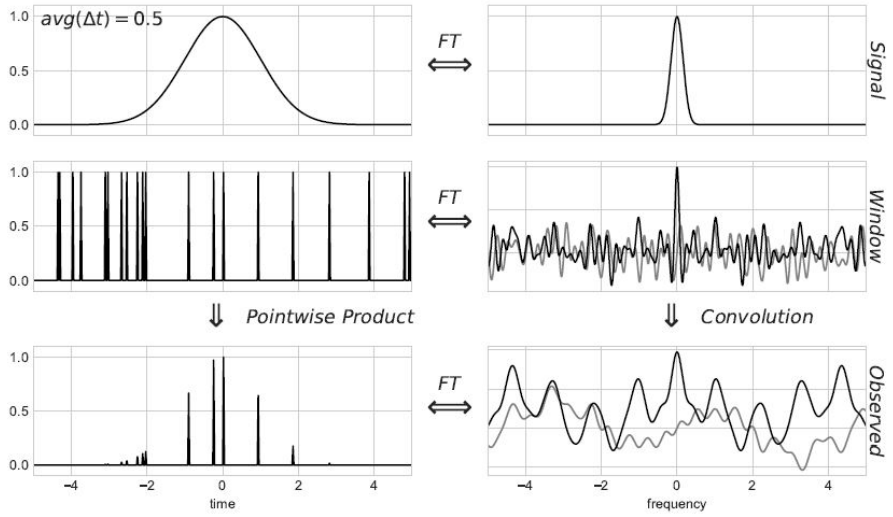

Figure 1.12: The middle left panel shows the dirac comb in the time domain showing the irregular spacing. The middle right panel highlights the complexity of the Fourier transform of this irregular sampling. The bottom right panel shows the convolution of a simple sinusoidal signal with the complex window function resulting in a complex power spectrum.(Reproduced from VanderPlas, 2017, Fig. 9, p. 17)

The Fourier transform will normally result in complex components; squaring the modulus of these components produces real amplitudes showing the strength or power of those frequencies (Scargle, 1982):

$$\begin{aligned} P_X(\omega) &= \frac{1}{N_0} |\mathrm{FT}_X(\omega)|^2 \\ &= \frac{1}{N_0} \left| \sum_{j=1}^{N_0} X(t_j) \exp(-i\omega t_j) \right|^2 \\ &= \frac{1}{N_0} \left[\left(\sum_j X_j \cos \omega t_j \right)^2 + \left(\sum_j X_j \sin \omega t_j \right)^2 \right] \end{aligned} \tag{1.13}$$

These can then be plotted against frequency as a power spectrum or a 'periodogram'. As noted in Sect. 1.3, the shape of RR Lyrae pulsations are a product of the combination of several harmonic signals. When these are broken down, or decomposed, using discrete Fourier transforms, the main pulsation frequency appears as the largest peak, with smaller peaks at other frequencies representing the harmonics as shown below in Fig. 1.13. For RRab class pulsators, the fundamental harmonic is the strongest with the higher frequency harmonics giving rise to the distinctive 'saw-tooth' shape made up from smaller peaks at small–integer multiples of this frequency.

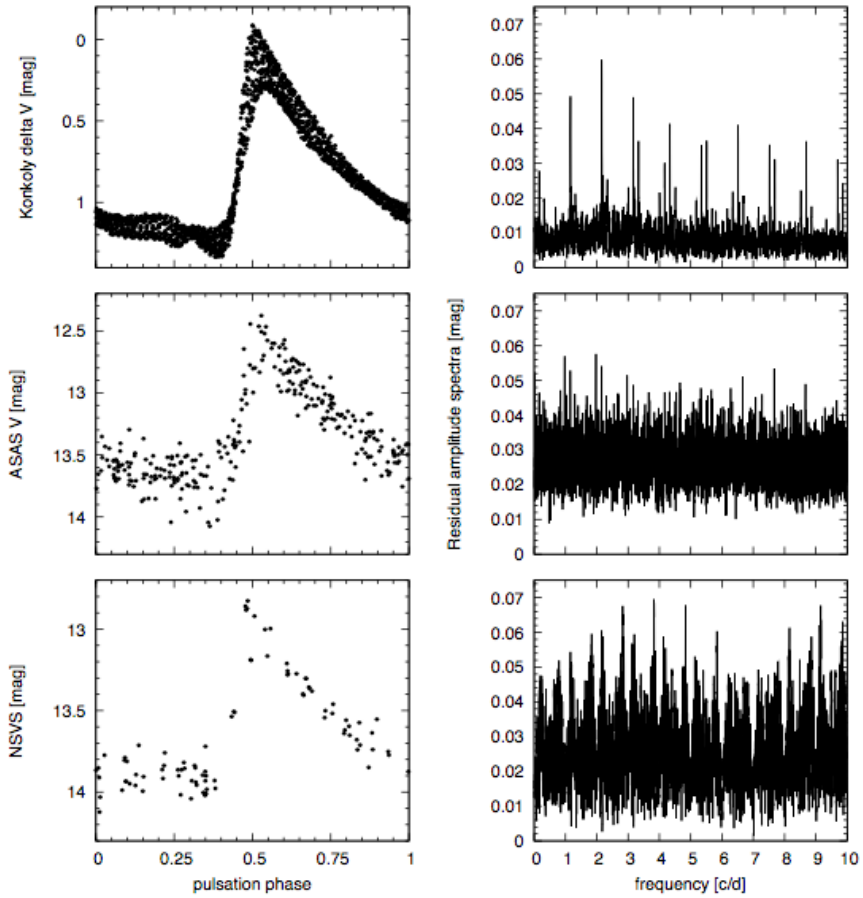

Figure 1.13: Light curve and periodograms for UZ Vir. The labels on the left give the survey used, the left hand plot is the light curve and the right hand column shows the periodogram calculated from the same data. The peaks represent the Fourier transforms of the pulsation frequency components, with their heights giving their amplitude. The top row demonstrates how good data results in both a well defined light curve and power spectra. (Reproduced from Jurcsik et al., 2009, Fig. 2, p. 4)

Fig. 1.13 above shows how periodograms can suffer from general white noise which appears as short spikes across the entire spectra, known colloquially as "Fourier grass" (Holdsworth et al., 2014) or from red noise at low frequencies (combinations of both red and white noise have been referred to as pink noise (Smith et al., 2009)).

Where if there is a strong peak in the spectral window function at a different frequency, ω_0, an alias of the real signal at ω will appear at $\omega - \omega_0$ due to the convolution of the real signal with the window function.

Ground based surveys such as ASAS and SuperWASP (see Chapter 2) are susceptible to this aliasing due to daily and seasonal windows of observation, which can create false peaks in Fourier transforms of light curves (Skarka, 2014a) as shown in Fig. 1.14, unless systematic detrending is performed. Aliases can also cause phase dispersion minimisation techniques to find the wrong minimum, resulting in the wrong pulsation or modulation period.

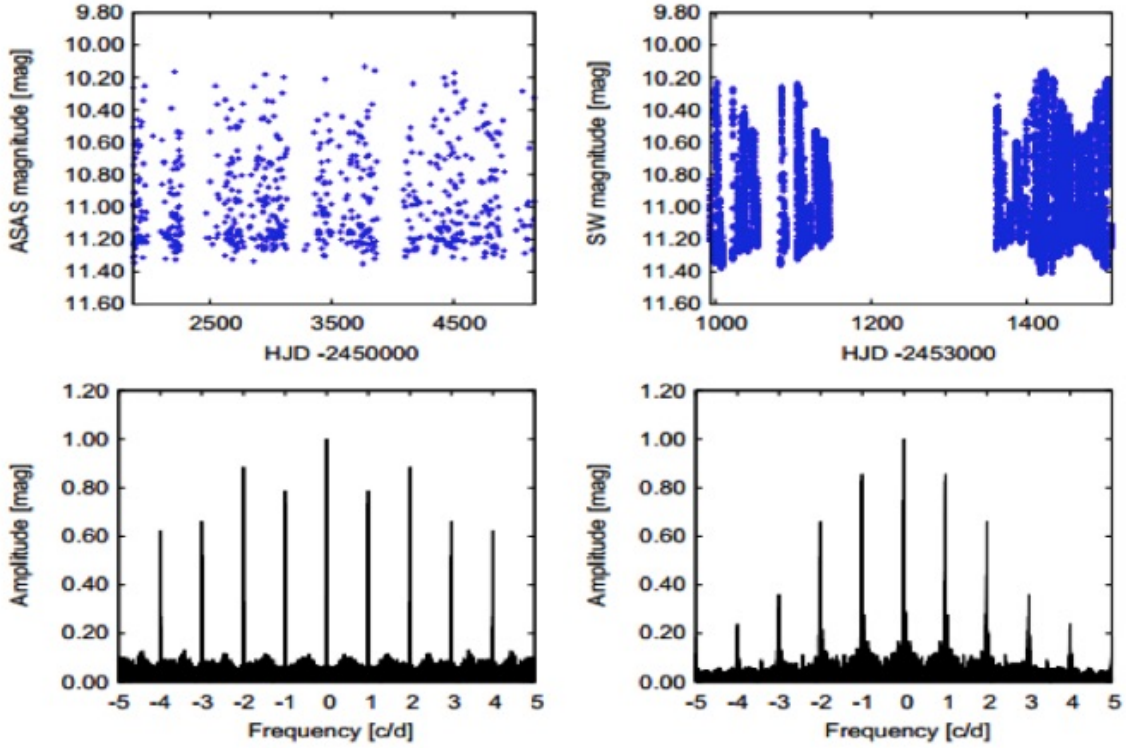

Figure 1.14: Differences in ASAS and SuperWASP (labelled SW in the figure) observations show a seasonal gap in the SuperWASP data. ASAS has smaller gaps in their data but the number of individual points is also greatly reduced. Each gap produces a sizeable Fourier component. (Reproduced from Skarka, 2014a, Fig. 1, p. 2)

This is demonstrated for SuperWASP object 1SWASPJ004929.43+142111.6 in Fig. 1.15 where the frequency spectrum from the sampling regime can be seen in the middle panel and the convolution of both signals in the bottom panel. The abscissa is logarithmic to highlight frequencies normally associated with the Blazhko effect. One day^{-1} equates to 1.16×10^{-5} Hz so 10^{-6} Hz is roughly a 10 d period and 10^{-7} Hz is roughly a 100 d period. The daily alias at 1.16×10^{-5} Hz is the strongest peak in the window function shown in the middle panel. The main pulsation frequency and harmonics that make up the non-sinusoidal shaped RRab light-curve can be seen at frequencies above 10^{-5} Hz in the top panel. The same right hand section in the bottom panel shows the effect of the complex combination of these peaks with the window function in Fourier space.

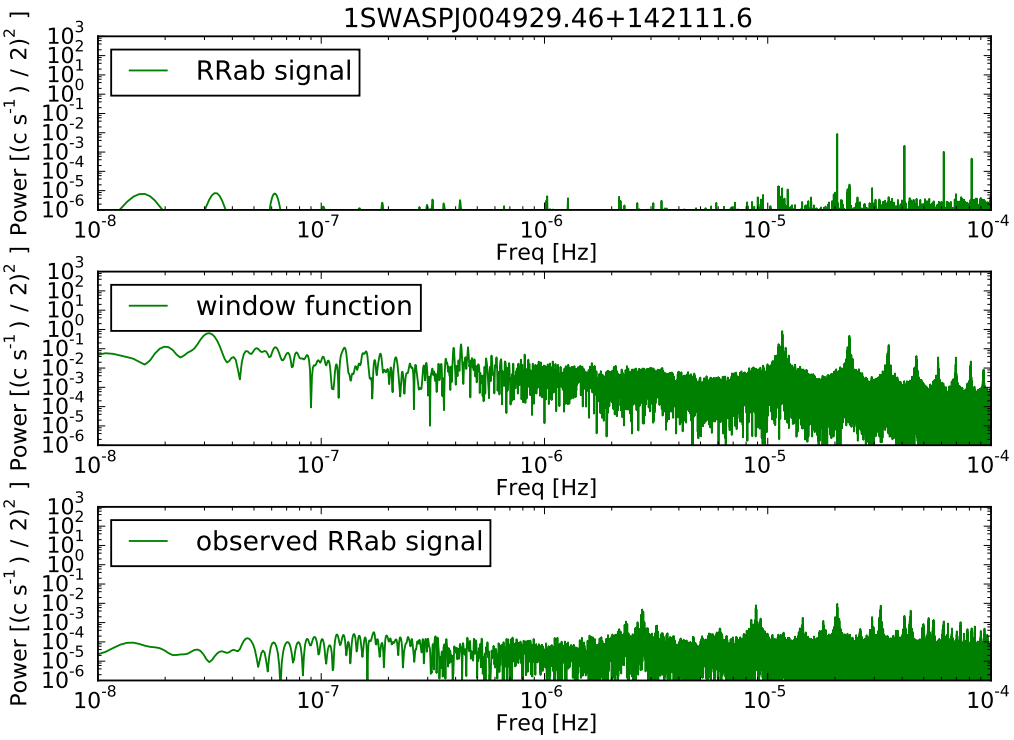

Figure 1.15: Effect of sampling on observations of a variable object. The top panel shows the Fourier spectrum of the pulsation which has to be separated out from the window function. The middle panel shows the Fourier transform of the window function created by the SuperWASP sampling regime. The bottom panel shows the combination of the top two panels which is how the actual Fourier spectrum of the variable object appears before any processing has been performed.

However such artefacts can be reduced or eliminated by pre–whitening which convolves a particular frequency with the window function and removes all or some of the resultant power spectrum from the signal's observed spectrum (Evans et al., 2015; Chadid et al., 2011). Computer programs such as Period04 (Lenz and Breger, 2005) can be used to systematically calculate the frequency spectrum of a single star using Fourier transforms (Holdsworth et al., 2014; Skarka, 2014a).

Period analysis can also be performed using the Lomb–Scargle statistical analysis algorithm (Sariya et al., 2014). The Lomb–Scargle technique produces a function which is an estimation of Fourier power against period. It is achieved by performing a least–squares fit of a series of candidate frequencies to the frequency spectrum created by a Fourier transform of the signal. The most likely frequencies thereby have the strongest power, which then appear as higher peaks in the plot of power against period. The benefit of the Lomb–Scargle method over classical periodograms is its ability to maintain a chi–squared distribution with unevenly sampled data, such as that from ground–based observations, and with it, the abil-

ity to determine a maximum likelihood through least–squares fitting. It accomplishes this through application of a phase delay term and appropriate scaling of the terms in the generalised periodogram. These defining changes mean the Lomb–Scargle periodogram is equivalent to fitting a single sinusoid wave function at each candidate frequency and recording the goodness of fit of each wave.

Damasso et al. (2014) uses an IDL version of the Lomb–Scargle algorithm (available at http://www.arm.ac.uk/~csj/idl/PRIMITIVE/scargle.pro). The later section about the CLEAN program (Sect. 4.2.2) describes how CLEAN iteratively convolves an amount of the strongest frequency (described as the gain) with the window function before removing this, which has the effect of gently removing the effects of the window function while having a minimal effect on weak signals.

Once the data has been prepared, separate components can be isolated and analysed. In the case of RRd this might be to identify different modes based on the phase difference to the fundamental mode, or the relative strength of secondary modes to the fundamental mode (Skarka, 2014b). It can also lead to the identification of non–radial modes that do not match any overtones of known radial modes.

Having explained how regular periodic signals from stars can be analysed in this section, the definitions, methods of discovery and investigations into the deviations from this regularity can now be described in the following section.

1.5 Modulation of a pulsation period

This section gives an overview of modulation of pulsations before the specific modulation of the Blazhko effect is discussed in the next section. The techniques described in the previous section for analysing periodic signals can also show the symptoms of pulsation modulation. They can therefore be used to identify and analyse the properties of this modulation if these symptoms can be understood and deciphered.

Modulation is a cyclic change in a periodic signal in either frequency or amplitude over timescales longer than the main signal's period, causing the regular periodic signal to change slightly over time. Modulation may be recognised as the superpositioning of one frequency onto another; for a star this would be placing a longer modulation frequency onto the main

pulsation period. How the two frequencies interact dictates whether interference between the frequencies causes the pulsations from the star to appear to grow brighter and fainter over time (amplitude modulation), or the main frequency increases or decreases (frequency modulation) due to the influence of the second frequency. These effects can be seen in the diagrams below in Fig. 1.16. Amplitude modulation (AM) is best seen in the time domain as the amplitude can be seen to regularly increase or decrease over time, and this is achieved by multiplying two sinusoidal functions together: $\cos \Omega t \cos \omega t$. It can also appear as a separate peak in frequency space at the modulation frequency if it causes a change in the mean pulsation amplitude. Frequency modulation (FM) can be seen in frequency space as it creates equidistant peaks on either side of the main pulsation frequency and its harmonics, known as sidepeaks or sidebands. Integrated over time, frequency modulation appears as phase modulation. FM can be achieved by applying a sinusoidal signal to the the frequency component of the carrier's sinusoidal waveform forming the $M \cos(\omega t \cos \Omega t)$ composite function.

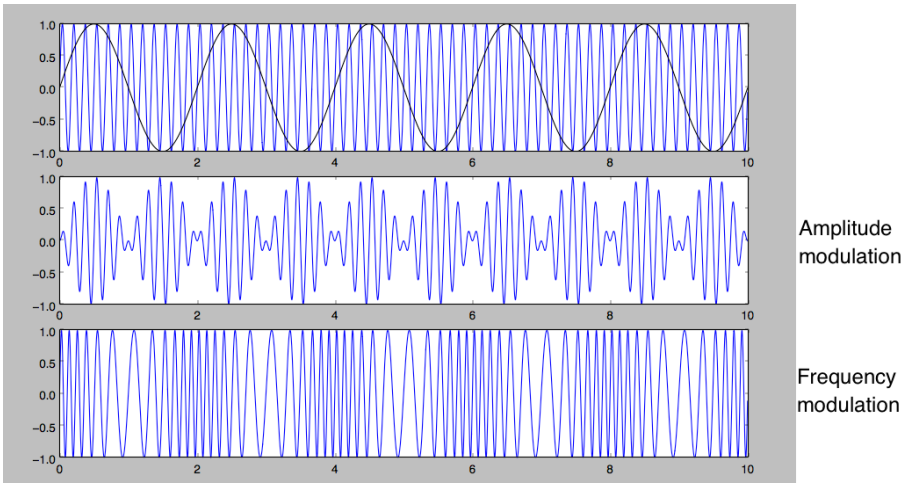

Figure 1.16: Schematic diagram of amplitude and frequency modulation created by the author. The top panel shows two sine waves plotted over each other. The middle panel shows amplitude modulation created by multiplying the two waves together. The bottom panel shows frequency modulation created by applying the lower frequency sine function to an existing sine wave of a different frequency. Both axes are in arbitrary units.

Resonance and beat frequencies both produce amplitude modulation. Resonance occurs when both signals complete a whole number of periods within a certain time, in a whole number ratio such as 3:2, 4:3 or even 9:2 (as shown later in section 1.7 on Blazhko effect models). The two frequencies therefore do not need to be a similar value but are locked together in the same phase.

Beat frequencies occur when one or two close pairs of radial modes (Kurtz, 2006) have similar frequencies but are not in phase. The higher frequency signal appears to slip past the slower one as the peaks of the two waves slowly approach each other before passing, leading to amplitude modulation effects. Both resonance and beat frequencies create interference and a higher amplitude at regular intervals. The following sections explain how amplitude modulation and frequency modulation can be seen and measured in time and frequency domains.

1.5.1 Phase folding

Phase folded light curves will appear blurred, or smeared, vertically in the case of amplitude modulation and horizontally in the case of frequency modulation. Folding the light curve at the correct modulation period will mean amplitude modulation appears as sinusoidal variations in the heights of individual pulsations: known as the envelope function. This envelope function is demonstrated in Fig. 1.17 for an object folded at its known modulation period of roughly 70 d.

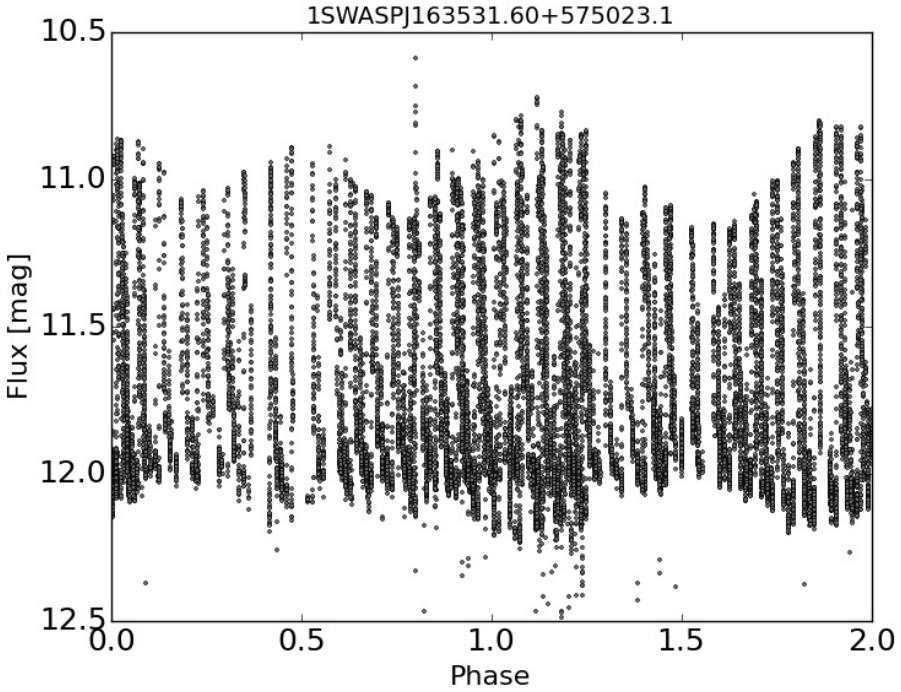

Figure 1.17: RW Dra phase folded at its known modulation period of 71.4 d

With sinusoidal amplitude modulation the modulation period can then be found by measuring the distance between successive peaks of the envelope function. However, this is difficult in cases where the modulation is multi–sinusoidal. Frequency modulation produces

a horizontal spread of the light curve, so a phase folded light curve can be used to identify the presence of frequency modulation and light travel time effects (section 1.5.3 below) although it cannot be quantified in the time domain. Phase folded light curve that are modulated due to the Blazhko effect are described in more detail later in section 1.6.3. Although phase modulation can affect the quality of the phase–folded light curve, it can be more easily identified and quantified using O–C diagrams, as described in the following section.

1.5.2 O–C diagrams

Since O–C diagrams show the difference in the timings of pulsations over time they can be used to identify cases where pulsations are phase modulated. This section describes how O–C diagrams are affected in three separate cases, with the final case being PM. When the modelled or calculated values matches the actual measurements, the O–C diagram is a horizontal straight line; there is no difference between observed and calculated timings across the timescale being investigated. In the case of a constant difference between observed and calculated, for example if the model simply had the wrong but constant period, the residuals in the O–C diagram still form a straight line, but it will be at an angle to the horizontal depending on how far off the correct period the model is, as shown schematically in Fig. 1.18a. The increasing distance from the x–axis represents an increasing difference with time, showing how the O–C value is cumulative; it is integrated across the amount of time being looked at. In the case where the *rate* of change is constant, such as in a period that is increasing or decreasing by a constant amount, the O–C line will be a parabola as drawn in Fig. 1.18b since the difference is now formed by the quadratic formula:

$$(O - C)(t) = aP(t)^2 + bP(t) + C \tag{1.14}$$

where $P(t)$ is the period of the pulsation for example (but could equally be the time between any event such as an eclipse, transit, or nova and is therefore sometimes represented by E for epoch), and a and b are constant coefficients. C is a constant that could represent the phase offset between the actual values and an otherwise correct model where a and b would be zero.

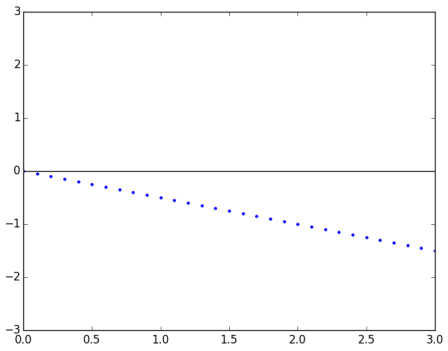

(a) Constant difference

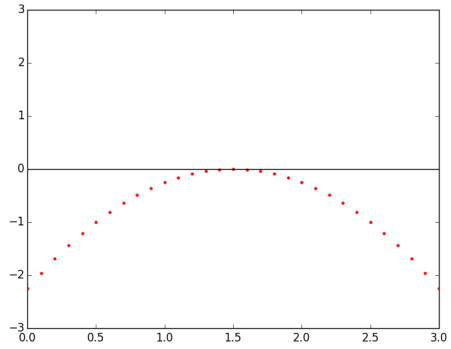

(b) Constant rate of change

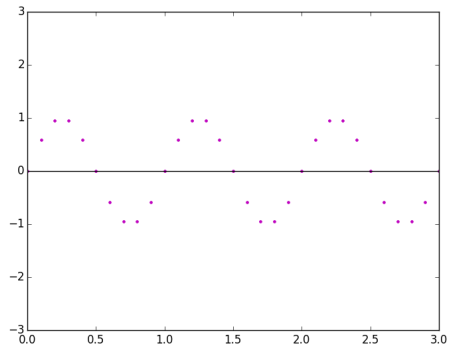

(c) Possible light travel time effect

Figure 1.18: O–C diagrams demonstrate how timing differences from a regularly occurring signal can be plotted. The O–C diagrams above show (a) a constant deviation, as in a period that is slightly too long, (b) a constant rate of deviation such as in a constantly decreasing period and (c) a sinusoidal curve such as in an idealised LTTE scenario, described below.

In the case of modulation, the O–C diagram will form a sinusoidal curve as the pulsation period increases and decreases periodically producing positive and negative O–C residuals. PM due to the Blazhko effect can be multiperiodic. It can produce an O–C diagram that varies from a pure sinusoidal and it can be highly asymmetric, as Sect. 1.6.3 will demonstrate. However, an O–C diagram of a non–modulated pulsator in a binary system will be

monoperiodic, even if the orbit (and therefore the sinusoidal O–C diagram) is eccentric, as described in the next section.

1.5.3 LTTE

Sinusoidal O–C diagrams (such as Fig. 1.18) can be due to light travel time effects (LTTE) and these provide clues to the presence of otherwise unobservable stars or even exoplanets. The finite speed of light becomes apparent over the distances involved in stellar systems, such as with binary stars where two stars orbit each other around a common centre of gravity. As one of the stars travels towards observers, the distance decreases, so the light takes less time to reach them. Pulsations from that star would arrive in smaller intervals, so the pulsation frequency appears to be increased. Likewise, the pulsation frequency of a variable pulsating star that is travelling away from an observer would appear lower. It should be noted that this is only an extrinsic effect created by the movement of the star around its orbit, the intrinsic pulsation frequency and light curve remain constant. The investigation of RR Leo by Alton (2014) demonstrates how variations in pulsation frequency can produce sinusoidal O–C diagrams, such as in Fig. 1.19 below.

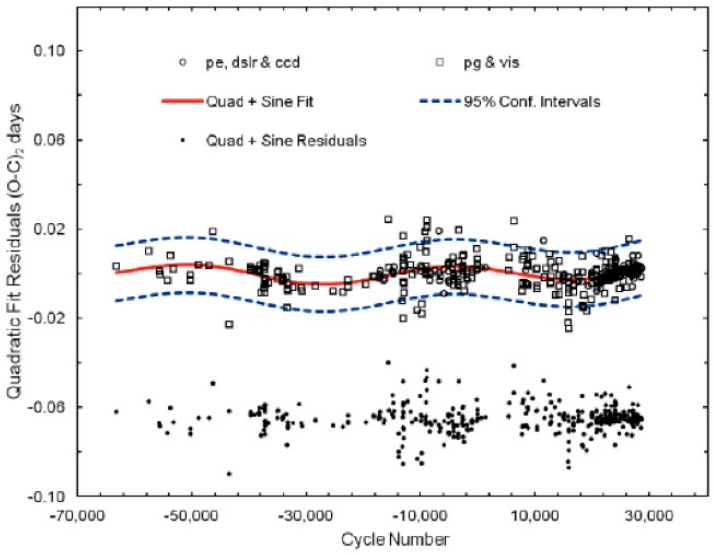

Figure 1.19: Period modulation of RR Leo. The clearly sinusoidal period modulation hints at a possibly kinematic solution due to light travel time effects caused by a companion object. See main text for how companion objects such as in a binary system can produce sinusoidal variations. (Reproduced from Alton, 2014, Fig. 4, p. 73)

LTTE is therefore an extrinsic phase modulation effect which is the result of external factors, in comparison to the intrinsic origins of amplitude modulation and frequency modu-

lation. The magnitude of LTTE depends on the distance between the two stars (which in turn depends on other physical attributes such as mass), and the angle of the plane of the orbit to our plane of observation, called the angle of inclination, i. LTTE therefore provides valuable information on the physical parameters of the components in a binary system, within a range of values governed by $\sin i$.

LTTE appear as an additional term in O–C equations (Li and Qian, 2014):

$$\tau = A\left[\left(1 - e^2\right)\frac{\sin(\nu + \omega)}{1 + e\cos\nu} + e\sin\omega\right] \tag{1.15}$$

where A is the projected semi major axis (which includes the inclination angle i), e is the eccentricity, ν is the true anomaly (the angle between the longitude of periastron and that of the object), and ω is the angle of the periastron in the orbital plane. In the case of LTTE, the O–C measurements will become sinusoidal as long as they are observed for long enough, otherwise the diagram could be misinterpreted as a segment of a parabola, rather than the cyclic effects of LTTE. Asymmetry in the curve (as compared to a normal sine curve) shows that the orbit is eccentric and the major axis is not along our line of sight. A sharp minimum tells us that the periastron, or point of closest approach of the star to the centre of gravity of the binary system (barycentre), is positioned closer to us than the centre of gravity.

Stothers (2006) stated that no companion objects to RR Lyrae stars have been found. More recent work by Li and Qian (2014) shows that some RR Lyrae are thought to exist in binary systems as shown by sinusoidal O–C diagrams for V894 (Fig. 1.20a) and FN Lyr (Fig. 1.20b).

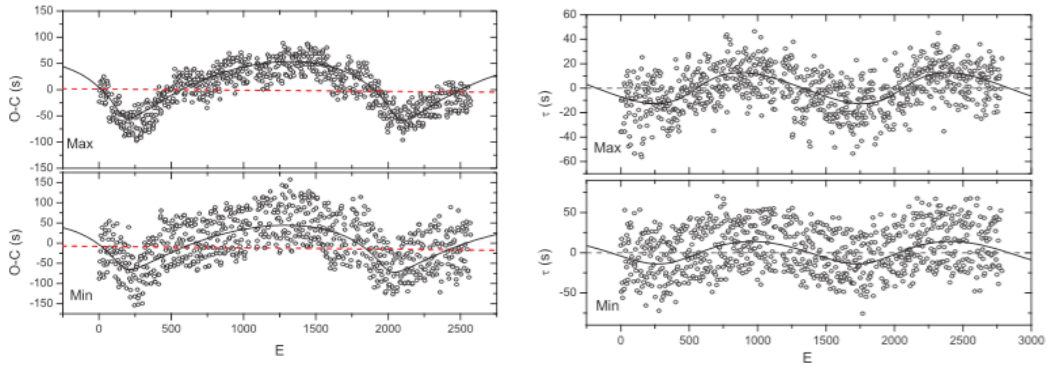

(a) O–C diagram for V894 Cyg (b) O–C diagram for FN Lyr

Figure 1.20: O–C diagrams for V894 Cyg and FN Lyr showing curves that hint at LTTE effects described in the main text. The asymmetry and sharp minima compared to a sine curve are due to the eccentricity of their orbits, and the length and orientation of the periastron to us. (Reproduced from Li and Qian, 2014, Fig. 7, p.604 and Fig. 6, p. 603)

Fig. 1.21 below from Murphy et al. (2014) shows the O–C diagram for the double pulsator binary system KIC 4471379. The highest 9 peaks in the Fourier spectrum are identified, time delays on these 9 frequencies are calculated over a 10 day segment of the light curve, which are then plotted as an O–C diagram.

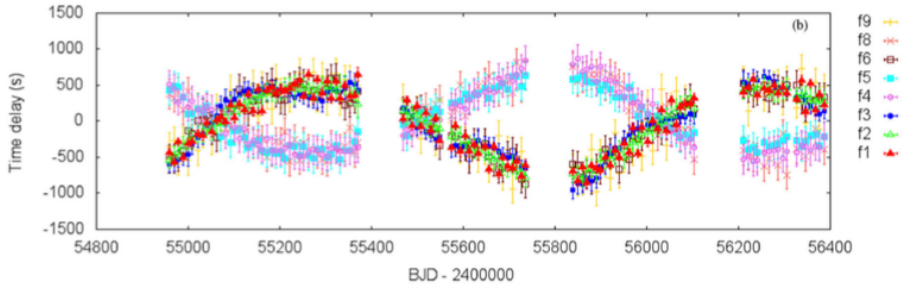

Figure 1.21: O–C diagram derived from the Fourier spectra for the δ scuti star KIC 4471379, forming two alternating sinusoidal curves. This system is interpreted as being a double pulsating binary system. The horizontal axis is in Barycentric Julian Dates and the period had been calculated as 960 ± 12 days. (Reproduced from Murphy et al., 2014, Fig. 7, p. 2524)

1.5.4 Fourier analysis

The previous two subsections described how modulation can be detected in the changes in pulsation amplitude or phase over time. Alternatively, both amplitude and frequency modulation can be identified simultaneously in frequency space, as this section now explains. A common approach to investigate the modulation of pulsating light curves is to analyse their Fourier spectra due to the characteristic multiplets that modulation produces in frequency

space: small peaks spaced symmetrically on either the main pulsation frequency and its harmonics. These sidepeaks produced by both AM and FM can be described in terms of the stars' pulsation being the carrier signal or wave, and the modulation being a second modulating signal or wave. How these two waves are combined creates AM or FM. AM is the more intuitive of the two forms of modulation, so it will be considered first. The following equations are taken from Benkő et al. (2011). The carrier signal's amplitude U_c is modulated with a modulating wave $U_M(t)$ defined as

$$U_m(t) = U_m^A \sin\left(2\pi f_m t + \phi_m^A\right). \tag{1.16}$$

where U_m^A, f_m, and ϕ_m^A are the modulating amplitude, frequency and phase respectively of the AM modulating signal.

This produces the modulated signal $U_{AM}(t)$:

$$U_{AM}(t) = [U_c + U_m(t)] \sin(2\pi f_c t + \phi_c). \tag{1.17}$$

The Fourier transformation of this AM modulates signal has a pair of sidepeaks at $f_c \pm f_m$, i.e. one on either side of the central peak of the carrier signal's frequency separated by the modulation frequency, forming a triplet. In the case of simple AM where there are no other modulation signals and sampling is regular, these sidepeaks have equal power.

In the case of FM the instantaneous frequency of the carrier signal is modulated by another periodic signal at a different frequency, whereas in PM the phase of the carrier signal is affected by the second signal. The phase modulated signal $U_{PM}(t)$ becomes

$$U_{PM}(t) = U_c \sin\left[2\pi f_c t + k_{PM} U_m^P(t) + \phi_c\right] \tag{1.18}$$

where k is the constant level of PM, and U_c, f_c and ϕ_c are the amplitude, frequency and phase of the carrier signal, respectively.

Since the instantaneous frequency is the derivative of the angle part of the signal (containing both signal frequency and phase), the modulated instantaneous frequency needs to be

integrated when inserting into the angle part of the main carrier signal:

$$f(t) = \frac{\mathrm{d}\Phi}{\mathrm{d}t} \tag{1.19}$$

where Φ is the angle part of the signal. With frequency modulation, it is this instantaneous frequency $f(t)$ that is modulated by $k_{FM}U_m^F(t)$ becoming $f(t) = f_c + k_{FM}U_m^F(t)$ where k_{FM} is the maximum change in f_c and U_m^F is the amplitude of the modulating signal. The angle part becomes

$$\Phi(t) = 2\pi f_c t + 2\pi k_{FM} \int_0^t U_m^F(\tau)\mathrm{d}\tau + \phi_c \tag{1.20}$$

The integral of the sine wave modulated by frequency f_m is:

$$U_m^F(t) = \frac{U_m^F}{2\pi f_m} \sin\left(2\pi f_m t + \phi_M^F\right) \tag{1.21}$$

Substituting the integrated modulation frequency into the angle part of the modulated signal, and then inserting this angle part into the full waveform gives

$$U_{FM}(t) = U_c \sin\left[2\pi f_c t + \eta \sin\left(2\pi f_m t + \phi_m^F\right) + \phi_c\right] \tag{1.22}$$

where η is known as the modulating index, defined as the ratio of the modulating signal strength and the modulating frequency: U_m^F/f_m. Converting Eq. 1.22 to a form using Bessel functions:

$$U_{FM}(t) = U_c \sum_{k=-\infty}^{\infty} J_k(\eta) \sin\left[2\pi f_c t + \sin\left(2\pi f_m t + \phi_m^F\right) + \phi_c\right] \tag{1.23}$$

This gives a clearer representation of the effect of modulation when looking at a frequency spectrum: the central peak has a series of sidebands at $f_c \pm f_m$ whose dampened amplitudes are defined by the Bessel function term. The modulation frequency f_m is still the difference between the central peaks and the sidepeak.

This section has described how modulation affects the methods used to observed and analyse the signals from pulsating stars. The background and examples of the particular modulation detected in RR Lyrae is the topic of the following section.

1.6 The Blazhko Effect

The Blazhko effect is a combination of amplitude modulation and frequency modulation of the pulsations of RR Lyrae stars (Le Borgne et al., 2014). Amplitude modulation is seen as a slight increase of a few percent in the amplitude of the pulsation over many pulsation cycles, before the amplitude decreases and the Blazhko cycle starts over. The timescale of the cycle of modulations is usually called the Blazhko period. The light curve retains the typical shape (and therefore the pulsation itself) of an RR Lyrae variable over the cycle, as shown in Fig. 1.22 below for an RRab variable. Frequency modulation is seen as a cyclic variation corresponding to a change in period of a few minutes (Kolenberg et al., 2014) and can be seen as a horizontal spread on a folded light curve since the light curve will be folded according to a mean frequency. Both modulations are discussed in more detail in the subsequent sections.

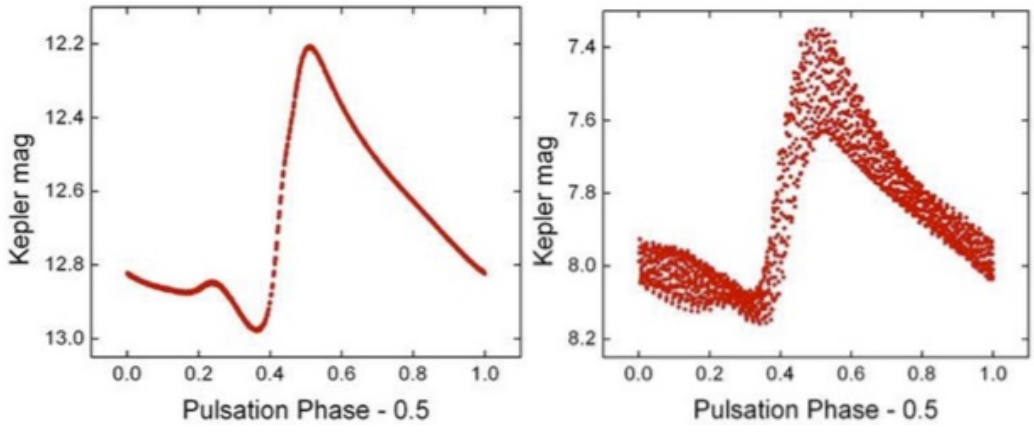

(a) Non–Blazhko (b) Blazhko

Figure 1.22: Light curve of the unmodulated variable star NR Lyr folded by its regular pulsation period on the left, and the light curve of the modulated star RR Lyr on the right. The x–axis is the phase of the pulsation (between 0 and 1). Note the spread of flux measurements for RR Lyr in both the vertical direction (amplitude modulation) and horizontal direction (frequency modulation). Also, the small bump just before the minimum is typical of RRab variables and is even included in the validation of some pulsation models. (Reproduced from part of Kolenberg, 2011, Fig. 1, p. 101)

1.6.1 History and surveys

The Blazkko effect is named after S. Blazhko who discovered frequency modulation while struggling to phase fold the light curve of RR Dra in 1907, followed by the discovery of the amplitude modulation of the prototype RR Lyrae itself by H. Shapley in 1916 (Szabó et al.,

2010) Despite being discovered over 100 years ago the physical cause of these modulations has not yet been explained.

Not all RR Lyrae exhibit the Blazhko effect, but the proportion of RR Lyrae stars with the effect has increased with recent Kepler observations: Skarka (2014a) gives the figure at about 31% of RRab stars using ASAS and SuperWASP surveys based on a sample of 321 RRab stars. Jurcsik et al. (2014) gives the figure as 48%, although this was from a much smaller sample of only 30 stars as part of the Konkoly Blazhko Survey of GC M3. The Blazhko effect has also been seen in 4 out of 10 RRd (double radial–mode) pulsators in their study of M3.

The variation of the shape of the light curve of the eponymous RR Lyr itself is shown in Fig. 1.23, demonstrating both features of the Blazhko effect: frequency modulation and amplitude modulation.

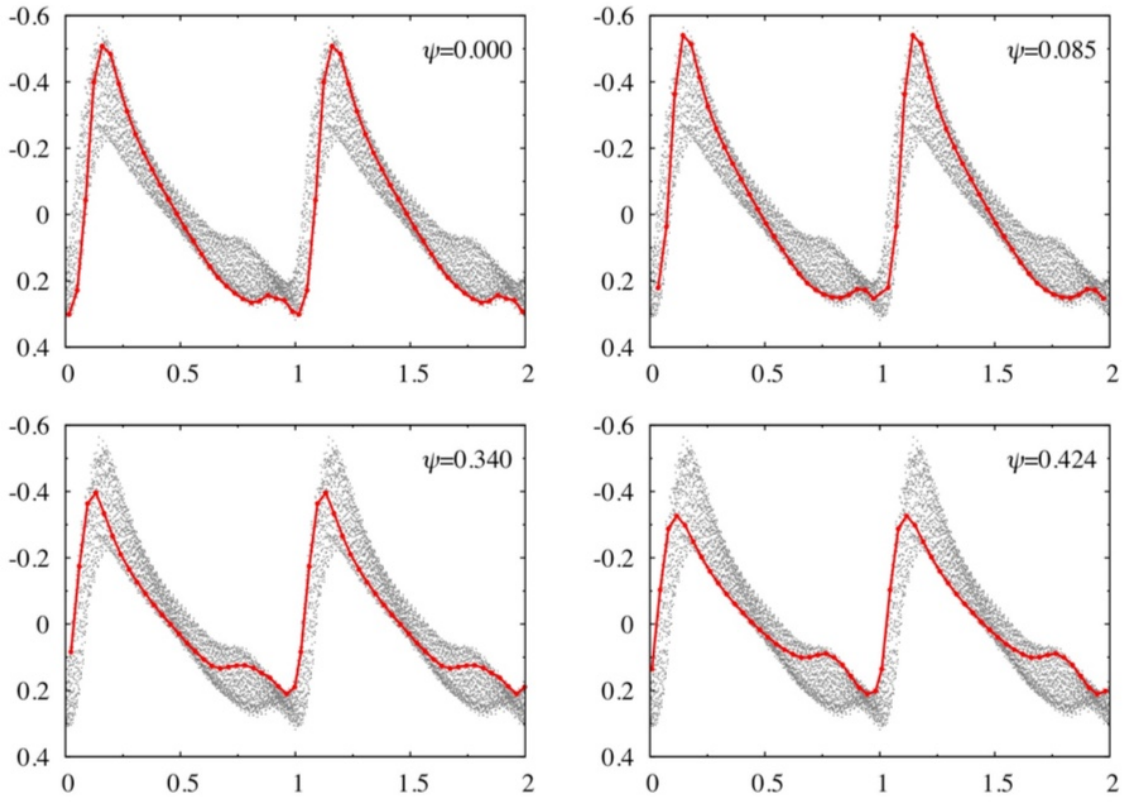

Figure 1.23: Change in the shape of the light curve of RR Lyr for two pulsation cycles throughout the Blazhko cycle. The grey sections show the combined light curves and the red lines show the light curve at the phase of the Blazhko period given in the top right of each panel. Note how the heights of the peaks vary due to amplitude modulation, and their slight change in pulsation phase demonstrates frequency modulation. (Reproduced from a section of Kolenberg et al., 2010a, Fig. 9, p. 8)

The Blazhko effect of RR Lyr has been the subject of in–depth analysis due to its posi-

tion within the Kepler space telescope's field of view (Le Borgne et al., 2014; Molnár et al., 2014; Nemec et al., 2013; Kolenberg, 2011; Kolenberg et al., 2010a). However, changes in its pulsations periods have not been regular, which would have been expected had the Blazhko effect period been constant (Le Borgne et al., 2014). The Blazhko effect of RR Lyra variously either has a period of 4 years Skarka (2014a), has a period of 14 years (Le Borgne et al., 2014), stopped for 4 years (Jurcsik et al., 2014), or paused at the start of the cycle (Chadid et al., 2011). However this variability in the variability also applies to RR Geminorum where no modulation was detected in a previous study in the 1970's and 1980's (Jurcsik et al., 2009). A study into RR Lyrae by Kolenberg et al. (2010a) using Kepler data gives a fundamental pulsation frequency of 1.76416 days^{-1} (a period of 0.5668 days) and a Blazhko frequency of 0.02560 days^{-1} (a 39.0625 day modulation period).

A comparison of Blazhko and non–Blazhko stars in Skarka (2014b), produces no correlation between Blazhko stars and the Oosterhoff groups. Also, their study revealed no propensity for Blazhko stars to have longer or shorter periods than other RR stars, stating mean periods of 0.532 d for Blazhko and 0.542 d for non–Blazhko RR Lyrae stars. The ratio of Blazhko to non–Blazhko stars in individual GC is thought to give a clue about the evolution of HB stars. The Blazhko effect may occur more in the first generation of RR Lyrae stars in globular clusters as the 10% of RRc stars in the cluster M3 exhibiting the Blazhko effect are thought to be the same generation of stars as the 50% of RRab and RRd stars also showing the effect (Jurcsik et al., 2014).

1.6.2 Amplitude modulation

The Blazhko effect causes the amplitude of the pulsations of RR Lyrae stars to vary periodically, although amplitude modulation is usually seen as a variation in flux in the folded light curve, which is the result of the combination of different pulsation modes. Modulations can be more pronounced in a single pulsation mode, such as in the first overtone (1O) rather than the fundamental (Jurcsik et al., 2014). The amplitude modulation of CoRoT ID 0105288363 is shown in Fig. 1.24 below.

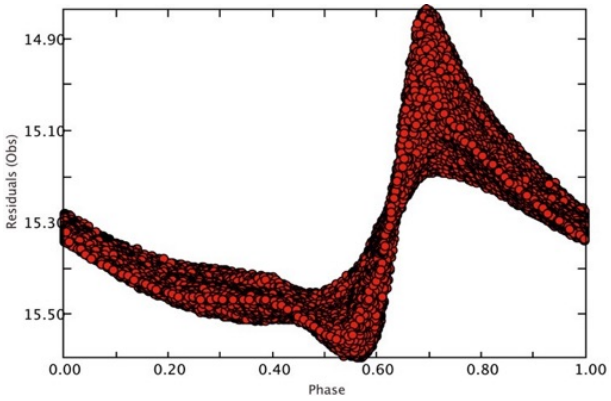

Figure 1.24: Modulation effect for CoRoT ID 01052888363. Even though this light curve was created from observations spanning only four Blazhko cycles, AM can be clearly seen for CoRoT ID 01052888363. Notice in particular the large spread of values at peak magnitude, a common feature of the Blazhko effect. (Reproduced from Chadid et al., 2011, Fig. 2, p. 4)

Another way of representing the Blazhko effect is by looking at the unfolded light cure over a long timescale. Groebel (2013) used the public SuperWASP archive to look at one star in the 2004 data designated GSC 02626–00896. Fig. 1.25 below shows 6 months of the light curve, individual 7.7 hour pulsations appear as vertical lines due to the compressed timescale, and the AM due to the Blazhko effect appears as an envelope function with a period of 26 d.

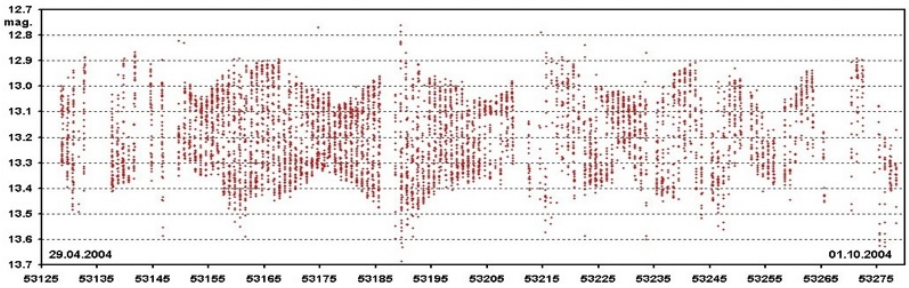

Figure 1.25: AM aspect of the Blazhko effect for GSC 02626–00896 over a five month timescale. On the long–timescale light curve of GSC 02626–00896 individual pulsations appear as vertical lines, and the AM is clearly visible as a variation in the maximum and minimum magnitudes. The variation in visible wavelengths is easily seen: this star has a variation in magnitude (Δ V) of 0.3 to 0.6 mag with a Blazhko period of 26 days. (Reproduced from Groebel, 2013, Fig. 3, p. 2)

Groebel (2013) noticed that the minima are fainter when the maxima are brighter – typical of the Blazhko effect. This can be seen in Fig. 1.25 above as a rough symmetry in the modulation pattern. Overall, Blazhko effect stars have a lower than average mean luminosity, only matching non–modulated stars at the Blazhko peak (Skarka, 2014b), but Nemec et al. (2011) put this as a mere 0.03 mag. V838 Cyg was cited as the lowest amplitude Blazhko

effect star found with oscillations of 0.02 mag in Nemec et al. (2013), but Skarka (2014a, and references therein) gives KIC 11125706 a magnitude fluctuation of 0.015 mag. No direct link between the mean amplitude of the star and the amplitude modulation has been found, for example V838 from Nemec et al. (2011) has the lowest oscillation magnitudes but is relatively bright compared to other stars in that survey.

Large levels of AM can subdue the pulsation amplitude until the distinctive sharp peak of the RRab class begins to resemble the more sinusoidal RRc class objects (see definitions in Sect. 1.3.4. This can lead to confusion about the actual pulsation mode as shown for example by Szosynski's assessment (Soszyński et al., 2014) of Drake et al. (2014). See Sect. 3.3.3 for SuperWASP object suffering from a similarly large scale AM. Fortunately, this can be resolved by checking the pulsation period: a change in pulsation mode must be accompanied by a corresponding change in pulsation period relating to the typical period ratios described above. In contrast, the following section describes the continuous and cyclic change in pulsation period associated with frequency modulations.

1.6.3 Frequency modulation

The second symptom of the Blazhko effect is the periodic modulation of the main pulsation frequency (the pulsation frequency appears to shorten and lengthen). This makes it difficult to find the exact period of the RR Lyrae pulsation using phase folding, as S. Blazhko originally discovered, because frequency modulation makes the periods longer and shorter which shifts each pulsation left or right on the plotted light curve producing horizontal scattering. Since frequency modulation is not as pronounced as amplitude modulation, as shown above in Fig. 1.24, analysing frequency modulation using phase dispersion minimisation techniques is restricted even if it can be visually identified by horizontal spread on the light curve.

Hoever, the phase modulation produced by the Blazhko effect can be detected using O–C diagrams. The results are distinct from LTTE type O–C diagrams, as can be seen from comparing Fig. 1.20 and Fig. 1.26 below. The LTTE O–C appears more sinusoidal than the Blazhko effect O–C where the position of the pulsation maxima change rapidly in parts of the Blazhko cycle. Hajdu et al. (2015) point out that the Blazhko effect is approximately two orders of magnitude larger than LTTE effect. Therefore, LTTE investigation should only be

attempted on non–Blazhko RRab stars.

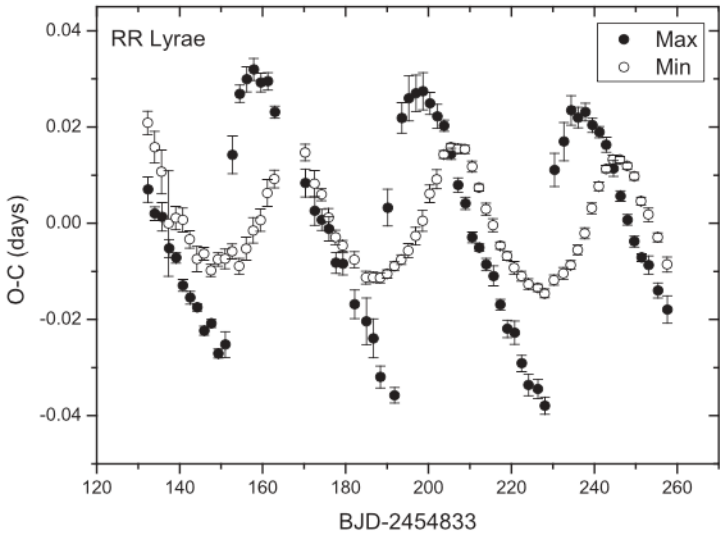

Figure 1.26: O–C diagram for Blazhko effect star RR Lyr showing the maxima as filled circles and the minima as empty circles. Note how the minima points form roughly sinusoidal curve but that the maxima points form a discontinuous curve with decreasing minima. (Reproduced from Li and Qian, 2014, Fig. 7, p. 602)

Fig. 1.27 below shows how the Blazhko effect manifests itself in the power spectrum of the RRab star CoRoT ID 0105288363: the inset shows a magnification of the base of the main pulsation frequency. The multiplet of small peaks are usually taken as evidence of additional pulsation modes in the case of Blazhko stars (Bryant, 2015; Kolenberg et al., 2010a).

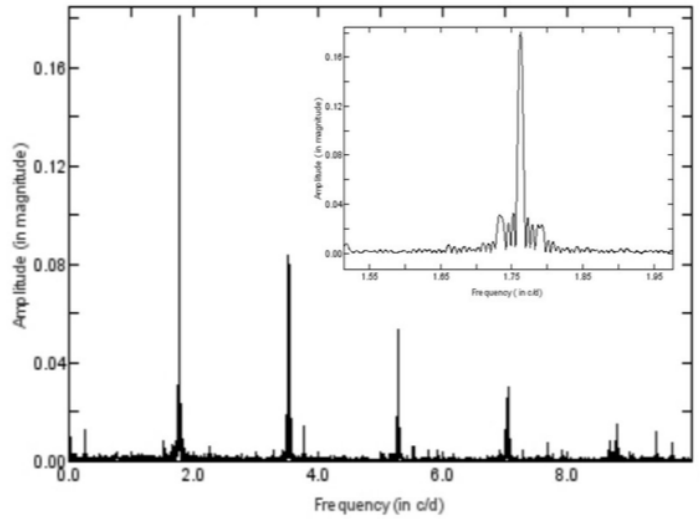

Figure 1.27: Fourier spectra for CoRoT ID 0105288363 showing the main pulsation frequencies (the largest peak) and overtones (the smaller peaks at higher frequencies). Note the number of symmetric side peaks at the base of the main frequency in the inset panel. (Reproduced from Chadid et al., 2011, Fig. 3, p. 4)

The symptoms of the Blazhko effect described in the time, phase and frequency domain analysis techniques give an idea of the scale of the modulations compared to the main pulsations, as well as the period of the modulation. However, the range of amplitudes and periods of the modulation do not assist in explaining the physical causes of the Blazhko effect itself. Several models have been developed to explain these causes, but they struggle to reproduce all the features described above, as discussed in the next section.

1.7 Blazhko effect models

Earlier sections described how stellar models are used to explain the observed characteristics of stars in terms of their size, age or evolutionary stage. This section describes the stellar pulsation models that are being developed in order to explain the physical causes of the Blazhko effect.

Although the overall pulsation mechanism is based on partial ionisation zones as described in the Pulsations section above, the causes and origins of the various different pulsation modes are poorly understood. For instance, models are still striving to reproduce the number of modes and ratio between frequencies: in the case of OGLE–BLG–RRLYR–24137 (Smolec et al., 2015a), the period ratio of 0.686 between an observed additional mode and the fundamental mode cannot be reproduced with current models using only radial modes, so the additional mode is suggested to be a non–radial mode.

So far modelling has been hindered by a lack of correlation between basic characteristics of the Blazhko effect and those of RR Lyrae stars and their pulsations. As noted earlier, the comparison of Blazhko and non–Blazhko stars in Skarka (2014a), produced no correlation between Blazhko stars and the Oosterhoff groups. Also, there is no propensity in this study for Blazhko stars to have longer or shorter pulsation periods than other RR stars: 0.532 d for Blazhko stars and 0.542 d for non–Blazhko effect stars. No direct link between the brightness of the star and amplitude modulation has been found, for example V838 from Nemec et al. (2013) has the lowest oscillation magnitudes but is relatively bright compared to other stars in that survey. Benkő and Szabó (2014) suggest the strength of the pulsation amplitude is proportional to the Blazhko period, but their results also show some outliers at remarkably high amplitude that are worthy of further investigation. At the other end of the scale, stars

such as V349 Lyr are very faint and have such a long potential Blazhko period that Nemec et al. (2013) suggest at least a year's worth of study to confirm if it actually is a Blazhko star.

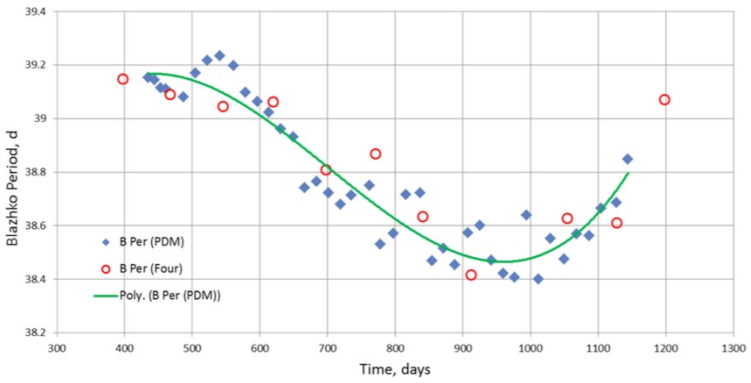

Figure 1.28: Long term variation in the Blazhko effect of RR Lyra shown by the blue points. The green line is a polynomial fit to the points and the red circles represent results of a Fourier analysis of segments of data. (Reproduced from Stellingwerf et al. 2013, Fig. 10, p. 90)

The variation of the Blazhko effect itself in some stars poses another problem for models. As mentioned in Sect 1.6.1, RR Lyrae itself appears to have a variable Blazhko period, see Fig. 1.28. Chadid et al. (2011) claim that RR Lyra's break at the start of a four year cycle is possibly due to a loss of the magnetic field, since the Blazhko effect is due to interation between a magnetic field and convection. However, RY Com shows a sudden drop of 0.08 mmag in a week, where noise from scattered data obscured the modulation effect, and RR Geminorum show no modulation during the 1970's and 1980's (Jurcsik et al., 2009). This behaviour has been used to rule out models relying on symmetry such as those with a resonant non–radial dipole pulsation, or convective instability created by a uniform magnetic field (Kolenberg, 2011) which would create completely regular Blazhko periods. This also leads to the possibility that modulation is a temporary feature of all RRab stars, and therefore a vital factor in trying to understand the true nature of stellar pulsations. Only long duration studies of stars over several years will show if this is typical of the Blazhko effect or not.

The dipole magnetic field model by Shibahashi (2000) was discredited in studies by Chadid et al. (2004) which ruled out a strong magnetic field around RR Lyr.

Spectroscopic studies of individual spectral lines such as H–α can give the rotational velocity of the star, which in turn give theoretical rotational periods given the star's radius. Interpretation of this data directly linked modulation to the star's rotation, implying a link between the Blazhko period and the main pulsation period. While these rotational periods

are within the range of 40–120 days, the variability of Blazhko periods given by Kolenberg et al. (2014) make solutions that rely on rotation unlikely.

Convection within stars is one of the most difficult aspects to model (Caputo, 1998) but Stothers (2006) has been refining his model where turbulence within the convective zone weakens the radial pulsation modes. The ionisation zones described in the pulsation mechanism section (1.3.1) sit within the convection zone of the star's interior and could therefore be directly influenced by the strength of convection. This theory has the added benefit of a built–in level of stochasticity (non–linearity) which allows it to fit cases where the Blazhko effect is not completely regular. The microturbulent model also predicts that the pulsation period should vary with the pulsation amplitude – something that could be investigated in many RRab stars using SuperWASP. Microturbulent velocity is studied spectroscopically by Fossati et al. (2014) who admit that this is only a fraction of the turbulence in the whole star and cannot explain the Blazhko effect on its own, but argue that it is a key ingredient in other models, such as those by Stothers (2006) and Gillet and Fokin (2014). Jurcsik et al. (2013) discusses how hydrodynamical models are more likely than rotation based models to describe the physical causes of the Blazhko effect.

Gillet has derived a model using shock waves whose presence in pulsating stars of different types has already been deduced from H–α emissions lines (Gillet, 2013) that have been observed during different phases of the pulsation. Although occurrences of the H–α line created by shock waves have only been observed at two points in the pulsation cycle, their models use five shock waves produced at different stages of the pulsation cycle due to either κ–mechanism or a combination of weaker compressions waves. The main shock is produced when all five shock waves from their stellar models combine. The second shock occurs when fast in–falling layers of the atmosphere catch up with slower in–falling regions. The suggested physical cause of the Blazhko effect is the interaction of the main shock wave with atmospheric effects due to an extra shock wave that is only present in stars where there is a transient first overtone pulsation mode. The physical origins of this overtone shock wave, however, cannot be explained, although the author suggested that it may be due to the interaction of the fundamental mode with the transient first overtone mode. This transient overtone mode theory appears to be based on two factors: firstly that a very weak first overtone mode as been detected in the prototype RR Lyr star; secondly, the mapping of Blazhko

stars to a region of the instability strip on the HR diagram where the first overtone is unstable to pulsation, and the mapping of non–Blazhko stars to the redder, cooler region where the first overtone mode cannot be maintained. However, no H–α emissions lines have been observed for RRc objects, so a shock–based explanation of the Blazhko effect needs to take this into account now that the Blazhko effect has been detected in RRc stars. Interestingly, He–I and He–II emission lines only appear in Blazhko effect stars, and at the maximum of the Blazhko cycle, therefore the very high shock wave velocities required to cause He–II emission are consistent with the Blazhko effect.

Molnár et al. (2014) claims Gillet's shock model is a result of the combination of the beating of the modes with uncertainties in the data due to sparse sampling of long cadence data, rather than being the result of stochastic processes. Instead, Molnar suggests that period doubling supports the theory that the Blazhko effect is caused by resonance between different pulsation modes.

In data from the *CoRoT* satellite, period doubling is seen exclusively in Blazhko effect stars (Szabó et al., 2010). Period doubling appears as alternating pulsation amplitudes, as though the pulsations come from two interlocked pulsations, each with twice the pulsation period of the star. Although not all Blazhko effect stars show period doubling, it is a promising clue to the nature of the Blazhko effect. Unfortunately, it is not likely to be visible from ground–based observations; firstly, due to the 0.5 d nature of RRab pulsations; secondly, because the difference in pulsation amplitude is only a few mmag. Hydrodynamical modelling by Kolláth et al. (2011) succeeded in explaining period doubling through a 9:2 resonance between the fundamental and the ninth overtone radial modes. This ninth overtone is thought to be a 'strange' mode as it only exists near the surface of the star.

The non–resonance model by Bryant (2015) is based on the Fourier spectra of Kepler field RR Lyrae deconstructed using the Period04 program. There are two steps to Bryant's model; first the normal saw–tooth RRab light curve is recreated using a combination of a heavily amplified sinusoidal overtone and a fundamental mode (Bryant, 2014). The amplification lowers the frequency so that the two modes have the same frequency and become locked resulting in a hybrid–mode, sawtoothed–shaped pulsation. Secondly, this model allows for another additional mode near 3/2 times the main frequency (Bryant, 2015). It is the phase difference of this additional radial mode, which is specifically not locked into a

resonance with the hybrid pulsation, that is claimed to cause the Blazhko effect. Variation in the Blazhko effect is created by the beat frequency effect as this pulsations created by this mode pass close to the main pulsation mode. Bryant's work is based on very detailed study of a handful of Kepler stars, but this type of Fourier analysis would suit expansion into a large dataset, such as that from SuperWASP, if the photometry is of high enough quality. Szabó et al. (2014) have already studied a sample of thirteen RR Lyrae stars observed using the French satellite *CoRoT*.

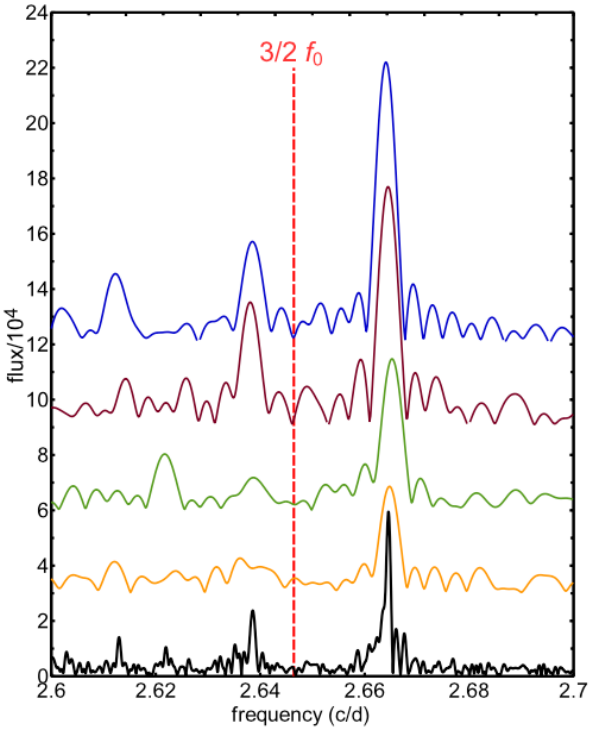

Figure 1.29: Fourier spectrum for Kepler object KIC 7198959 centred around the overtone frequency claimed by resonance models to be the cause of the Blazhko effect, shown as the red dashed line labelled 3/2 f_0. Bryant highlights how the difference between the peak on the right side created by the observed overtone mode and the expected 3/2 f_0 creates a beat mode phenomenon, using it to explain both the Blazhko modulation effect and the long term variations in that effect. (Reproduced from Bryant, 2015, Fig. 1, p. 2)

Despite uncertainty in the underlying physical mechanisms of the Blazhko effect, it has proved useful from a stellar evolutionary standpoint by differentiating populations within GC. For example, Smolec et al. (2015a) suggest that OGLE–BLG–RRLYR–24137 mentioned above is transitioning from RRab to RRd as its period ratios are not consistent with other RRd stars. Work by Jurcsik et al. (2014) on double mode RRd stars in M3 also suggests that RRd stars are evolved from RRab stars, and they retain their Blazhko modulations from when they were RRab. Bright, over–luminous RRc stars are also considered to be members

of this highly evolved group, based on higher mass and lower helium content. Of these 8 bright RRc stars, 4 are Blazhko. This contrasts with 34 less evolved RRc objects in the GC where only 1 shows the Blazhko effect. A larger proportion of RRc than RRab are therefore thought to be second generation GC stars. This hysteresis concept, first mentioned in Sect. 1.3.2, is echoed in studies of the GC M53 by Fiorentino et al. (2012) where the RRab and RRd are suspected to be highly evolved first generation stars.

1.8 Summary

As pulsating HB stars, RR Lyrae are helping to narrow down the parameters calibrating metallicity and luminosity in the HB, leading to improvements in their use as distance markers and age indicators. The benefit of RR Lyrae as distance markers and age indicators, based on their pulsations and the period luminosity relationships, does not appear to be affected by the Blazhko effect. It also does not seem to affect mean luminosity, maintaining their function as distance markers. There is no correlation between Oosterhoff groups and the Blazhko effect, with the categorisation of GC remaining unaffected by it.

RR Lyrae can be easily classified according to their light curve but further research is required to explain the dominance of different individual modes for RRab, RRc, RRd and RRe stars. A growing number of double mode RRd stars and second overtone RRe stars have led to recent hysteresis theories portraying the evolution of RR Lyrae within the HB. The Blazhko effect appears to be retained as the stars evolve from RRab to RRc types. Since Blazhko modulation tends to predominantly affect the first generation of GC stars, it has also led to a possible way to detect separate generations within GC. The study of pulsations, overtones and their various interactions provides an excellent method of investigating the internal structure of stars through asteroseismology. Studying modulation is therefore extremely important when trying to understand the driving mechanisms behind pulsations in variables stars.

There are several methods to represent and analyse modulation in stellar pulsations, by phase folding the light curve, plotting O–C diagrams or creating power spectra, depending on whether the features appear in time or frequency domains. Phase folding is particularly useful at identifying amplitude modulation, whereas the presence of multiplets in Fourier

spectra shows the presence of frequency modulation. Kepler data has led to the discovery of new features in RR Lyrae pulsations such as period doubling and non–radial modes when investigated using Fourier analysis. Long term studies have revealed that the Blazhko modulation varies randomly in magnitude and cycle length. Phase folding has the additional benefit of leading to O–C diagrams by helping to create a model light curve that can then be used as a template when measuring the horizontal shifting of the pulsation due to phase modulation.

Modulation can also be created by LTTE created by a nearby companion but investigation of LTTE can only be attempted once Blazhko stars have been excluded, due to the magnitude of the Blazhko effect phase modulation. However, evidence of amplitude modulation during the phase folding stage makes identification of the Blazhko effect relatively easy.

The physical causes of the amplitude and frequency modulation of the pulsations in RR Lyrae stars, known as the Blazhko effect, are still unknown even after more than one hundred years of observations. All theories involve intrinsic features of the star, depending on excitation of existing pulsation modes, either through additional shocks, resonances or beat frequencies; no external bodies or companions are mentioned. The number of RR Lyrae binary systems masked by the Blazhko effect is unknown. Current models are able to replicate some of the modulation features, periods doubling and non—radial modes. However, none are able to provide physical sources for their additional pulsation modes or shock waves.

As subsequent chapters will discuss, SuperWASP has detected thousands of candidate RRab stars, ready to be identified as either Blazhko or non–Blazhko stars. Future wide field photometric surveys by TESS, GAIA and PLATO will continue to provide excellent data on variable stars as they hunt for exoplanets. Large scale surveys of RR Lyrae will allow photometric patterns to be identified and developed, such as the relation between the Blazhko period and main pulsation period, modulation frequency and pulsation modes, or the Blazhko amplitude and the main pulsation amplitude. Large data sets such as those from SuperWASP will prove invaluable in looking for these trends.

Perhaps, as more features of detailed spectra are investigated a more holistic model of pulsations generation will emerge. Perhaps RR Lyrae pulsations are always modulated but sometimes this effect is below noise thresholds. Perhaps the pulsation modes required for modulation are always present but they change in amplitude as the RR Lyrae evolve through

the IS, so modulation is a temporary feature of all RR Lyrae. This trend towards a single adaptable theory mirrors the progression of RR Lyrae classification from separate static classifications to stars evolving through several different classifications during their time on the HB. The validity of such a theory can be tested by a survey such as SuperWASP, covering many RR Lyrae field stars. This provides the motivation for the project of this thesis.

Chapter 2

Wide Field Surveys

2.1 Introduction

Before discussing the WASP project in particular, it is useful to describe the concept of astronomical wide–field photometric surveys and the reasoning behind them.

Paczyński (2000, 1997) presented an overview of the motivations for wide–field surveys and what their goals should be. The first objective is the simplest: to obtain large samples of different objects or events. If a large number of a certain type of variable object have been observed, follow up observations allow the best examples to be selected for calibration purposes. For example, bright eclipsing binaries in the LMC and SMC allow better calibration of the Hubble constant as their distances can be geometrically determined by using their photometric light curves and radial velocities (Riess et al., 2016). The chances of observing rare events, such as the helium flash, or rare objects, such as triple mode radial–non–radial RRd objects (Moskalik et al., 2015; Chadid et al., 2010; Benkő et al., 2010) are increased. Transient events such as supernovae and Near Earth Objects (NEO) can be rapidly followed up as the wide–field survey acts as an early alarm system. Finally, the wide–field surveys were expected to produce so much data that they would require a future–proof archival system to allow the workload to be shared across teams, and to allow for investigations beyond the original remit of the project.

SuperWASP accomplishes the first objective listed above: it has recorded a large number of pulsating variable stars from which a large dataset of exemplary RRab light curves can be extracted. These light curves have enough nightly data points from up to nine years of

seasonal data to characterise both short–term features of the pulsation shape as well as long–term modulation effects.

This chapter continues with a description of the SuperWASP instruments (Sect. 2.2.1) and the data processing stages (Sect. 2.2.2). This idea that the data from wide–field surveys can be harvested for many types of objects can be seen throughout Sect. 2.3 on other wide–field surveys that have resulted in RRab catalogues. Finally these surveys are discussed in Sect. 2.4.

2.2 WASP

The original purpose of the Wide Angle Search for Planets project (Pollacco et al., 2006) was to identify transiting exoplanets *en masse* using the dips in the light from the bright host star. These observations are made using SuperWASP instruments at two sites. The level of detail allows follow–up investigations, either using higher resolution photometry or spectroscopic studies to investigate Doppler shifts in the host star's spectrum due to the reflex motion as it is pulled by the exoplanet's gravity.

Although originally designed to detect transiting exoplanets, SuperWASP has recorded the light curves of over 30 million objects over a lifespan of 10 years. It is estimated that at least 10,000 of these belong to recognisable pulsating stars based on the classification by a neural network designed by Payne (2013). The amount of sky covered by SuperWASP since 2004 is shown in Fig. 2.1 below:

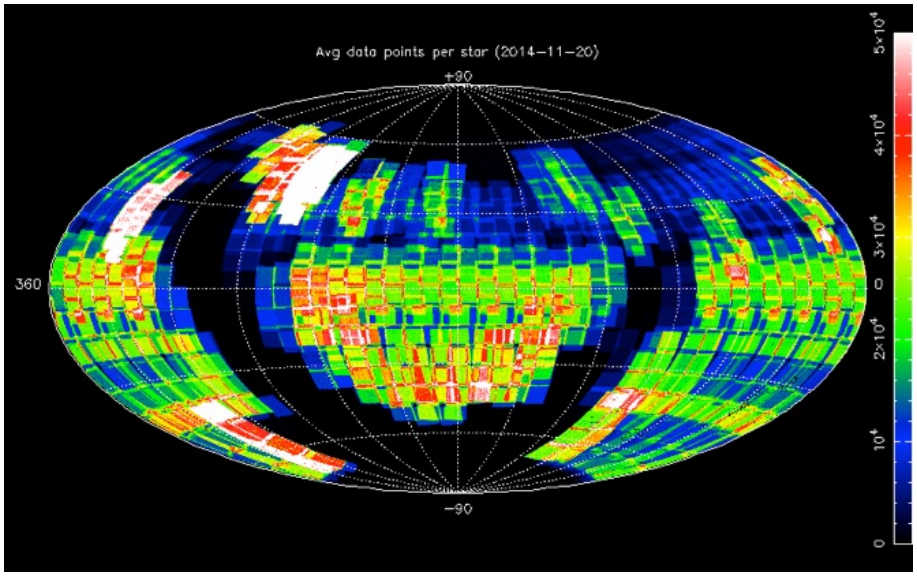

Figure 2.1: Recent sky map showing the areas SuperWASP North and South have surveyed and the density of the pointings. (Image from http://wasp.warwick.ac.uk/status/skycov.shtml)

SuperWASP is capable of observing objects down to 15th magnitude at a cadence of approximately 10 minutes. As Fig. 2.1 shows, SuperWASP avoids areas near the Galactic disc and bulge, as crowding in these densely packed areas leads to blending of objects at SuperWASP's resolution.

2.2.1 SuperWASP Hardware

SuperWASP has two installations located in La Palma, in the Canary Islands, and Sutherland, South Africa, inside custom built enclosures with sliding roofs to accommodate the rapid slewing ability of the mount and software. Each instrument consists of eight cameras by Andor Technology with Canon 200mm focal length, f/1.8 lenses with an 11 cm aperture, which are considered fast and apochromatic, mounted on a custom built Torus mount, as shown in Fig. 2.2.

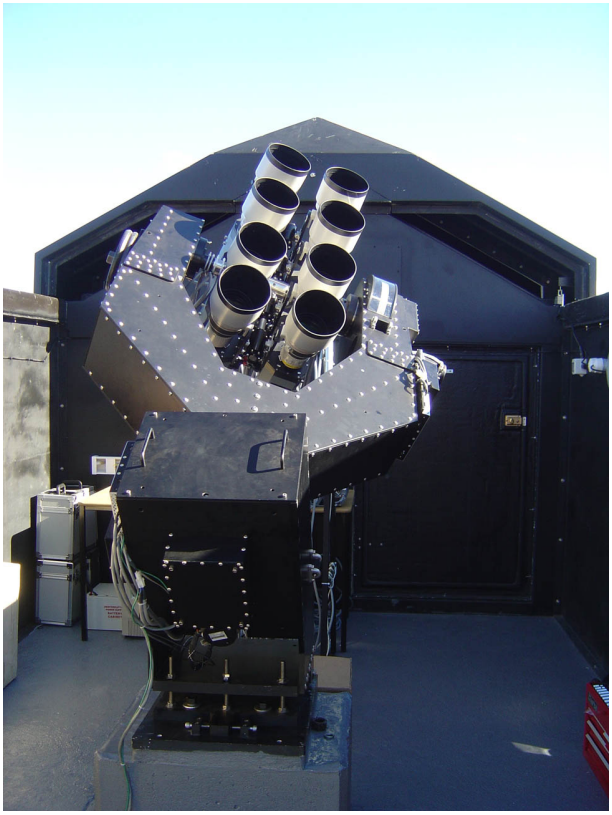

Figure 2.2: SuperWASP North showing the array of 8 cameras, each with its own CCD, in its enclosure with the roof rolled back. (Reproduced from Pollacco et al. (2006))

The CCDs at the focus of the 8 cameras were manufactured by e2v contain 2048 x 2048 pixels, 13 microns each side with an angular scale of 13.7 arcsec per pixel giving a field of view of $\sim$ 64 deg^2, and a total field of view 482 deg^2 for all 8 cameras. For 30 s exposures the cameras are lowered to an operating temperature of –50 °C. The Linux–based Talon software controls the enclosure, robotic mount and cameras, and allows automated data acquisition.

New lenses with smaller apertures have been fitted at SuperWASP–South from July 2012 (Turner et al., 2015) aimed at capturing exoplanets transiting brighter host stars without saturating the CCDs.

2.2.2 SuperWASP Data Pipeline

Individual objects from SuperWASP are identified using a custom designed data pipeline and then stored in a bespoke archive database. The data pipeline consists of several stages from calibration, to identification, to photometric measurement. Calibration frames comprising of bias and darkframes and flat–field exposures are taken each night of observation, and master bias, dark and flat–field frames are created once these have been statistically validated. A subcatalogue of the Tycho–2 catalogue is projected onto the area of the sky centred on each of

the camera's field of view (given by the mount coordinates and camera offsets). The Starlink EXTRACTOR program (Bertin and Arnouts, 1996) is used to pick out roughly 10,000 objects from the camera frame, and the brightest 100 from these results are fitted to the Tycho–2 results through scaling and translation to achieve a plate solution for coordinates.

Objects are matched against items in the USNO–B1.0 catalogue (Monet et al., 2003) that are brighter than about magnitude 15 before being added to the input catalogue (15 mag can be used as a zero point in calculations converting flux to magnitudes where 1 count per second equates to approximately $M_V = 15$). The point spread function is calculated on each object using the ratios of the fluxes from 3 circular apertures of radius 2.5, 3.5 and 4.5 pixels. These sizes were arrived at after looking at blended and unblended images. The sky background is removed using a larger annulus of 13–17 pixel radii with images being rejected if the χ^2 value of the background is too high or 50% of it is clipped in the quadrature sky fit. The end result is a collection of files containing the calibrated photometry of all the objects in that image.

Air mass extinction and the system zero point are calibrated during the Post–Pipeline Calibration stage using SYSREM (Tamuz et al., 2005) to detrend the data using four main trends. Although this improves the quality of the data there is a limit to its capabilities due to some systematic red noise, but only at a level of ~3 mmag for stars of ~9.5 mag: 'SYSREM is highly effective at reducing the level of red noise, but fails to remove it entirely' (Smith et al., 2006, p. 1156). Variable stars are inverse–variance weighted so as not to hinder the air mass calibration process. The adaptive WASP V magnitude is calibrated against the Tycho–2 V bandpass using 100 non–variable Tycho–2 catalogue stars over a few nights, providing a zero–point correction of only one or two thousandths of a magnitude for every frame.

The data archive has been designed with data mining of the photometric data of thousands of objects in mind. FITS files of indices sorted by object identifier allow quick access to the FITS files containing the bulk photometric data. Restricting these to 'sky–tiles' of 5 square degrees keeps the file size manageable. The 'SWASP' object identifier is used to uniquely identify each object in the database; when a user needs to query the database by object all the photometric data for that object is collated from all the bulk FITS files using the sky–tile files. Using an SQL database enables the data to be stored hierarchically for faster access and also allows for further properties of individual objects to be added in the future. The

SQL database is currently held and maintained at Warwick University.

A bespoke query language, WQL, has been designed based on SQL to allow easy access to FITS files for individual objects based on coordinates, regions of sky, or SIMBAD identifier (http://simbad.u-strasbg.fr/simbad/). Queries can be written in WQL which return lists of SuperWASP identifiers and lists of objects can also be entered manually in bulk. Light curves are then extracted based on these lists or individually. WQL is compiled into SQL between the user interface and the archive.

Detrending steps are taken to systematically identify and remove frequencies due to seasonal and daily duty cycles from the data. Otherwise a false daily frequency would appear in the frequency spectra of each object. Signals at whole and integer factors of a day have already been identified for many of the objects in the database and this information is kept in a separate table. This is particularly useful in the case of many RR Lyrae due to their pulsation periods being roughly half a day.

SuperWASP has therefore provided an excellent tool with which to investigate the Blazhko effect, through a combination of good photometry, large sky coverage, automated identification and cataloguing of thousands of RR Lyrae stars.

2.2.3 Other type of variables and SuperWASP

SuperWASP has been used in the study of several other types of variable objects thanks to its inherit ability to record variability in so many objects in each observing season. Norton et al. (2007) demonstrated the diversity within the types of variables detected in the first few years of SuperWASP operation. Objects recorded during the 2004 season of SuperWASP observations were compared to objects from the ROSAT survey (Voges et al., 1999) and 4562 objects were found to be coincident. A search for periodic variation was made on 3558 of these coincident objects which had enough data points for the period search. The identification of the periodic variability was made using a combination of Fourier analysis using the CLEAN algorithm, and phase dispersion minimisation (PDM) using both PDM and Epoch Folding techniques. This led to the identification of 428 unique periodically variable objects in the SuperWASP database that were coincident with X–ray sources from the ROSAT survey. The coordinates and periods of the 428 objects were compared with known objects from existing catalogues including the General Catalogue of Variable Stars, and the Robotic Optical Tran-

sient Search Experiment (ROTSE) (Akerlof et al., 2000). 68 objects were previously known and 360 were newly identified as being periodic. Within the 68 previously listed objects there are 11 types of variable object, ranging from pre–main sequence, to accreting and eclipsing binaries, to cataclysmic variables, to RR Lyrae and Cepheid pulsators.

The rate of change of period of 53 periodic variables from Norton et al. (2011) were investigated in Lohr et al. (2012). These objects are close to the short period limit of main sequence, W UMa class, contact binaries of around 5.5 hours. Thanks to the accurate observations of SuperWASP, observed–minus–calculated (O–C) analysis showed that 3 of these objects had rapid decrease in their orbital periods, a sign of a possible future merger event in those binary systems. A much larger search of the SuperWASP archive soon led to a total of 143 short period eclipsing binaries (Lohr et al., 2013), 93 of which were previously unknown and 74 had statistically significant period change. Of particular note, using a technique reminiscent of the pre–whitening of certain frequencies in Fourier spectra, in–depth analysis of the O-C diagram of one binary system led the authors to discover a quadruple binary system, consisting of a contact binary and and Algol–type binary, with the SuperWASP identifier 1SWASPJ093010.78+533859.5.

Maxted et al. (2008) have used SuperWASP data to return the main pulsation frequency of the high amplitude pulsating subdwarf B class (sdB) object Balloon 090100001 from 128 nights of observations in 2004. Smalley et al. (2011) describes how SuperWASP observations can be combined with data from the Kepler mission (Gilliland et al., 2010) to investigate oscillations down to SuperWASP's millimag limit happening in metallic–lined Am class stars which reside at the intersection of the classic instability strip and the main sequence in the HR diagram. They were then able to classify 169 as δ Scuti pulsators, 30 as γ Doradus pulsators, and 28 as hybrids of these two classes. A review of Am, Ap and rapidly oscillating Ap (roAp) stars is also given in Smalley (2013). A summary of the definitions of these stars based on their spectral class and metallic line strengths is given in the introduction of Holdsworth et al. (2014). This study uses SuperWASP data to detect 10 new roAp stars and 13 new pulsting Am stars, with 350 stars being found with periods below 30 mins. These stars are all hotter than mid–F spectral class. If SuperWASP objects with a minimum of 1000 data points are used then the detection limit can be as low as 0.5 mmag. They defined their maximum frequency limit as 300 d^{-1}. roAp stars are so called because

their pulsations periods are 5 – 24 mins, due to high overtone pressure (p) modes. These are caused by the same kappa–mechanism as the p–modes in RR Lyrae but the source is a partially ionised hydrogen zone and not the He^+ zone as in RR Lyrae.

2.3 Other wide–field surveys

SuperWASP is not the only photometric wide–field survey of the Milky Way that has been making observations of pulsating variable stars. Below are details of four surveys commonly associated with variability studies.

2.3.1 OGLE

The Optical Gravitational Lensing Experiment (OGLE) project (Udalski et al., 1992), running since 1992 at Las Campanas in Chile, uses gravitational microlensing to detect exoplanets. The OGLE telescope is shown in Fig. 2.3 with the latest iteration of its high resolution instrument shown underneath.

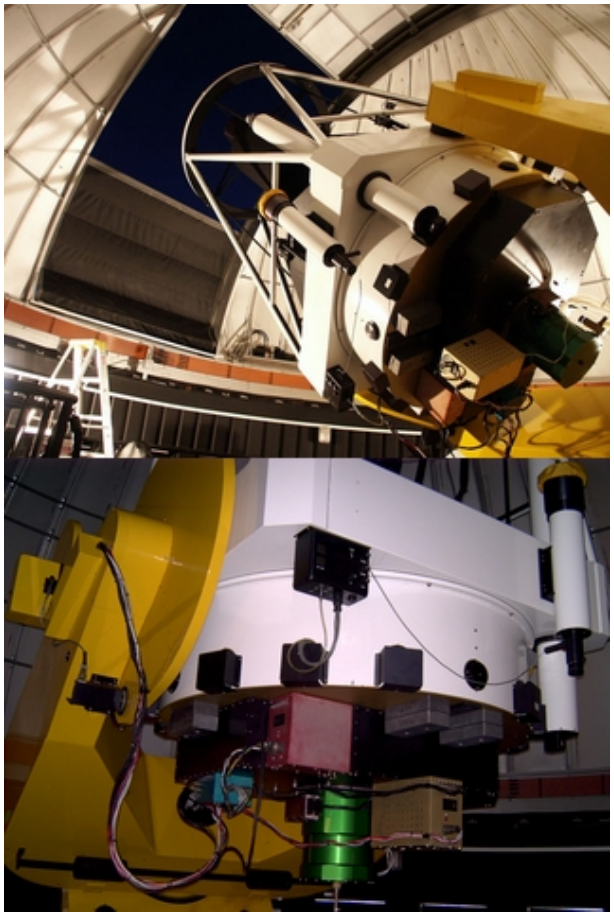

Figure 2.3: OGLE telescope. Top panel: the 1.3 m telescope in its dome at Las Campanas. Bottom panel: the third generation mosaic camera at the base of the telescope. (Image from http://ogle.astrouw.edu.pl)

In order to maximise the chances of such events (which are only ever expected to occur once for each object) the telescope is pointed towards the centre of the Galaxy. This means that it has a sky coverage map that is almost the negative to the WASP project, as the bulge, disc, Large and Small Magellanic Clouds have been observed extensively. OGLE uses high resolution CCDs due to the density of objects in these areas. For instance, the original instrument described in 1992 had a scale of 0.44 arcsec / pixel, with each observing frame being 15 $\times$ 15 arcmin. There is extensive use of Baade's Window which gives a relatively low obscured view of the Galactic centre, by covering a 40 $\times$ 40 arcmin area using nine CCD fields centred on this region. The latest OGLE hardware at Las Companas, installed in 2010, has a field of view of 1.4 square degrees and is capable of observing objects between 10th and 19th magnitude. It has large catalogues of variable objects recorded in survey phases from OGLE–I to OGLE–IV, notably 'RR Lyrae Stars in the LMC' (Soszyński et al., 2009), 'RR Lyrae Stars in the SMC' (Soszyński et al., 2010), 'RR Lyrae Stars in the Galactic Bulge' (Soszyński et al., 2011), and the impressive 'Over 38000 RR Lyrae Stars in the OGLE

Galactic Bulge Fields' (Soszyński et al., 2014) which used data from the OGLE–IV phase. The fields covered by OGLE-IV are shown in Fig. 2.4 with the fields used in the surveys for stellar variability shown in black.

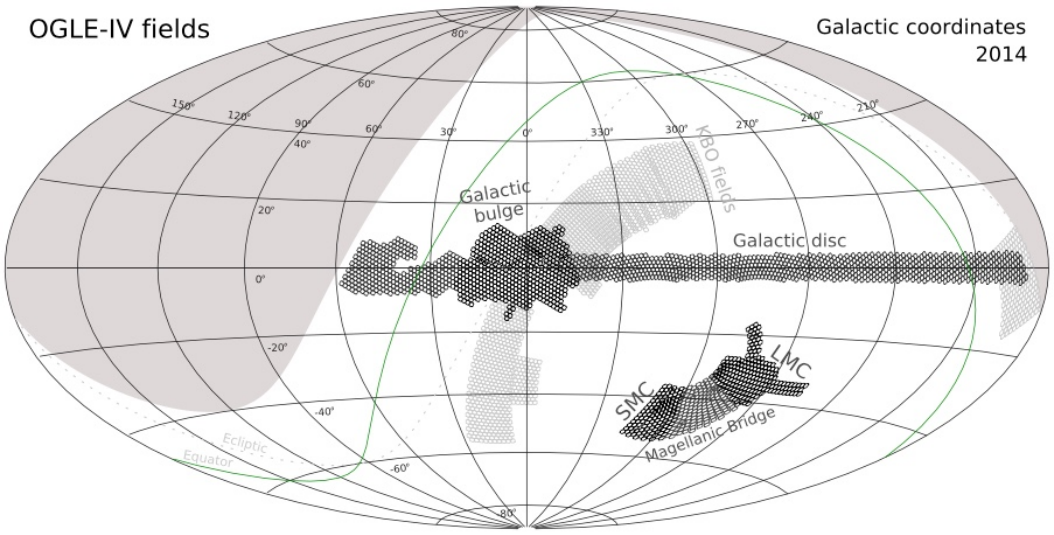

Figure 2.4: OGLE–IV sky map of coverage as of 2014 in galactic coordinates. The black circles show the variability / microlensing survey across the bulge, disc, LMC and SMC. (Reproduced from Udalski et al., 2015, Fig. 13, p. 26)

Fig. 2.5 shows the density of RRab objects. The faintness of the objects towards the centre of the bulge is coincident with reddening due to dust extinction.

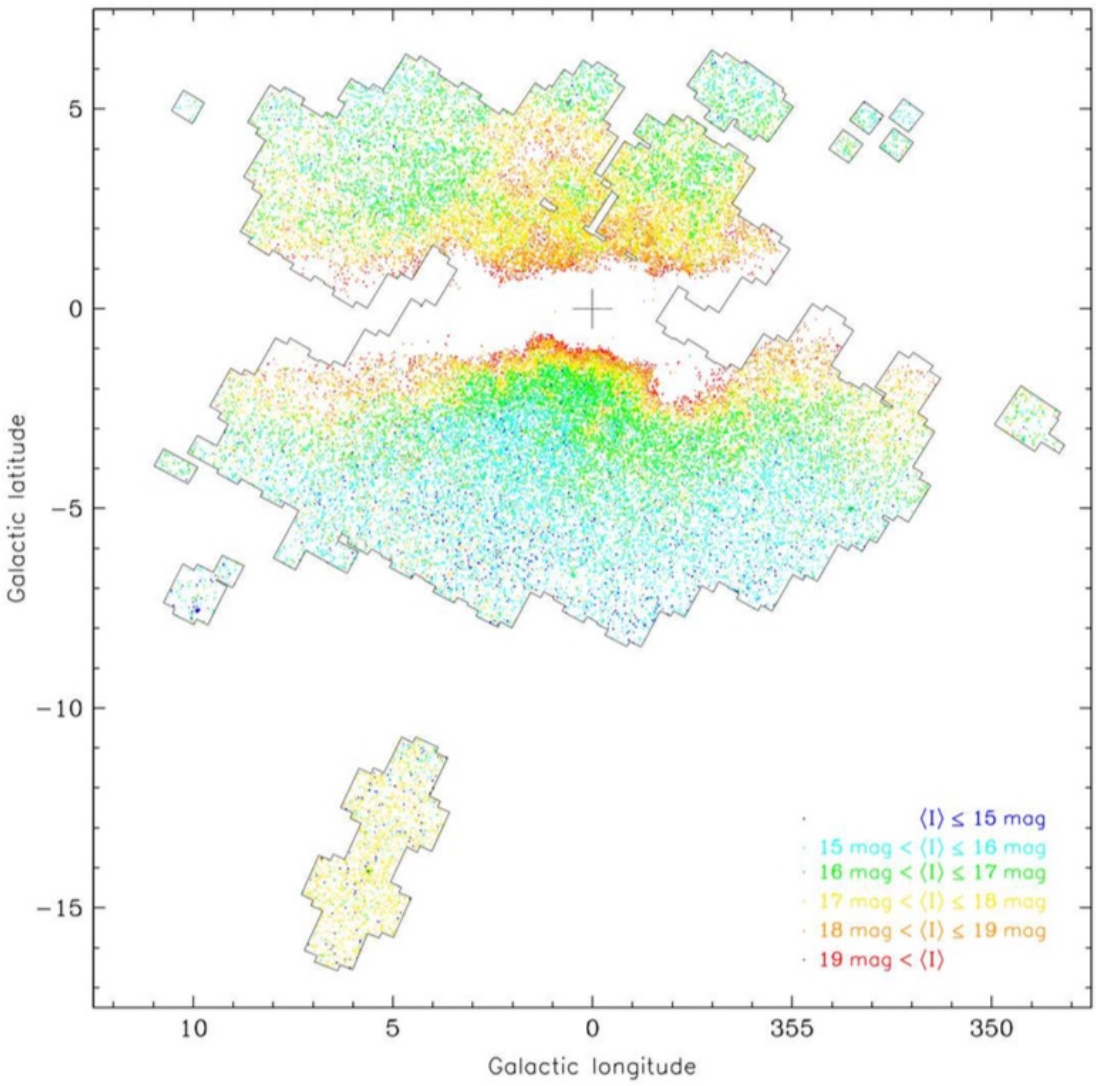

Figure 2.5: OGLE–IV coverage of the Galactic bulge showing the spatial distribution of RRab. The colour scale represents brightness from blue at $\geqslant$ 15 mag to red at $\leqslant$ 19. (Reproduced from a section of Soszyński et al., 2014, Fig. 2, p. 8)

The cadence of OGLE observations varies depending on the region being observed, with the inner bulge being observed every 19 – 60 minutes and the remaining regions being observed every 1 – 3 days. The long–term surveys cover several seasons and are mainly focused on detecting variability. The data from these surveys are available at CDS.

2.3.2 ASAS

The All Sky Automated Survey (Pojmanski, 1997) was built in 1996 at Warsaw University Observatory with the primary aim of observing variability. Capable of observing down to 13th magnitude, its instruments originally had 14.2 arcsec / pixel with 3×2 degree field of view, but it has been upgraded regularly since this original configuration. ASAS–3 consisted

of 2 instruments at Las Companas, Chile, close to the OGLE site. These are shown in Fig. 2.6. Objects brighter than 14th magnitude were observed using 3 independent 14 micron pixels instruments: two wide–field instruments with a 8.8 square degree field of view in V and I filters; 1 narrow field instrument with a 2.2 square degree field of view using an I band filter. The coverage rate is roughly 1–3 days.

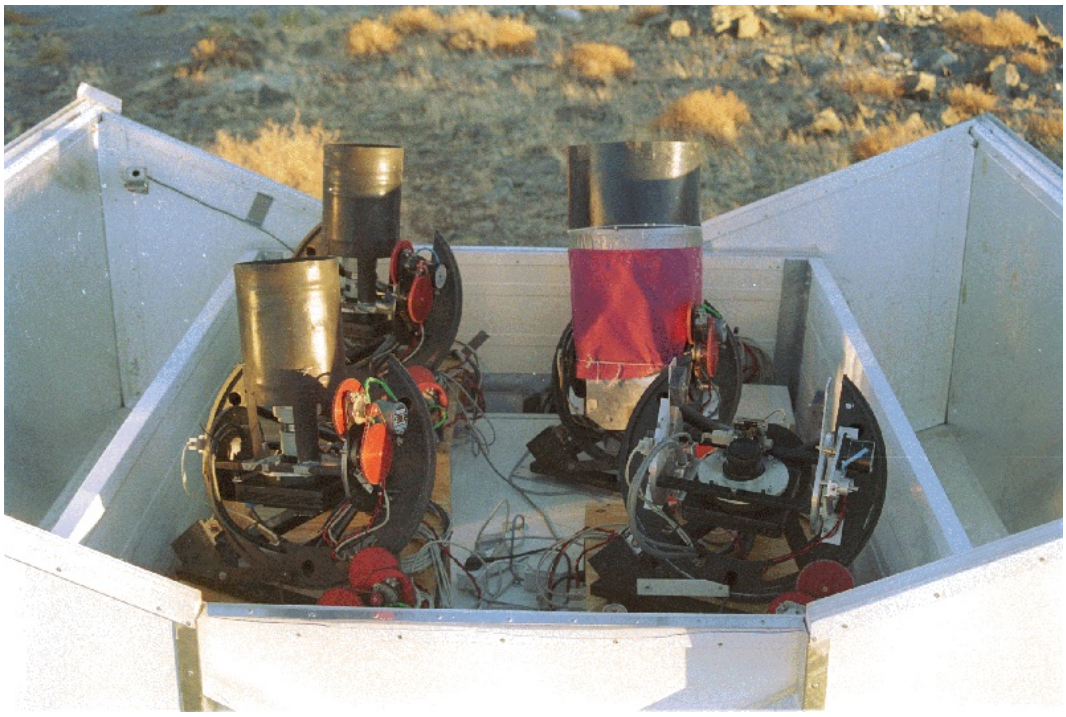

Figure 2.6: ASAS–3 instruments in their automated enclosure. The horseshoe design of the mounts can be seen on the two left–hand instruments. (Reproduced from 'ASAS - Gallery', Pojmanski, 2010)

The ASAS website at http://www.astrouw.edu.pl/asas/?page=main states that the ASAS-3 hardware at Las Companas was replaced in 2010 by ASAS-4 with an increased field of view of 10.9 square degrees. The ASAS catalogue available at CDS consists of 50122 records, with a catalogue released in 2000 (Pojmanski, 2000) of 382 periodic and 3497 miscellaneous variables. The ASAS catalogue of variable stars has been released in five parts from 2002 to 2005 covering different parts of the sky. As well as the Skarka (2014a) paper on bright RRab using ASAS data, Szczygieł et al. (2009) have also published an investigation into the metallicity of RRab pulsators and the Oosterhoff groups using ASAS data covering 75% of the sky. The sky coverage of ASAS is shown in Fig. 2.7. The robotic nature of ASAS should be noted: both scheduling and telescope control, along with the data pipeline and transfer to the ASAS catalogue are fully autonomous.

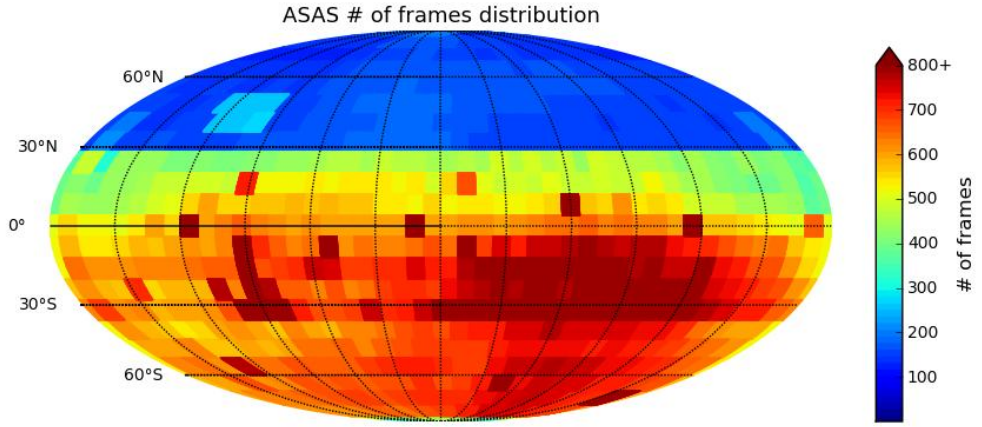

Figure 2.7: Schematic showing the number of observations during the sky coverage of ASAS. The most covered areas are in dark red and areas of the sky that have not been covered are in blue. (Reproduced from 'ASAS Gallery - Statistics', Pojmanski, 2010)

2.3.3 CRTS

The Catalina Real–time Transit Survey evolved from the Catalina Sky Survey, investigating Near Earth Objects (NEO), in 2007 (Drake et al., 2009). The survey uses three telescopes: a 1.5 m telescope at Mount Lemmon, near Tucson in Arizona (MLS); a 0.7 m Schmidt telescope at Mount Bigelow, also near Tucson (CSS); and a 0.5 m telescope at the Siding Springs observatory in New South Wales, Australia (SSS). Within the CRTS context the abbreviation CSS refers to the Catalina Schmidt Survey. CRTS covers roughly 30,000 square degrees of the sky. The CCD from the 0.7 m telescope has a field of view of 8 square degrees. Catalina Surveys Data Release-1 (CSDR1) includes objects from 12th to 20th magnitude taken with 4 30 s exposures set 10 mins apart.

Figure 2.8: CSS 0.7 m Schmidt telescope at Mt. Lemmon. (Reproduced from CSS Telescopes gallery, The University of Arizona, 2008)

Drake et al. (2013a) investigates the outer halo of the Galaxy and the Sagittarius stream using 12,227 RRab objects observed with the CSS telescope and combined with spectroscopic data from Sloan Digital Sky Survey (SDSS) DR8 to define the stream up to 60 kpc from the Galactic centre. This work is continued in Drake et al. (2013b) using a further 1,207 RRab from the MLS site where the stellar stream is now defined up to 110 kpc. Drake et al. (2014) uses data from the large CSDR1 to find another 2039 new RRab bringing their total to 16,797 RRab objects from CSS, including 223 Blazhko effect objects. As well as the

discovery of more RRab objects this work also provides useful training data to neural networks and machine learning algorithms that will be required for the automated classification of pulsating objects by LSST.

The SSS data explores 14,800 square degrees of the southern hemisphere in Torrealba et al. (2015), providing a list of a further 10,540 RRab objects with $11 < V < 19.5$. This work demonstrates their automated Fourier decomposition and automatic period selection algorithms. The SSS data from CSDR-2 has recently been investigated further in (Drake et al., 2017) providing another 4319 RRab objects.

The above CRTS catalogues are available at the Variable Star Index (VSX) (Watson, 2006), administered by the American Association of Variable Star Observers (AAVSO). A map in equatorial coordinates of RRab objects from all CSS surveys up to 2015 is shown in Fig. 2.9.

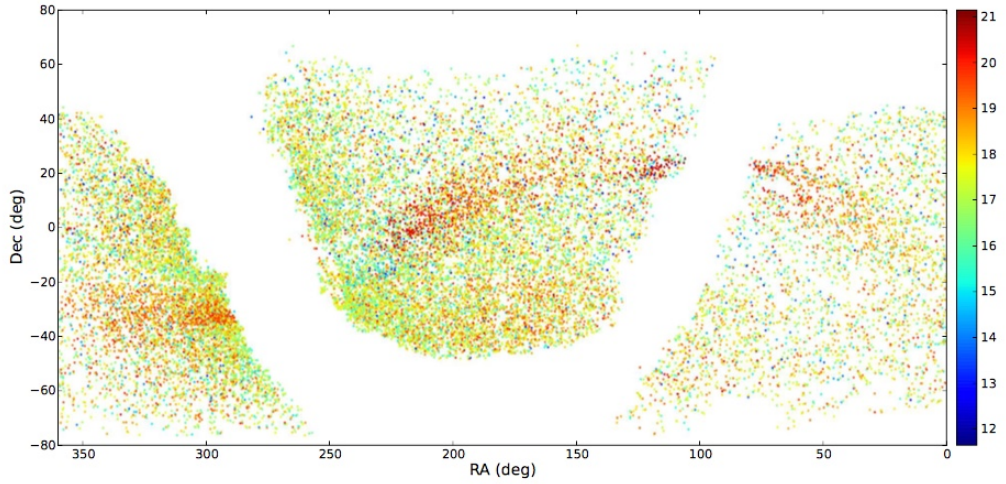

Figure 2.9: Map in equatorial coordinates showing the coverage of RRab objects alone by the combined CRTS surveys. (Reproduced from Torrealba et al., 2015, Fig. 10, p. 11)

CRTS rapidly disseminates their optical transients to the public via the VOEvent protocol and event distribution network (Drake et al., 2007), even adding data to Google Sky. The aim is to develop a discovery and classification system that allows for fast follow up by robotic telescopes of LSST objects.

2.3.4 Pan–STARRS

The Panoramic Survey Telescope and Rapid Response System (Pan–STARRS) Kaiser et al. (2010) is a system of 1.8 m wide–field telescopes, each with a field of view of 7 square

degrees. The first telescope (PS1) is based at Haleakala in Hawaii, shown in Fig. 2.10. It operates in g, r, i, z, and y (visible and near infra–red) wavebands covering a wavelength range from 400 to 1000 nm with a 1.4 Gigapixel camera. A major element of the objectives of the PS1 Science Consortium (PS1SC) is a census of solar system objects, but part of the objectives are to identify variables and explosive transients. The observation scheduling is based around the majority of time being taken up with a wide–field '3π' survey (see below), with less time being devoted to the medium– and ultra– deep surveys, which require smaller areas of sky. Exposure time varies depending on the depth of observations required. The plan to detect moving and variable objects was to use differential photometry, subtracting the observed area of sky and a template image of that area. An object catalogue search is available on the Pan–STARRS public archive, available online at `http://archive.stsci.edu/panstarrs/search.php`. This has been made possible through development of an image processing pipeline and a published science products subsystem.

Figure 2.10: PanSTARRS PS1 telescope at Maui, Hawaii. (Reproduced from Rob Ratkowski / PS1SC, 2015)

The 3π Steradian Survey by Pan–STARRS observed the sky above -30° declination between 2004 and 2010, in all 5 bands, to 22nd magnitude. Observations are not made simultaneously in all bands. Instead, 2 exposures 25 minutes apart are taken twice per year, per filter. This 3π survey was used to produce create a catalogue of 45,000 RRab objects,

classified using machine learning techniques Sesar et al. (2017), shown in Fig. 2.11. This catalogue started with 500 million PS1 objects, scored 240,000 objects using a machine–learning algorithm in their RRab and RRc classification stage. Four years of observations resulted in approximately 67 observations per object. The distances to these objects were used to map out tidal streams in the galactic halo. The work by Sesar et al. (2017) increased the completeness and purity of work by Hernitschek et al. (2016) which identified a large sample of ~150,000 RR Lyrae objects across three quarters of the sky and up to a depth of 120 kpc from the Sun using the second internal PS1 data release.

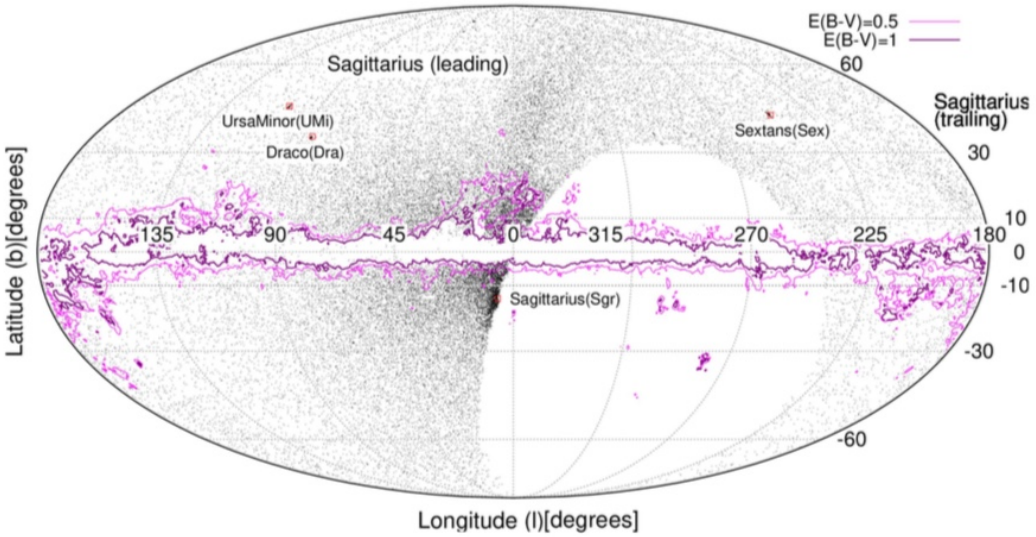

Figure 2.11: Skymap of the ~45,000 RRab objects identified in the 3π survey using PS1. (Reproduced from Sesar et al., 2017, Fig. 12, p. 14)

2.4 Summary

Several wide–field surveys have been compared in regards to their sky coverage, cadence and duration of observation. Some have been designed specifically to look into crowded areas of the sky, and some have been designed with field stars in mind. The benefits of a large study can be seen in the RRab population mapping of Drake et al. (2013a,b) or the occurrence rate of the Blazhko effect as in Skarka (2014a).

The WASP project with its two installations SuperWASP–North and SuperWASP–South have been described. Its data are stored in a database, which can be queried in a wide range of ways, based on spatial coordinates or object type for example, and new results can be accessed years after observations have been made. In comparison to the other wide–field surveys shown above, thanks to its wide–field, SuperWASP has an excellent combination of

both high cadence giving short term variations such as pulsations, and long baseline. OGLE has a deeper view than SuperWASP but does not have the same amount of sky coverage as its purpose is to observe the densely packed areas of the Magellanic Clouds and the Galactic bulge. Its cadence is also lower than SuperWASP's, although the baseline of its observations is longer. ASAS has good southern sky coverage but a lower cadence than SuperWASP, affecting the quality of its RR Lyrae observations. CRTS and Pan–STARRS are the most similar to SuperWASP of other wide–field surveys in terms of sky coverage. They are both able to observe down to fainter objects than SuperWASP but do not match the high cadence of SuperWASP. The catalogues created using the Pan–STARRS 3π survey have measured their completeness against the CRTS data and is able to see to greater depths than the other surveys, making it ideal at observing Galactic halo objects. The developers of Pan–STARRS considered the distributed aperture nature of their multiple sites, the Gigapixel camera and their data pipeline as a practical way to meet the large synoptic nature of the science goals for an LSST.

The following chapter describes the investigation into the RR Lyrae type of pulsating variable object, in possibly the most intuitive of the three domains of investigation described in the Introduction: the time domain. It shows how the SuperWASP archive has been used to create a catalogue of RR Lyrae objects, and investigates how the mysterious Blazhko effect manifests in the time domain.

Chapter 3

SuperWASP RR Lyrae stars in the time domain

3.1 Introduction

Having described both the properties of the complete class of RR Lyrae stars, and the SuperWASP archive, my aim is now to present a catalogue of RRab objects within the archive, along with some of their characteristic properties. Although these properties could be statistically significant in themselves due to the large number of RRab objects expected to be within the SuperWASP database, they should prove even more useful in characterising the Blazhko population in the archive, once the Blazhko effect objects have been identified.

This chapter deals with techniques based in the time domain. The next section (Sect. 3.2) describes the creation of a new catalogue of RRab class SuperWASP RR Lyrae objects based on the shape of their light curves and pulsation periods. The creation and validity of this catalogue is paramount as the catalogue forms the basis of subsequent Blazhko effect analyses in the time domain using scatter in light curves (this chapter), frequency space using Fourier analysis (Chapter 4), and finally, the phase domain using O–C techniques (Chapter 5).

Section 3.3 then investigates the Blazhko effect in the time domain by measuring periodic changes in the properties of RRab light curves due to amplitude modulation. As well as being more intuitive, amplitude modulation due to the Blazhko effect is more readily quantifiable in the time domain than frequency modulation, as the changes in the amplitude of the stars' pulsations can be seen at a wide range of time–scales.

3.2 The SuperWASP RRab catalogue

This section describes the refinement of the initial list of 8556 RRab objects by Payne (2013) into a new catalogue of 4963 RRab objects.

3.2.1 SuperWASP data

A machine learning algorithm by Payne (2013) made a preliminary identification and classification of variable objects in the SuperWASP archive based on the shape of their phase folded light curves. The algorithm was capable of identifying sub–categories of pulsating variable objects to the level of segregating RR Lyrae objects into their standard subclasses of RRab and RRc. It produced a list of the SuperWASP unique identifiers and pulsation periods for 8556 potential RRab objects. These objects comprised our initial sample and were extracted from the SuperWASP archive. Cameras operational at SuperWASP South from July 2012 use different filters and lenses to capture brighter objects (Turner et al., 2015). Data from these cameras were recorded at a higher cadence but lower signal-to-noise ratio and were removed to maintain a quality consistent with SuperWASP North objects. Outlier data were also removed at this stage. Firstly, spurious data points containing negative fluxes were removed. Then, points with uncertainties beyond 3σ were removed. Finally, an iterative clipping algorithm based on Holdsworth et al. (2014) was used, where flux outliers at greater than 5σ from the mean were removed and the remaining data were fed back into the clipping routine to be clipped at 5σ again, for a total of 5 iterations. Together, this removed a median of 0.18% points and a mean of 1.5% points. The typical light curve used throughout this work consists of 30,000 data points with an average duration of 5.5 years, offering the opportunity to directly detect Blazhko effect signals with frequencies of up to a year or so.

3.2.2 Phase folding of light curves

Before Blazhko objects could be identified and analysed, the 8556 SuperWASP objects needed to be verified by visually inspecting their phase–folded light curves and then catalogued. The phase folding was performed using a custom phase dispersion minimisation (PDM) and epoch folding routine based on Davies (1990), where the aim is to minimise the χ^2 value within each bin while maximising the χ^2 value from the bin medians across the en-

tire epoch. The initial parameters were set to use 50 bins with a range of trial periods centred on the period given by Payne (2013). To find the pulsation period for each object the folding routine used 3 iterations, decreasing the width of the trial period range from 2000 s to 10 s, then to 1 s, while concurrently reducing the interval steps from 2 s, to 0.01 s, to 0.001 s so as to maintain resolution. The epoch folding scores were calculated as

$$\chi^2_{EF} = \sum_{bin=1}^{M} \frac{\left(\tilde{F}_{\rm bin} - \tilde{F}_{\rm LC}\right)^2}{\tilde{F}_{\rm LC}}$$

where $\tilde{F}_{\rm bin}$ is the median flux in each bin, M is the number of bins and $\tilde{F}_{\rm LC}$ is the median flux of the whole light curve.

The PDM reduced χ^2 value for each bin was calculated as

$$\chi^2_{red} = \sum_{j=1}^{M} \left(\frac{\Sigma_{i=1}^{i=N_{bin}} \left(F_i - \tilde{F}_{\rm bin}\right)^2}{\tilde{F}_{\rm bin}} \right) / \left(N_{bin} - 1\right)$$

where F_i is the ith flux point in the bin, $\tilde{F}_{\rm bin}$ is the median flux in the bin, and N_{bin} is the number of flux points in the bin, and M is the number of bins. The best period was the trial period with the highest ratio of epoch folding to PDM values. Visual inspections led to 2876 SuperWASP objects (33.6%) being removed: either the re-folded light curve was flat with a gap due to a periodic gap in observations (e.g. Fig. 3.1); or the light curves looked like a non–variable star being contaminated by light from a nearby bright pulsating variable, identifiable by the similarity in their light curve shapes and coordinates.

A further visual check was made on objects with periods below 0.32 d. If their light curve looked similar to the RRc type, their classification was checked using the online Vizier system. A further 20 objects were removed at this stage due to being classified as RRc in AAVSO or GCVS. An example of an RRc–like light curve is shown in Fig. 3.2.

Objects with periods above 1.2 d were also checked online and a further 9 were removed as they were classified as BL Her type objects. BL Her objects are classical pulsators with periods of up to 8 days, and luminosities between that of RR Lyrae and W Virginis objects. They are also known as AHB1 for ‘above horizontal branch’. It was now possible to cross reference this remaining dataset of 5651 RRab against known RRab and known Blazhko effect stars (which resulted in the removal of more duplicate objects as described below).

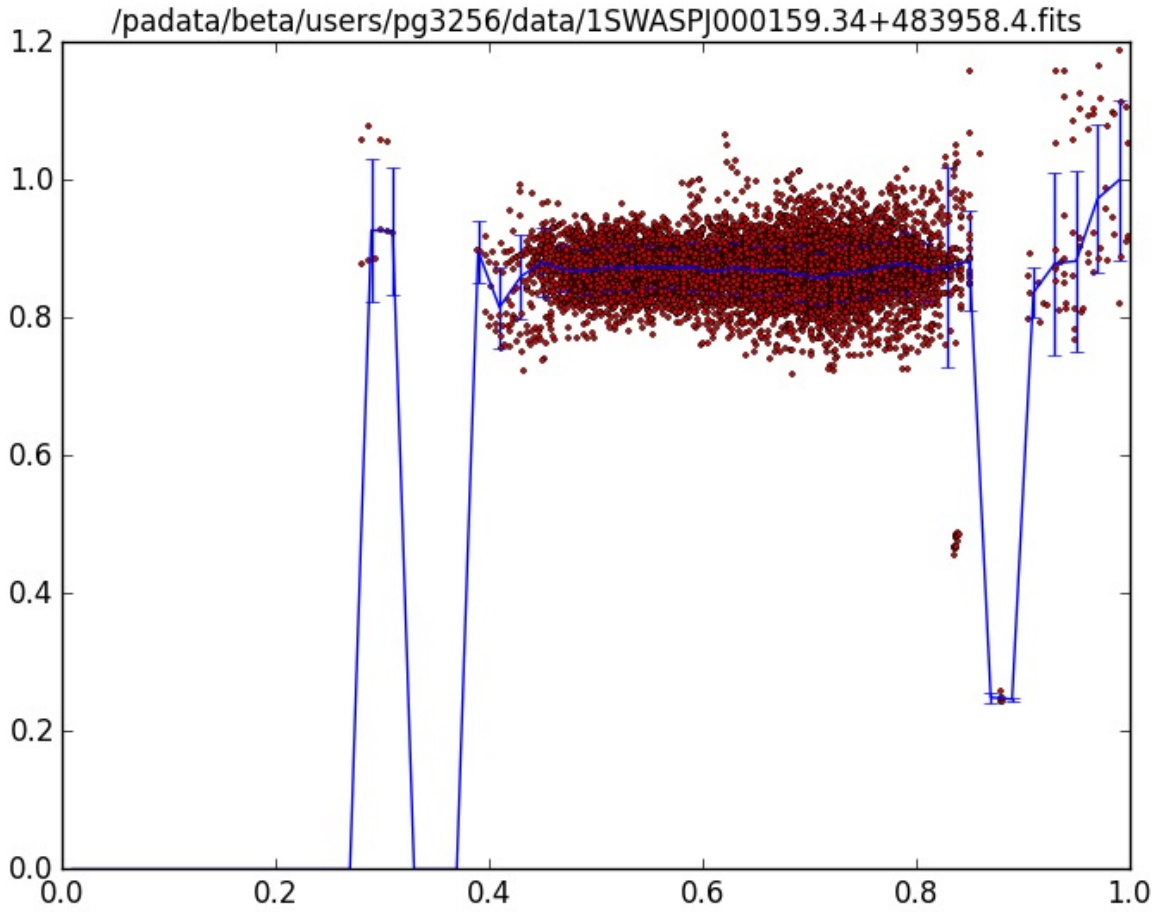

Figure 3.1: Non–varying LC where the periodicity is due to the observing cycle and not the object being viewed. These light curves were among the first to be removed during definition of the RRab catalogue.

The phase folded light curves could also be analysed for signs of the Blazhko effect, see Sect. 3.3.

The distance d to each object in kiloparsecs was calculated using an absolute magnitude M_V of 0.6 ± 0.1 based on figures cited in Sesar et al. (2017) and the median light curve magnitude $\tilde{m}_{LC}$. The value of absolute magnitude used here is the same as RR Lyra itself, therefore all SuperWASP RRab objects are assumed to have the same metallicity as RR Lyra. The distance uncertainty was calculated by firstly adding the errors in M_V and $\tilde{m}_{LC}$ in quadrature, before multiplying this by $0.461\times d$, derived using standard error propagation.

3.2.3 Catalogue comparisons

The type of objects from the SuperWASP catalogue need to be verified, and the number of known and new objects defined, by comparing the catalogue thus far to an existing catalogue that covered similar areas of the sky and listed the same type of objects. Therefore the

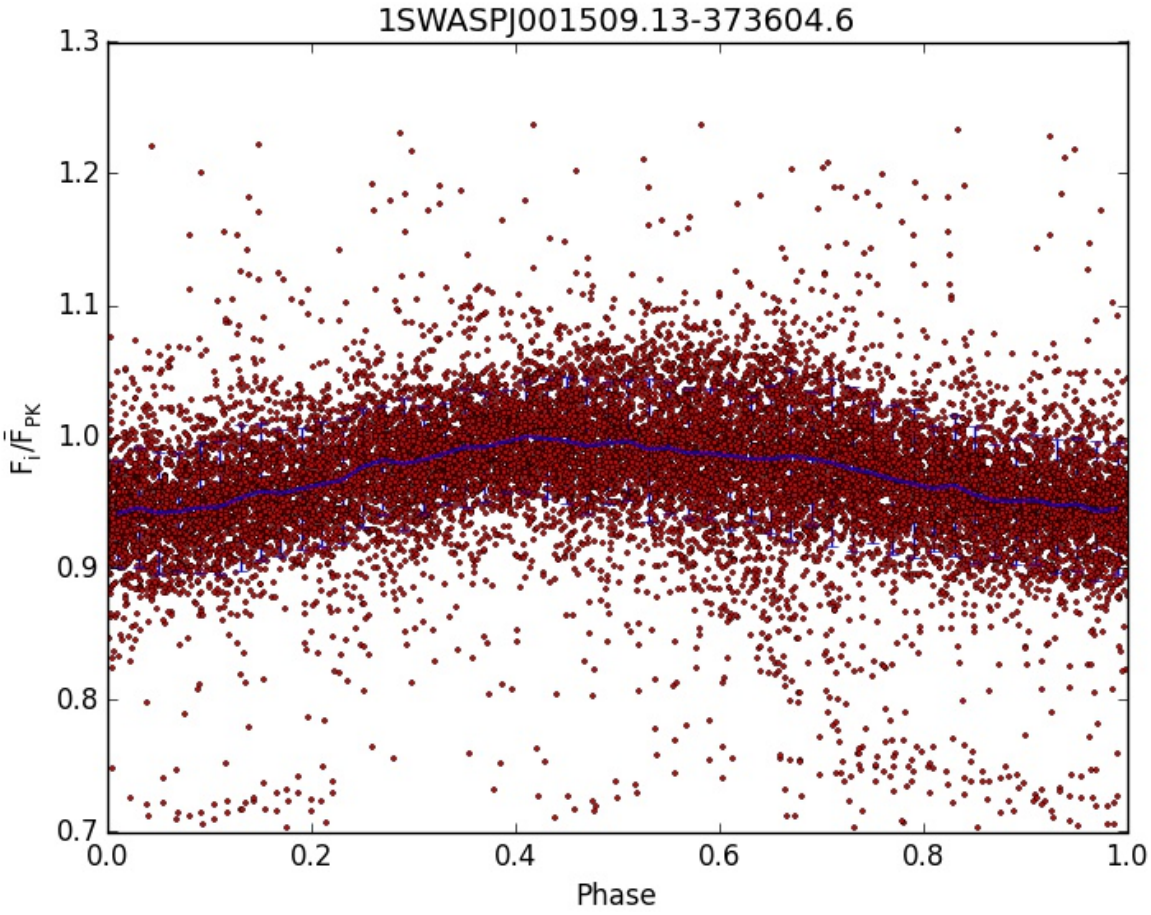

Figure 3.2: RRc–like light curve showing a more sinusoidal shape than a true RRab class RR Lyrae. Light curves such as this were removed after visual inspection.

remaining SuperWASP RRab objects were cross–matched to 8076 'RR', 'RR:', 'RRAB' and 'RRAB:' objects in the General Catalogue of Variable Stars (GCVS) (Samus et al., 2009). The 'RRAB:' and 'RR:' lists were included in order to avoid declaring any existing objects as new variable stars. The SuperWASP RRab coordinates were taken directly from their unique SuperWASP identifier.

The comparison algorithm had the additional benefit of highlighting when several SuperWASP objects fell within the same search aperture. Some of these objects would be the same object given different coordinates when compared to the USNO-B1 catalogue, or a non–variable object misclassified as RRab through being contaminated by variable flux overspilling from a nearby bright RRab. The closest SuperWASP object to the GCVS object was kept as the matching one and remaining objects within a 2 arcminute radius were listed as duplicates. This radius was selected after correctly matching a SuperWASP RRab to a known Blazhko star at 100 arcseconds while a larger radii risked falsely matching objects. To identify duplicate RRab within the SuperWASP RRab dataset the cone search routine was

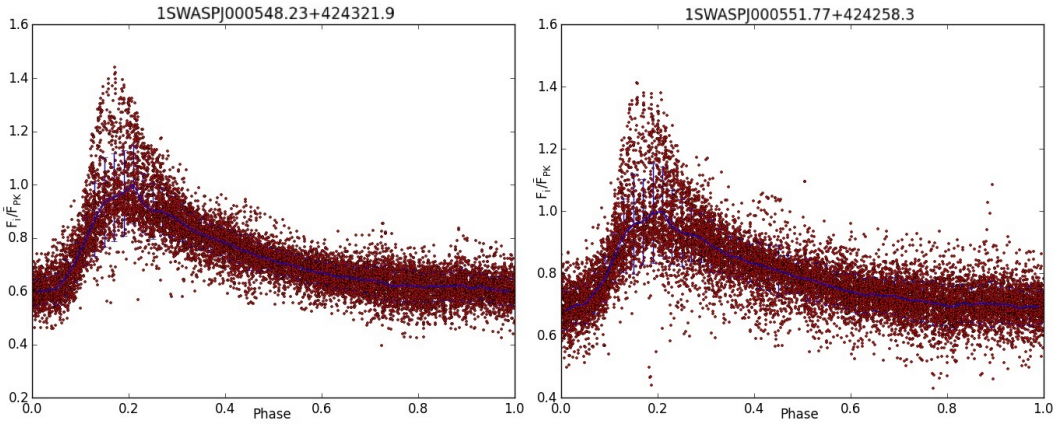

(a) 1SWASPJ000548.23+424321.9 (b) 1SWASPJ000551.77+424258.3

Figure 3.3: Duplicate light curve assigned different coordinates from the USNO–B1 catalogue. As well as similar spatial coordintates they have extremely similar pulsation periods: 1SWASPJ000548.23+424321.9 is phase folded on a period of 48036.2 s, whereas 1SWASPJ000551.77+424258.3 is folded on 48035.8 s. The first object remains in the RRab catalogue while the second object was removed.

Table 3.1: Number of objects removed.

Group	No. objects
Non–periodic	2876
RRc type	20
Magnitude < 11	65
BL Her	9
Duplicates	688

run again with the remaining SuperWASP objects being used as both input catalogues. Duplicates were defined as those stars within the same search radius, with periods within 1.5 s of each other. After manually checking light curves of several groups of duplicate objects, the object with the highest amplitude was selected to remain as the distinct RRab. One such duplicate pair is shown in Fig. 3.3 where the SWASPid gives different coordinates, but the phase–folded light curve is clearly identical.

4963 RRab objects remained once 688 duplicates were removed. A summary of the number of objects removed at each stage of the RRab catalogue preparation is given in Table 3.1. A sample of the full SuperWASP RRab catalogue available in Appendix A is shown in Table 3.3.

The number of objects found in both the SuperWASP RRab catalogue and GCVS RRab subclasses mentioned above is 1552, and is represented visually in the Venn diagram Fig. 3.4. The number found in both catalogues is 19.2%, meaning just over 4/5 of the GCVS RRab

list were not found in the SuperWASP catalogue. The SuperWASP RRab include many at low amplitude so the lack of completeness is unlikely to have been caused by low pulsation amplitude RRab objects being missed. Inspection of the GCVS objects not found in the SuperWASP RRab catalogue shows fewer than 80 objects that are brighter than 11th magnitude. There are, however, over 1700 objects that are fainter than 16th magnitude. Finally, the low level of completeness could be due to the larger area of the sky covered by the GCVS catalogue as shown in Fig. 3.5 (produced using the 'Aladin sky atlas' developed at CDS, Strasbourg Observatory, France Boch and Fernique, 2014; Bonnarel et al., 2000). In particular, this figure shows more objects at larger positive and negative declinations when compared to the SuperWASP sky map shown in Fig. 2.1, and includes many objects along the galactic plane.

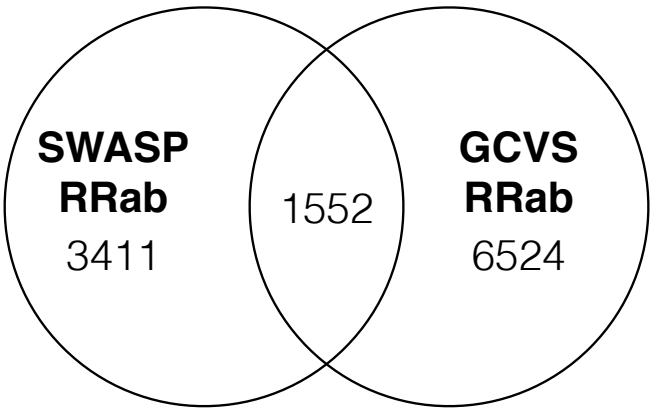

Figure 3.4: Venn diagram representing the overlap between the SuperWASP RRab and GCVS catalogues.

The numbers of GCVS objects not found in the SuperWASP RRab catalogue are shown in Table 3.2. Firstly, objects higher than 64 degrees declination and lower than -70 degrees declination were identified. Then, from the remainders, objects of 16th magnitude or fainter, and objects brighter than 11th magnitude were identified. Lastly, remaining objects of class RR, RR: or RR(B) were identified as these may not have been identified as RRab objects in the initial set of 8556 SuperWASP RRab objects. This leaves 2956 GCVS RRab objects that were not matched against SuperWASP RRab objects. A relatively small number of these objects may lie along the galactic plane in areas that are too crowded for SuperWASP's level

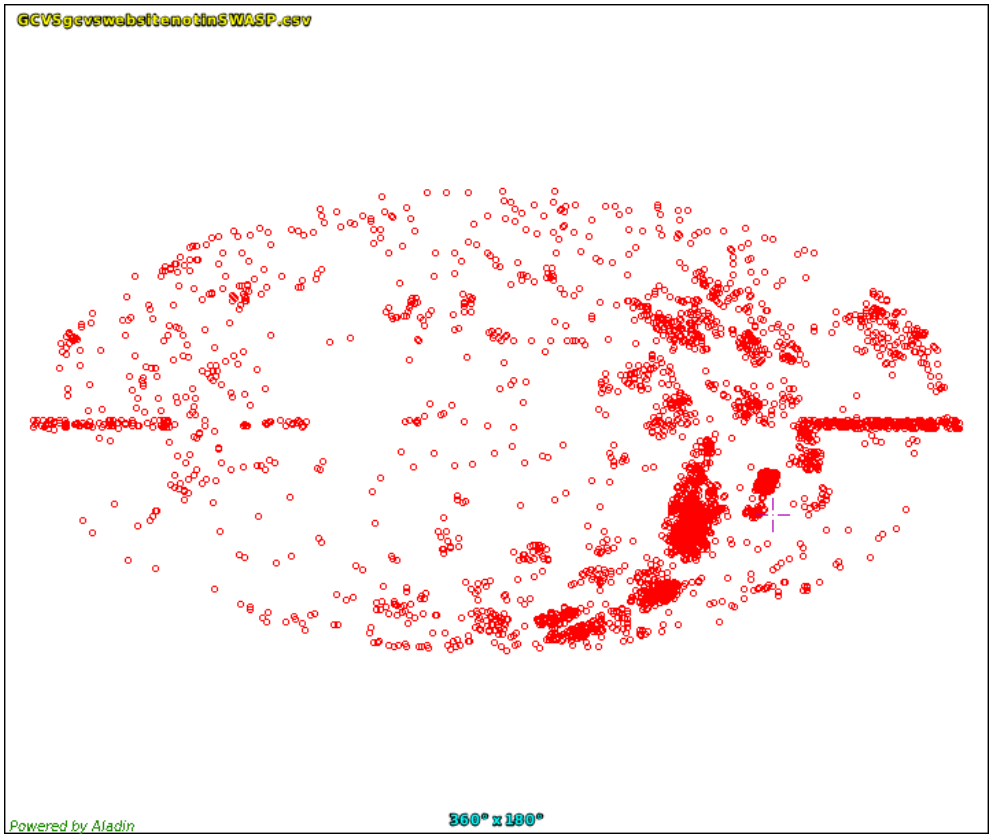

Figure 3.5: Sky map showing the location of GCVS RRab objects (Produced using 'Aladin sky atlas').

Table 3.2: GCVS RRab not in SuperWASP RRab catalogue.

Group	No. objects
Dec ≥ -70 deg	388
Dec $> +64$ deg	74
Magnitude < 11	65
Magnitude ≥ 16	1573

of resolution.

The 4963 SuperWASP RRab objects were also compared, using the CDS Xmatch facility, with RRab objects from 5 CRTS catalogues: Drake et al. (2013a), Drake et al. (2013b), Drake et al. (2014), Torrealba et al. (2015), and Drake et al. (2017). Where a CRTS catalogue contained several classes of variable objects, these were restricted to RRab and Blazhko classes only before cross-matching with the SuperWASP RRab catalogue. The combined list of 44686 CRTS objects were cross–matched with the 4963 SuperWASP RRab objects at a radius of 1 arcminute, producing 3477 distinct matches. As with the GCVS catalogue, these figures are represented visually in the Venn diagram Fig. 3.6. When inspecting the CRTS objects that were not included in the SuperWASP RRab catalogue, there are only a handful that are brighter than 11th magnitude. However, over two thirds of the objects are

fainter than 16th magnitude which explains why such a large proportion of RRab objects were not found in the SuperWASP database. As Fig. 2.9 in Chapter 2 showed, the CRTS surveys cover approximately the same regions of the sky as SuperWASP, but extends down from -15 deg declination to -75 deg declination.

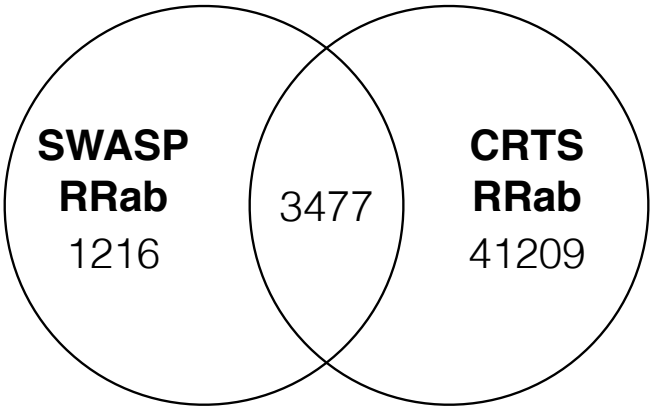

Figure 3.6: Venn diagram representing the overlap between the SuperWASP RRab and CRTS catalogues.

3.2.4 The layout of the SuperWASP RRab catalogue

This finalised the creation of the SuperWASP RRab catalogue, a subset of which is shown in Table 3.3 and a full version in Appendix A. The pulsation periods have been converted to days for easier comparison of periods; the amplitude in magnitudes has been calculated from the peak–to–peak amplitude of the light curve; the median light curve magnitude is given in magnitudes; the distance in kiloparsecs; where the object has been cross–matched with GCVS or CRTS objects, the name of the object from the respective catalogue is given in the final two columns. The full catalogue is available in the supplementary media.

Table 3.3: Subset of the SuperWASP RRab catalogue

SWASP id	P_{Pulse} [d]	A_{LC} [mag]	$\tilde{m}_{LC}$ [mag]	d [kpc]	GCVS name	CRTS name
1SWASPJ000003.66+352146.1	0.70675802	0.8±0.2	13.2±0.2	3.3±0.3	GM And	
1SWASPJ000017.72-101317.1	1.14682496	0.9±0.7	14.6±0.5	6.3±1.5		
1SWASPJ000018.15+193255.3	0.54549599	0.8±1.0	15.9±0.7	11.5±3.7	V0420 Peg	J000018.2+193253
1SWASPJ000023.75+361942.7	0.56246299	0.8±0.5	14.6±0.4	6.3±1.2		
1SWASPJ000035.58+263949.6	0.56606603	0.8±0.4	13.5±0.3	3.8±0.6	GV Peg	
1SWASPJ000049.23-284900.4	0.58303499	0.5±0.6	14.8±0.4	6.9±1.3	TZ Scl	J000049.3-284901
1SWASPJ000126.73-001344.2	0.555749	0.5±0.6	14.9±0.4	7.2±1.4		
1SWASPJ000128.97-411541.5	0.50587398	1.3±1.0	15.5±0.7	9.5±3.1		J000129.0-411542
...						
...						
1SWASPJ115945.36+025146.3	0.76770997	0.5±0.2	12.2±0.1	2.1±0.1		J115945.2+025147
1SWASPJ115953.34-282929.3	0.52957499	0.3±0.2	13.7±0.1	4.2±0.3	V0598 Hya	J115952.1-282945
1SWASPJ115953.79-113627.8	0.46502399	0.5±0.3	12.4±0.2	2.3±0.2		J115954.0-113629
1SWASPJ115954.71+100311.1	0.597215	0.9±0.7	15.0±0.5	7.6±1.8		
1SWASPJ120015.97+034308.2	0.45242199	0.9±0.8	13.8±0.7	4.4±1.4	V0363 Vir	J120016.0+034308
1SWASPJ120034.52-263657.5	0.52060199	0.7±0.6	14.1±0.3	5.0±0.7		
1SWASPJ120114.80-072618.5	0.47926301	0.4±1.0	14.7±0.6	6.6±1.8		J120114.7-072618
1SWASPJ120136.40+315412.1	0.61030799	0.5±0.5	14.3±0.3	5.5±0.8	CK UMa	J120136.4+315412
...						
...						
1SWASPJ235742.03-340111.2	0.556032	1.0±0.6	14.9±0.5	7.2±1.7	DP Scl	
1SWASPJ235749.03-363016.9	0.47006199	1.2±0.7	14.7±0.6	6.6±1.8		
1SWASPJ235801.02+233620.6	0.55598801	0.9±1.3	15.6±1.0	10.0±4.6		
1SWASPJ235806.72-334509.7	0.65022701	0.8±0.4	14.1±0.3	5.0±0.7	TY Scl	
1SWASPJ235810.74-200037.9	0.53132099	0.7±0.4	13.8±0.2	4.4±0.4		
1SWASPJ235811.74-452704.5	0.70424098	0.2±0.3	14.3±0.2	5.5±0.6		
1SWASPJ235839.98+005753.7	0.55037701	0.6±0.5	14.1±0.3	5.0±0.7		
1SWASPJ235842.19+412919.7	0.60307598	0.9±0.4	13.6±0.3	4.0±0.6	DY And	J235842.1+412919

The distribution of pulsation periods for the SuperWASP RRab objects is shown in Fig. 3.7. The mean period is 0.574 d, with a range of 0.258 to 1.28 d and a standard deviation of 0.094 d. The dip in the number of sources with 0.33 d and 0.5 d periods could be a result of more objects being discarded due to sampling effects after visual inspection of these integer fractions of a day. This causes artefacts to appear at these values in Figs. 3.10 and 3.12 where the pulsation period is plotted on the horizontal axis.

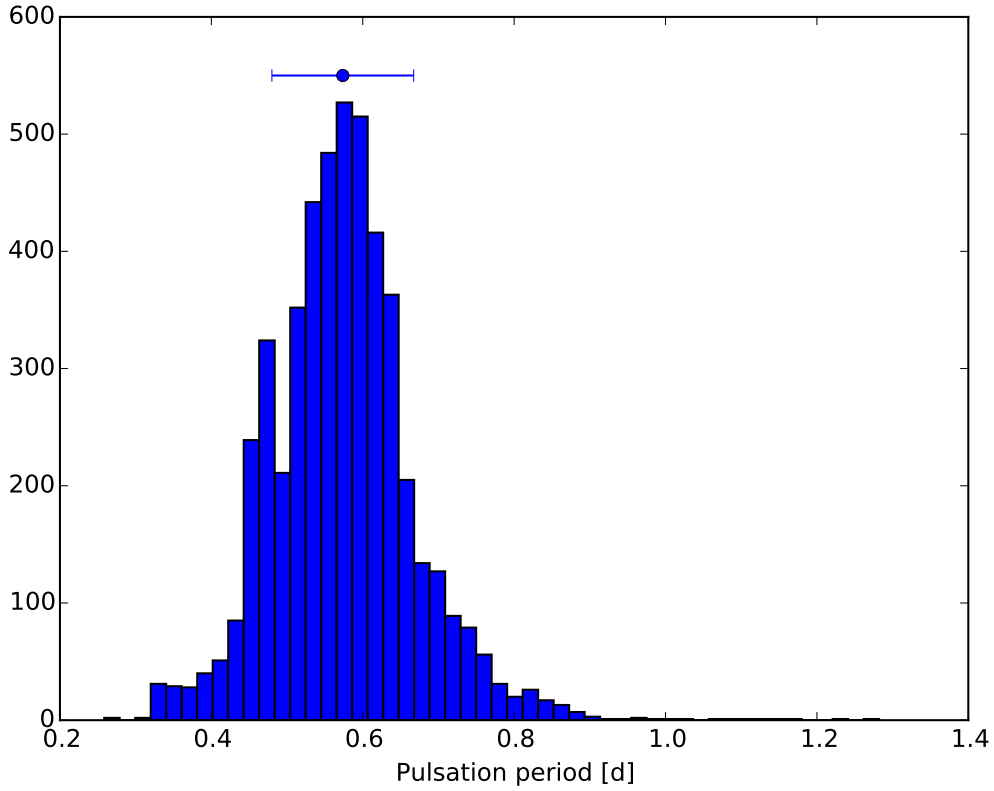

Figure 3.7: Distribution of pulsation periods of SuperWASP RRab objects. The horizontal error bar shows the mean and standard deviation of the distribution.

The distribution of pulsation amplitudes for the SuperWASP RRab objects is shown in Fig. 3.8. The mean amplitude is 0.589 mag, with a range of 0.020 mag to 2.22 mag and a standard deviation of 0.351 mag.

The distribution of median light curve magnitudes for the SuperWASP RRab objects is shown in Fig. 3.9. The mean magnitude is 14.1 mag, with a range of 9.2 mag to 16.7 mag and a standard deviation of 1.0 mag.

The three parameters used so far (pulsation amplitude, pulsation period, and median light curve magnitude) were compared to see if any long period objects were also abnormally bright or faint, or had too large or small a pulsation amplitude, which could suggest another

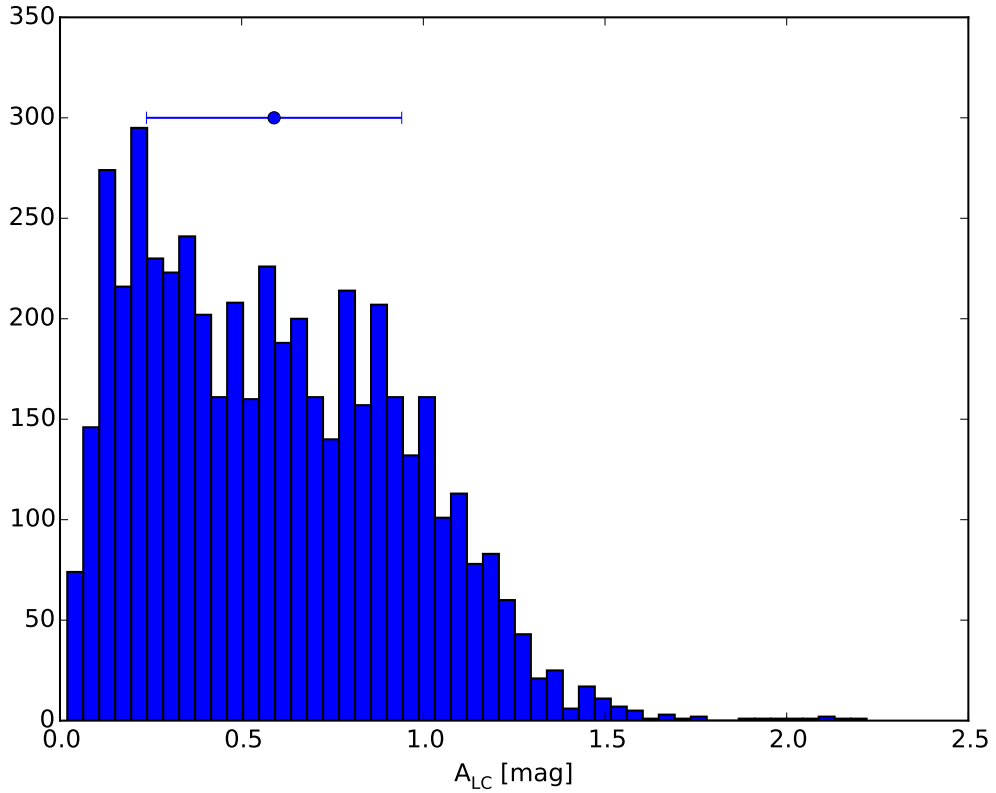

Figure 3.8: Distribution of pulsation amplitudes of SuperWASP RRab objects.

type of stellar object being misclassified as an RRab. showing several objects with high amplitude and low brightness. There appears to be no correlation between pulsation amplitude and period as shown in Figure 3.10. The majority of amplitudes appear to be constrained below 1.5 mag. There also appears to be more objects with low amplitudes at long periods. The cut–off at a pulsation period of 0.3 d is due to objects with periods below 0.32 d being manually checked in case they were RRc objects. Figure 3.11 shows a lack of objects in the bottom right of the diagram suggesting that the very faint objects were detected thanks to at least part of their light curve being above SuperWASP's detection limit. It also shows several faint objects with very large amplitudes in the top right, but otherwise most objects have amplitudes below 1.5 mag across a wide range of light curve median magnitudes. However, no visible correlation can be seen between pulsation amplitude and the light curve median for SuperWASP RRab objects. This could be due the variation in light curve morphologies where the median brightness could be raised by a particularly high peak, or suppressed if the peak is narrow and the light curve is near the minimum for most of the pulsation period.

There does not appear to be any correlation between the median magnitude of the RRab

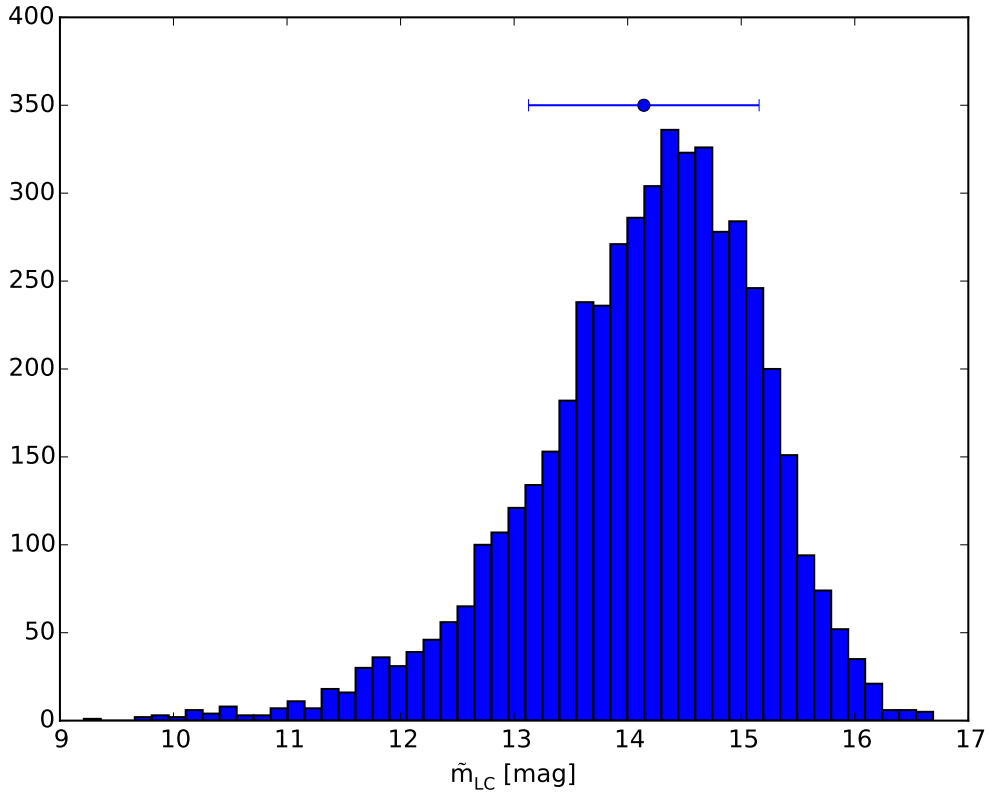

Figure 3.9: Distribution of the median light curve magnitudes of SuperWASP RRab objects.

objects and their pulsation period, as shown in Fig. 3.12. Some bright RRab are observed brighter than 12th magnitude, but the majority are grouped from ~13.5 to ~15.5 mag.

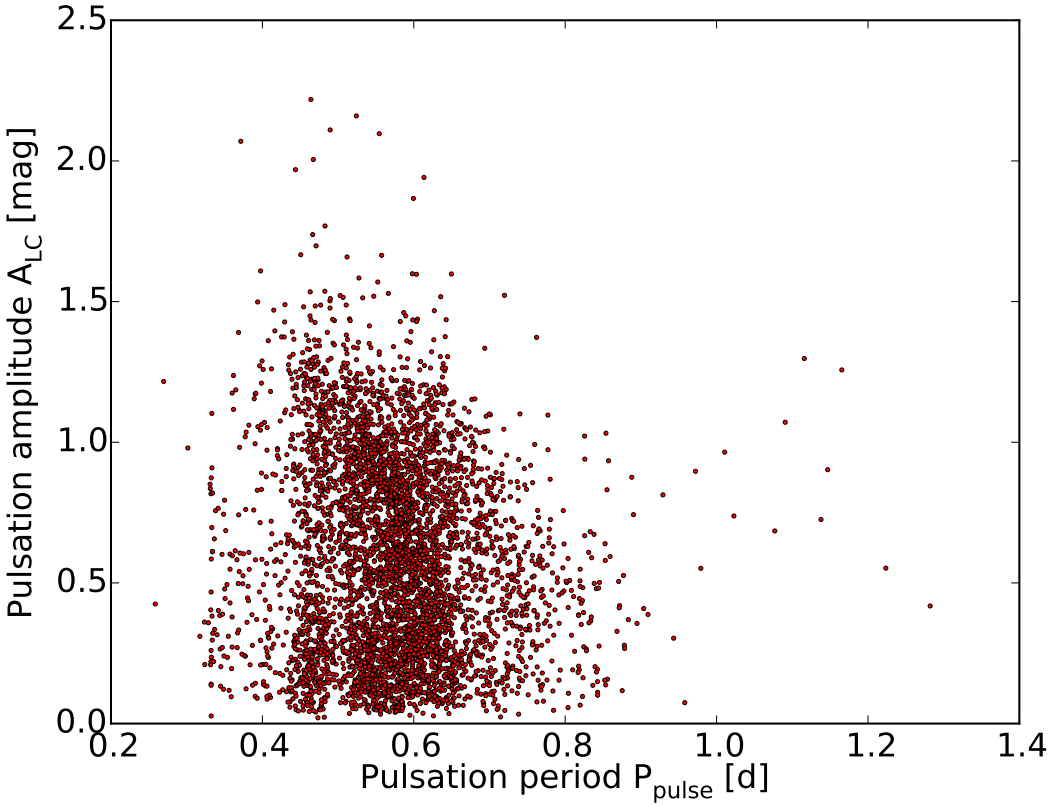

Figure 3.10: Comparison of the pulsation amplitude against period.

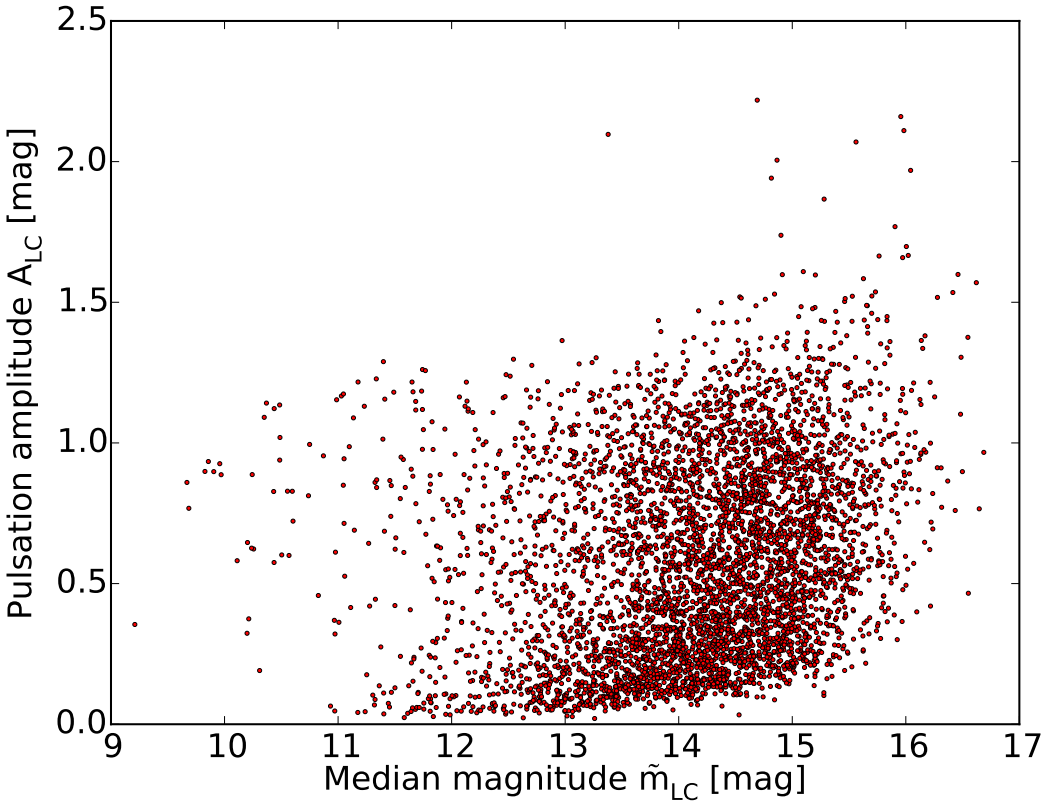

Figure 3.11: Comparison of the pulsation amplitude against the light curve median magnitude showing no visible correlation between brightness and amplitude of RRab objects.

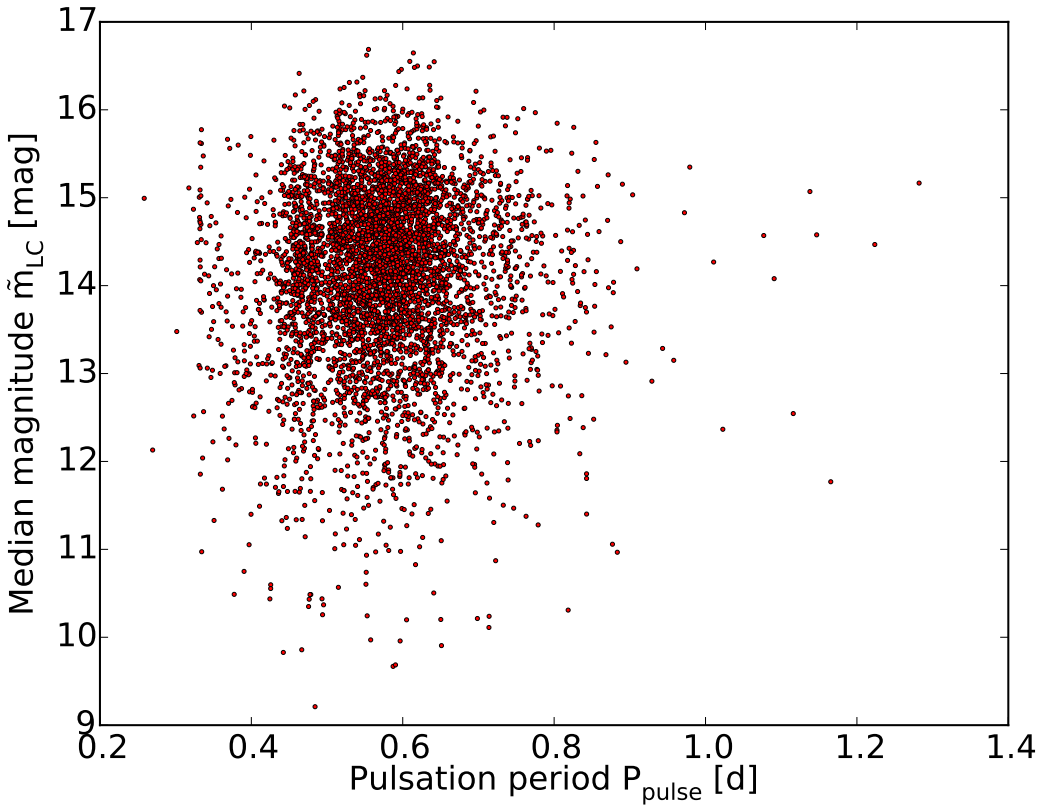

Figure 3.12: Comparison of the light curve median magnitude against the pulsation period.

This section has described the many stages required to transform the initial SuperWASP observations into a catalogue of RRab objects containing the basic parameters required for further analysis. It has been shown that many objects were not previously classified as RRab in the venerable GCVS, and some were not identified as such in the larger series of Catalina surveys. This catalogue now provides the opportunity to investigate the phase–folded light curves of a large sample of RRab objects for signs of the Blazhko effect.

3.3 The Blazhko Effect in the Time Domain

One of the more obvious features of the Blazhko effect is amplitude modulation (AM): the periodic increase and decrease in the amplitude of the RR Lyrae object's pulsations. This section describes an attempt to quantify the Blazhko effect in the time domain using the symptoms of AM on phase–folded light curves, in order to automatically identify Blazhko effect objects in large samples of RRab objects. Firstly, the methodology of using the amount of scatter at different points in the light curves is described. Secondly, the validity of this technique is assessed for known Blazhko and non-Blazhko effect stars, before comparing it to other characteristic parameters such as pulsation amplitude and period. Thirdly, a collection of objects with intriguing light curves are investigated as cases of extreme AM, before using them as case studies to investigate whether the Blazhko period can be calculated from phase folding the envelope function created by AM.

3.3.1 Quantifying Blazhko effect Amplitude Modulation

In initial phase folding tests using objects from Skarka's list of known Blazhko effect stars (Skarka, 2013) the scatter at the peak of the pulsation was seen to be more pronounced than elsewhere in the light curves, which seemed to be a symptom of AM, as noted by Skarka (2014a). The phase folded light curves for 6 of these test stars are shown in Fig. 3.13.

Examples of known non–Blazhko candidate objects taken from Table 1 of Nemec et al. (2011), are shown in Fig. 3.14.

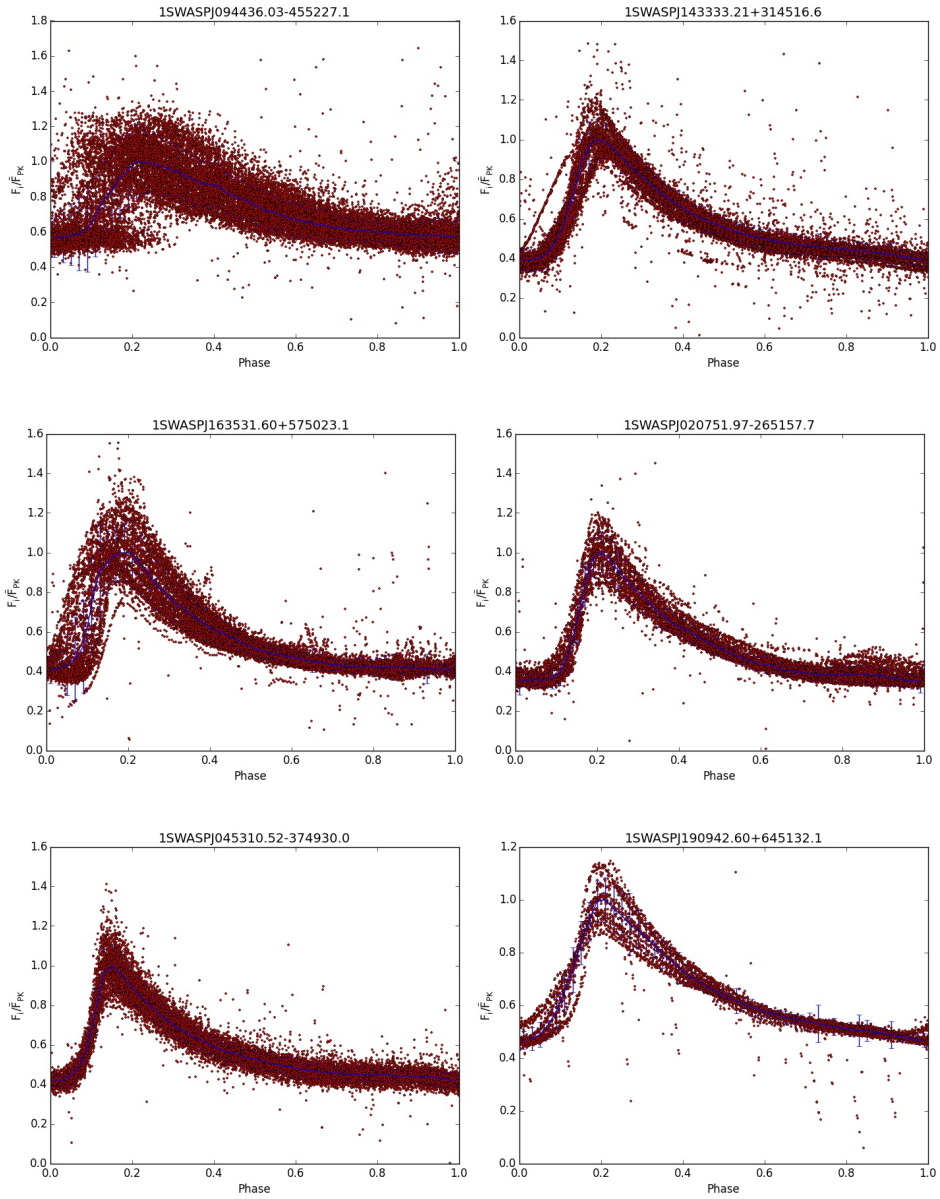

Figure 3.13: Phase folded SuperWASP light curves for 6 objects known to be Blazhko effect stars. The vertical scale is in flux relative to the median flux of the peak bin. Visual inspection of these known objects led to the concept of quantifying the scatter at the peak as an indicator and measure of the Blazhko effect in the time domain.

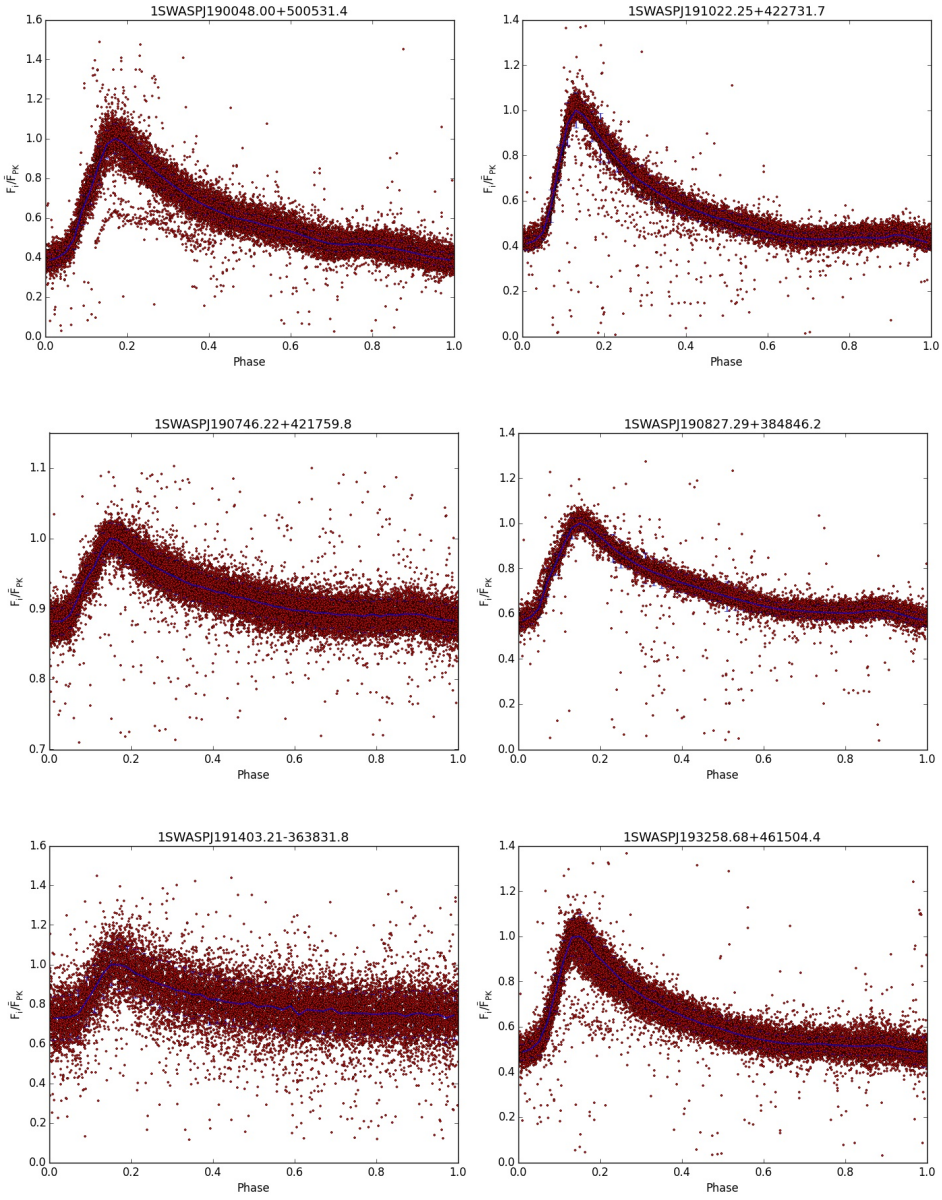

Figure 3.14: Phase folded light curves for 6 known non–Blazhko objects from the SuperWASP catalogue. The vertical scale is in flux relative to the median flux of the peak bin.

Payne (2013) also noticed this abnormally large amount of scatter at the peak and suggested considering the level of scatter at the peak of the light curve as a 'Blazhko Indicator'. Hence, in order to compare levels of scatter between different light curves, the phase folded light curves were normalised by dividing each curve's flux counts by its peak bin median flux and phase shifted so the minimum corresponds to the first bin. We now define the envelope function as the variation in the peak and minimum of the light curve. We calculated the ratio of noise in the peak area to the noise in a quiet part of the descending section of the light curve in order to give a relative scatter parameter. Using the same 50 bins as the PDM routine, this quiet area is from bins 20 to 29 and labelled as 'Unaffected area' in Fig. 3.15 because the amount of noise in this descending section appeared to be dependent only on the overall quality of the light curve, and not on AM. Later bins near the minimum of the phase–folded light curve were not used as AM caused a large amount of scatter in this region, making it unsuitable as a comparison to the peak area of the light curve. With the light curve split into 50 bins, the peak bin and the 2 adjacent bins of the folded light curves were defined as the peak area as shown in Fig. 3.15.

The standard deviation in each of the bins, σ_{bin}, is defined as

$$\sigma_{bin} = \left(\frac{\Sigma_{i=1}^{i=N_{bin}} \left(F_i - \tilde{F}_{\rm bin} \right)^2}{(N_{bin} - 1)} \right)^{1/2}$$

where F_i is the i-th flux point in the bin, $\tilde{F}_{\rm bin}$ is the median flux in the bin, and N_{bin} is the total number of flux points in the bin. The relative scatter was quantified as $\sigma_r = \sigma_p/\sigma_q$ where σ_p is the mean of $\sigma_{\rm bin}$ across the 3 peak bins and σ_q is the mean of $\sigma_{\rm bin}$ across bins 20 to 29.

Example light curves of Blazhko candidate objects, created using the PDM algorithm, are shown in Fig. 3.16.

The first 25 rows of results of the relative scatter parameter program are shown in Table 3.4 in descending order of relative scatter, where $P_{\rm pulse}$ is the main pulsation period in seconds, σ_p is the scatter at the peak of the light curve in flux, σ_q is the scatter at the quiet area on the late descending section of the light curve in flux, σ_r is the relative scatter parameter produced by the ratio of σ_p to σ_q, $A_{\rm LC}$ is the pulsation amplitude in mag, $\delta A_{\rm LC}$ is the uncertainty in this pulsation amplitude in mag, $\tilde{m}$ is the median magnitude of the light curve, and $\delta\tilde{m}$ is the uncertainty in this median magnitude.

Table 3.4: Relative scatter results for SuperWASP RRab objects

SWASP id	P_{pulse} [d]	σ_p	σ_q	σ_r	A_{LC} [mag]	δA_{LC} [mag]	$\tilde{m}_{LC}$ [mag]	$\delta\tilde{m}_{LC}$ [mag]
1SWASPJ210128.08-151426.9	0.44774	0.202	0.04	5.114	0.88	0.56	11.66	0.34
1SWASPJ202044.47-410705.9	0.55293	0.157	0.031	5.107	0.84	0.78	11.59	0.28
1SWASPJ091348.80-091908.8	0.53722	0.19	0.038	4.972	0.84	0.53	11.34	0.31
1SWASPJ203231.55+003507.0	0.57801	0.204	0.043	4.792	1.17	0.55	11.05	0.29
1SWASPJ084142.27+492516.7	0.50163	0.374	0.079	4.745	1.14	0.99	14.1	0.73
1SWASPJ222748.76-072901.4	0.46955	0.39	0.086	4.525	1	0.92	12.3	0.72
1SWASPJ181258.44+420346.1	0.44207	0.297	0.067	4.459	0.63	0.67	13.16	0.37
1SWASPJ143709.04+254446.6	0.46673	0.248	0.057	4.363	0.99	0.69	13.92	0.48
1SWASPJ132922.47-055259.2	0.5764	0.199	0.046	4.343	0.8	0.57	11.92	0.34
1SWASPJ140324.07-362420.1	0.49396	0.164	0.04	4.077	0.86	0.42	11.33	0.25
1SWASPJ000248.10-245643.1	0.49336	0.105	0.026	4.049	1.12	0.44	10.44	0.24
1SWASPJ193229.30+562317.5	0.4666	0.116	0.029	4.034	0.93	0.34	9.86	0.23
1SWASPJ153039.23+354704.3	0.6223	0.142	0.035	4.009	1.17	0.52	11.03	0.3
1SWASPJ163531.60+575023.1	0.44292	0.151	0.038	3.956	0.98	0.52	11.84	0.35
1SWASPJ234158.75+181301.5	0.52964	0.144	0.036	3.951	0.74	0.35	12.78	0.22
1SWASPJ040638.89+552959.6	0.36872	0.15	0.039	3.859	0.74	0.51	12.02	0.24
1SWASPJ010510.70+341306.2	0.56311	0.173	0.045	3.847	0.98	0.48	12.95	0.32
1SWASPJ172238.71+175304.8	0.43605	0.145	0.038	3.821	1.3	0.42	13.27	0.35
1SWASPJ134815.94+395403.0	0.47852	0.168	0.044	3.817	0.83	0.48	11.8	0.36
1SWASPJ114710.65-413143.3	0.39745	0.176	0.047	3.767	1.04	0.58	13.46	0.31
1SWASPJ204033.93-254030.6	0.46079	0.206	0.056	3.7	1.28	0.74	13.12	0.48
1SWASPJ155229.33+100834.1	0.51139	0.2	0.055	3.657	0.97	0.54	13.09	0.34
1SWASPJ050747.04-335154.3	0.48735	0.21	0.058	3.624	0.85	0.62	12.62	0.35
1SWASPJ123421.42+160743.3	0.30147	0.413	0.114	3.615	0.98	1.01	13.48	0.88
1SWASPJ215202.79+223429.3	0.39038	0.08	0.022	3.596	0.99	0.26	10.75	0.21

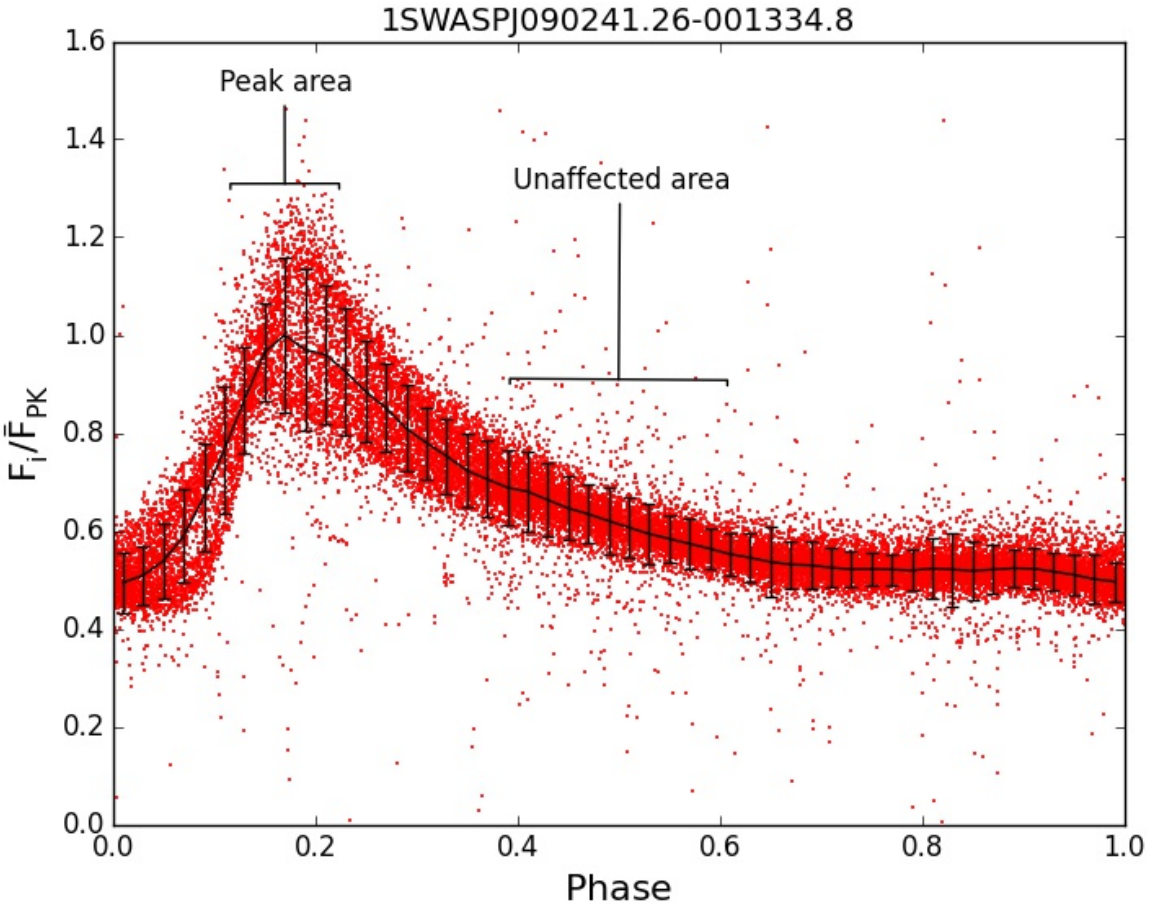

Figure 3.15: Phase folded light curve for 1SWASPJ09024.26-001334.8 showing the areas used to create the relative scatter parameter, labelled 'Peak area' and 'Unaffected area'. The median flux level for each bin is shown in blue with 1σ error bars. The vertical axis is in flux units relative to the peak bin median flux level.

3.3.2 Analysis of relative scatter

Fig. 3.17 shows that there is a smooth distribution of levels of relative scatter across a range from 0.45 to 5.11 with a mean value of 1.35 and a standard deviation of 0.48. The longer tail at high relative scatter compared to a symmetrical distribution suggests that there may be a subset of objects with high levels of relative scatter. However, the lack of bimodality implies that it would impossible to define a threshold in the relative scatter above which Blazhko candidates can be reliably identified because there are not two clearly defined populations. The relative scatter parameter for the small set of known Blazhko objects used in the definition of relative scatter are shown in Table 3.5 in order of right ascension. It shows a range of relative scatter from 2.267 to 3.956 which are all in the asymmetric high value section of Fig. 3.17. These high values explain why it was worth applying the relative scatter parameter to the entire SuperWASP RRab catalogue. Table 3.6, by contrast, shows the relative scatter

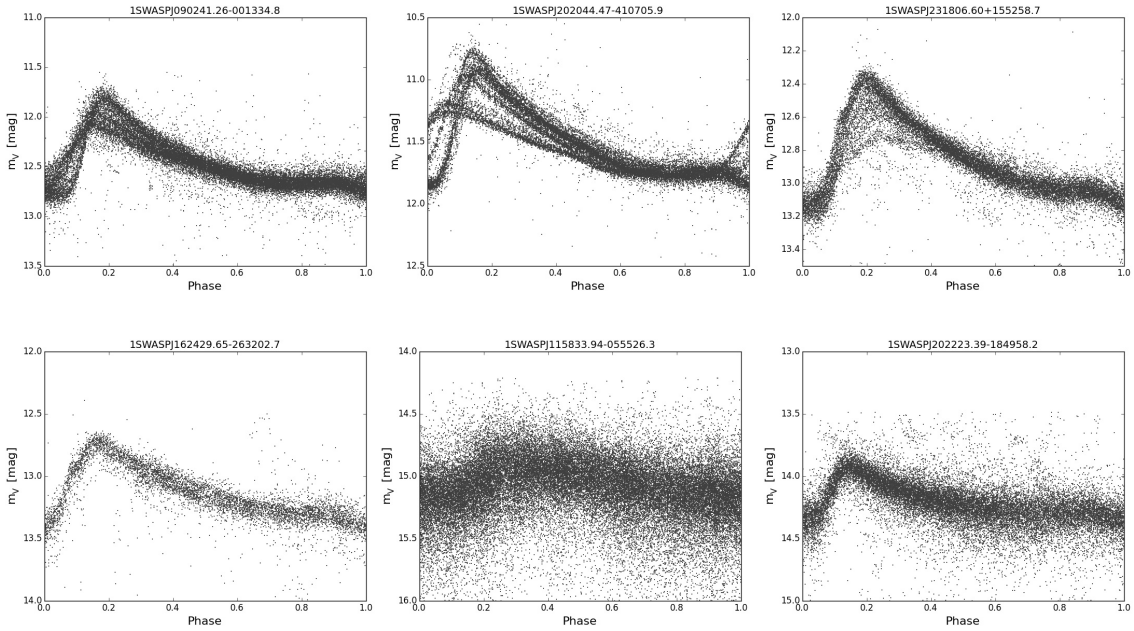

Figure 3.16: Phase folded light curves for SuperWASP RRab catalogue objects. The vertical scale is in magnitudes. The top row shows objects with high relative scatter parameter values. The bottom row show Blazhko candidates with low relative scatter values.

parameter values for known non–Blazhko stars, taken from Nemec et al. (2011), also shown in order of right ascension. Although these objects have relative scatter values that start from 1.083, which is similar to the entire SuperWASP RRab population, their relative scatter parameter increases to 2.945, demonstrating that the relative scatter parameter can extend into high values even without the AM from the Blazhko effect.

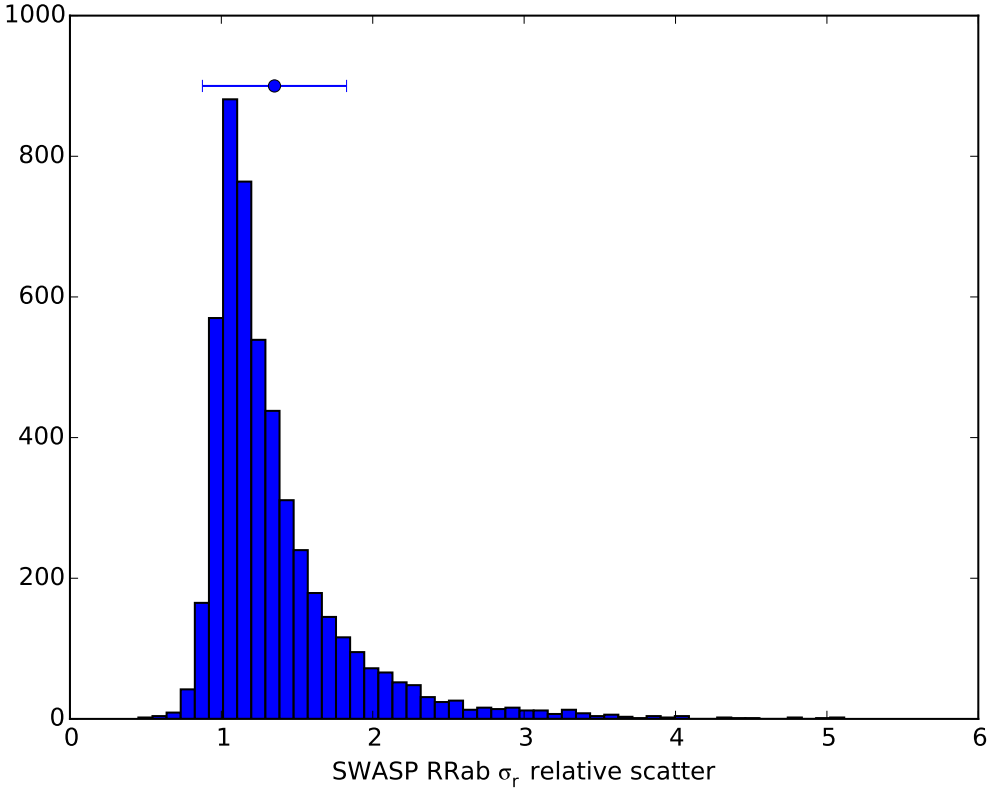

Figure 3.17: Distribution of relative scatter σ_r for SuperWASP RRab objects. The error bar shows the mean and standard deviation for the population.

Table 3.5: Relative scatter for known Blazhko effect objects.

SWASP id	Name	σ_r
1SWASPJ020751.97-265157.7	SS For	3.107
1SWASPJ045310.52-374930.0	U Cae	2.991
1SWASPJ094436.03-455227.1	CD Vel	3.188
1SWASPJ123030.50-260251.1	SV Hya	2.440
1SWASPJ134815.94+395403.0	SS CVn	3.817
1SWASPJ143333.21+314516.6	RS Boo	2.267
1SWASPJ163531.60+575023.1	RW Dra	3.956
1SWASPJ190942.60+645132.1	XZ Dra	2.612

Table 3.6: Relative scatter for known non–Blazhko effect objects.

SWASP id	Name	σ_r
1SWASPJ190048.00+500531.4	AW Dra	2.200
1SWASPJ190746.22+421759.8	NQ Lyr	1.083
1SWASPJ190827.29+384846.2	NR Lyr	1.181
1SWASPJ191022.25+422731.7	FN Lyr	2.945
1SWASPJ191403.92+481158.9	V0838 Cyg	1.543
1SWASPJ193258.68+461504.4	V0894 Cyg	2.585

It is therefore worth checking the relative scatter parameter for the entire Skarka dataset of known Blazhko objects that can be found in the SuperWASP RRab catalogue. These objects are defined as those found during the cross–matching of the SuperWASP RRab catalogue and Skarka datasets using the same catalogue comparison technique as with the GCVS and CRTS datasets. This results in 188 SuperWASP RRab objects that are known Blazhko objects based on Skarka's online dataset. The population distribution of the relative scatter parameter for these objects is shown in Fig. 3.18. Although this histogram shows that Blazhko objects have high relative scatter values, it also demonstrates that the value of the parameter extends down to the low relative scatter parameter values associated with known non–Blazhko objects from Nemec et al. (2011) given in Table. 3.6.

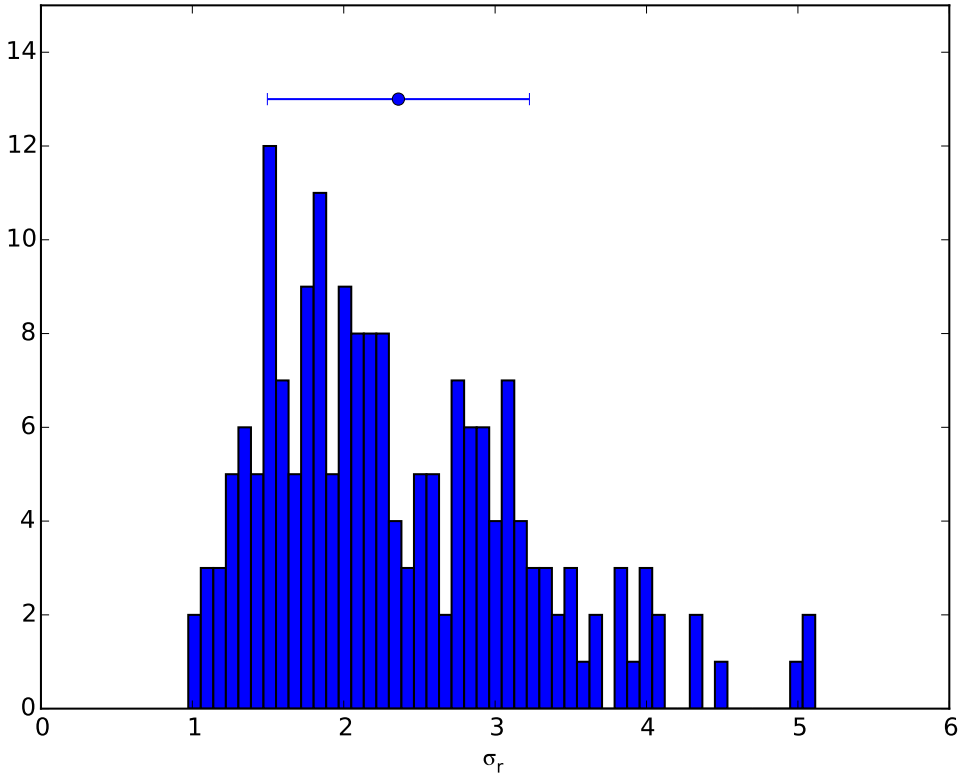

Figure 3.18: Distribution of relative scatter σ_r for the Skarka dataset of known Blazhko objects found in the SuperWASP RRab catalogue. The error bar shows the mean and standard deviation for this population.

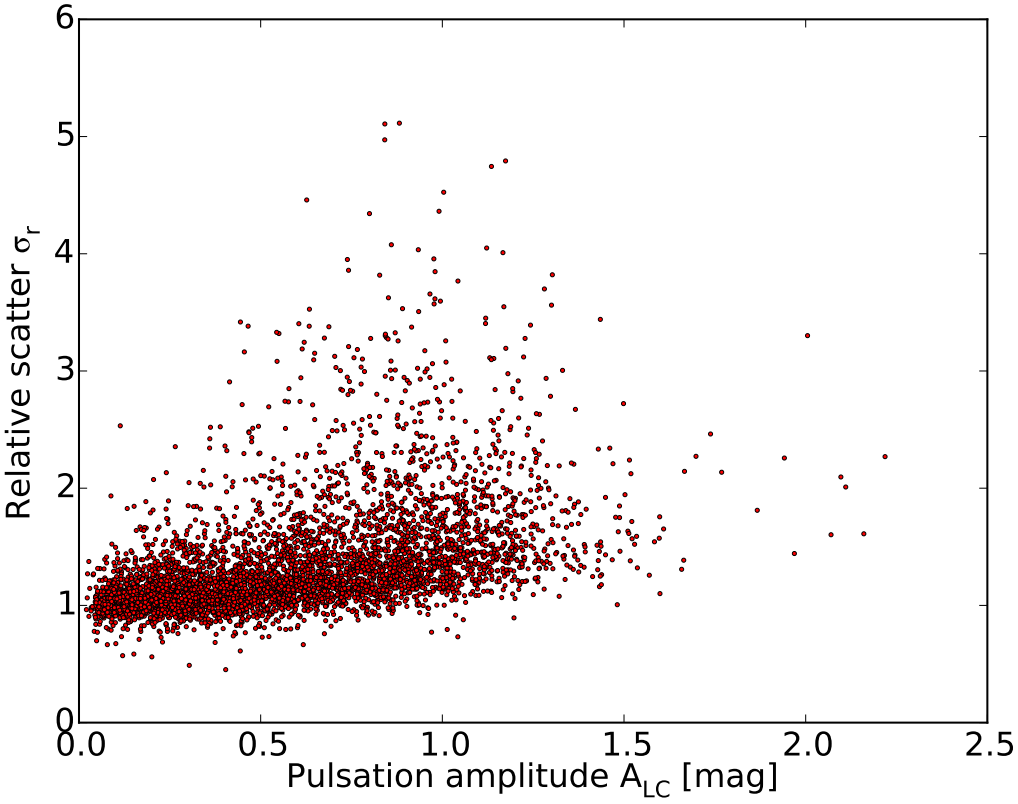

Figure 3.19: Comparison of relative scatter against pulsation amplitude for SuperWASP RRab showing a slight dependence on pulsation amplitude for the relative scatter parameter at high amplitudes.

The increase in the spread of relative scatter with pulsation amplitude (Fig. 3.19) is reflected in their Spearman coefficients of 0.61 (p-value = 0.0). This implies that either the amount of scatter at the peak of RRab light curves is proportional to the pulsation amplitude, or conversely, the scatter at the base of the descending section is inversely proportional to the pulsation amplitude.

Fig. 3.20 shows relative scatter against median magnitude. The apparent lack of correlation is confirmed by the low Spearman coefficient of −0.11 (p-value = 0.0).

The lack of correlation between relative scatter and pulsation period is shown in Fig. 3.21 with a low Spearman coefficient of −0.24 (p-value = 0.0). However, there appears to be a lack of high relative scatter values for objects with pulsation periods greater than 0.7 days.

This implies that there may be an upper threshold value above which there is a high probability that the RRab object will suffer the Blazhko effect. However, this threshold needs to be set so high that it risks excluding many objects with a more subtle Blazhko effect than the extreme AM examples given above. The same unimodal nature of the distribution

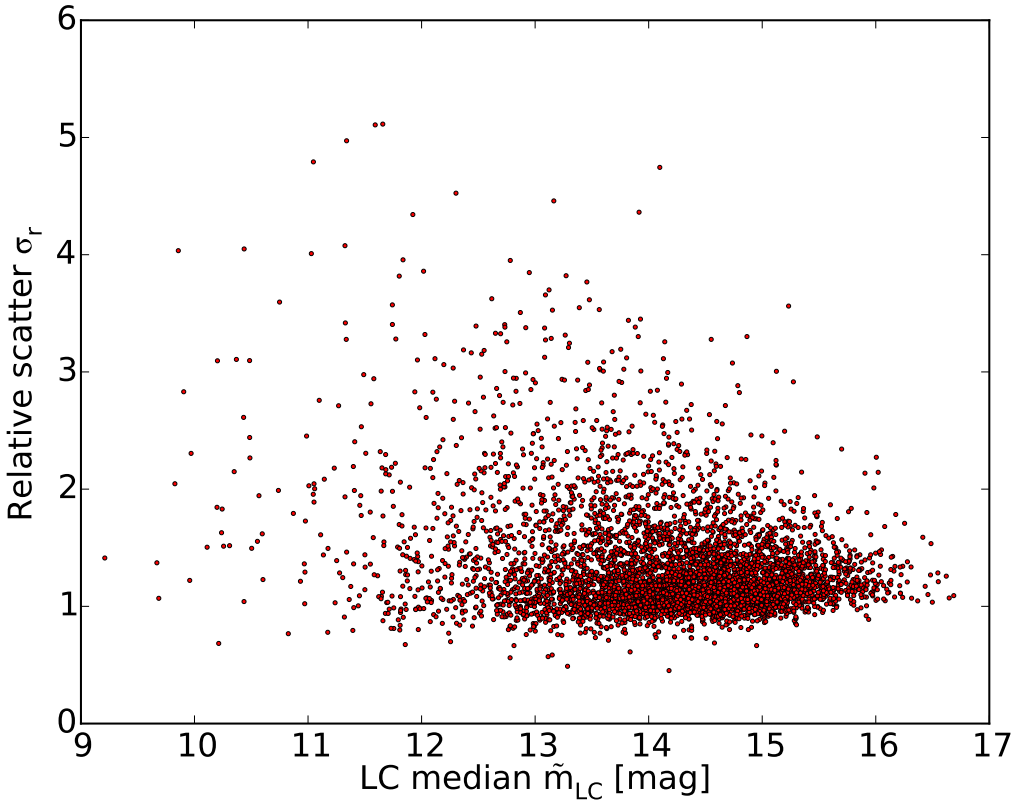

Figure 3.20: Comparison of relative scatter against median light curve brightness showing a lack dependence on brightness for the relative scatter parameter.

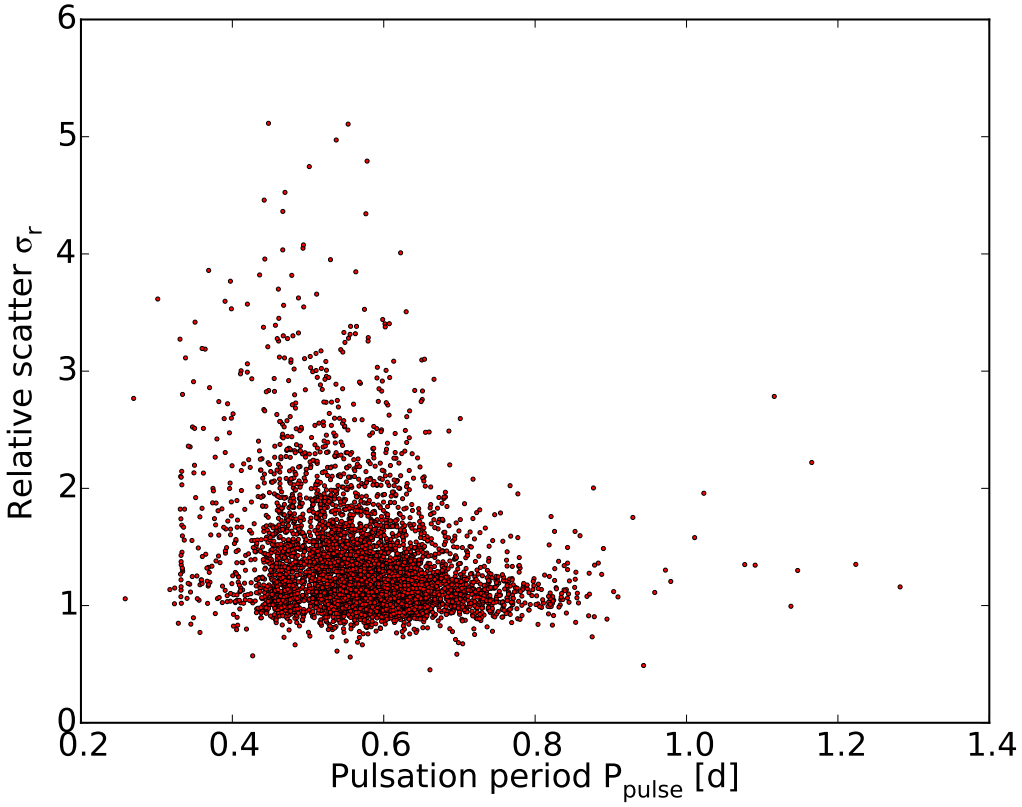

Figure 3.21: Comparison of relative scatter against pulsation period.

means that it would be very difficult to specify a lower threshold limit, below which there would be a high probability that the RRab object is not a Blazhko effect object. This lack of a lower threshold is even more apparent in the distribution of the relative scatter parameter for known Blazhko effect objects only. In this case, there is no difference in the lower limit of the relative scatter parameter to the short list of known non–Blazhko effect objects. Therefore, the amount of scatter at the peak, in relation to the rest of the light curve, does not appear to be a good indicator of the Blazhko effect.

Apart from the pulsation amplitude, the previous relative scatter plots show that this parameter does not appear to be correlated to the other photometric parameters of RRab objects, i.e. pulsation period or average apparent brightness. Hence it is not pursued further as a potential Blazhko indicator.

Despite this lack of success, the investigation into a relationship between the amount of light curve scatter and amplitude modulation revealed some very interesting light curves that could be mistaken for RRab objects switching between different pulsation modes. These objects are the subject of the following subsection.

3.3.3 Examples of high levels of AM

A visual search was made on the catalogue of 4963 SuperWASP RR Lyrae light curves for examples of clearly defined, high levels of AM in order to check the long tail in the relative scatter distribution at high values. 36 light curves were found that showed light curve pulsations at several distinct amplitudes due to high levels of AM with relatively little or no phase modulation. In some cases SuperWASP observations allow the AM of Blazhko candidates' folded light curves to be inspected over the course of an individual cycle.

The observations for the 36 extreme AM candidates were split into their constituent years to give each season of observation. In all cases the seasonal light curves were phase folded at the same average period found for that object using the PDM program described in subsection 3.2.2. The pulsation periods of the 36 candidates range from 0.347 to 0.668 d. The resultant well–phased light curves means that there was little, if any, period change between years (ruling out any form of mode–switching).

Visual inspections were made of the light curve for each year, leaving 20 objects where strong AM produces several distinct stages in the changing shape in their year long phase folded light curves. These stars are listed in Table 3.7 along with their pulsation period, and relative scatter parameter (σ_r).The pulsation periods range from 0.35 d to 0.65 d for these 20 objects. Their relative scatter parameters range from 2.176 to 4.972, which is a good match to the high values in the population distribution of the relative scatter parameter in Fig. 3.17, apart from object 1SWASPJ204432.08-342404.6.

The entire light curves of these 20 high AM objects are shown in Figures 3.22, phase folded by their pulsation period, demonstrating the shape of the light curve that was manually searched for in the SuperWASP RRab catalogue.

Table 3.7: Extreme AM objects

Object	SWASP id	P_{pulse} [d]	σ_r
a)	1SWASPJ004757.06+114223.5	0.45568	2.827
b)	1SWASPJ010510.70+341306.2	0.56311	3.847
c)	1SWASPJ091348.80-091908.8	0.53722	4.972
d)	1SWASPJ091809.74-193718.4	0.49108	2.504
e)	1SWASPJ093731.34-181612.9	0.52092	2.737
f)	1SWASPJ095515.90+034532.3	0.53109	2.736
g)	1SWASPJ120447.27-274043.2	0.65030	3.095
h)	1SWASPJ121206.15-261248.0	0.39877	3.532
i)	1SWASPJ123810.96+385027.9	0.34737	2.524
j)	1SWASPJ123811.99-442231.8	0.52353	3.082
k)	1SWASPJ132922.47-055259.2	0.57640	4.343
l)	1SWASPJ134815.94+395403.0	0.47852	3.817
m)	1SWASPJ141345.50-225441.8	0.44796	2.835
n)	1SWASPJ145315.45-143556.4	0.54008	2.694
o)	1SWASPJ152304.26-385153.6	0.57797	2.074
p)	1SWASPJ153911.88+035524.6	0.46347	2.569
q)	1SWASPJ161255.64-082727.6	0.54875	3.245
r)	1SWASPJ195926.63-340015.6	0.37967	2.421
s)	1SWASPJ204432.08-342404.6	0.56797	1.124
t)	1SWASPJ225247.51-244213.2	0.52955	2.176

Where there are signs of AM within a given year, each year was split further into weeks. In the weekly light curves, the change in pulsation shape from a sharp, high peak to a lower, more rounded peak demonstrates the suppression of the pulsation amplitude by AM. The yearly then weekly light curves for each object are shown in Appendix B, in the same order and using the same labels as in Table 3.7. In some cases, such as 1SWASPJ010510.70+341306.2 during 2013 (Fig. 3.23), the weekly light curves from observations show well defined pulsations shapes for each week, but only a subtle change in the amplitude and shape of the light curve over this timescale.

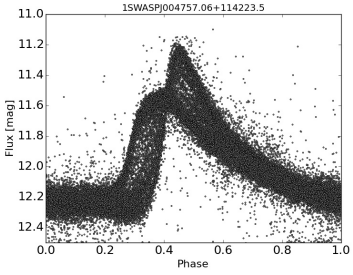

(a) 2.827

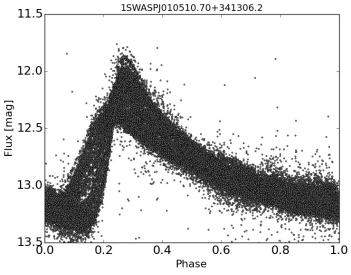

(b) 3.847

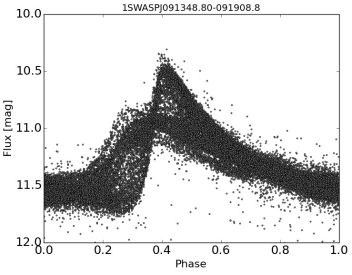

(c) 4.972

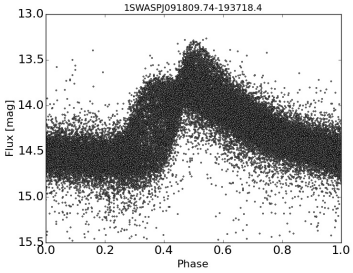

(d) 2.504

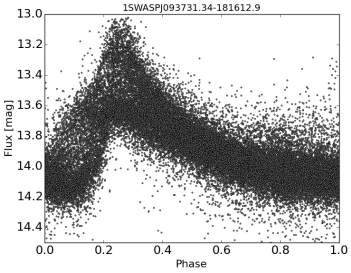

(e) 2.737

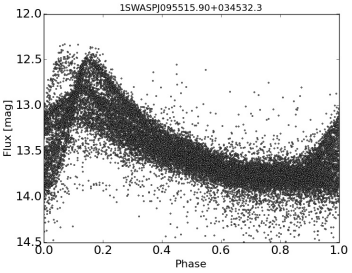

(f) 2.736

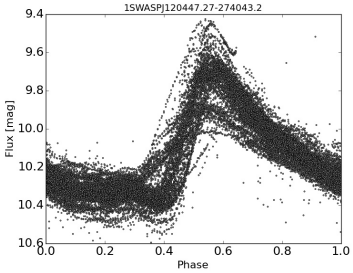

(g) 3.532

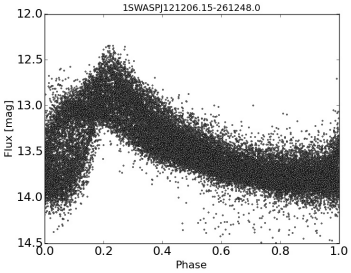

(h) 3.532

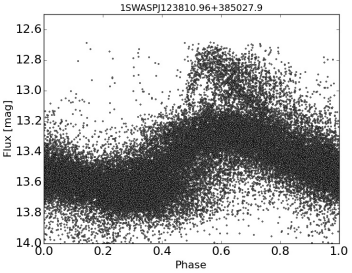

(i) 2.524

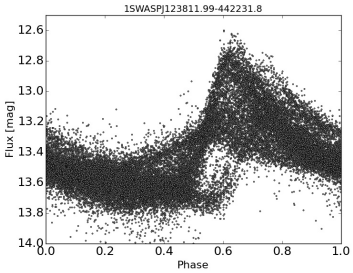

(j) 3.082

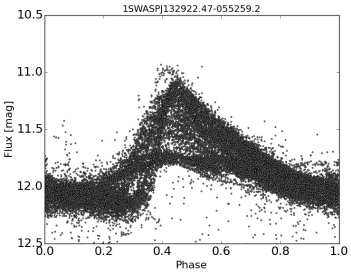

(k) 4.343

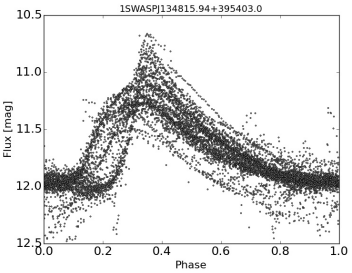

(l) 3.817

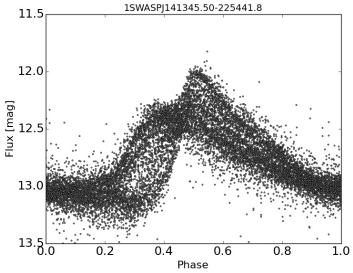

(m) 2.835

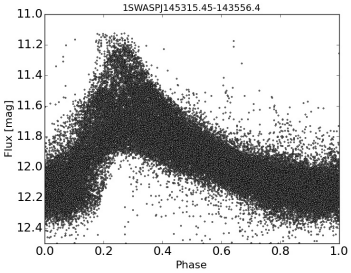

(n) 2.694

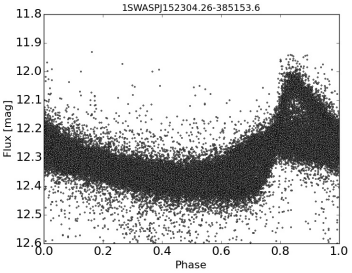

(o) 2.074

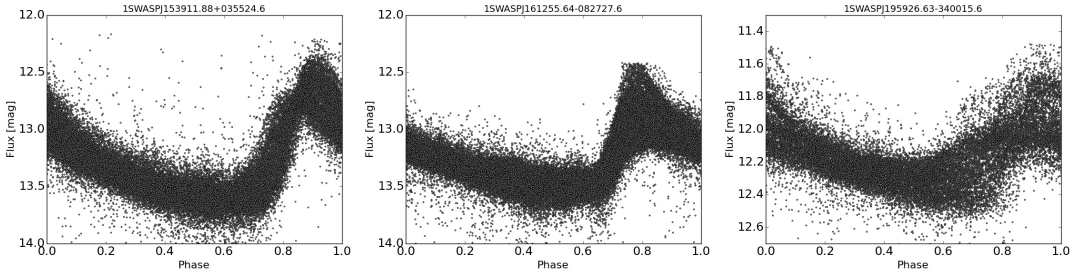

(p) 2.569 (q) 3.245 (r) 2.421

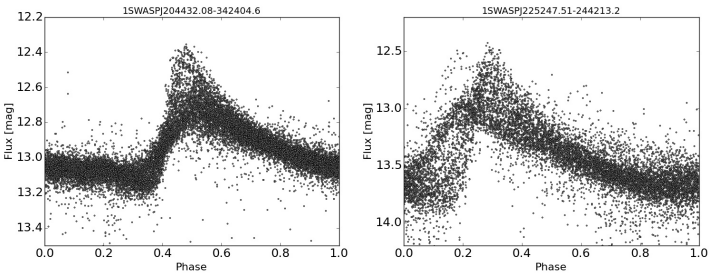

(s) 2.907 (t) 2.176

Figure 3.22: Phase folded light curves for the 20 high AM SuperWASP RRab objects. The relative scatter parameter value is given below each light curve.

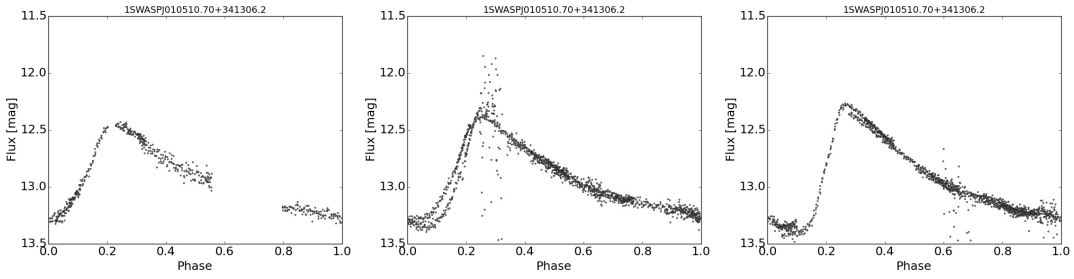

(a) 495 (b) 496 (c) 497

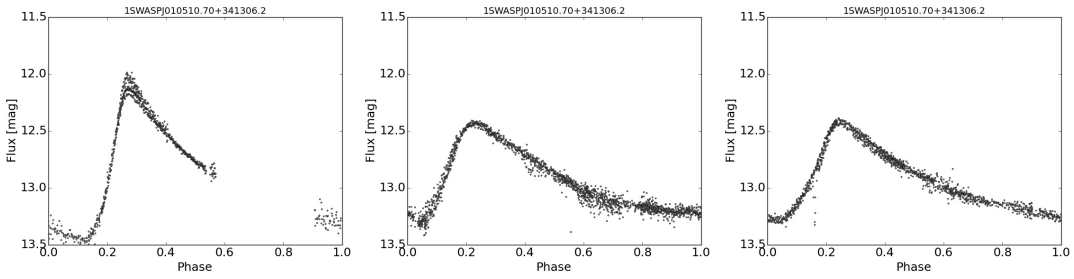

(d) 498 (e) 502 (f) 504

Figure 3.23: Weekly sections of the light curve of 1SWASPJ010510.70+341306.2 for the weeks 495 to 504 showing the change in pulsation amplitude and shape.

3.3.4 Calculating the Blazhko period in extreme AM cases

Since the Blazhko effect is periodic and its AM causes an envelope function to appear in the maxima and minima of the light curve over the cycle of the Blazhko effect, it should in theory be possible to calculate the Blazhko period for each object based on the PDM of this envelope function. A good candidate Blazhko period is one where the upper and lower parts of the AM envelope functions each form a smooth and continuous waveform, with a single cycle over the candidate Blazhko period. Initial testing of whether the envelope function can be used to find the Blazhko period is best done on cases where this envelope function is more pronounced, hence the use of the extreme AM cases from the previous subsection.

The PDM program used to calculate the pulsation period was updated in order to phase fold the upper envelope function of the AM, as defined by the change in the maxima of each pulsation, since the amplitude of the upper envelope is far greater than the lower envelope. The maxima were extracted by phase folding the light curve using the pulsation period and 50 bins as before, and selecting all observations within a range of 3 bins at the peak. This range is 1 bin higher in phase compared to the original pulsation period finding program, in order to only capture the second, higher peak in cases where 2 peaks are visible. These maxima were then phase folded using only 20 bins as the envelope functions are much more sinusoidal than the RRab pulsations. Unlike the full light curve, the maxima trace out a line when folded at the correct period, as shown in Fig. 3.24. The mean magnitude at each point in the cycle is therefore constantly varying, allowing the use of both the PDM and epoch folding techniques described in Sect. 3.2.2.

The improvement in finding the candidate Blazhko period using only the maxima to define the envelope function is demonstrated in Fig. 3.25, where the left panel shows the phase folded light curve when folded using a period found using the all the points in the light curve, and the right panel shows the same light curve folded using the period calculated using only the pulsation maxima.

Estimations of the Blazhko period were made based on the unfolded light curve for an entire year's worth of observations for each object, or the entire light curve if the Blazhko period looked longer than a year, which was then used as the initial trial period in the phase folding of the light curve maxima. If the initial trial period was greater than 50 d then the initial intervals were 0.05 d over a 50 d range centred on the initial trial period. The next

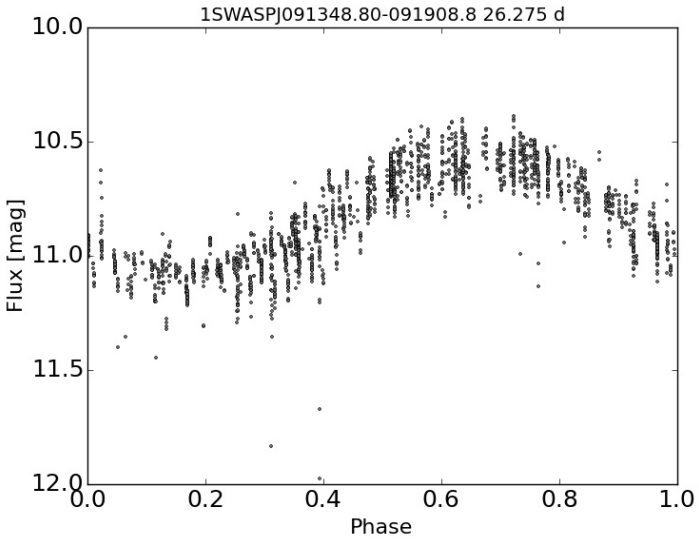

Figure 3.24: Sinusoidal waveform of the upper envelope function traced out by the maxima from object 1SWASPJ091348.80-091908.8, phase folded by a candidate Blazhko period of 26.275 d.

pass used 0.01 d over a 10 d range, and the final set of trial periods were 0.001 d over a range of 1 d. If the initial trial period was less than 50 d the initial 50 d range was not used.

If both AM and PM are present the pulsation peak not only increases and decreases, but also moves to an earlier phase and out of the peak phase range used by the PDM program. However, the program continues to record the change in the upper envelope function using the decrease in amplitude of the light curve in the same bins, even as the pulsation peak has shifted to earlier phase bins. In the second half of the Blazhko effect cycle the shifting of the pulsation peak is reversed. The PDM program thereby records the full Blazhko cycle, and calculates the correct Blazhko period after phase folding this continuous envelope function. This is demonstrated later by object 1SWASPJ004757.06+114223.5 in Figs. 3.26 and 3.27.

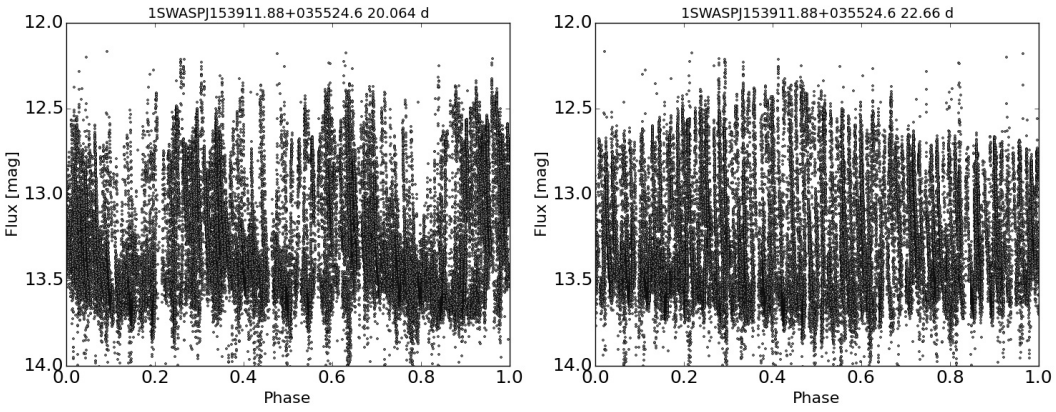

(a) (b)

Figure 3.25: Light curves for object 1SWASPJ152911.88+035524.6 phase folded by 2 candidate Blazhko periods. The panel on the left shows the ~20 d period found using the entire light curve, whereas the right panel shows the light curve folded by the ~23 d period found using only the pulsation maxima. The well defined envelope function can be seen on the right hand panel where the pulsation maxima and minima form smooth curves with a single cycle over the 23 d period.

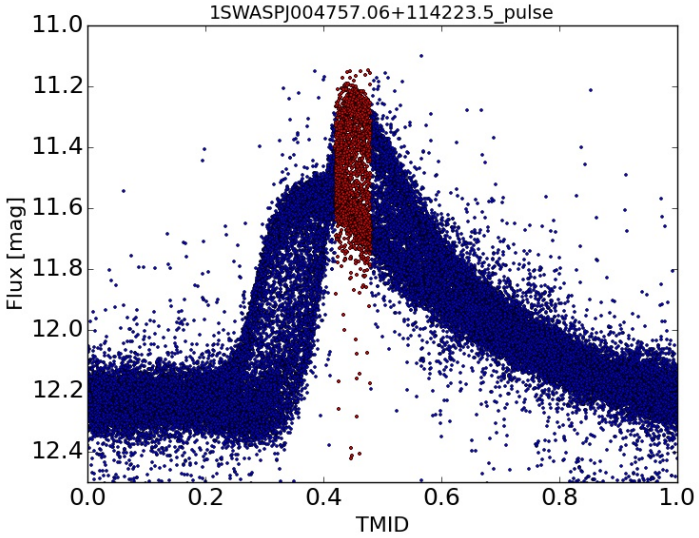

Figure 3.26: Light curve for 1SWASPJ004757.06+114223.5 phase folded by the pulsation period. The points defined as the maxima are shown in red. Notice the lower peak appearing earlier in the cycle than the higher peak, indicating some PM.

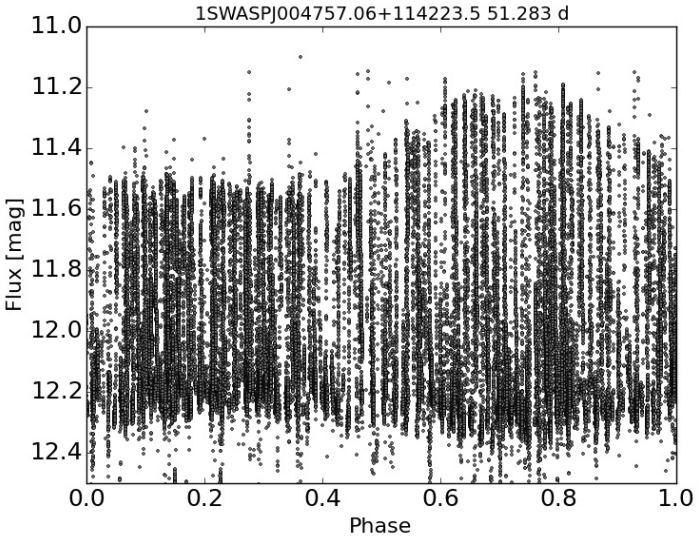

Figure 3.27: Light curve for 1SWASPJ004757.06+114223.5 phase folded by a candidate Blazhko period of 51.3 d showing an accurately folded envelope function.

Table 3.8: Candidate $P_{\rm BL}$ for extreme AM objects.

Object	SWASP id	P_{pulse} [d]	σ_r	Trial P_{BL} [d]	$P_{\rm BL}$ [d]
a)	1SWASPJ004757.06+114223.5	0.45568	2.827	50	51.3
b)	1SWASPJ010510.70+341306.2	0.56311	3.847	50	49.9
c)	1SWASPJ091348.80-091908.8	0.53722	4.972	30	26.3
d)	1SWASPJ091809.74-193718.4	0.49108	2.504	60	49.4
e)	1SWASPJ093731.34-181612.9	0.52092	2.737	100	88.2
g)	1SWASPJ120447.27-274043.2	0.65030	3.095	140	75.7
h)	1SWASPJ121206.15-261248.0	0.39877	3.532	120	48.4
i)	1SWASPJ123810.96+385027.9	0.34737	2.524	115	115.1
j)	1SWASPJ123811.99-442231.8	0.52353	3.082	150	122.7
k)	1SWASPJ132922.47-055259.2	0.57640	4.343	700	676.2
l)	1SWASPJ134815.94+395403.0	0.47852	3.817	120	74.0
m)	1SWASPJ141345.50-225441.8	0.44796	2.835	50	26.5
o)	1SWASPJ152304.26-385153.6	0.57797	2.074	90	99.5
p)	1SWASPJ153911.88+035524.6	0.46347	2.569	20	22.7
q)	1SWASPJ161255.64-082727.6	0.54875	3.245	40	39.2
r)	1SWASPJ195926.63-340015.6	0.37967	2.421	40	44.6
s)	1SWASPJ204432.08-342404.6	0.56797	1.124	60	53.7
t)	1SWASPJ225247.51-244213.2	0.52955	2.176	200	180.8

Based on the quality of the envelope functions in the Blazhko period phase folded light curves shown above, the program to find Blazhko candidate periods using PDM and epoch folding of the upper envelope function, taken from the pulsation maxima, has succeeded in all but 2 out of 20 cases (90%). The first doubtful Blazhko period, f) 1SWASPJ095515.90 +034532.3, has a sharp drop in the envelope function suggesting a discontinuity. In the second case, n) 1SWASPJ145315.45-143556.4, the candidate Blazhko period showed 2 peaks in the envelope function, despite repeated attempts to find a Blazhko period by folding at around half this period. The candidate Blazhko periods for the remaining 18 objects are summarised in Table 3.8.

3.4 Discussion

This chapter has examined at the SuperWASP RR Lyrae objects in the time domain, in order to produce a new catalogue of RRab objects, before attempting to identify and quantify the Blazhko effect. This investigation has led to a relative scatter parameter based on the amount of scatter at the peak of the light curve folded by the pulsation period, and to a method of calculating the Blazhko period using the upper envelope function in the case of stars with extreme AM.

The classification of the SuperWASP objects as RRab took several stages but there remains the chance that a high amplitude or slow pulsating RRc type object, or a faint AHB1 (for 'above horizontal branch', also known as XX Vir) type object has been misclassified as RRab. A more in–depth Fourier analysis of the relative strengths and phases of the pulsation harmonics would be required to more robustly define objects as RRab.

The examples shown in Sect. 3.3.3 demonstrate how the AM caused by the Blazhko effect can be asymmetric, with the change in maxima different in magnitude from the change in minima, leading to a change in average brightness over the course of the Blazhko period. If there were systematic or instrumental effects the vertical offset would not change the amplitude of the pulsation. The examples have been selected to highlight AM so their light curves exhibit a minimal change in phase which causes a horizontal shift in the light curve. However, both effects are commonly seen together in the Blazhko effect where the horizontal shifting widens the light curve.

The single modal relative scatter distribution could be caused by several factors. There could be instrumental differences in the brightness of observations replicating small levels of AM for non-Blazhko objects over seasonal timescales when the light curves are phase folded (false positives). Large amplitude pulsators could have measurably lower scatter at the bright peak compared to the fainter minimum of the light curve, reducing the relative scatter parameter for large amplitude Blazhko objects (false negatives). The Blazhko effect itself may have a continuum of AM starting from barely observable levels.

The validity of using PDM to calculate the Blazhko period was tested using the previously identified cases of strong amplitude modulation. Restricting the phase folding algorithm to only the pulsation maxima produces better results as both PDM and epoch folding techniques can be utilised. Only 2 out of 20 extreme amplitude modulation light curves

failed to exhibit a well defined envelope function, and thereby fail to provide a robust candidate Blazhko period. The Blazhko folded light curves for the following four objects each show a section where the envelope function appears flat: 1SWASPJ004757.06+114223.5 (a), 1SWASPJ091348.80-091908.8 (c), 1SWASPJ091809.74-193718.4 (d), and 1SWASPJ 204432.08-342404.6 (s). The light curves of these objects all show some phase modulation when phase folded by the pulsation period, as shown in Fig. B.1, where the lower amplitude phase of the Blazhko cycle appears at a slightly earlier phase than the large amplitude phase. It is unlikely that either the AM or PM only acts during part of the Blazhko cycle. Instead, it is hereby proposed that the envelope functions in these cases are still increasing or decreasing in these phases of the cycle, but that the change is being cancelled out by a change in pulsation phase due to PM, during which a different part of the light curve is captured in the so–called peak bins. It is also possible that some small change in the envelope is being hidden by the noise of the light curve.

Therefore, suitable candidate Blazhko periods can be discovered via well defined envelope functions providing the following conditions are met: the initial trial period range is close enough to the true period that integer multiples or fractions of it are not covered by the PDM algorithm; the object exhibits strong AM; the object also has very little PM as the pulsation peak should be clearly defined in order to select the pulsation maxima for phase folding. The first of these conditions can be mitigated by inspecting the resultant light curve and checking for multiple envelope function peaks. As with the initial program to find the pulsation period, a benefit of this method is that it can be used on large datasets of RRab objects, or even other types of pulsating variable objects, as long as the above prerequisites are met. Although the initial trial period range requires some visual checking of light curves, initial results can be easily checked and trial periods improved.

It appears that the relative scatter parameter is a good indicator of the relative level of scatter at the peak, because objects with high levels of scatter at the peak are accurately represented by a high relative scatter parameter, as shown in two sets of examples given in previous sections. However, some caution may be required as the correlation with pulsation amplitude may be due to the increase in the gradient of the light curve at the peak with larger pulsation amplitude, which then mistaken to be an increase in scatter.

The relative scatter initially appeared to be a good Blazhko effect indicator for two rea-

sons. Firstly, the known Blazhko effect stars, where the excessive scatter at the pulsation peak was first noticed, all have reasonably high values of relative scatter. Secondly, the high values of the relative scatter parameter for the extreme amplitude modulated stars, which all clearly exhibit large levels of amplitude modulation with little phase (frequency) modulation, also all correspond with the long tail in the distribution at high relative scatter values. However, the unimodal distribution of this parameter suggests that the Blazhko and non–Blazhko populations overlap in terms of levels of scatter at the peaks of their pulsations. This is confirmed by both the set of known Blazhko and the set of known non–Blazhko effect stars. In the set of known non–Blazhko stars, the two highest relative scatter values in this group are 2.585 and 2.945, which would place V894 Cyg and FN Lyr, respectively, within the group of known Blazhko effect stars. This could be caused by other factors, such as the faintness of the objects and the subsequent low ratio of signal to noise in the phase folded light curve. However, the values of the relative scatter parameter for the set of known Blazhko effect objects shows that the relative scatter value for these objects can be as low as for known non–Blazhko effect objects. This could be due to phase modulation which increase levels of scatter in both the peak and quiet areas of the phase folded light curves, nullifying the relative scatter parameter. It is this lack of a clear lower threshold value, above which we can be confident that the RRab object is indeed a Blazhko effect object, that means that the relative scatter parameter is not a robust indicator of the Blazhko effect.

This analysis has purely been on RRab class objects. The use of this technique to identify modulation in other pulsating objects relies on those objects having a clearly defined single peak area, a second area unaffected by AM to compare it to, and a lack of PM. For example, RRc class RR Lyrae do not have a clearly defined peak area, making the use of this technique questionable for this particular type of object. They would also need to be only susceptible to low levels of frequency modulation compared to amplitude modulation, just as in the case of RRab shown above. Observations would require long timescales in the case of long period variables in order to produce the quality of light curves that provide low enough levels of scatter for a good comparison of modulated to non–modulated sections.

The quality of the relative scatter parameter hinges on the level of scatter in the light curve of each object. With better quality light curves such as those from Kepler and the K2 campaigns the overall level of scatter in the light curves is reduced, allowing the opportunity

for better distinction between the amount of scatter at the pulsation peak and elsewhere in the light curve. Future surveys, such as TESS and the LSST should provide high quality light curves with which to investigate the Blazhko effect in the time domain.

3.5 Conclusions

This chapter has demonstrated how the distinctive light curve of the RRab type pulsating variable object can be used to create a catalogue of these objects using the high–cadence photometry of SuperWASP. The first symptoms of the Blazhko effect, amplitude modulation, have been identified through its effect on phase–folded light curves.

After the relative scatter parameter proved to be unreliable at identifying Blazhko effect objects in the time domain, we now turn to the frequency domain, where the majority of Blazhko effect investigations are performed. Unlike time domain analysis, both amplitude and frequency modulation aspects of the Blazhko effect can be detected in the frequency domain, using Fourier analysis.

Chapter 4

SuperWASP RR Lyrae stars in the frequency domain[1]

4.1 Introduction

Having investigated the Blazhko effect in the time domain using phase folded light curves, attention is now turned to the frequency domain where the Fourier transforms of modulated pulsations are reproduced in power spectra. This chapter continues with a description of the power spectra of SuperWASP RRab objects and the processes required to identify the Blazhko effect within these spectra (Sect. 4.2). This is followed by an analysis of the characteristic parameters of the RRab objects in Sect. 4.3. The final section 4.5 is a discussion of the analysis of the properties of SuperWASP Blazhko effect objects.

The catalogue of Blazhko effect objects from this chapter, along with the SuperWASP RRab catalogue in the previous chapter have been published in Greer et al. (2017).

4.2 The SuperWASP Blazhko catalogue

The aim of this section is to identify and quantify both the AM and FM aspects of the Blazhko effect in SuperWASP RRab–type RR Lyrae objects, and thereby produce a catalogue of SuperWASP Blazhko effect objects. If current estimations of the proportion of Blazhko to non–Blazhko objects is correct, then the large number of objects in the SuperWASP RRab

[1]The work in this chapter made use of the International Variable Star Index (VSX) database, operated at AAVSO, Cambridge, Massachusetts, USA.

catalogue should offer a statistically significant analysis of their visible photometric characteristics.

4.2.1 SuperWASP observations in the frequency domain

Low frequency peaks at the Blazhko frequency itself are not often detected in conventional observations of RR Lyrae type stars, owing to the limited baselines usually available. The unique feature of SuperWASP data are their long baselines and high cadence, meaning that there is a chance to detect Blazhko modulations directly in the power spectrum. Sidebands, which are pairs of peaks close to either side of the main pulsation peak, can be created by both frequency (FM) and amplitude (AM) modulation, as described in 1.5.4, which explained how the difference between the main pulsation peak and each sideband provides the modulation frequency. Modulation has been observed forming triplets and quintuplets of peaks in high–resolution Blazhko effect studies (Benkő et al., 2011). However, some care is still needed as sidebands can also be caused by systematic periodic variation in flux due to diurnal and synodic cycles in the case of ground–based observations. The combination of AM, FM and irregular sampling causes asymmetry in sideband amplitude, sometimes to the extent that one component may be missing entirely, as shown in the top panel of fig. 4.1, which was created using a synthetic sinusoidal signal with a pulsation period of 0.456 d and modulation period of 50.1 d. The separation between sidebands and the central peak is 2.31×10^{-7}, equivalent to 50.1 d, with the pulsation peak in the centre at 2.9×10^{-5} Hz. Note the difference in the power of the peaks on opposite sides of the central peak: one of the peaks on the left is missing entirely; and the sidebands on the right of the central peak are stronger than those on the left.

The irregular sampling regime of ground–based observations has created a complex window function, as described in Sect. 1.5.4. The effect of this on a simple sinusoidal wave is shown by the pre–CLEANed (or 'dirty' spectrum) shown in green in the bottom panel of Fig. 4.1, where the Fourier transform of the modulated sinusoidal wave has been convolved with the Fourier transform of the window function, spreading the power of the signal across a range of frequencies, as shown in Fig. 1.12. The signal used in Fig. 4.1 was created using the the actual timings from SuperWASP object 1SWASPJ120447.27-274043.2. Realistic levels of uncertainty were created by also taking the uncertainties for each point from

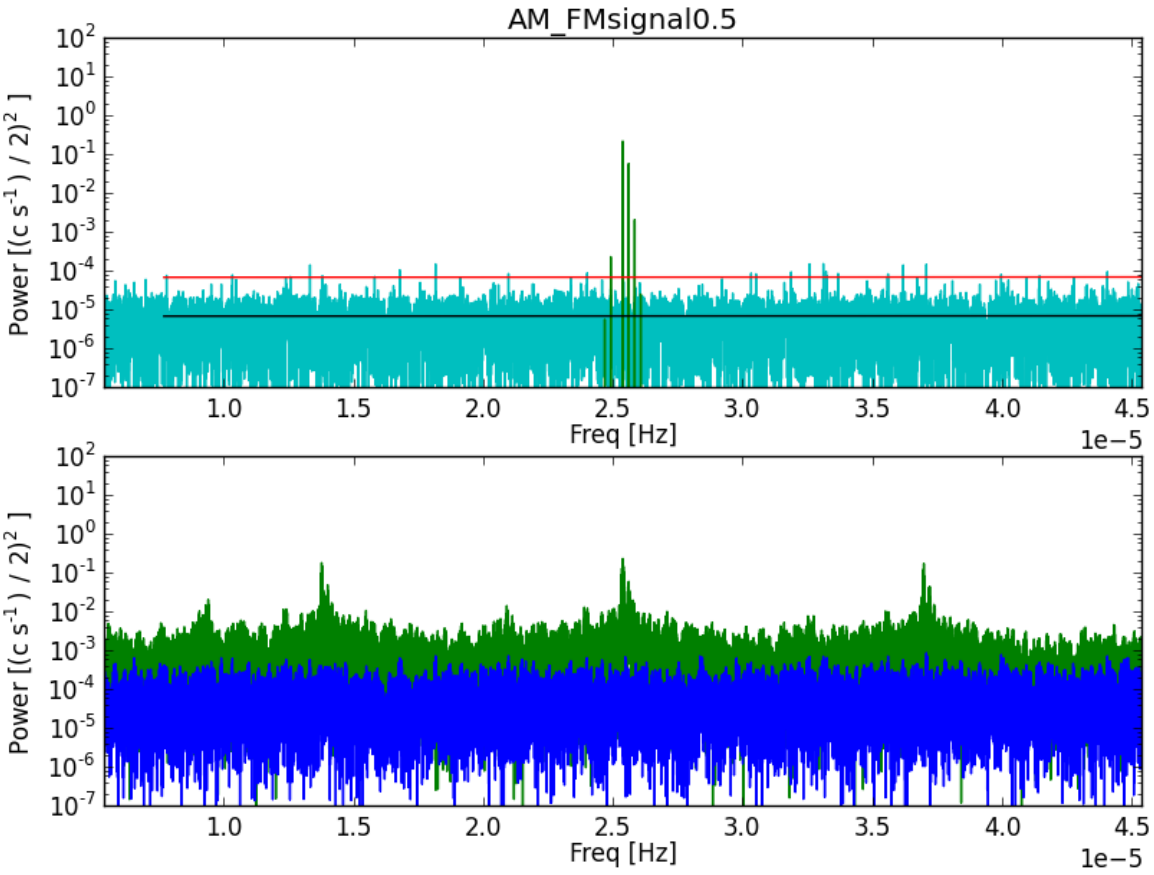

Figure 4.1: Section of a CLEANed power spectrum from 0.34 d to 0.48 d of an artificial signal with a pulsation period of 0.456 d. The series of sidebands on either side of the main pulsation peak are set 2.3×10^{-7} Hz apart, equating to the modulation period of 50.1 d. The title of the plot refers to how the modulating signal is a combination of both AM and FM, with a strength 0.5 × the signal strength. The colours of the various spectra are explained later in the main text. The sampling regime used is from object 1SWASPJ120447.27-274043.2.

1SWASPJ120447.27-274043.2. The sampling regime has created aliases of the 0.456 d period in the dirty spectrum at approximately 0.3 d and 0.8 d.

The CLEAN algorithm (Roberts et al., 1987; Högbom, 1974) deconvolves the signal from the complex window function, and is particularly well suited to light curves containing multiply periodic signals. The effect of the CLEAN program can be seen in the green spectra in the top panel of Fig. 4.1, where the window function has been removed, including the two aliases at 0.3 d and 0.8 d, and the modulated 0.456 d signal has been recovered with the modulation sidebands. The dark blue spectrum in the bottom panel, and light blue spectrum in the top panel of Fig. 4.1 are both representations of a non–variable version of that particular SuperWASP RRab stars, before and after CLEANing, respectively. The procedure and reasons for creating this will be explained in subsection 4.2.3. The red and black lines are part of the

peak identification stage which will be covered in subsection 4.2.4.

In order to counteract the spectral effects due to ground–based observations, an investigation of the power spectra of the SuperWASP RRab objects was carried out using the CLEAN algorithm as described in the following section.

4.2.2 The CLEAN algorithm

The CLEAN algorithm first calculates the window function of the light curve based on the sampling regime. It then convolves this window function with a delta function corresponding to a certain percentage (defined by the gain) of the highest peak in the power spectrum. The result of this convolution is the contribution to the raw uncleaned spectrum caused by that part of the actual signal being convolved with the complex window function, as demonstrated in Fig. 1.12. This convolved function is then subtracted from the actual power spectrum, known as pre–whitening. This process is then repeated until a pre–defined maximum number of iterations has been reached or there is no further change to the power spectrum. The accumulated delta functions which are used are then recombined with the residual power spectrum from the last iteration to produce the cleaned spectrum. In this way the pre–whitening of the spectrum is performed gradually on all peaks in the power spectrum while removing the majority of the effects of the window function: the aliased peaks caused by the convolution of the actual signal with the window function have been systematically removed. Peaks maintain virtually all of their power while the rest of the spectrum is reduced to the underlying noise level. The version of CLEAN implemented in this work utilises a variable gain factor, where the program adjusts the gain depending on the relative strength of the maximum peak in relation to other peaks in the multiperiodic signal (Lehto, 1997).

There were 4 parameters in CLEAN that were set to remain constant across all SuperWASP RRab objects, as well as enabling the option to include the flux uncertainties. The first was the maximum number of data in the input file, which had to be increased to 50×1024 (51200) due to the long duration of SuperWASP observations. The second parameter was the maximum frequency, which was set to 1×10^{-3} Hz in order to identify enough pulsation harmonics to allow accurate removal of the window function. During early testing, the maximum frequency was set to 10^{-4} Hz, but an excess amount of power remained at throughout the entire spectrum, as the spectral power of the higher harmonics was not identified and

allocated to their correct frequencies. The third parameter was the number of points in the power spectrum. This was increased to $3 \times 1024 \times 1024$ (3,145,728) when the maximum frequency was increased to 10^{-3} Hz, to allow the maximum resolution of the power spectra to be calculated based on the duration of observations, rather than a previous arbitrary upper limit set in the program.

The final parameters were the number of iterations and the gain factor described above. The effect of changing the number of iterations is demonstrated in Fig. 4.2 where the clean algorithm uses 10, 100, 1000 then 10,000 iterations in parts (a) to (d) respectively. Figure 4.2 uses a logarithmic scale from 1×10^{-8} Hz (1157 d) to 1×10^{-4} Hz (0.1157 d) to focus on the low frequency regime where Blazhko frequencies are commonly found. When the CLEAN program completely removes the effects of the window function using between 100 and 1000 iterations no residual spectrum remains, since there is no noise associated with this artificial light curve, which is not the case in real light curves. After testing on known Blazhko effect stars, a maximum number of 10000 iterations was set as a parameter in the CLEAN program to work in conjunction with the smallest recommended gain factor of 0.1 as this allowed the optimum removal of the window function at in the low frequency region of the spectra, while minimising the risk of the program removing legitimate peaks.

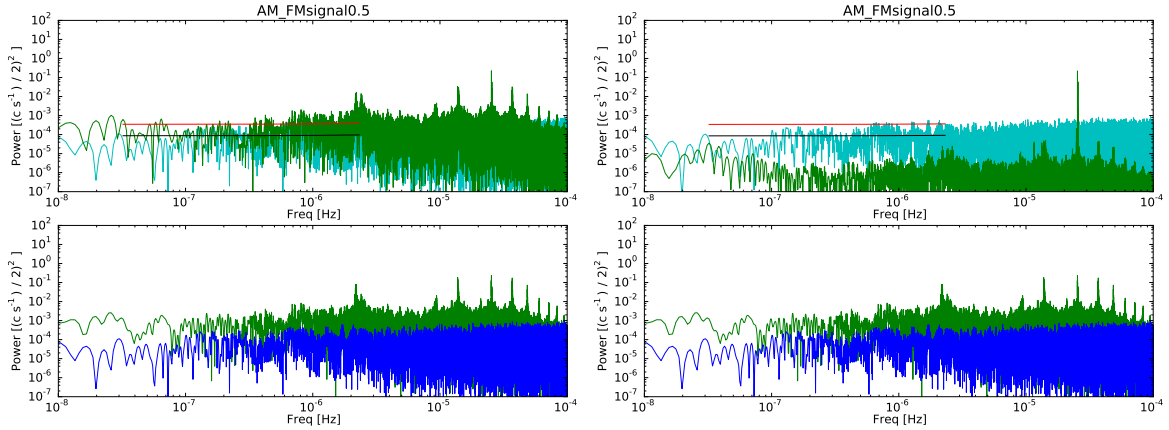

(a) 10 iterations

(b) 100 iterations

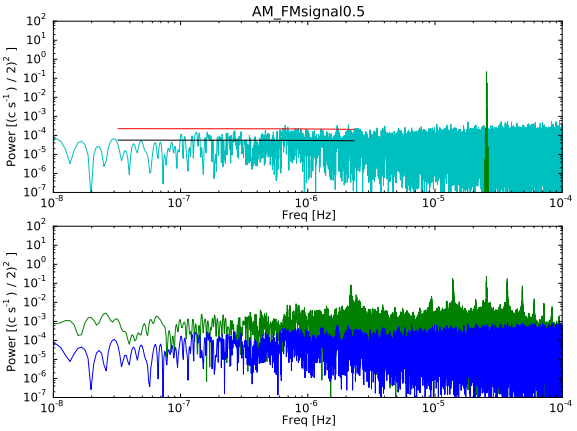

(c) 1,000 iterations

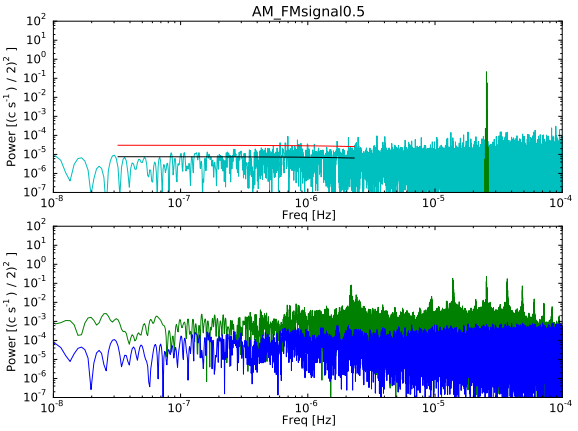

(d) 10,000 iterations

Figure 4.2: Power spectra of the synthetic light curve with a modulation period of 50.1 d. The number of iterations used in the CLEAN program is given under each panel.

4.2.3 The randomised light curve

In order to identify the specific noise level in the power spectrum for each object after CLEANing, a spectral representation of a non–varying version of that object was obtained using the object's flux, average brightness and spectral window. Removal of the variability was achieved by creating a copy of each object's light curve with the actual fluxes randomly reassigned to the times of observation. These randomised light curves were also CLEANed with the same parameters as the actual observations in order to duplicate the removal of the average brightness and number of CLEAN iterations that the actual signal underwent. Figure 4.2d shows how the power of the pale blue coloured randomised spectrum is also reduced by using 10000 CLEANing iterations, compared to 1000 iterations (Fig. 4.2c). Since there is no signal to convolve with the window function and then be CLEANed out, the power spectrum of the randomised light curve (labelled CLEANed RDM in subsequent figures) is therefore a good indicator of the noise level in the power spectrum of a non–varying object, against which to measure the signal in all regions of the actual CLEANed power spectrum.

4.2.4 Identifying candidate Blazhko spectral peaks

To identify a candidate Blazhko period from a CLEANed power spectrum, we required at least one of the following matching criteria to be satisfied. Either there was a significant low frequency peak in the power spectrum whose frequency matched the modulation frequency determined from a significant (positive or negative) sideband, and/or there was a symmetrical pair of significant positive and negative sideband peaks. Identification of candidate Blazhko periods therefore focused on two frequency ranges and required us to define a noise level in the power spectrum for each region. For low frequency peaks in the region of the Blazhko effect signal itself, the noise level was calculated between 3.17×10^{-8} Hz and $2.3{\times}10^{-6}$ Hz (corresponding to periods between 1 year and 5 days). The limit of 1 year was made to ensure that observations covered several cycles during most SuperWASP observations and to reduce the likelihood of an annual systematic signal being mistaken for a Blazhko period. The lower limit was selected after checking the minimum Blazhko period in the Skarka (2013) list of known Blazhko objects. The noise level in the vicinity of the sidebands was calculated between $7.7{\times}10^{-6}$ Hz and 10^{-4} Hz, equating to periods between 1.5 d and 0.1 d. In both

the low frequency and sideband frequency range, an initial first order polynomial was fitted to the power spectrum of the randomised data to define an initial noise baseline. Any peaks in the power spectrum of the randomised data found above 4 times this first baseline were removed, and the remaining power spectrum of the randomised data was then fitted again with a first order polynomial to determine a final noise level. Thresholds for acceptance of a peak in the power spectrum of the actual data were set at 4 times this noise level for low frequency peaks and at 10 times this noise level for sidebands. The higher sideband limit was set in order to avoid the higher level of noise and spurious peaks surrounding the base of the main frequency without excluding any genuine sidebands. As described above, rather than finding many harmonic orders of side peaks around the main pulsation frequency, the aim was to detect a strong sideband to link with a low frequency peak, or a pair of symmetrical sidebands. Only those peaks in the power spectrum of the actual data which exceeded these multiples of the noise level were considered genuine. Peaks which did exceed these levels were then each fitted with a Gaussian curve in order to yield a measurement of the peaks' maximum power, central frequency and the uncertainty in frequency, based on the Gaussian width.

As already noted, candidate Blazhko periods were defined for those objects whose sideband peak's separation from the fundamental mode peak matched a low frequency peak, and/or where symmetrical pairs of modulation sidebands existed on either side of the fundamental mode. In both cases a match was defined to exist where the 1σ limits of each measured frequency overlapped with each other. In other words, at least two peaks at the same modulation frequency within a 1σ uncertainty were required for identification of Blazhko candidates.

Following their identification from the CLEANed power spectra, all candidate Blazhko frequencies were then refined by fitting each individual Blazhko frequency to their respective object's light curve using the Period04 program (Lenz and Breger, 2005). The resulting Blazhko periods and amplitudes, along with the analytical uncertainties from Period04, are given in Appendix B, with a subset shown in Table 4.1.

4.2.5 CLEAN results

As shown in Figs. 4.3 and 4.4, the CLEAN algorithm proved to be excellent at deconvolving the window function from the actual signal allowing low frequency periodic signals to appear above the baseline noise level defined by the fit to the randomised noise signal. This was particularly useful when distinguishing Blazhko candidate peaks in the low frequency range described above. The 'dirty' power spectrum of the light curve and corresponding randomised spectra are shown in the bottom panel of Figs. 4.3 and 4.4 for comparison.

Close–ups of the low frequency peaks and areas of the spectra around the main pulsation frequency containing the modulation sidebands are shown in Figs. 4.5 and 4.6 for object 1SWASPJ000548.23+424321.9 and Figs. 4.7 and 4.8 for object 1SWASPJ001321.94-425511.2. The matching sidebands and low frequency peaks are highlighted by the blue dotted line for clarity. In the case of object 1SWASPJ001321.94-425511.2, one Blazhko period was discovered based on a pair of equidistant sidebands, marked with dashed lines, and the second Blazhko period was discovered by a matching low frequency peak and sideband, highlighted with dotted lines again.

The final fitting stage using Period04 resulted in some candidate Blazhko periods being longer than the original limit of 365 d. A good example of this is object 1SWASPJ124945.38+434625.2 (Z CVn) which is listed with a candidate Blazhko period of 370.6±0.5 d. Figure 4.9 shows that the low frequency peak centred at 304±44 d is only just over the threshold limit, and at this resolution is merged with adjacent peaks. In the case of a low frequency–to–sideband match, the sideband's more accurate frequency of 356±12 d, shown in Fig. 4.10, is recorded and fitted to the entire light curve in Period04. Period04 then finds the larger peak at 3.18×10^{-8} Hz, shown below the minimum frequency of the signal to noise threshold in Fig. 4.9.

The following two examples demonstrate the low–to–sideband, and symmetrical–sideband matching processes, and therefore the frequencies refer to candidate Blazhko periods before they were processed by Period04 to give the final candidate Blazhko periods referred to in the SuperWASP Blazhko catalogue. The low frequency and pulsation frequency regions of the spectrum for 1SWASPJ145137.56+292126.6 (XX Boo) are shown in detail in Figs. 4.11 and 4.12. The peak at the Blazhko frequency of 3.34×10^{-8} Hz (P_{BL} = 346.3 d) Fig. 4.11 is matched with the low sidepeak in Fig. 4.12. A matching pair of sidepeaks are

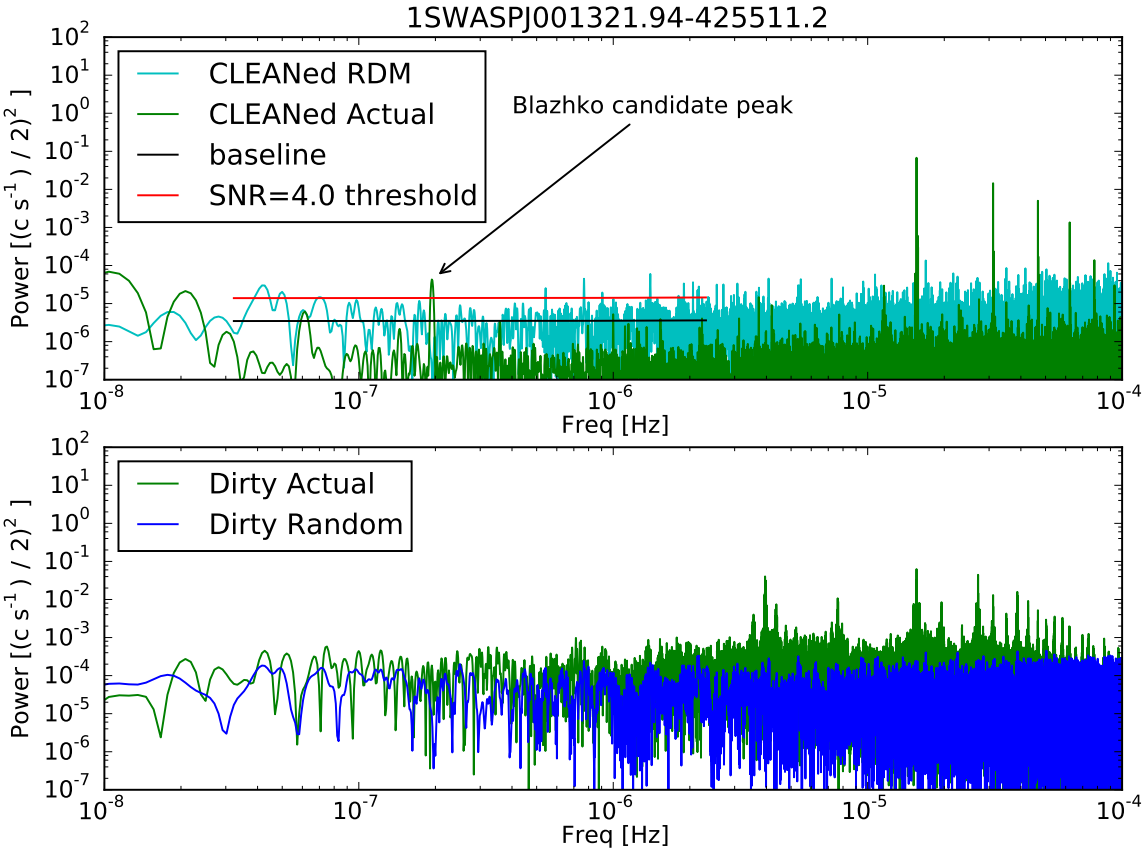

Figure 4.3: CLEANed power spectrum of object 1SWASPJ001321.94-425511.2 from 10^{-8} Hz to 10^{-4} Hz. The top panel shows the power spectra of the original and randomised light curves after deconvolution with the CLEAN algorithm whilst the bottom panel shows the raw (or 'dirty') power spectra of the actual and randomised data. Peaks due to the actual signal can be seen more clearly once noise due to the convolution of the signal with the window function has been reduced. The red line in the top panel is the noise threshold calculated for frequencies below 2.3×10^{-6} Hz (equating to Blazhko periods of at least 5 days).

denoted with the red dashed lines in Fig. 4.12 giving a second candidate Blazhko frequency of 1.09×10^{-7} Hz (P_{BL} = 106.1 d).

The low frequency and pulsation frequency regions of the spectrum for 1SWASPJ205854.79-385628.8 (XZ Mic) are shown in detail in Figs. 4.13 and 4.14. The peak at the Blazhko frequency of 1.12×10^{-7} Hz (P_{BL} = 103.5 d) in Fig. 4.13 is matched with the low sidepeak in Fig. 4.14. A matching pair of sidepeaks are denoted with the red dashed lines in Fig. 4.14 giving a second candidate Blazhko frequency of 1.35×10^{-7} Hz (P_{BL} = 85.9 d).

As a result of the analysis described above, a disproportionate number of Blazhko candidate periods were detected below 10 d. This appears to be due to a dominance of systematic aliases at around 5 d and 7 d, most likely due to the sampling regime. Since only 4% of Blazhko periods are below 10 d in the online Skarka database, the decision was taken to exclude Blazhko candidates below 10 d in our Blazhko catalogue. Furthermore, 356 objects

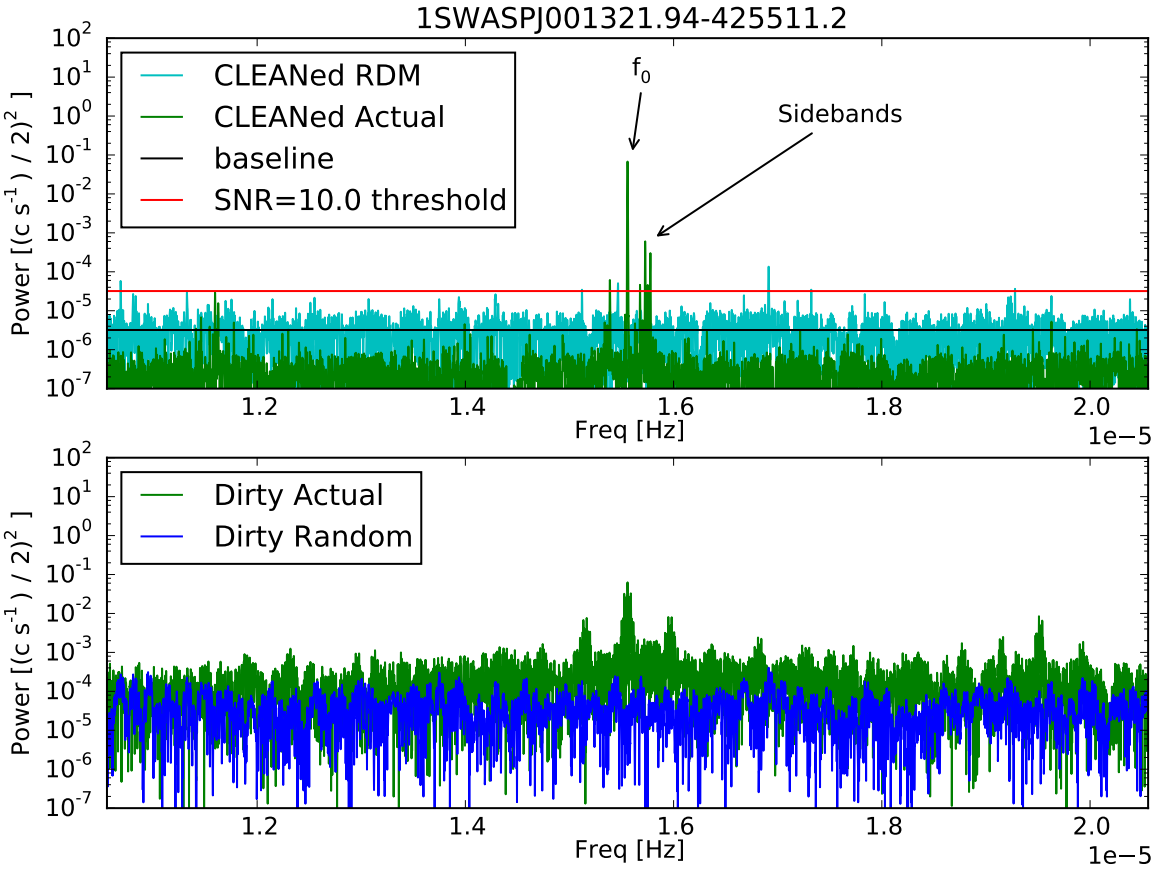

Figure 4.4: CLEANed power spectrum of object 1SWASPJ001321.94-425511.2 focusing on the range 5×10^{-6} Hz on either side of the main pulsation peak at 1.56×10^{-6} Hz (1.344 c d^{-1}). The panels are arranged as in Fig. 4.3. The main pulsation peak, f_0, and some of the modulation sidebands on the right side of the main pulse frequency have been labelled.

had an excessive number of candidate low frequency peaks and they too were excluded from further consideration.

Following these cuts, a total of 983 candidate Blazhko effect stars were identified from the SuperWASP sample of RR Lyrae. This is 19.8% of the 4963 RRab objects in the SuperWASP RRab catalogue. Of these candidate Blazhko objects, 89 were previously known Blazhko effect stars listed by Skarka. This leaves 894 Blazhko stars newly discovered in the SuperWASP archive. The 983 Blazhko candidates had a total of 1386 Blazhko periods, with 272 objects having more than one potential Blazhko period. Multiplets, such as triplets or quintuplets, of sidepeaks can produce sets of modulation frequencies at integer multiples of the actual modulation frequency. Each candidate Blazhko object with multiple Blazhko periods was checked to see if any periods were small integer multiples of each other, and then if any remaining periods were duplicates (due to multiple clean periods for the same object converging to the same period in Period04). 31 harmonic periods were found, including ob-

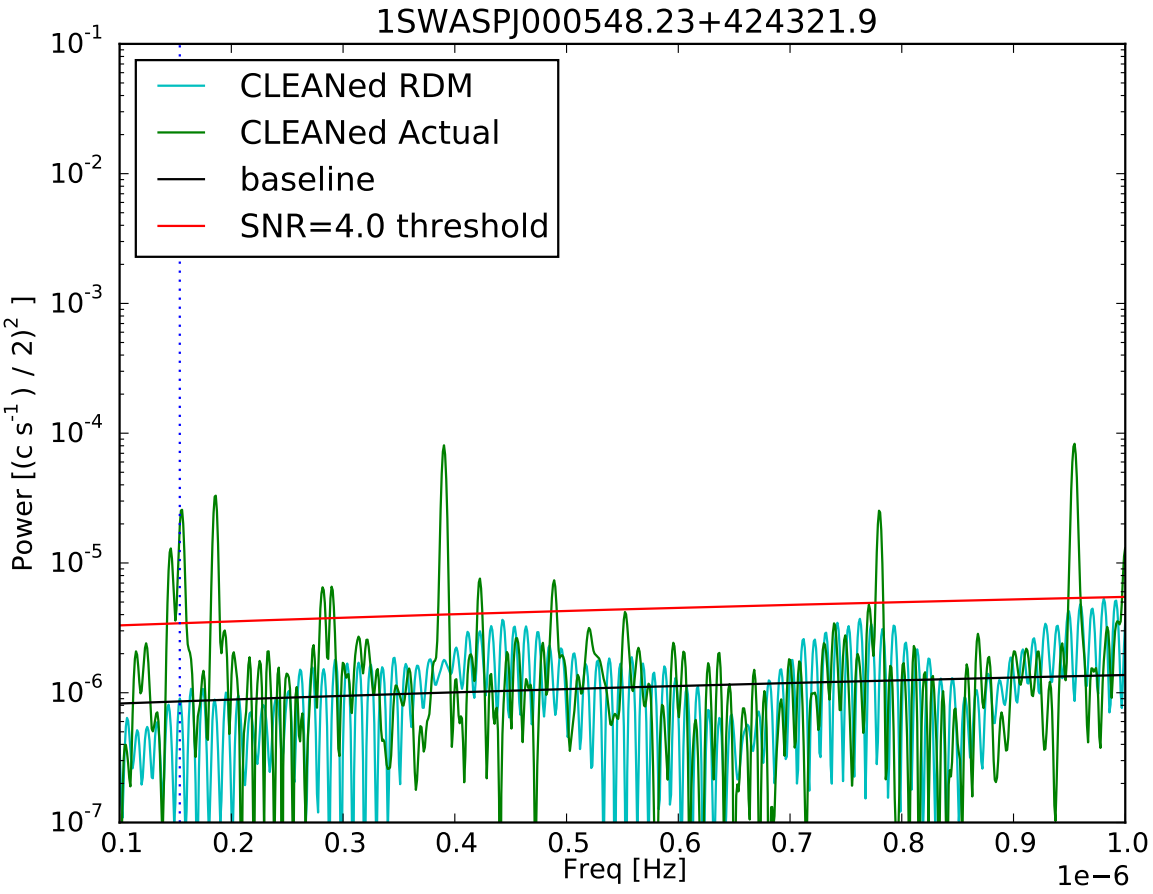

Figure 4.5: Low frequency section of the CLEANed power spectra showing in greater clarity the low frequency peak for object 1SWASPJ000548.23+424321.9, highlighted by the vertical dotted line. The baseline created using this randomised signal is in black, with the signal to noise threshold at 4 times this shown in red.

ject 1SWASPJ132305.17-205939.0 which had periods in the ratio of 2 : 3 : 6.These small integer multiples were removed, along with any duplicate periods resulting a total number of independent Blazhko periods of 1324 for the same 983 objects. Our results still show 261 objects with more than 1 independent Blazhko period. 1552 of the SuperWASP RRab catalogue objects match objects of the same type in the GCVS catalogue, amongst which are 361 of our Blazhko candidates. These figures are represented in Fig. 4.15.

Existing studies have focused on identifying the Blazhko effect using modulation sidebands only, whereas we also allowed Blazhko candidates identified from the presence of a low frequency peak. However, it should be emphasized that a match was required between either a low frequency peak and a sideband, or a pair of sidebands, before an object was accepted as a candidate. So two matching signals in the power spectrum were required for each candidate object. There are 99 known Blazhko effect stars that are in the list of SuperWASP RRab objects which were not identified as Blazhko using the processes described

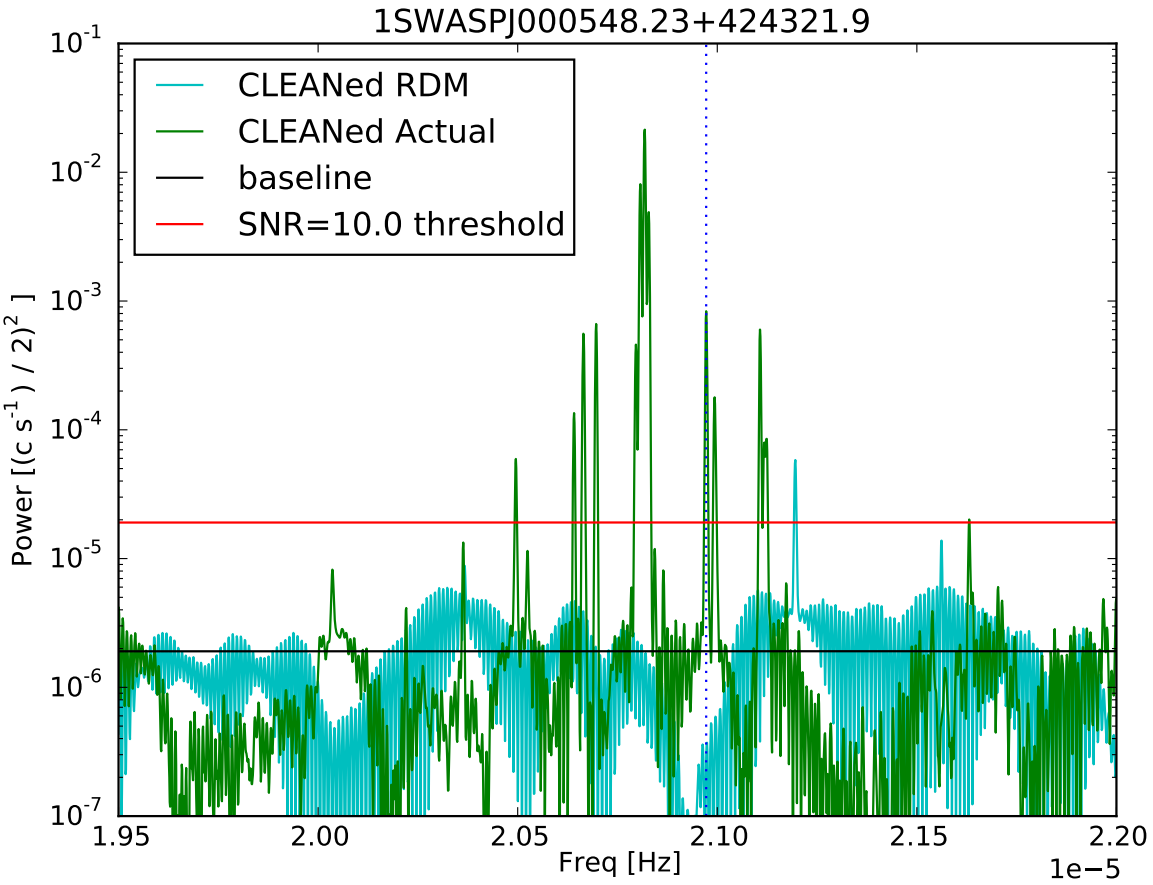

Figure 4.6: Section of the CLEANed power spectra for object 1SWASPJ000548.23+424321.9 around the main pulsation frequency, showing in greater clarity the side peak, highlighted by the vertical dotted line. The difference between this peak and the central main pulsation frequency matches the low frequency peak shown in Fig. 4.5. The resultant P_{BL} is 74.8 d. Note the higher signal to noise threshold of 10 shown in red, which is above the noisy peaks further from the group of sidepeaks.

above, possibly because of the strict criteria we adopted.

The first 20 rows of the Blazhko catalogue sorted by right ascension are listed in Table 4.1, showing the pulsation amplitude A_{LC} and the amplitude of the Blazhko effect peak as A_{BL}, both in magnitudes. Where the RRab object matched a Skarka object, their Skarka name is listed along with any previously known Blazhko periods. The full version of the table is available in Appendix B.

Three of the CRTS catalogues (Drake et al. (2013b), Drake et al. (2014), and Drake et al. (2017)) contain a flag denoting objects as Blazhko. Of these 394 Blazhko objects, 104 were also in the SuperWASP RRab catalogue. These 104 objects were cross–matched against the SuperWASP Blazhko candidates catalogue using the Vizier Xmatch service and a search radius of 1 arcminute. There were 43 CRTS Blazhko objects in the SuperWASP RRab catalogue, but not in the SuperWASP Blazhko catalogue, giving a completion percentage of

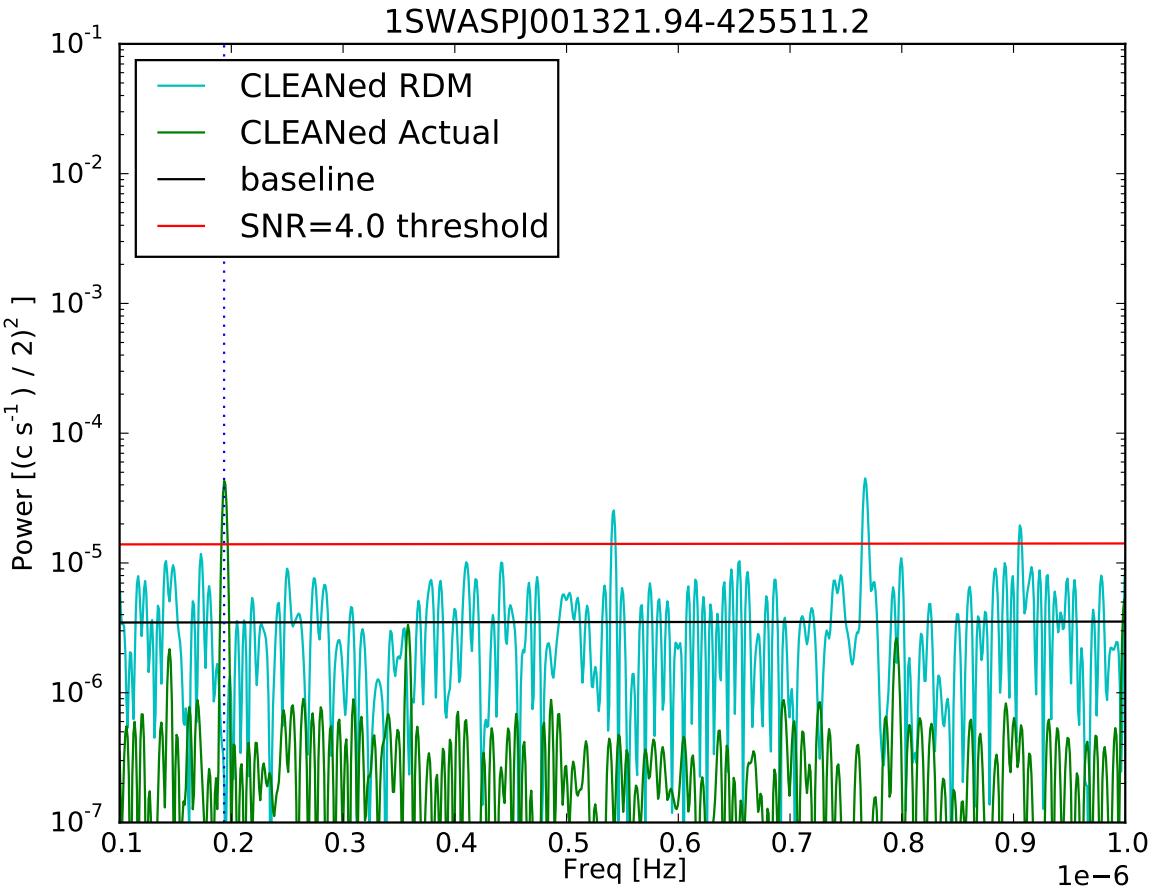

Figure 4.7: Section of the CLEANed power spectra showing in greater clarity the low frequency peak for object 1SWASPJ001321.94-425511.2. The colour scheme is the same as in Fig. 4.5. The low frequency peak (P_{BL} = 59.8 d) is marked with a dotted vertical line.

58.7%. There were 922 SuperWASP Blazhko objects not listed in the CRTS Blazhko objects in the SuperWASP RRab catalogue. Table 4.2 shows 20 Blazhko candidates with the CRTS name of matching objects. Objects listed as a Blazhko type or class in the CRTS catalogues, are denoted with 'Bl' in this catalogue. The full catalogue of 983 Blazhko candidates with the CRTS details is shown in the appendices.

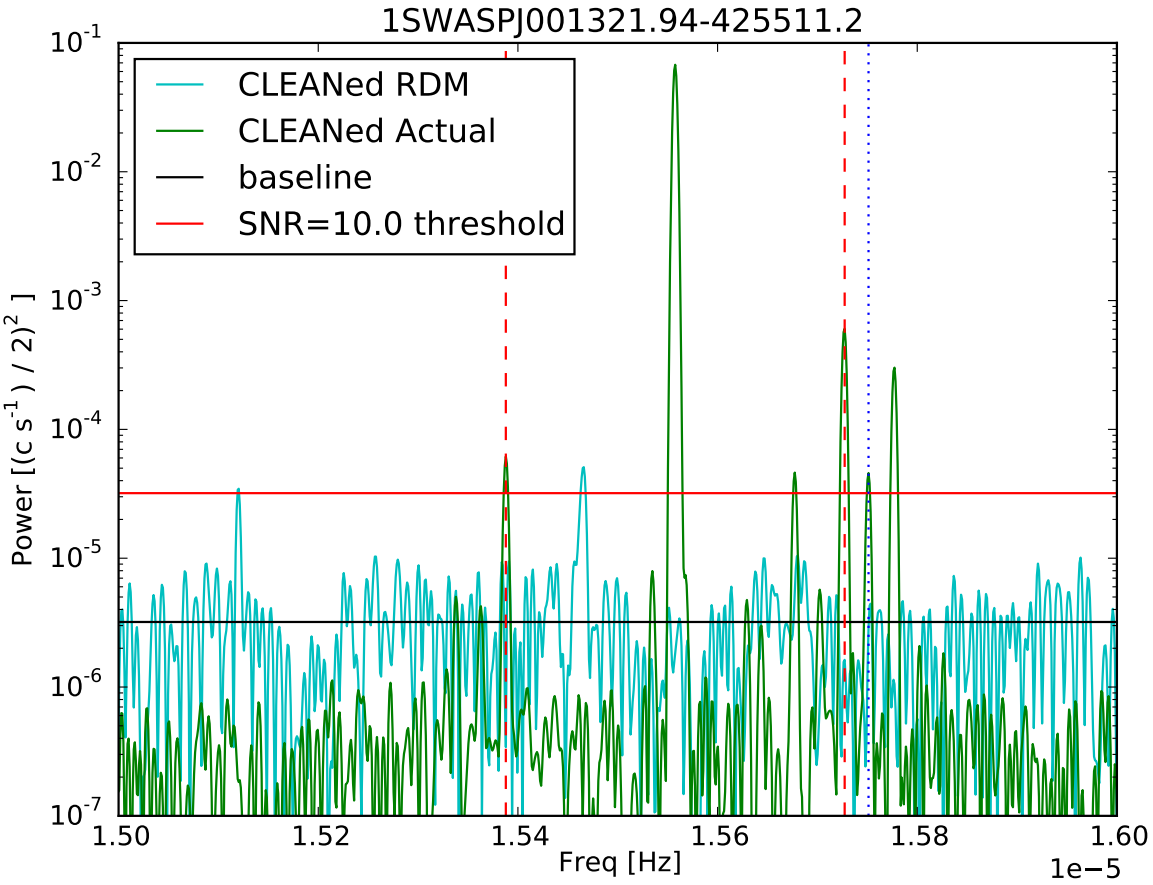

Figure 4.8: Section of the CLEANed power spectra for object 1SWASPJ001321.94-425511.2, showing the area around the pulsation frequency in greater clarity. The pair of matching sidebands (P_{BL} = 68.3 d) are marked with red dashed vertical lines. The peak corresponding to the low frequency peak seen in Fig. 4.7 is marked with a blue dotted vertical line.

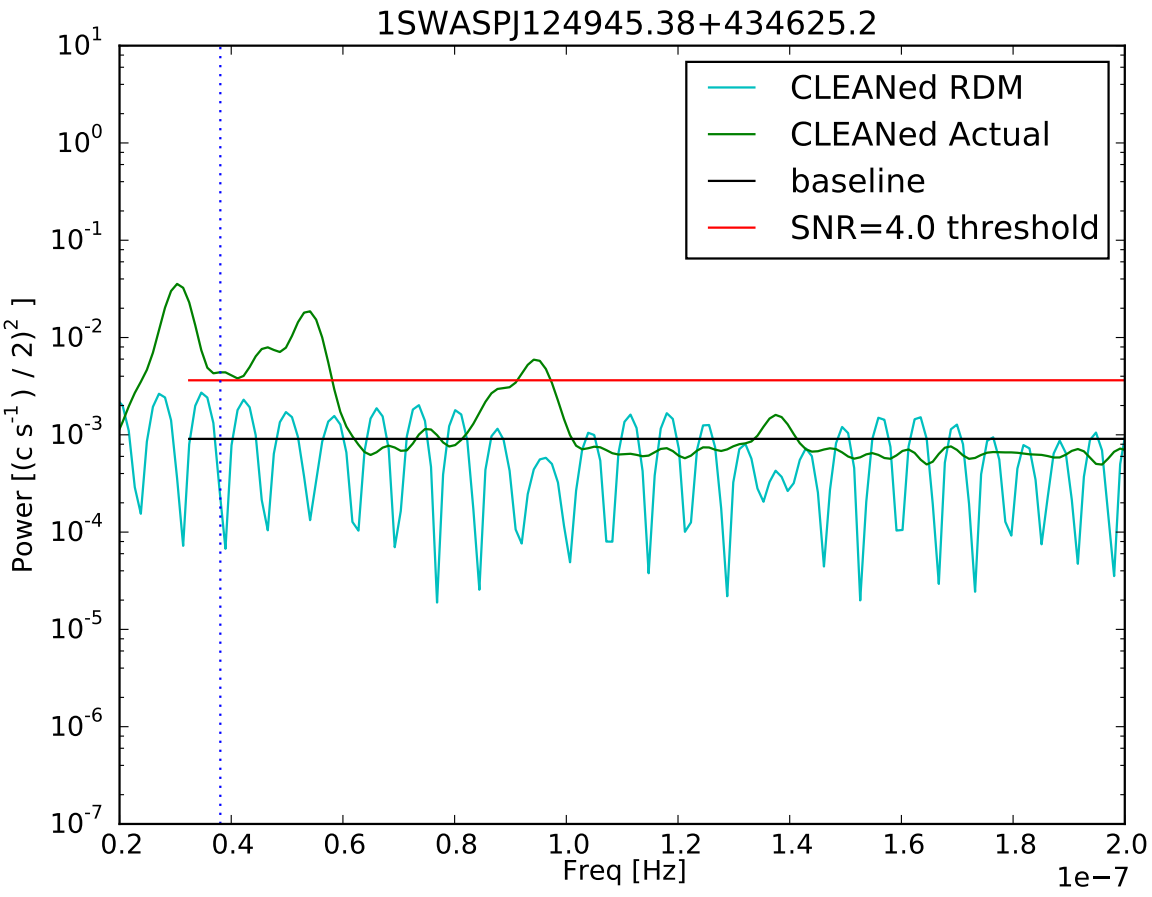

Figure 4.9: Section of the CLEANed power spectra for object 1SWASPJ124945.38+434625.2, showing the group of low frequency peaks beyond 3.8×10^{-8} Hz.

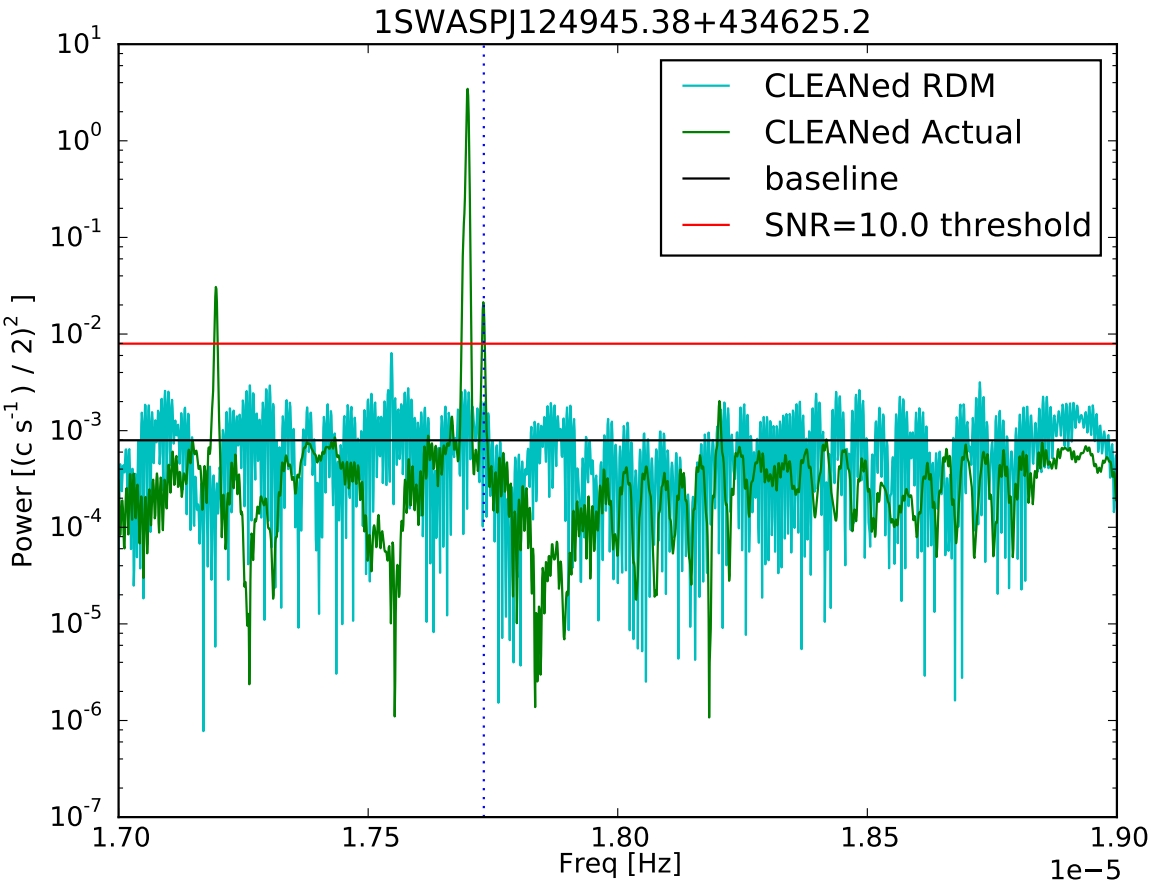

Figure 4.10: Section of the CLEANed power spectra for object 1SWASPJ124945.38+434625.2. The sideband giving the candidate Blazhko period of 356 d is marked with a blue dotted vertical line.

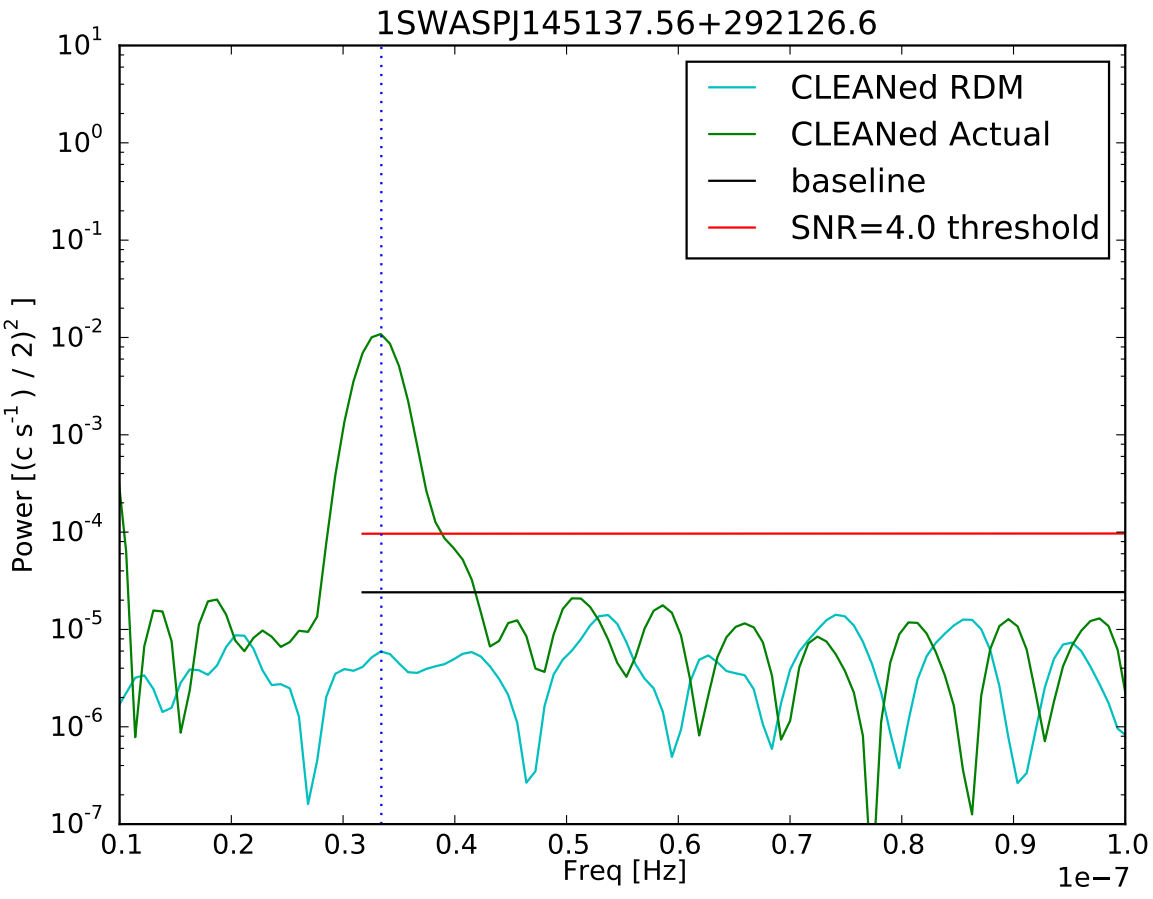

Figure 4.11: Section of the CLEANed power spectra for object 1SWASPJ145137.56+292126.6, showing the low frequency peak at 3.34×10^{-8} Hz.

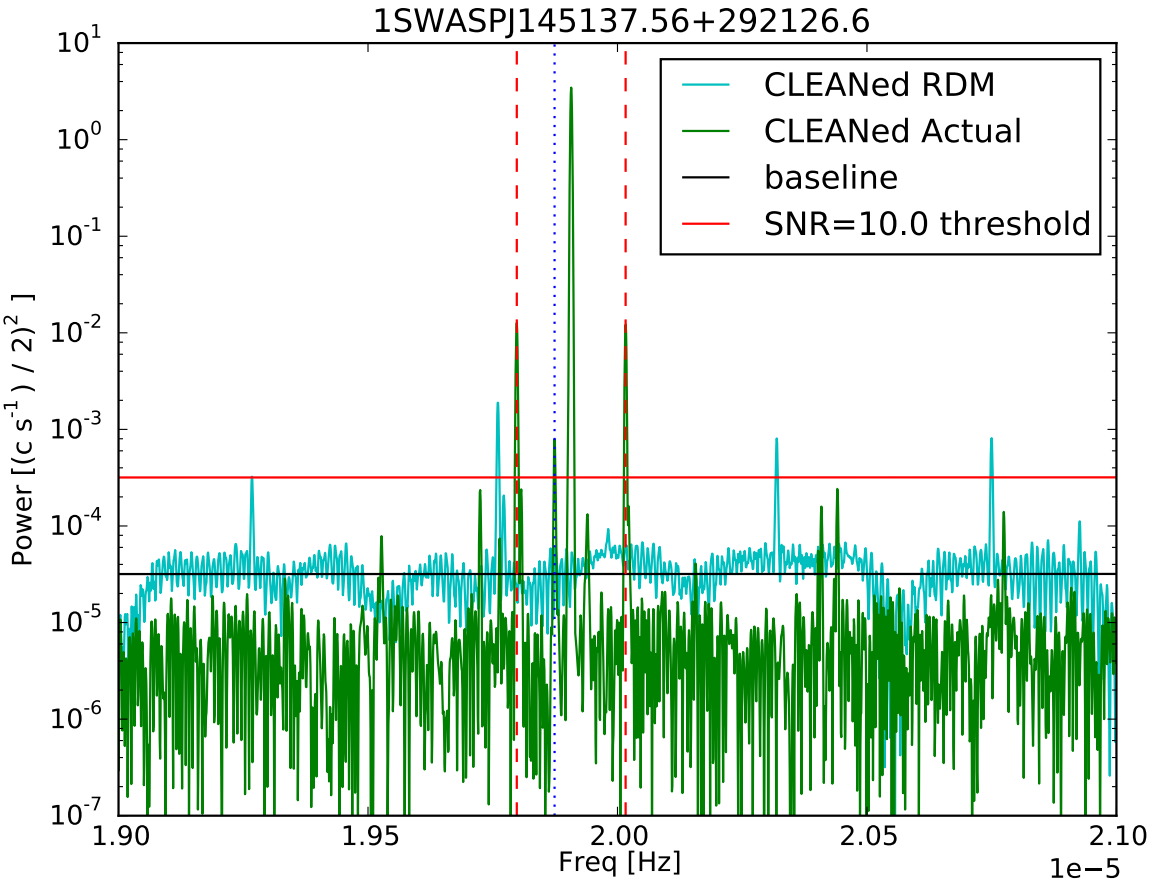

Figure 4.12: Section of the CLEANed power spectra for object 1SWASPJ145137.56+292126.6. The sideband giving the candidate Blazhko period of 346 d is marked with a blue dotted vertical line. The pair of symmetrical sidebands marked in red dashed lines gives a candidate Blazhko period of 106.1 d.

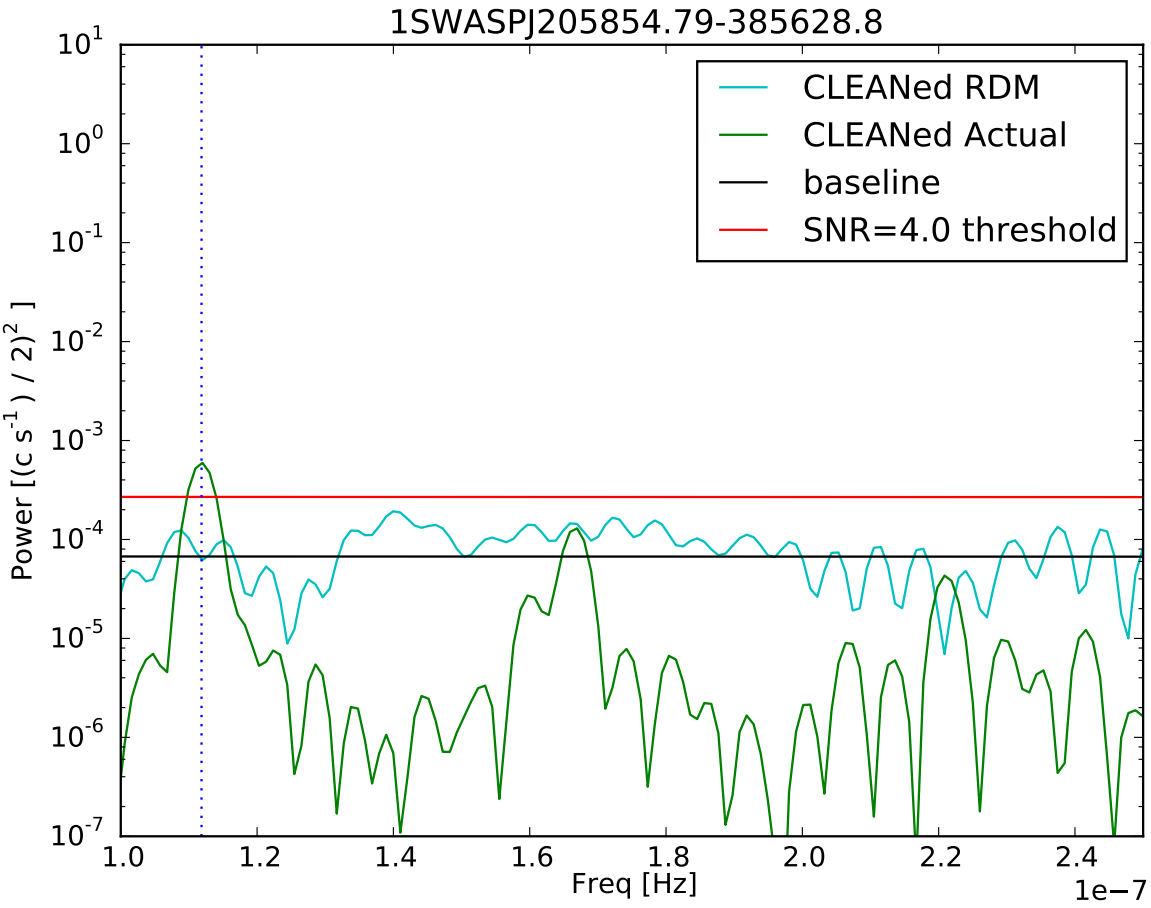

Figure 4.13: Section of the CLEANed power spectra for object 1SWASPJ205854.79-385628.8, showing the group of low frequency peaks beyond 3.8×10^{-8} Hz.

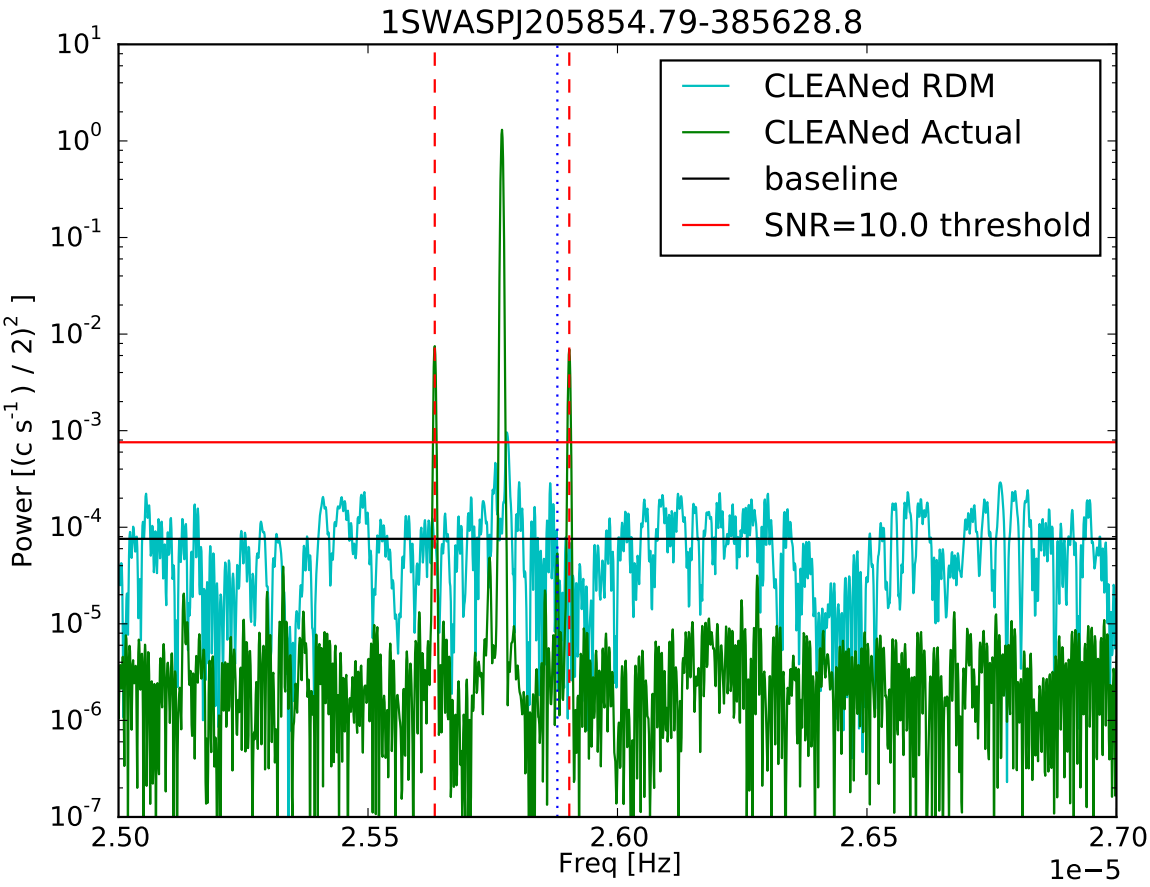

Figure 4.14: Section of the CLEANed power spectra for object 1SWASPJ205854.79-385628.8. The sideband giving the candidate Blazhko period of 356 d is marked with a blue dotted vertical line.

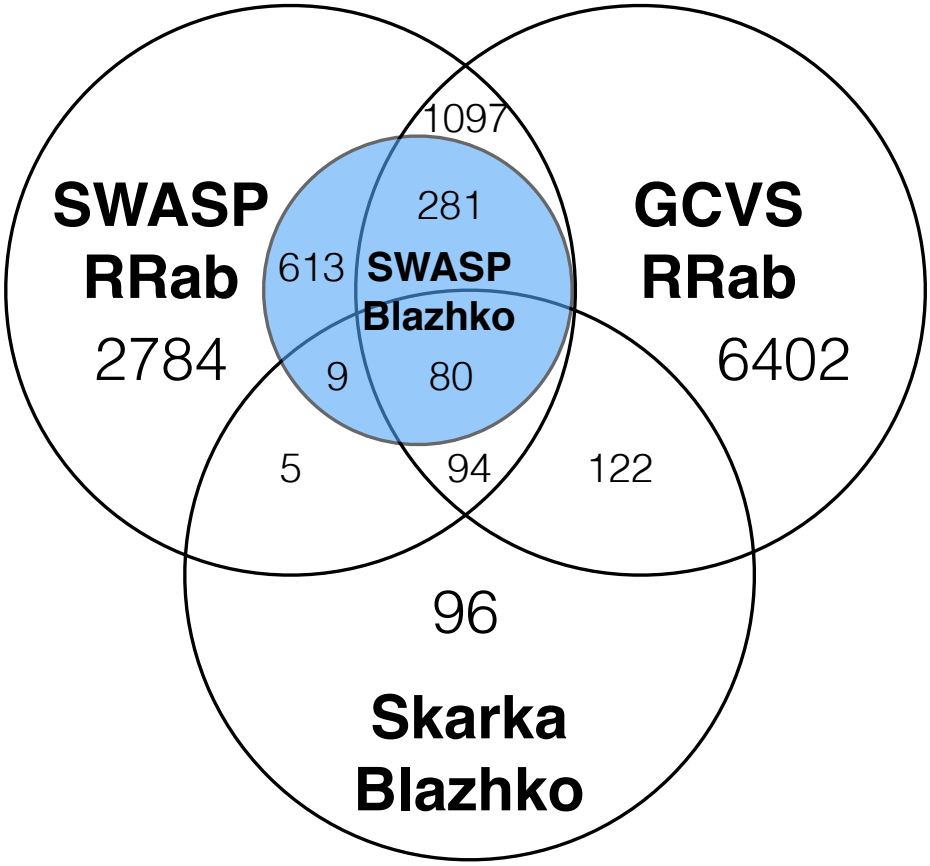

Figure 4.15: Quantities of objects from the 3 main catalogues used in this study. The 983 Blazhko objects discovered using the CLEAN routine are labelled 'SWASP Blazhko'. The 613 newly identified Blazhko objects are distinguished from those found in existing lists.

Table 4.1: Subset of Blazhko candidate results with Skarka details

SWASP id	P_{Pulse} [d]	A_{LC} [mag]	P_{BL} [d]	A_{BL} [mmag]	Skarka name	Skarka P_{BL} [d]
1SWASPJ000035.58+263949.6	0.56606638	0.750	120.0±0.3	106	GV Peg	80
1SWASPJ000049.23-284900.4	0.58303469	0.479	73.3±0.1	34		
1SWASPJ000126.73-001344.2	0.55574918	0.544	155.2±0.8	23		
1SWASPJ000157.75-364042.4	0.63752764	0.454	27.0±0.0;26.6±0.0	37; 52	J000157.75-364042.4	...
1SWASPJ000409.77-410810.8	0.52548796	0.968	201.6±0.8	46		
1SWASPJ000548.23+424321.9	0.55597466	0.557	74.8±0.1	59		
1SWASPJ000552.59-335119.2	0.53367919	0.788	42.6±0.1;46.0±0.1	10; 14		
1SWASPJ000624.38+170443.3	0.53171468	0.755	340.5±3.4	33		
1SWASPJ000652.94+114114.0	0.58486086	1.002	52.1±0.2;285.8±1.5	19; 67		
1SWASPJ000823.86+263323.3	0.53028244	0.675	37.1±0.0;28.4±0.0;282.6±1.4	35; 22; 58		
1SWASPJ001033.40-142439.9	0.60850245	1.029	125.9±0.7	44		
1SWASPJ001321.94-425511.2	0.74395519	0.548	59.4±0.1;67.6±0.1	29; 20		
1SWASPJ001333.20+282942.9	0.47242147	0.409	53.6±0.1	22		
1SWASPJ001334.56-095019.3	0.56786352	0.572	33.6±0.2	4		
1SWASPJ001408.92-092905.4	0.61616677	0.893	27.2±0.0	31		
1SWASPJ001512.51-351541.6	0.60572129	0.694	78.5±0.4	6		
1SWASPJ001748.57+095322.3	0.70111263	0.876	314.8±3.3	242		
1SWASPJ002322.79+134541.0	0.53127819	1.033	163.6±0.4;290.7±1.1	359;469	FI Psc	>120
1SWASPJ002521.68-363024.1	0.69991457	0.744	36.0±0.1	9		
1SWASPJ002843.08-440022.6	0.59996766	0.765	117.9±0.2;117.9±0.2	135;135		

Table 4.2: Subset of Blazhko candidates results with CRTS details

SWASP id	P_{Pulse} [d]	A_{LC} [mag]	P_{BL} [d]	A_{BL} [mmag]	CRTS name	CRTS Blazhko
1SWASPJ162007.21-173714.9	0.550325	0.407	40.2±0.0	59	J162007.1-173714	Bl
1SWASPJ162027.40-304551.0	0.558862	0.519	46.6±0.1	47		
1SWASPJ162252.84-153543.6	0.333318	0.909	25.9±0.0	55		
1SWASPJ162253.42-272436.4	0.766944	0.685	19.7±0.0	123	J162253.3-272437	
1SWASPJ162309.25-263000.8	0.626974	0.136	271.6±3.2	324		
1SWASPJ162325.97+102017.3	0.684819	0.638	41.3±0.0	25	J162325.9+102017	
1SWASPJ162354.20-262942.0	0.522348	0.238	285.7±1.0	963		
1SWASPJ162400.46-112101.6	0.514161	1.034	41.2±0.0	33	J162400.5-112104	Bl
1SWASPJ162401.17-262155.5	0.522475	0.333	285.8±1.4	398	J162358.4-262138	
1SWASPJ162407.47-263839.0	0.454787	0.19	10.8±0.0	135	J162407.6-263840	
1SWASPJ162429.65-263202.7	0.579106	0.675	217.1±1.5	211	J162429.8-263204	
1SWASPJ162433.37-262057.6	0.614842	0.874	244.5±1.8	347	J162433.4-262100	
1SWASPJ162449.67+080414.2	0.644729	0.919	174.9±0.5	245	J162449.6+080413	
1SWASPJ162538.03-174401.0	0.541308	0.491	92.7±0.3	13	J162538.1-174357	
1SWASPJ162558.65+174252.1	0.67887	0.51	283.9±4.7;89.4±0.5;187.1±1.3	34; 35; 52	J162558.6+174252	
1SWASPJ162609.56-031153.0	0.431817	0.671	121.1±0.3	27	J162609.5-031153	Bl
1SWASPJ162640.02+012001.2	0.474937	0.427	319.8±2.2	35	J162638.6+012037	
1SWASPJ162704.60+325415.9	0.607786	0.565	32.8±0.0	13	J162704.5+325415	
1SWASPJ162735.65+112608.9	0.538254	0.26	32.9±0.0	33	J162736.8+112535	
1SWASPJ162803.45-030312.7	0.515016	0.574	272.8±1.5	27	J162803.4-030313	Bl

4.2.6 Revisiting the relative scatter parameter

The previous Time Domain chapter investigated the efficacy of the relative scatter parameter as an indicator of the Blazhko effect, using small sets of known Blazhko effect and known non–Blazhko effect objects coincident with objects in the SuperWASP RRab catalogue. This analysis can now be expanded using the larger populations of Blazhko and non–Blazhko effect objects defined using the spectral analysis techniques described above. This AM derived parameter can also be compared to the characteristic Blazhko effect properties such as the Blazhko period and amplitude.

After analysis of Blazhko and non-Blazhko subsets, the suspected relation between the relative scatter and the Blazhko effect in the time domain is still inconclusive. Fig. 4.16 shows that despite a higher number of Blazhko objects having relatively high levels of scatter at the peak, they have very similar lower limits. The non-Blazhko subset has a mean relative scatter of 1.29 and uncertainty of 0.42, and the Blazhko candidates have a mean relative scatter of 1.59 with an uncertainty of 0.59. The lack of bimodality makes it impossible to define a threshold in the relative scatter above which Blazhko candidates can be reliably identified.

Fig. 4.17 shows an increasing spread of relative scatter values with increasing Blazhko power. This produces a moderate monotonic correlation with a statistically significant Spearman ρ coefficient of 0.50.

The increase in the spread of relative scatter with pulsation amplitude for both non-Blazhko (Fig. 4.18) and Blazhko objects (Fig. 4.19) is reflected in their Spearman coefficients of 0.61 and 0.56 respectively. This similarity between populations implies that the amount of scatter at the peak of RRab light curves is dependent only on pulsation amplitude, and is not a signature characteristic of the Blazhko effect.

Benkő and Szabó (2014) refer to a possible link between the Blazhko period and the amplitude of the AM effect, the so-called 'envelope function'. The relative scatter parameter described in Sec. 3.3.1 is our equivalent measure of this envelope function. However, I am unable to confirm the correlation between the Blazhko period and AM in this study as no correlation can be seen in Fig. 4.20 and the Spearman coefficient is 0.02, which is not statistically significant. Likewise, there is no correlation between the relative scatter parameter and the main pulsation period as shown in Fig. 4.21 where there appears to be a wide range of scatter values around the typical RRab pulsation period of roughly half a day.

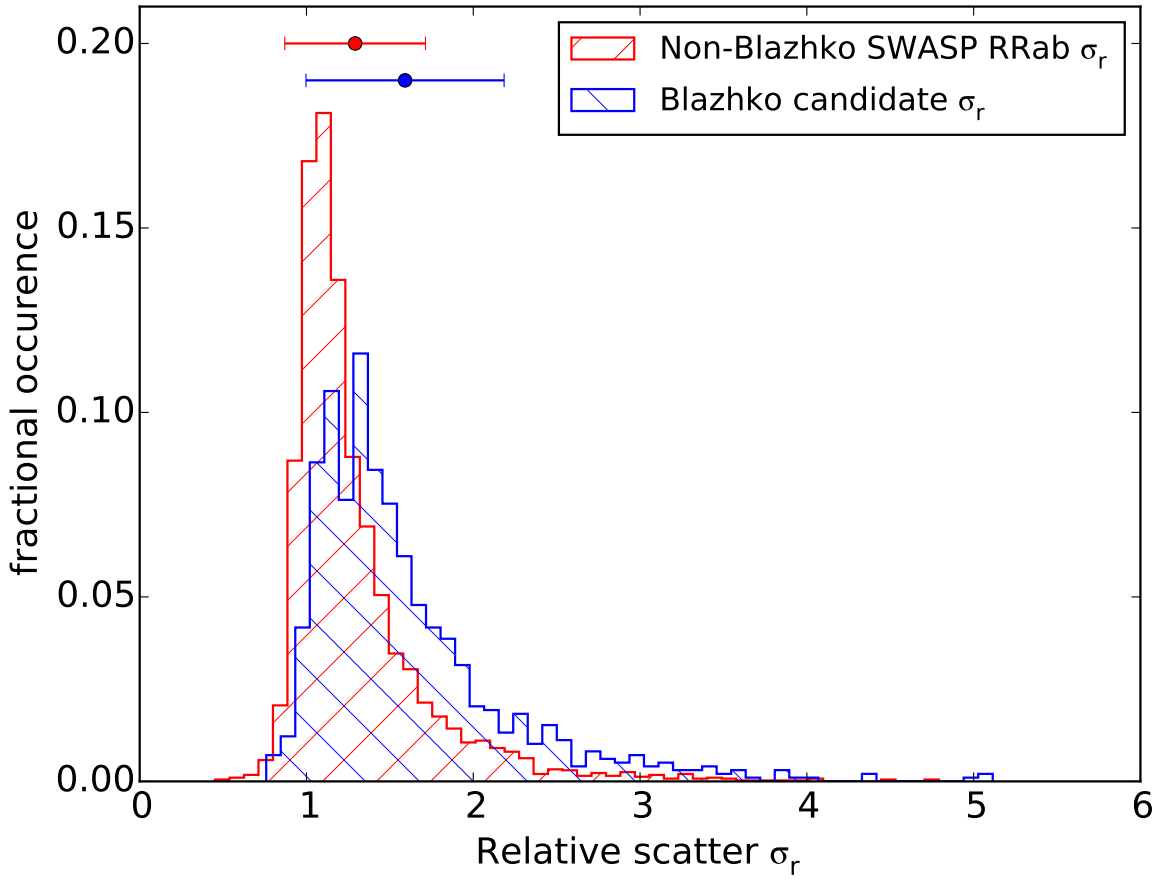

Figure 4.16: Distribution of relative scatter σ_r for Blazhko and non-Blazhko populations. The error bars represent the mean and standard deviation for each population.

This relation has a Spearman coefficient of -0.24.

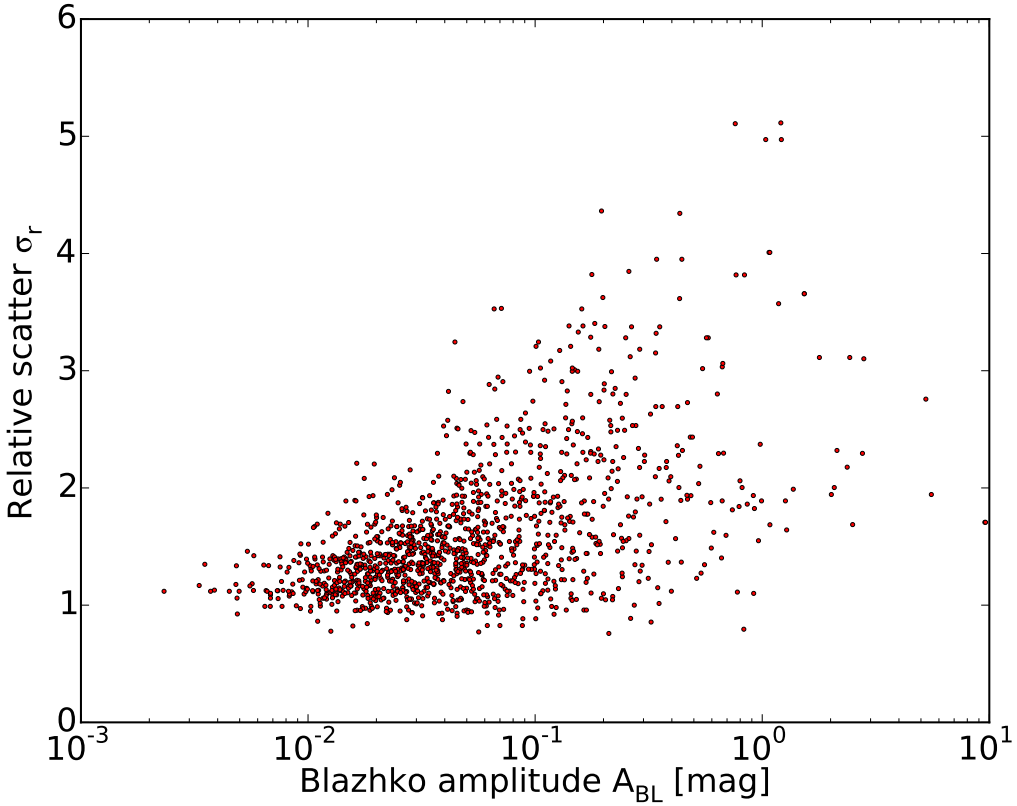

Figure 4.17: Comparison of the relative scatter parameter from the phase folded light curves and the Blazhko amplitude from the CLEAN power spectra. Despite a visible lack of correlation this relation has a Spearman value of 0.5, implying a moderate correlation between relative scatter and Blazhko amplitude.

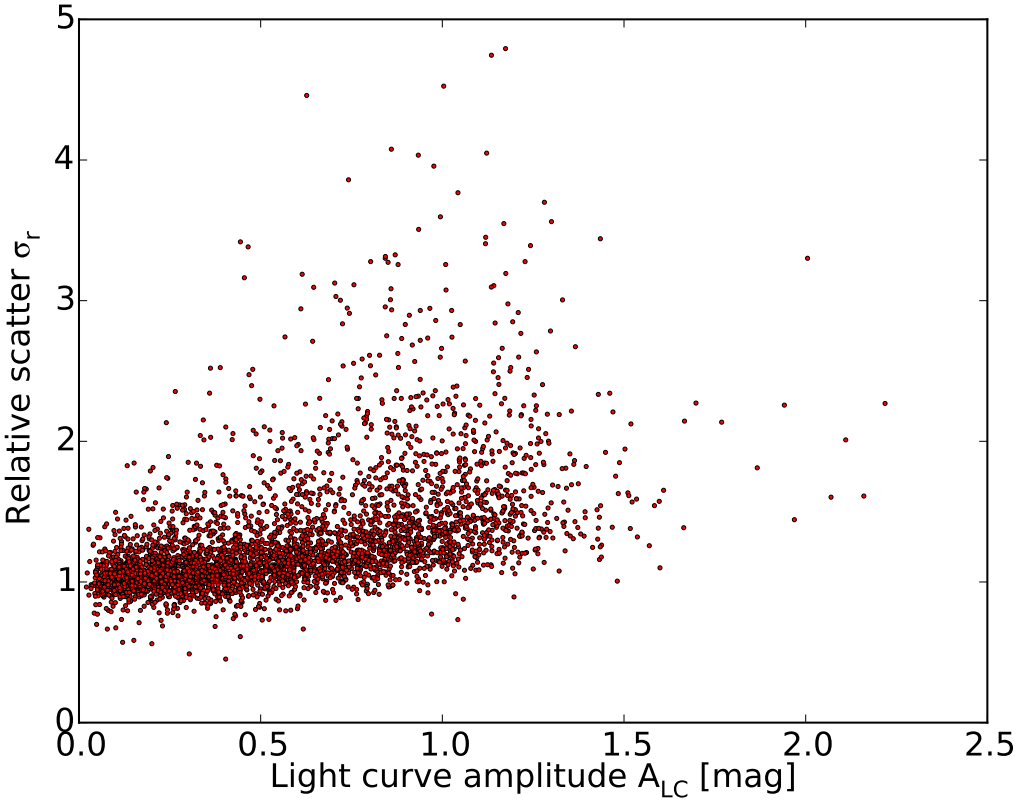

Figure 4.18: Comparison of relative scatter against pulsation amplitude for the non–Blazhko population from SuperWASP, showing a slight dependence on pulsation amplitude for the relative scatter parameter at high amplitudes.

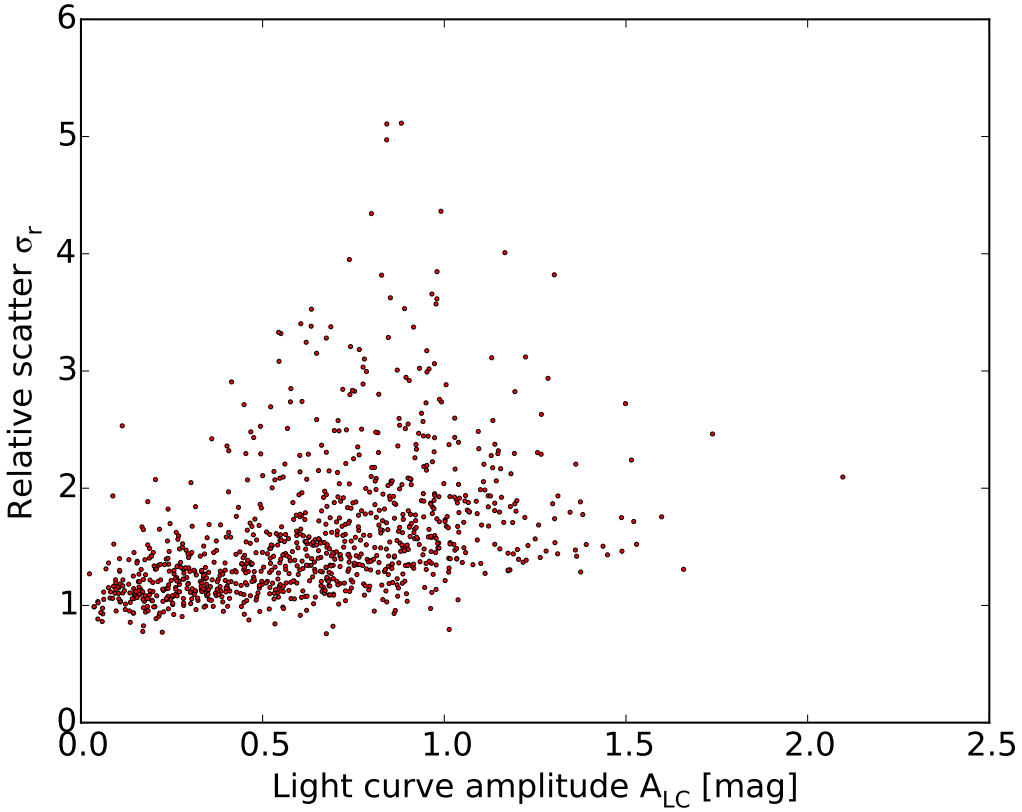

Figure 4.19: Comparison of relative scatter against pulsation amplitude for the Blazhko candidates from SuperWASP, showing the same dependence on pulsation amplitude for the relative scatter parameter at high amplitudes as for the non–Blazhko population.

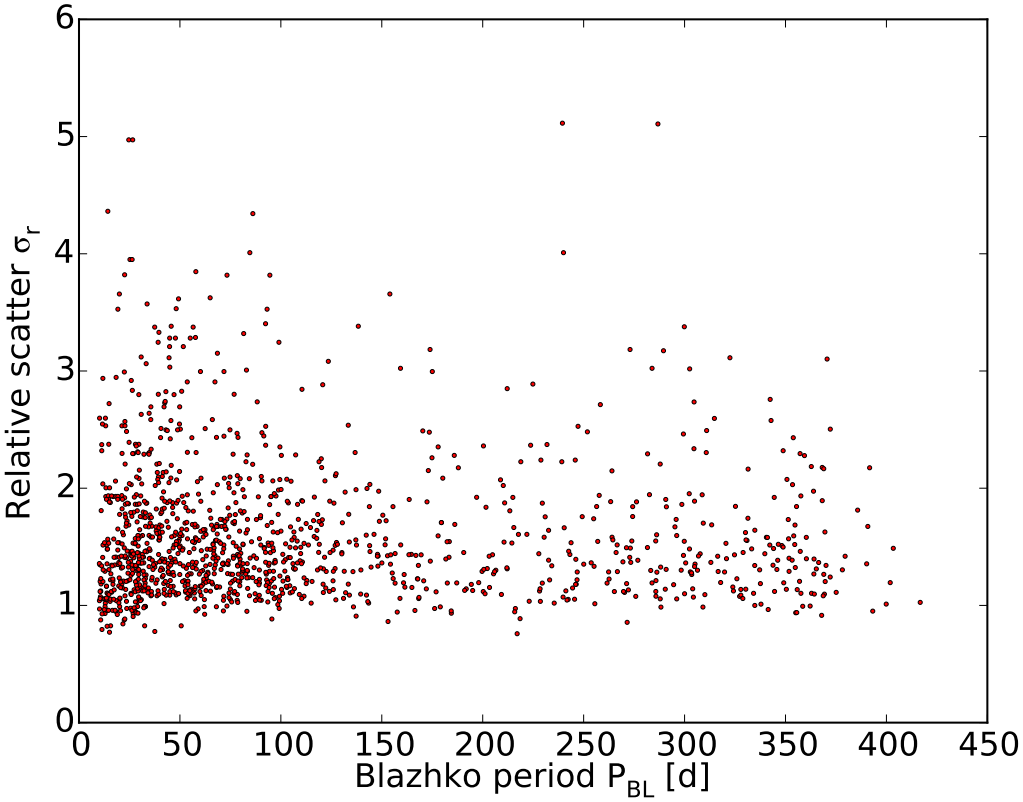

Figure 4.20: Relative scatter parameter against Blazhko period. There appears to be no correlation between the level of scatter at the light curve peak, σ_r, and the Blazhko period P_{BL}.

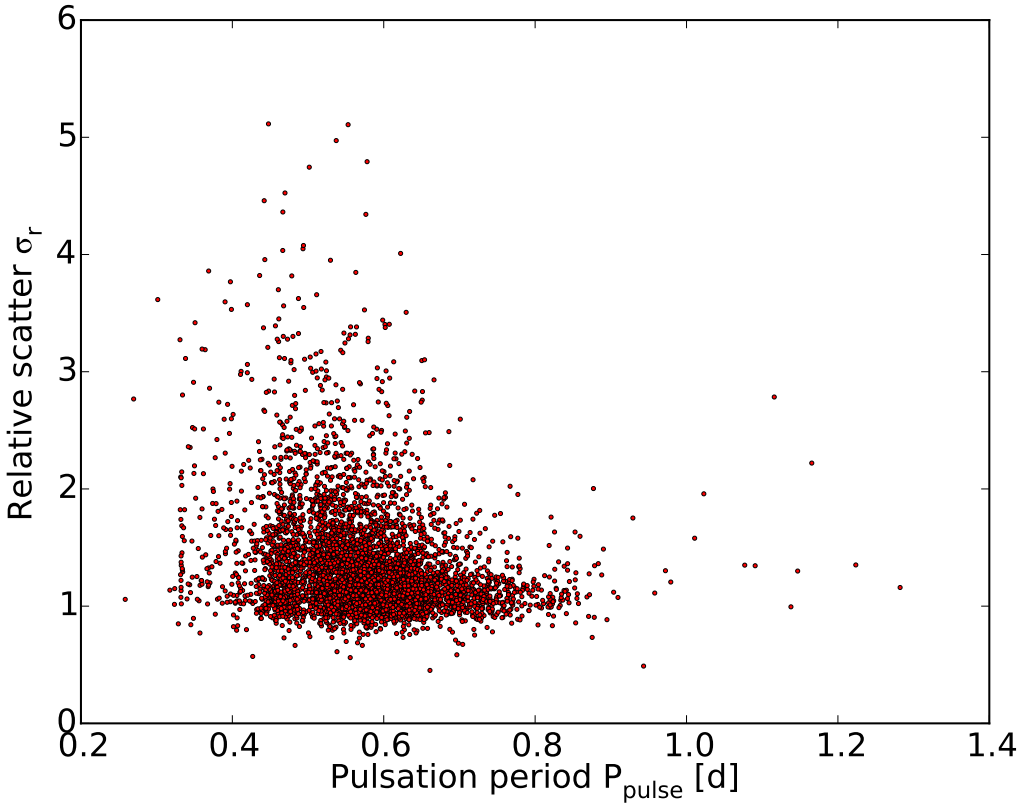

Figure 4.21: Relative scatter parameter against pulsation period. As with the Blazhko period, there appears to be no correlation between the level of scatter at the light curve peak, σ_r, and the pulsation period P_{pulse}, with most objects having a low relative scatter parameter and pulsation periods typical of RRab stars.

4.3 Investigations of parameter correlations

Several of the basic characteristics of the SuperWASP RRab and their Blazhko effect parameters were compared to search for any correlations.

The pulsation periods for SuperWASP RRab and Blazhko objects are compared in Fig. 4.22. The slight deficit of pulsation periods between 0.45 and 0.50 d is thought to be an effect of the ground–based sampling regime. The mean pulsation period of the Blazhko candidate subset is 0.56 d with a standard deviation of 0.08 d. The non-Blazhko subset's mean pulsation period is 0.58 d, with a standard deviation of 0.10 d. The Blazhko candidates' pulsation periods range from 0.30 to 1.01 d, whereas the non-Blazhko subset have a wider range from 0.26 to 1.28 d.

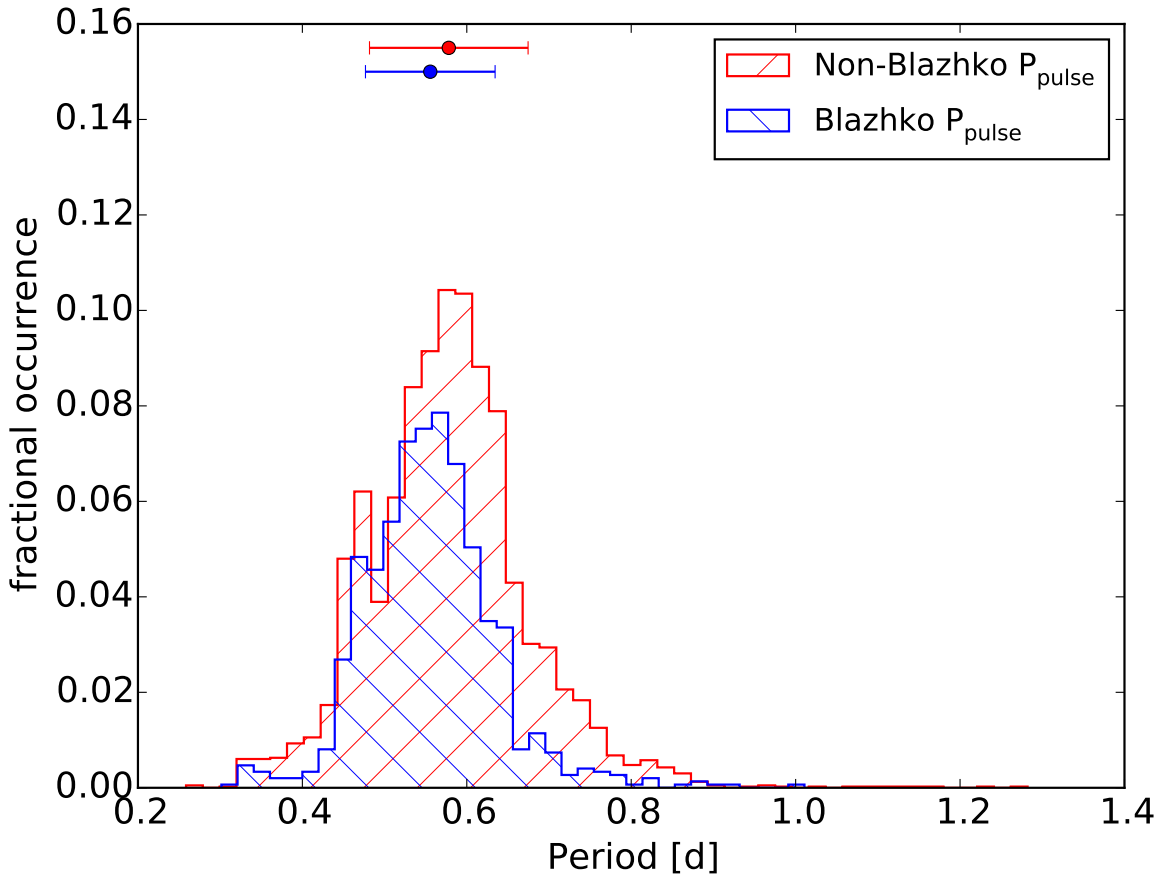

Figure 4.22: Comparison of pulsation periods for SuperWASP Blazhko and non-Blazhko objects. The mean and 1σ deviation are shown by the horizontal error bars, where the colours correspond to the respective SuperWASP RRab populations.

Fig. 4.23 shows that Blazhko and non-Blazhko effect objects have similar ranges of pulsation amplitudes, apart from a very small number of high pulsation amplitude non-Blazhko objects. The slight deficit of pulsation amplitudes between 0.3 and 0.5 mag in the Blazhko

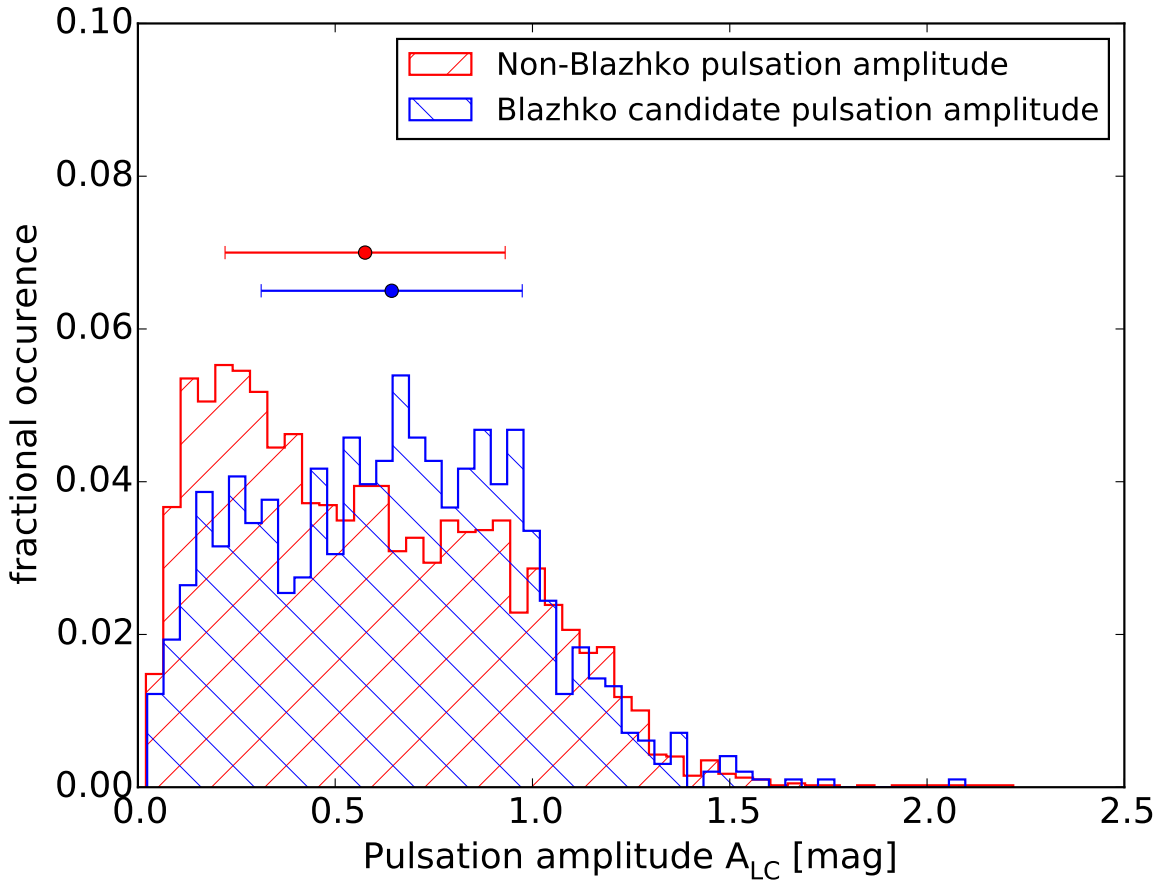

Figure 4.23: Comparison of pulsation amplitudes for SuperWASP Blazhko and non-Blazhko objects. As in the previous figure, the mean and 1σ deviation are shown by the horizontal error bars, where the colours correspond to the respective populations.

dataset still appears after running a bootstrap algorithm to check if it was a sampling effect. The ability to detect smaller amplitudes suggests that it is not a systematic limitation. The non–Blazhko populations shows more objects with pulsation amplitudes between 0.0 and 0.5 mag than 0.5 to 1.0 mag, whereas the Blazhko population is higher between 0.5 and 1.0 mag. This may be a selection effect where objects with higher amplitudes produce stronger low frequency Blazhko peaks due to a larger change in pulsation amplitude over the Blazhko cycle, making these objects easier to identify as Blazhko effect objects using the technique described above.

Blazhko periods were compared to pulsation periods, as shown in Fig. 4.24, but no correlation was found between these basic characteristics of our Blazhko candidates, with the statistically significant Spearman rank coefficient of 0.068.

The amplitude of the Blazhko effect, A_{BL}, was taken from the amplitude of the fitted modulation frequency returned by Period04 as described in Sec. 4.2.5. This amplitude was compared with the Blazhko period (Fig. 4.25), however, there is a lack of correlation between

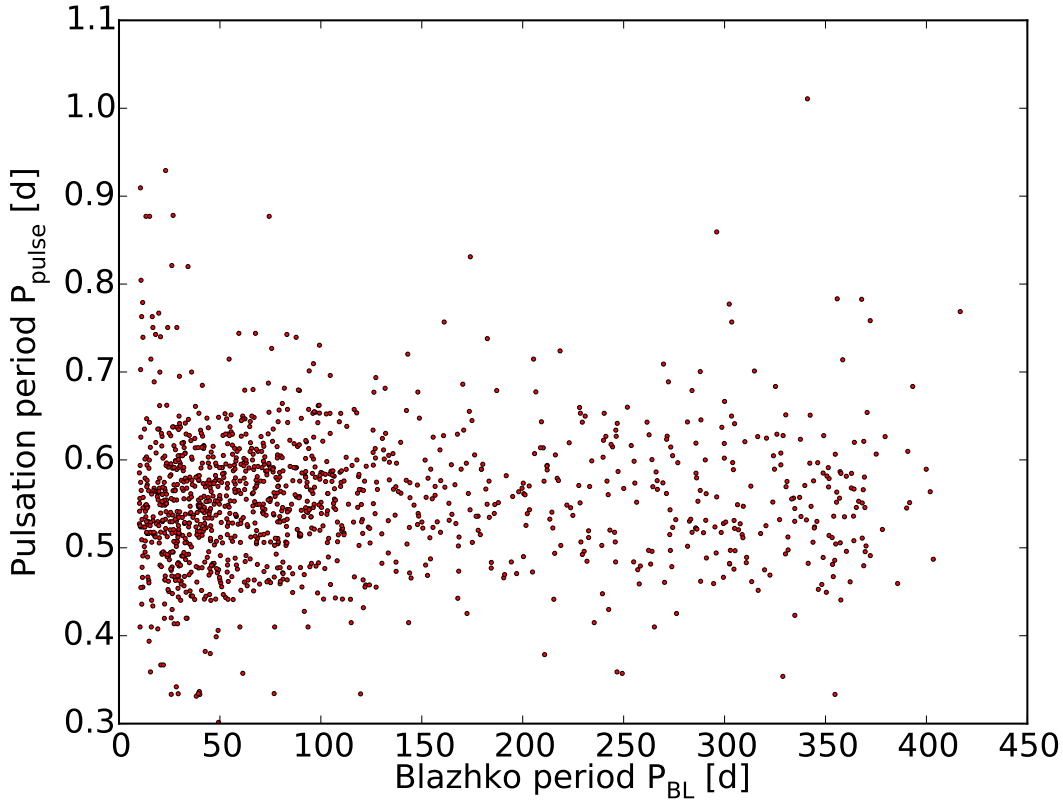

Figure 4.24: Comparison of pulsation period (P_{pulse}) against Blazhko period (P_{BL}) showing a similar distribution across a wide range of Blazhko periods.

them over a wide range of values, producing a Spearman coefficient of 0.11. Additionally, Fig. 4.26 shows how the Blazhko amplitude is not related to the main pulsation period either, with a Spearman coefficient of −0.199.

Finally we compared candidate Blazhko periods and amplitudes with pulsation amplitudes calculated from the peak to peak amplitude of the phase folded light curve, denoted as A_{LC}. The pulsation amplitude is shown compared to the Blazhko period in Fig. 4.27, where no correlation is found despite a wide range of candidate periods. The Spearman value in this case was 0.17. The correlation between the Blazhko amplitude and the pulsation amplitude (Fig. 4.28) has a strong Spearman coefficient of 0.735. However, CLEANing a synthetic light curve which included a modulation effect (see Fig. 4.1) demonstrated that when the main pulsation amplitude was increased, the strength of the modulation peaks in the CLEAN power spectrum also increased. Therefore the apparent correlation between Blazhko amplitude and pulsation amplitude may be a systematic effect of the power spectrum and not a property of the Blazhko effect itself.

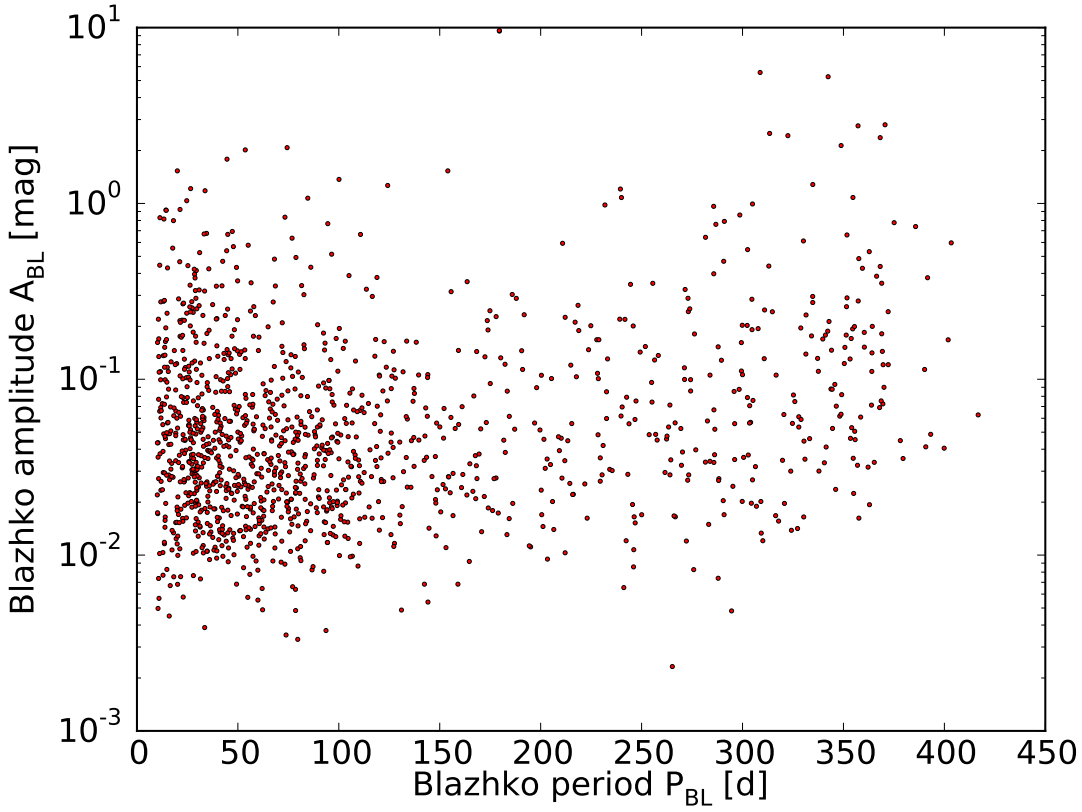

Figure 4.25: Comparison of the Blazhko amplitude A_{BL} and the Blazhko period P_{BL} showing no correlation between Blazhko characteristics.

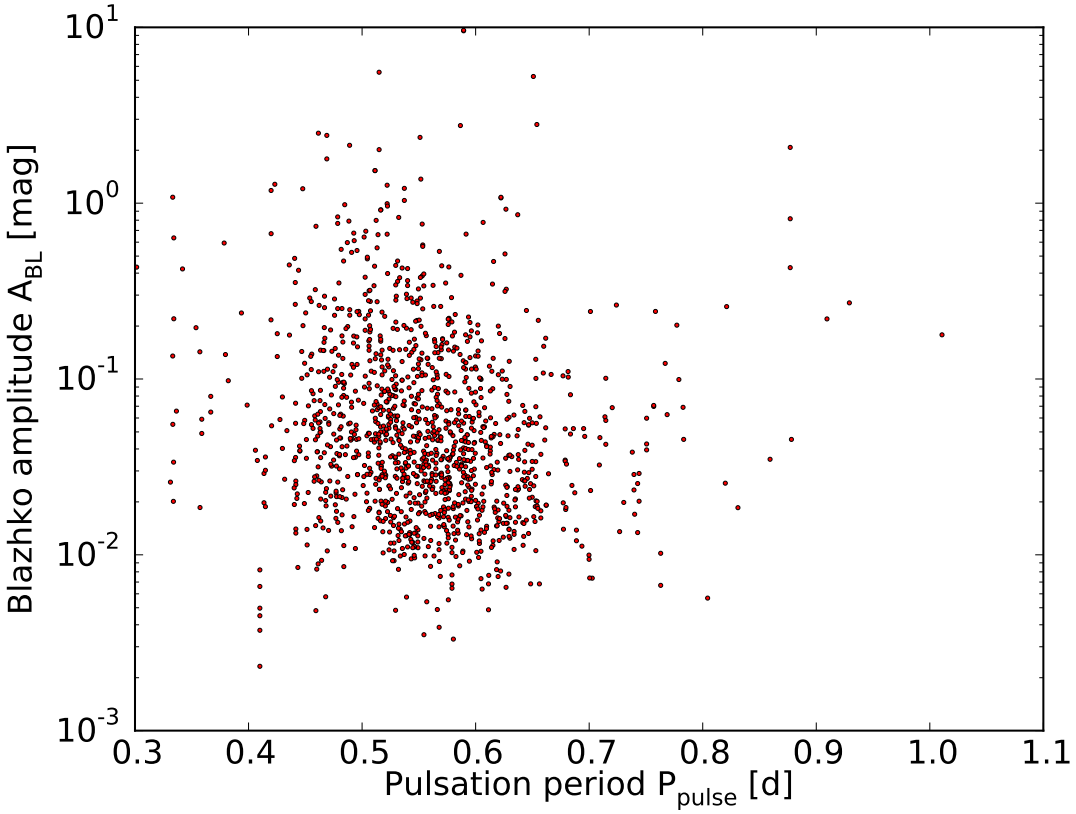

Figure 4.26: Comparison of the Blazhko amplitude A_{BL} and the pulsation period P_{pulse} showing that the pulsation period does not appear to have any effect on the power of the Blazhko effect.

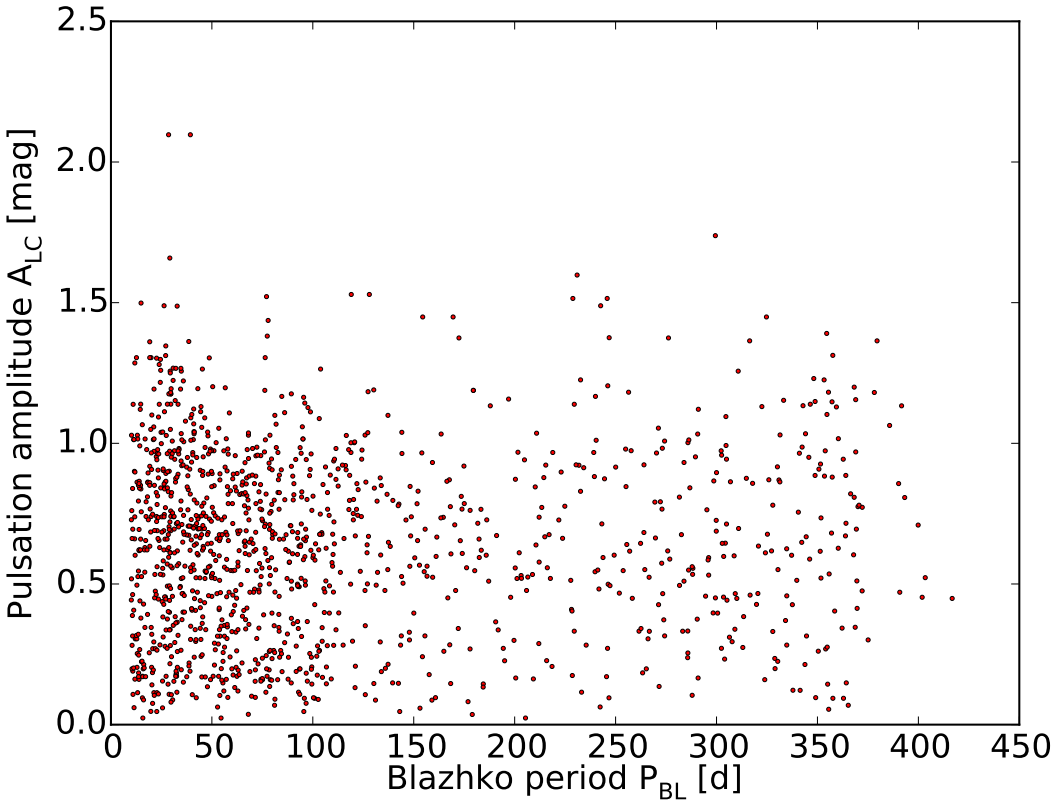

Figure 4.27: Comparison of the pulsation amplitude A_{LC} and the Blazhko period P_{BL} showing an increase in the number of Blazhko periods under 100 days but no correlation between the pulsation amplitude and the Blazhko period.

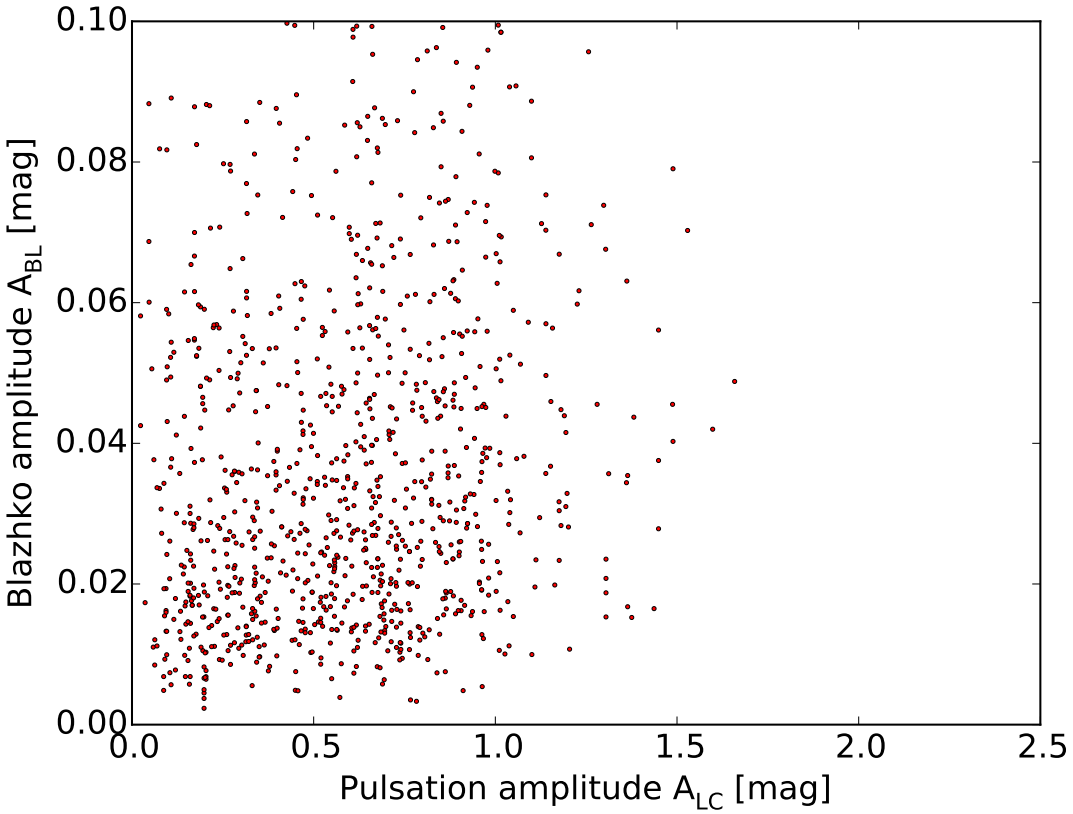

Figure 4.28: Comparison of the Blazhko amplitude A_{BL} and the pulsation amplitude A_{LC} showing most Blazhko candidates have pulsation amplitudes under 1.0 mag, but with no correlation to the Blazhko amplitude.

4.4 Notable exceptions from the Blazhko catalogue

The Blazhko parameters and their correlations described in the previous section were derived from the identification of the Blazhko effect in a large number of RRab objects from the SuperWASP RRab catalogue. However, 2 of the high AM examples investigated in the previous chapter do not appear in the Blazhko catalogue, despite showing clearly periodic modulations. This section examines those notable exceptions from the Blazhko catalogue in order to find any systematic deficiencies in the Blazhko identification methodology.

4.4.1 1SWASPJ120447.27-274043.2

The first extreme AM object missing from the Blazhko candidate catalogue is the intriguing Blazhko object IK Hya (1SWASPJ120447.27-274043.2), which also appears as a known Blazhko effect object in the Skarka online compilation of stars. Figure 4.29 shows how the randomised spectrum has not been lowered enough to be comparable to the noise level of the CLEANed actual spectrum. The high amount of signal power in the actual flux remains distributed throughout the low frequency regime of the spectrum of IK Hya, keeping the signal to noise ratio threshold above the 3 peaks in the actual signal.

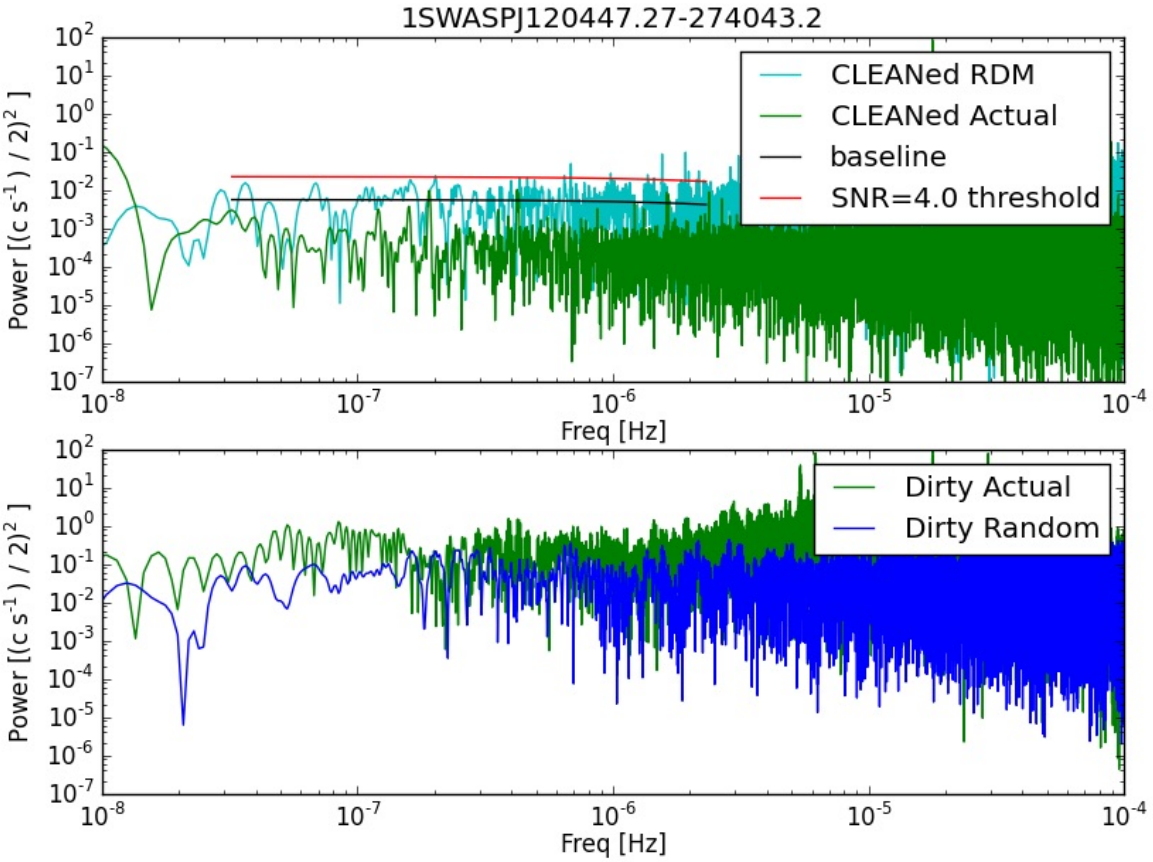

Figure 4.29: Power spectrum of 1SWASPJ120447.27-274043.2 showing how the power of the randomised flux is too high to allow any peaks from the actual signal to emerge above the threshold signal to noise ratio.

4.4.2 1SWASPJ123810.96+385027.9

SuperWASP RRab object 1SWASPJ123810.96+385027.9 clearly shows signs of the Blazhko effect in the time domain, but was not listed in the SuperWASP Blazhko candidate objects catalogue. This was due to an excessive amount of power in the low frequency regime of the actual signal, as shown in Fig. 4.30, compared to the randomised flux. This has the effect of lowering the threshold power level, so that any sidepeaks detected around the main pulsation frequency could be matched against low frequency noise, making any candidate Blazhko periods found by matching low frequency peaks to sidepeaks unreliable. Unfortunately, this also masks any true Blazhko period peaks. Six peaks can be seen above the noise of the spectrum in Fig. 4.30 but these cannot be systematically identified before matching against sidepeaks, preventing this object from being recognised as a new Blazhko candidate that was not previously listed in either Skarka or the CRTS Blazhko stars.

Visually checking the power spectrum around the pulsation period of 0.347 d (3.335×10^{-5} Hz) found by the PDM program described in Chapter 3 showed a lack of any peaks, i.e. the PDM period was not correct. This may be due to a large amount of phase modulation distorting the light curve horizontally. A manual check of the object on the CDS system shows an object, ROTSE1 J123811.00+385028.0, within 10 arcseconds of 1SWASPJ123810.96 +385027.9 in the AAVSO VSX catalogue, which has already been identified as a Blazhko object, but with an undefined Blazhko period. The pulsation period of this object is listed as 0.53303 d. Using this period to find the main peak and sidebands in the power spectrum of 1SWASPJ123810.96+385027.9 allowed the detection of symmetrical sidebands at 78.9824 d, 9.95027 d and 67.7195 d (see Fig. 4.31), fulfilling one of the two criteria for finding candidate Blazhko peaks in the power spectra of SuperWASP objects described in earlier sections. However, just as for low frequency peaks, the detection of sidebands also relies on an accurate threshold level being defined, which cannot be guaranteed for 1SWASPJ123810.96+385027.9, so this object has not been added to the SuperWASP Blazhko catalogue.

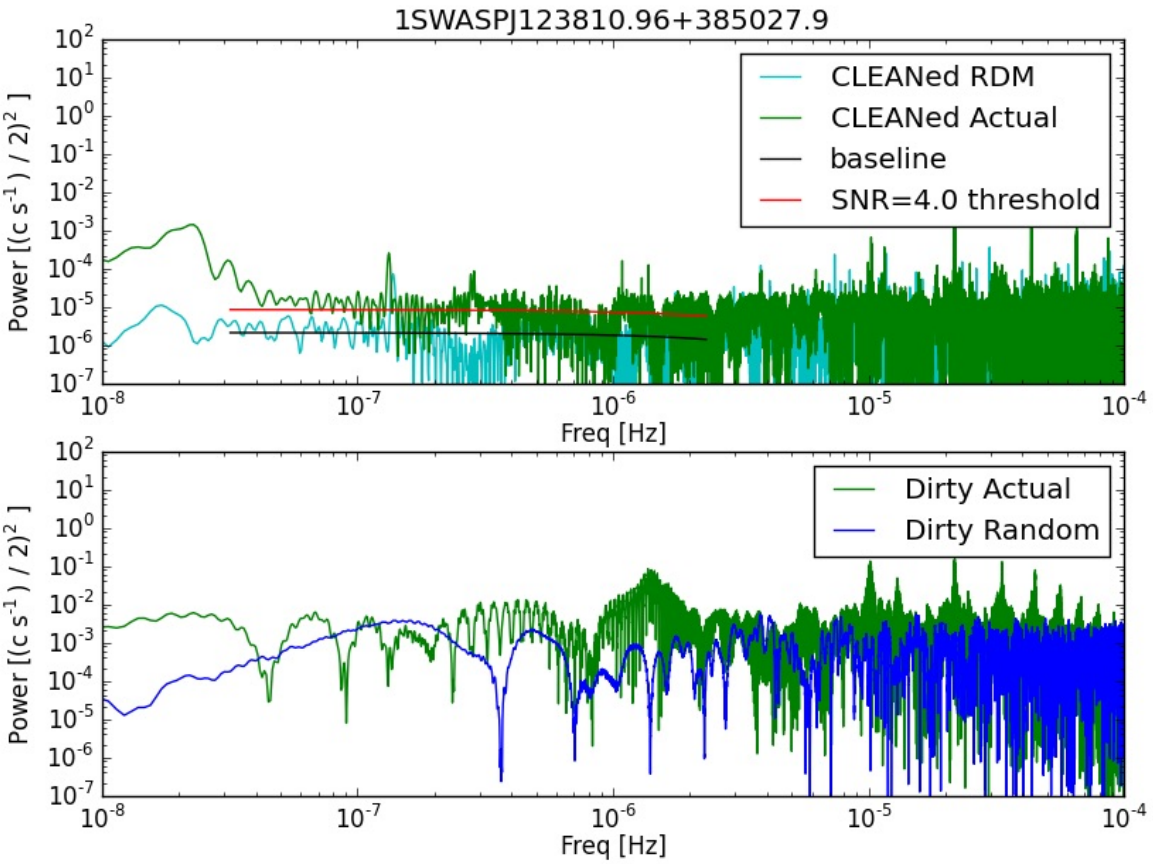

Figure 4.30: Power spectrum of 1SWASPJ123810.96+385027.9 showing how the noise of the actual signal is almost continuously above the signal to noise (SNR) threshold at the range of low frequencies associated with Blazhko periods.

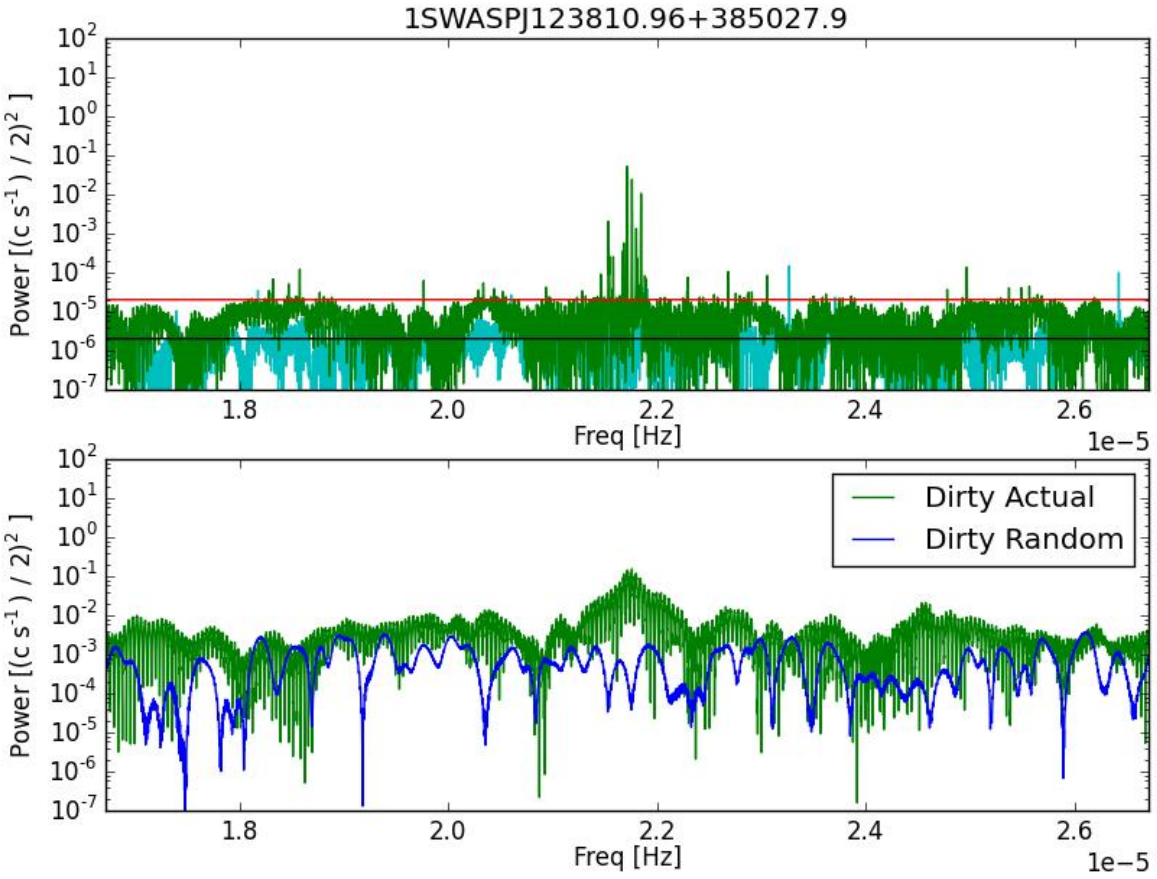

Figure 4.31: Power spectrum of 1SWASPJ123810.96+385027.9 showing the spectrum around the main pulsation frequency and the large number of sidebands. 6 of which are symmetrical, leading to 3 potential Blazhko periods, but the threshold shown by the red line is too low to have enough confidence in the detected peaks to add them to the Blazhko catalogue.

4.5 Discussion

Section 4.3 highlighted the lack of correlation between the pulsation and modulation parameters of our SuperWASP RRab population. No relation was found between the pulsation period and the Blazhko period, which concurs with Skarka (2014a), or between the pulsation period and the Blazhko amplitude. The lower occurrence of longer pulsation periods in the Blazhko candidate subset is in agreement with Prudil and Skarka (2017); in our case this deficit starts at ~ 0.6 d. However, there is still a large overlap in the range of pulsation period in both Blazhko and non-Blazhko populations.

The 20% incident rate of Blazhko effects stars in this catalogue is lower than the figures from ground-based surveys of the Galactic field: 31% found in Skarka (2014a) using a sample of 321 bright stars from ASAS and SuperWASP; and 47% found by the Konkoly Blazhko Survey (Jurcsik et al., 2009). It is also lower than the 39% occurrence from the space-based Kepler mission (Szabó, 2014). Our proportion is, however, higher than the 10% occurrence of the Blazhko effect in first overtone RRc stars in the globular cluster M3 recorded by Jurcsik et al. (2014). Hypotheses tests for two proportions were performed between the SuperWASP population and each of the above four populations in turn, in order to identify any statistically significant differences between the proportion of Blazhko objects in SuperWASP and the other proportions given above. Testing the above proportions for statistically significant differences gives p–values of 0.003 and 0.006 for the Skarka (2014a) and Jurcsik et al. (2009) proportions respectively, meaning the SuperWASP proportion is significantly different, statistically, to these two studies, which suggests that they are not from the same underlying population. The Szabó (2014) and Jurcsik et al. (2014) proportions have p–values of 0.027 and 0.697 respectively, meaning they are not significantly different from the proportion of Blazhko objects in the SuperWASP population, despite the Jurcsik et al. (2014) population consisting of RRc type objects.

This low occurence rate may be a consequence of our strict acceptance criteria for recognising a Blazhko candidate, in that we require either a match between a low frequency peak and a sideband peak, or a match between two sideband peaks, in the power spectrum. This matching of sidepeaks relies on detecting an overlap within the widths of each side peak, which can be reduced if peaks are narrow. However, the more obvious problem with detecting symmetrical peaks was as shown in Fig. 4.1, where the complex nature

of the combination of AM and FM can result in one side peak being completely removed. For example, the spectrum shown in Fig. 4.10 for object 1SWASPJ124945.38+434625.2 (Z CVn), shows a large single sideband at 1.71948×10^{-5} Hz giving a modulation frequency of 5.04105×10^{-7} Hz and therefore a modulation period of 22.96 d, which is extremely close to the figure given in Skarka (2013) of 22.98 d for Z CVn. However, this peak has no symmetrical sideband on the other side of the main pulsation frequency, nor a matching low frequency peak, and so has not been recorded as a candidate Blazhko period.

It may also be that we are missing objects whose Blazhko signal is very weak and therefore below our noise levels. The Blazhko signal is derived from the change in average pulsation brightness over the Blazhko cycle if the upper envelope function of the pulsation maxima, varies more than the lower envelope function from the pulsation minima, which is not always the case, see Fig. 1.25 in Chapter 1 for example.

A third cause for the lower detection rate could be the use of the randomised flux as the basis of the signal to noise threshold. In the first of two cases in Sect. 4.4, the power spectrum of the randomised flux remains too high in the low frequency regime as the power of the actual flux is CLEANed out of the window function. In the second case, the power of the actual flux signal is not removed enough from the window function, and thereby remains too strong compared to the randomised flux. This latter problem resulted in a list of 16 objects which were excluded due to an excessive number of peaks above the threshold set by the randomised flux power spectrum. It is unclear if this is due to the amount of noise in the objects' light curves, or a symptom of the clean program being unable to completely remove power from the window function for the actual flux signal, or the opposite issue of too much power being removed from the randomised flux power spectrum. However, the low threshold results in candidate Blazhko periods being dismissed, rather than false positives being included, as the noisy objects can be detected due to their excessive number of peaks and excluded. Using the randomised flux, rather than taking a baseline level from the actual flux, only removes the window function from a non–varying light curve as there is no signal to be removed, making the Blazhko peak–defining threshold more robust to over–CLEANing. The low occurrence rate may be the price to pay for this robustness.

Interestingly, only 2 objects from Skarka's list of known Blazhko effect stars that were not detected as Blazhko in this work have periods of less than 10 d. This suggests that the

10 d limit is not unreasonable, and does not account for the lower occurrence rate detected in comparison to Skarka (2014a).

Despite matching low frequency peaks to sidebands, some systematic aliases appear to remain at 14 and 29 days judging by the slight increase in the number of Blazhko candidates in these two regions. These are most likely the result of noise occurring in the SuperWASP light curves on the lunar cycle, and as such any candidate Blazhko periods around these values should be treated with caution.

Benkő and Szabó (2014) suggested a link between the period and amplitude of the Blazhko effect but Fig. 4.25 shows that this cannot be confirmed in this study. Also, the Blazhko period does not appear to have any correlation with the RRab pulsation amplitude (Fig. 4.27).

As discussed in the previous chapter about the Blazhko effect in the time domain, the lack of bimodality in the distribution of the relative scatter parameter for all SuperWASP objects made it difficult to produce a threshold value for identifying the Blazhko effect in the time domain without excluding a large number of potential candidates. Now that the Blazhko population has been defined in the frequency domain, this overlap between Blazhko and non–Blazhko populations is even more apparent in Fig. 4.16.

The increase in the spread of relative scatter with light curve amplitude for both non-Blazhko (Fig. 4.18) and Blazhko objects (Fig. 4.19) implies that high relative scatter could be a feature of large RRab pulsations rather than a symptom of the Blazhko effect. The similarity between plots of relative scatter against Blazhko amplitude and relative scatter against light curve amplitude (Figs. 4.17 and 4.19) could merely be due to the strong correlation between Blazhko amplitudes and pulsation amplitudes in power spectra.

Since the Fourier analysis of the SuperWASP RRab catalogue has shown that the main pulsation peak and the first few harmonics can be easily recovered, the RRab classification stage could be improved by using the ratio of power and phase of the pulsation harmonics. The pulsation shape of RRab is due to the combination of pulsation harmonics of certain amplitudes and phases. If these properties can be identified automatically in large numbers their amplitude and phase ratios can be used to quickly distinguish RRab objects from RRc, rather than using several visual inspection stages. This more systematic approach could then be extended to similar types of variable objects that may have been misclassified, such as δ

Scuti and BL Her (AHB1) types.

4.6 Conclusions

A total of 983 candidate Blazhko effect stars were identified from the SuperWASP sample of 4963 RR Lyrae. 894 of these Blazhko candidates were previously undetected in the SuperWASP archive, and 89 were previously known Blazhko effect stars listed by Skarka. No relation was found between the pulsation period and the Blazhko period, or between the pulsation period and the Blazhko amplitude in this large number of Blazhko candidates. It can be concluded, at the level of precision afforded by SuperWASP and in the visible waveband photometry, that there are no connections between RRab pulsation parameters and characteristic Blazhko parameters. The physical causes of the Blazhko effect therefore may therefore rely on some stellar mechanics that are too subtle to be detected in ground–based photometry. Alternatively, considering the proportion of RRab stars exhibiting the Blazhko effect, perhaps the modulation process is so stochastic that the final modulation properties bear little relation to the initial stellar pulsation mechanism.

The overlap in the levels of scatter at the peak of the pulsation between Blazhko and non–Blazhko populations has been confirmed with this larger set of Blazhko candidates. This unfortunately means that a threshold level of scatter for identifying the Blazhko effect cannot be defined.

It is possible to further investigate the FM aspect of the Blazhko effect by isolating the modulation in phase space using O-C techniques. This phase domain work is the subject of the next Chapter.

Chapter 5

SuperWASP RR Lyrae stars in the phase domain

5.1 Introduction

The previous chapters have described the SuperWASP RR Lyrae catalogue of nearly five thousand objects, and the SuperWASP Blazhko catalogue of over nine hundred objects. This chapter looks at how we can use measurements of phase modulation (PM) to identify not just more Blazhko objects, but to also calculate the Blazhko period. PM can also be used to determine if the pulsator is part of a rare class of binary system, even if the companion object is undetected. Due to their age, the companion object in binary systems containing RR Lyrae objects are expected to be faint un–evolved red dwarfs, or even white dwarf objects that have somehow lost their outer layers without disturbing the RR Lyrae component.

The O–C technique consists of fitting a template to each night of observation, then measuring the difference in time between the best fitting position of the template and the expected, or calculated, position of the pulsation on that night. This difference is commonly referred to as the residual. Once the residuals have all been calculated for an object, the O–C diagram can be plotted. Trends in the residuals can then be detected by fitting them with linear, quadratic (parabolic) or sinusoidal models. In some cases more than one trend can be present, for instance a sinusoidal trend can be seen in combination with a longer period parabolic trend (see Fig. 2 of Hajdu et al. (2015) for several examples).

This chapter continues with the following sections: firstly, Sect. 5.2 explains the pro-

cesses involved in creating the O–C diagrams; then the phase dispersion minimisation (PDM) process used to find Blazhko candidates is described in Sect. 5.3; Sect. 5.3.2 shows the results of this PDM process; Sect. 5.4 describes the fitting of models to the unfolded O–C diagrams in order to find any symptoms of binarity; Sect. 5.4.1 shows the results from the hunt for binary systems containing a pulsator; this is followed by Discussion and Conclusions.

Preliminary results from this chapter, including phase–folded O–C diagrams and some model fitting of unfolded O–C diagrams, are to be published as conference proceedings in the Proceedings of the Polish Astronomical Society, edited by Radek Smolec, Karen Kinemuchi and Richard Anderson.

5.2 Creating the O–C diagrams

All light curves used in this O–C investigation are from the RRab objects listed in the SuperWASP RRab catalogue created in earlier chapters, so they have all undergone the same iterative outlier removal process described in Sect. 3.2.1. The first stage of the O–C technique was to create a template by phase folding the light curve by the known pulsation period, dividing the phase–folded light curve into 50 bins and then using the medians of those bins to create an average phase–folded light curve. This average light-curve was then duplicated twice more in order to create a template that spans 3 concatenated pulsation cycles. This extra length was to allow for more than a full pulsation period being observed in one night, and for a large change in period which would result in observations extending beyond either the start or end of a single period template. The algorithm then divided the light curve into individual nights. This was accomplished by subtracting the SuperWASP HJD offset from each TMID, dividing it by 24 hours and then comparing the integer part of the result with a list of each unique night of observations. Only nights with at least 50 observations, or that spanned a third of a pulsation, were fitted with the template in order that the template was fitted to enough of the light curve to result in meaningful O–C values.

The template fitting involved an iterative process of finding the best fit across a range of time offsets and decreasing the step size while retaining the same number of steps until there was negligible improvement in the quality of the fit. The O–C residual value for each night equates to the total offset from the initial template position.

The template was shifted horizontally through the observations for each night, initially covering a range of 1 cycle in 9 steps. The template was first moved to the calculated TMID position minus a third of the period (close enough to the expected value not to give a false minimum χ^2 value later). If the TMID of the last observation of the night was greater than the TMID of the last point in the template the template was shifted horizontally by 1 full period, and this additional offset was recorded so it could be added to the residual value.

During each step, a series of 9 vertical shifts was also applied to the template. During each step the quality of the fit of the template to the observations was recorded using a reduced χ^2 value based on the equation below:

$$\chi^2 = \sum \left(\frac{F_i - F_t}{\sigma_i} \right)^2 /N - 1 \tag{5.1}$$

where F_i is the detrended flux measurement at a specific SuperWASP TMID (time) value, F_t is the flux level of the template interpolated at the same TMID value, σ_i is the uncertainty of the flux measurement, and N is the number of points in that night.

The combination of horizontal and vertical shifting created a 2–dimensional array, or grid, of χ^2 values. The amount of each horizontal and vertical shift from the initial template position was also recorded and stored in a separate 2–dimensional array.

If the lowest χ^2 value was at the edge or corner of the χ^2 grid then the centre of the fitting grid was moved to this position and the template was fitted again, but without shrinking the step size. This was allowed to happen a total of 3 times before the night was discarded as being unable to be fitted by the average light curve template.

Once the 9 by 9 grid of fitting had been completed, the minimum χ^2 value was compared to that of the previous iteration. If the fractional change in min χ^2 was below 0.1 then the fitting process for that night was ended, and the uncertainty of the fit was calculated. If the fractional difference was above 0.1, then the horizontal offset with the lowest χ^2 was identified and the value of the offset one step before this minimum became the starting position of the next iteration. This next iteration of the fitting grid ranged from the offset before the best fit from the previous iteration to the offset after the best fit. In other words, the subsequent grid was the width of two of the previous grid's steps. This also guaranteed that the position with the best fit was crossed in the next iteration. The number of steps remained constant be-

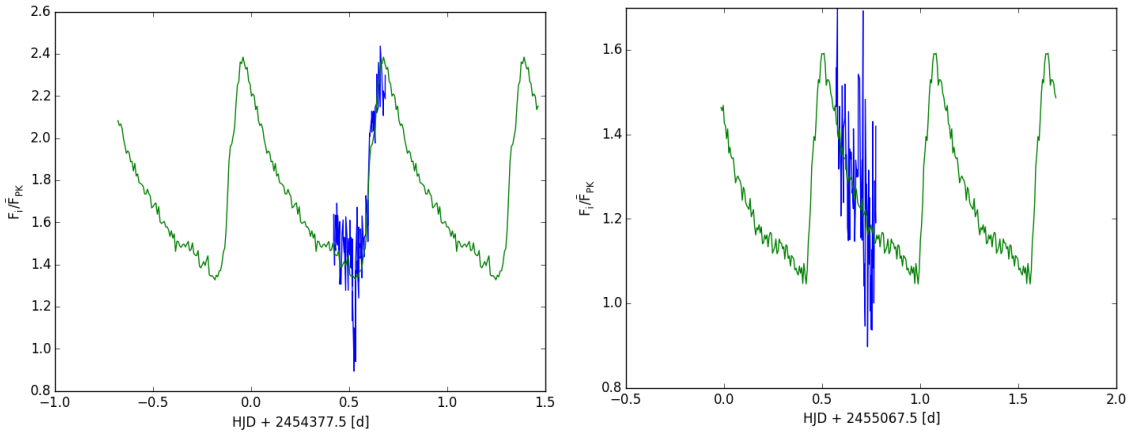

Figure 5.1: Final template positions for individual nights of observation for objects 1SWASPJ000152.61+473311.6 and 1SWASPJ003127.65+022610.2. The vertical axis shows flux levels in counts per second. The horizontal axis is the TMID field, the time in seconds from the initial date of 1/1/2004. Observation points are joined by blue lines, the light curve template is in green, and the part of the template interpolated for the times of the actual observations are shown in red.

tween iterations, thereby decreasing the horizontal step size between each iteration increased the O–C resolution with each iteration. Examples of the final template positions are shown in Fig. 5.1 for objects 1SWASPJ000152.61+473311.6 and 1SWASPJ003127.65+022610.2.

The uncertainty in the fit for each night was calculated by fitting a Gaussian curve to these minimum χ^2 values, taken during the final iteration for that night. The χ^2 values of all the vertical steps for each horizontal offset were compared and the minimum χ^2 value of each horizontal offset was recorded as a set of χ^2 values. This set of fit values was used, rather than simply taking the row from the grid containing the minimum χ^2 value, after tests showed that the best fits for a night could lie along a diagonal line in the grid, for instance if the segment of the light curve in a particular night fell along the descending part of the template. Using the minimum χ^2 from all vertical shifts produced a more shallow Gaussian curve, and therefore a larger uncertainty, than simply using the row containing the minimum χ^2 value. If the Gaussian fitting failed due to less than half of the curve being obtained, then the night was discarded as the uncertainty could not be calculated. The centroid of the Gaussian became the final part of the total offset for that night.

The residual value for each night was calculated by subtracting the initial offset of a third of a period from the accumulated offset values from the previous fitting iterations, and adding the Gaussian centroid from the final iteration. This resulted in a O–C value and its uncertainty for each night fitted.

5.3 Using PM and PDM to find the Blazhko effect

Since the PM aspect of the Blazhko effect is periodic and results in sinusoidal variations in the phase of the star's pulsations, identification of Blazhko effect objects can be made by phase–folding the O–C diagram to find the Blazhko period and then fitting the resulting diagram with a sinusoidal model to confirm if the folded residuals show the Blazhko effect (rather than a systematic variation, for example).

5.3.1 Phase–folding the O–C residuals

Before the linear, quadratic and sinusoidal models could be fitted to the O–C residuals the residuals underwent two outlier removal stages. Firstly, residuals were trimmed twice using a 3σ limit on their uncertainties. Secondly, points with outlying O–C values were clipped. However, removing outliers based on the mean residual value could lead to valid residuals at the extremities of a quadratic trend being removed. Therefore, an iterative process was devised where the residuals were fitted by both a linear and quadratic fit before outliers were removed beyond 3σ of the better of the two fits. This limit was based on tests using 3 and 4 σ clipping where visual inspection of O–C diagrams highlighting the removed outliers showed that outliers were best removed by combining a closer 3σ clip with preliminary linear and quadratic fits to the residuals. It was assumed that a sinusoidal fit would not be required at this stage as it would not vary enough from the quadratic fit at 3σ. This process of fitting then clipping was repeated until no further residuals were removed.

Each object's O–C residuals were folded using a PDM / Epoch folding routine, similar to the one used to fold the light curves by their pulsation period in order to find the period of the PM and therefore the Blazhko effect. Tests with known Blazhko objects using 20, 50 and 75 bins showed that 75 bins produced periods closest to the known Blazhko period. The minimum number of points required to perform the PDM folding was set at 50 as this tested well with the use of 75 bins. Unlike the light curve folding algorithm however, the O–C folding routine used the same logic as the template fitting stage: the range of trial periods was reduced until the fractional difference between the current and previous χ^2 measured across all bins was below 0.01. The uncertainty in the PDM period was the standard deviation of a Gaussian fit to the χ^2 values across the last set of trial periods, again, similar to when the

light curve templates were fitted to each night's observations.

Once the O–C diagram was folded to find a candidate Blazhko period it was fitted with linear, quadratic and sinusoidal models. The same curve fitting algorithm was used to create the linear, quadratic and sinusoidal models to the residuals. This algorithm used a Levenberg–Marquardt algorithm during the least squared calculations. The linear, quadratic and sinusoidal models were given the initial period of 1.0 to represent the full phase of the cycle found by the PDM routine (if a periodic phase modulation was found). The constant offset was set to the mean of the light curve, and any other initial parameters were set to zero, except for the sine model's amplitude which was initially set to the standard deviation of the residuals from the mean. The goodness of fit χ^2 value was calculated for each of the three models. Throughout the remainder of this chapter the term sine χ^2 refers to the goodness of fit of the sinusoidal model to the phase–folded O–C diagram. The terms linear χ^2 and quadratic χ^2 likewise refer to the goodness of fit of the linear and quadratic models to the phase–folded O–C diagrams, respectively.

The PDM period, uncertainty and goodness of fit were recorded, along with the sine fit's amplitude and the final number of residuals left after the clipping stages described earlier. If the χ^2 values from any of the fits were below 1.0, due to over–estimation of residual uncertainties, all the uncertainties were multiplied by the lowest χ^2 value in order to scale the minimum χ^2 to 1.0. The χ^2 values of all three fits were re–calculated before being recorded.

A visual inspection was made of the PDM folded O–C diagrams for all the objects in the SuperWASP RRab catalogue. This was done in order to check the quality of the PDM folds as the sine fitting function tended to over–fit the data, especially if there were few residuals left after the clipping stage. Objects were considered to be Blazhko candidates even if their sinusoidal shapes contained a lot of scatter at the maximum or minimum e.g. object 1SWASPJ161657.40+160954.8 (Fig. 5.2), indicating a change in the amplitude of the PM over several Blazhko cycles due to the multi-periodic nature of the Blazhko effect.

Based on the number of folds with multiple peaks compared to the number of folds showing half of the true Blazhko period, the PDM program period seems to favour shorter periods. Alternatively, the initial search range set for all objects may not wide enough, leading to detection of the wrong local minimum (at an integer multiple of the true period).

A total of 52 objects (1.06%) had multiple peaks in the PDM–folded O–C diagram.

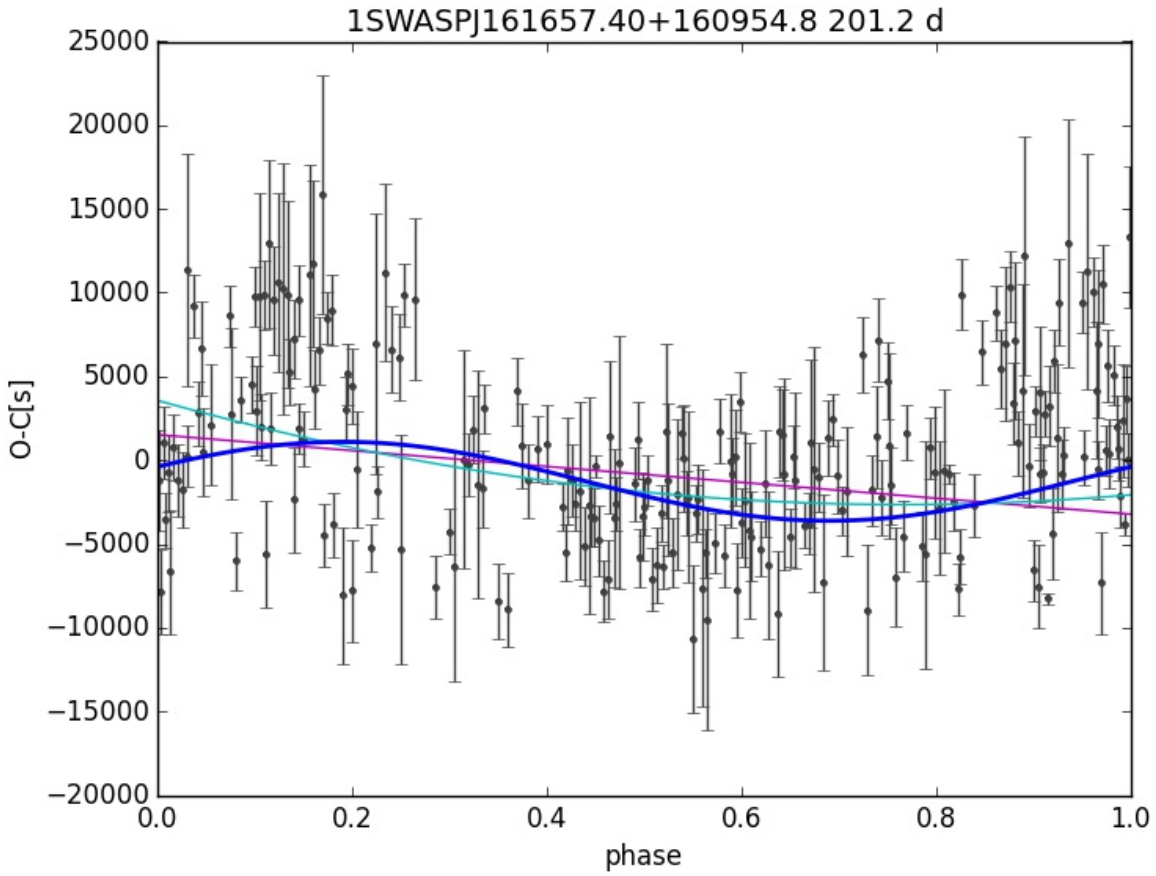

Figure 5.2: O–C diagram of Blazhko candidate object 1SWASPJ161657.40+160954.8. The sinusoidal model shown in blue is a poor fit due to the level of noise in the residuals which may be due to a multiperiodic Blazhko effect producing a poorer PDM solution than other Blazhko candidates.

In these cases the PDM folding was performed again but at a smaller initial trial period, calculated by dividing the original 200 d trial period by the number of peaks noted during the visual inspection stage. These objects were only listed as Blazhko candidates if this second fold resulted in a sinusoidal phase–folded O–C curve. Objects 1SWASPJ020142.78-035830.6, 1SWASPJ121206.15-261248.0, and 1SWASPJ221003.82-423834.2 showed clear signs of variation in their O–C residuals but required a narrower range of trial periods. As shown in Fig. 5.3 for object 1SWASPJ020142.78-035830.6, this was achieved within the PDM routine by manually setting the initial trial period to that found by the original PDM solution divided by the number of apparent peaks, and setting the range of trial periods to only 10 d,

Examples of O–C residuals folded by their candidate Blazhko periods are shown in Fig. 5.4 which include the sinusoidal models fitted to the phase–folded residuals. Each model provides the amplitude of the PM, but the recorded candidate PM / Blazhko periods are the

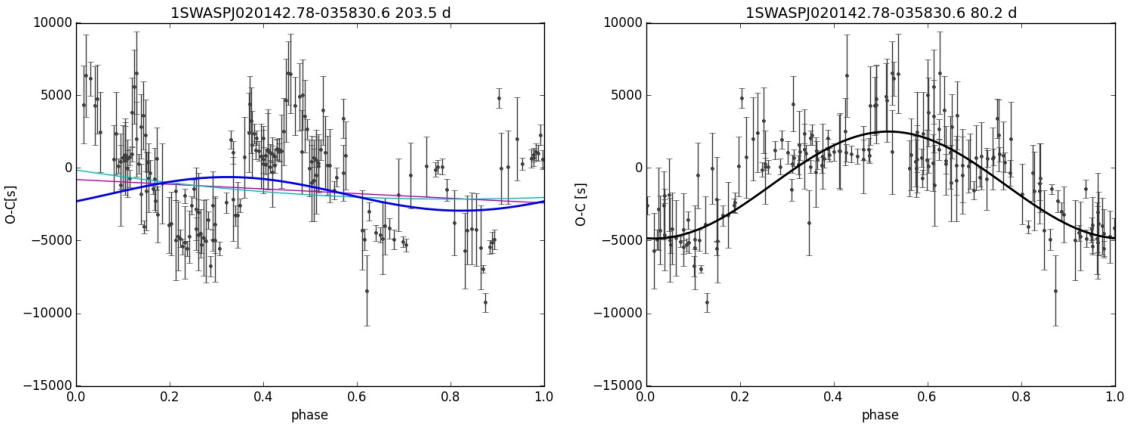

Figure 5.3: Example folded O–C diagrams for object 1SWASPJ020142.78-035830.6. The left panel shows the initial period found by the PDM program with multiple peaks. The right panel shows the same O–C diagram folded at the best fit 80.2 d period.

those derived directly by the PDM routine.

5.3.2 Results of phase–folding O–C diagrams

The focus of the phase-folding of O–C residuals was to identify candidate Blazhko effect candidates by the cyclic nature of their phase modulations. The changes in phase due to PM are expected to be roughly sinusoidal, and should therefore be identified by a reasonably good fit to a sinusoidal model. Out of the original 4963 RRab catalogue objects, O–C results were available for 4891 after the template fitting stage. 1557 objects could not have a sine wave fitted to their PDM curves by the fitting program due to fewer than 50 residuals being left after the clipping stage, and so were excluded from the analysis stage. Out of the remaining 3334 objects, 429 objects had a sine $\chi^2 < 1.0$ where the sine χ^2 was the lowest value out of the linear, quadratic and sinusoidal fits, so their residual uncertainties were rescaled in order to increase their sine χ^2 to unity.

The largest sine χ^2 values appear to be due to bad PDM folds for objects whose residuals have very low uncertainties. The combined PDM and epoch folding stage does not use the residual uncertainty, rather it uses the scatter within each bin.

A visual inspection was carried out on all 4891 folded O–C diagrams in order to identify sinusoidal trends in residuals. O–C diagrams were selected as being Blazhko candidates during this visual inspection stage if they showed a clear curve to their residuals. There could be differing levels of noise across different phases of the diagram as long as it did not obscure the shape of the curve. Discontinuous curves were not accepted. 140 visual Blazhko

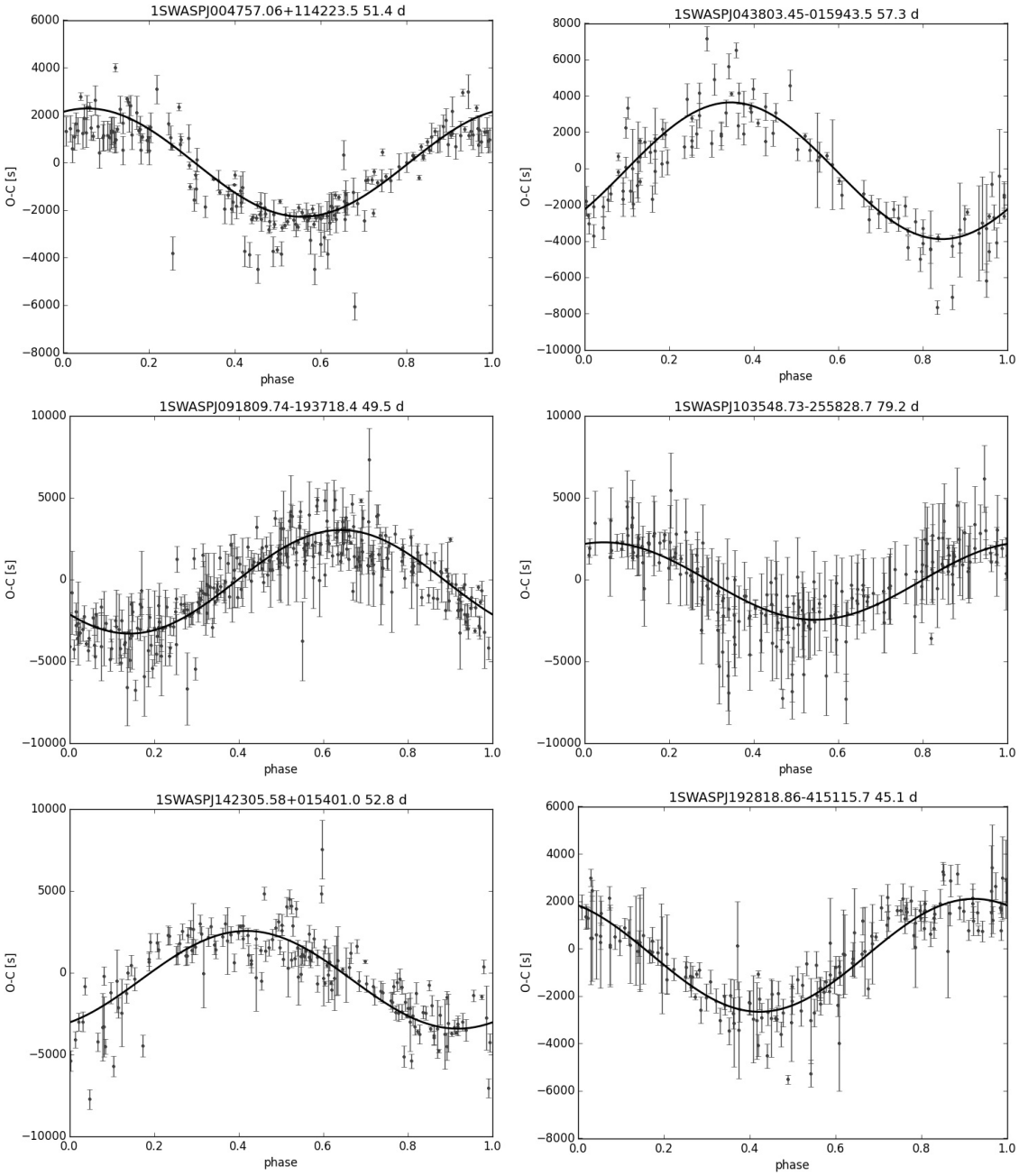

Figure 5.4: Examples of O–C diagrams folded by their candidate Blazhko periods. The vertical axis is in seconds and the residuals have been fitted with a sinusoidal model. The candidate Blazhko periods for each objects are shown in the plot title after the SuperWASP identifier.

objects were found (2.8% of the 4963 RRab catalogue objects) and are listed in Table 5.1, where SWASP id is the unique SuperWASP identifier; P_{PDM} is the candidate Blazhko period found through PDM of their O–C diagrams; $\sin\chi^2$ is the goodness of fit measurement for the sinusoidal model; A_{sin} and ϕ_{sin} are the amplitude in days and phase of this model; P_{BL} is the Blazhko period found from the Fourier analysis in the previous chapter; Skarka name and P_{Skarka} are the object name and known Blazhko period in days from the Skarka database, if available. 87 (62%) of these 140 stars were identified as Blazhko candidates from the Fourier analysis process in preceding chapters. 22 of the 140 visually identified Blazhko objects have known Blazhko periods in the Skarka database of Blazhko objects, representing a completion of 15.7%. This rate of coincidence with the Skarka database is higher than the 10% of 983 SuperWASP Blazhko candidates identified using Fourier analysis. These values are represented in Fig. 5.5, along with the number of PM objects in the same GCVS RRab dataset used in Chapter 4. Of the 22 objects in both the SuperWASP PM candidates and Skarka database, 13 are also in the SuperWASP Fourier analysis candidates found in Chapter 4. This means a total of 44 of the 140 PM objects were previously unknown within either the Skarka dataset or from the Fourier analysis stage of this work.

The 140 candidate Blazhko objects found using O–C diagrams were also compared to the Blazhko RRab objects from the CRTS list. However, no overlap was found between the 140 PM Blazhko candidates in SuperWASP and the 104 CRTS Blazhko objects also in SuperWASP.

Table 5.1: Blazhko candidate objects from O–C PDM

SWASP id	N	P_{PDM} [d]	sin χ^2	A_{sin} [d]	P_{BL} [d]	Skarka name	P_{Skarka} [d]
1SWASPJ000409.77-410810.8	210	201.4±0.6	7.905	0.027±0.001	201.6±0.8		
1SWASPJ004757.06+114223.5	191	51.39±0.02	10.098	0.0264±0.0008	50.9±0.1	FR Psc	51.31
1SWASPJ010510.70+341306.2	126	57.64±0.01	14.772	0.033±0.002	57.9±0.0	DR And	57.11
1SWASPJ013301.91+384149.1	132	171.9±0.6	4.050	0.026±0.002	168.3±0.1		
1SWASPJ013813.28-065711.2	57	103±75.2	1.038	0.005±0.003	62.3±1.5		
1SWASPJ020142.78-035830.6	174	80.2±0.3	4.815	0.043±0.002	78.7±0.2		
1SWASPJ021952.30+091648.0	108	224.5±0.1	5.173	0.018±0.001			
1SWASPJ022809.84+032753.0	111	135.7±0.8	3.303	0.007±0.002	65.1±0.3		
1SWASPJ025118.39-200325.2	151	68.6±1.7	4.357	0.015±0.001	57.5±0.1		
1SWASPJ031533.86-442816.0	88	197.7±0.7	1.911	0.022±0.003			
1SWASPJ032208.41-335205.8	89	217.47±0.03	15.078	0.031±0.007			
1SWASPJ032241.57-362006.0	110	162.68±0.05	12.243	0.029±0.003			
1SWASPJ033641.85+052141.4	170	123.7±0.6	16.495	0.015±0.001		SS Tau	123.3
1SWASPJ035047.50+202808.2	104	201.51±0.04	5.476	0.021±0.002			
1SWASPJ035345.24-113719.9	166	174.79±0.03	1.000	0.017±0.002			
1SWASPJ035537.55-380703.0	83	190.53±0.02	5.372	0.036±0.002	130.2±0.8		
1SWASPJ040010.75-194936.9	140	168.9±0.8	26.553	0.029±0.003	78.4±0.1;127.0±0.3	LR Eri	123.5
1SWASPJ043803.45-015943.5	111	57.3±0.3	6.882	0.044±0.001	57.7±0.1	BE Eri	57.38
1SWASPJ050748.61-192752.0	128	107.2±0.3	2.006	0.0219±0.0008	108.1±0.3		
1SWASPJ052502.17-182717.6	106	61±0.2	2.214	0.021±0.005			
1SWASPJ052525.42-430228.6	184	157.1±0.5	2.175	0.012±0.001			
1SWASPJ055045.51-273959.3	99	195.8±0.6	3.185	0.026±0.002			
1SWASPJ055931.22-295921.2	177	154.83±0.04	5.363	0.023±0.002	147.9±1.0		
1SWASPJ062342.92-303953.7	119	197.65±0.03	13.829	0.037±0.004	253.8±2.2		
1SWASPJ062605.61+333547.2	116	159.9±0.8	1.215	0.015±0.001	299.5±1.1;166.9±0.5		
1SWASPJ080432.32+443714.3	135	65.1±0.4	3.675	0.02±0.001			
1SWASPJ083257.03+025902.8	181	66.91±0.06	10.450	0.018±0.002	35.6±0.0;66.1±0.2	V487 Hya	64.4
1SWASPJ083729.57-004635.8	103	154.72±0.02	1.239	0.015±0.001	294.6±12.7		
1SWASPJ091607.01-140458.6	124	155.722±0.005	1.000	0.021±0.002	97.1±0.3		

Table 5.1 (cont.)

SWASP id	N	P_{PDM} [d]	$\sin \chi^2$	A_{sin} [d]	P_{BL} [d]	Skarka name	P_{Skarka} [d]
1SWASPJ091809.74-193718.4	296	49.52±0.02	6.991	0.037±0.001	372.2±1.1;50.2±0.1		
1SWASPJ093023.90-124916.4	218	150.115±0.002	5.231	0.015±0.001	127.4±0.2		
1SWASPJ093215.26-251158.7	179	121.78±0.07	8.494	0.032±0.002	93.3±0.3		
1SWASPJ093657.67-133711.9	152	63.919±0.002	3.414	0.029±0.002	64.8±0.1		
1SWASPJ093731.34-181612.9	276	87.42±0.34	12.542	0.043±0.002	88.3±0.2	ASAS093731-1816.2	87.73
1SWASPJ094842.65-032959.2	152	53.05±0.02	4.891	0.023±0.001			
1SWASPJ095515.90+034532.3	150	158.3±0.9	31.137	0.03±0.003	304.7±2.2		
1SWASPJ100136.78-411225.3	97	139.9±0.6	6.617	0.015±0.002	104.8±0.6		
1SWASPJ103548.73-255828.7	202	79.21±0.04	2.316	0.027±0.001	79.8±0.2		
1SWASPJ110520.26-385646.5	252	153.17±0.51	8.206	0.041±0.003	264.0±0.8		
1SWASPJ112715.51-251020.0	215	121.375±0.006	22.981	0.041±0.005			
1SWASPJ112718.10-231046.9	187	157.2±0.6	12.514	0.015±0.003	295.8±1.0		
1SWASPJ113912.96-435708.0	234	197.5±0.7	4.049	0.021±0.002	92.4±0.1;118.7±0.2		
1SWASPJ115304.54-391354.6	121	180.45±0.05	5.410	0.046±0.002			
1SWASPJ115953.34-282929.3	159	144.1±0.6	1.000	0.0029±0.0006			
1SWASPJ121206.15-261248.0	230	48.494±0.003	9.675	0.0301±0.0009	48.1±0.1	V552 Hya	48.53
1SWASPJ122135.92-270021.5	189	90.9±0.2	4.868	0.049±0.002	89.9±0.3		
1SWASPJ123030.50-260251.1	158	63.23±0.02	23.429	0.011±0.0005		SV Hya	63.29
1SWASPJ123757.17+295805.7	136	207.7±0.5	5.220	0.012±0.002	204.9±2.0		
1SWASPJ123810.96+385027.9	125	105.5±0.5	23.957	0.028±0.005			
1SWASPJ123811.99-442231.8	215	172.07±0.04	41.715	0.046±0.003	123.5±0.3	ASAS123812-4422.5	1307.7
1SWASPJ124139.81-014949.0	126	70.8±0.2	2.438	0.011±0.001	66.5±0.1		
1SWASPJ125345.04-433539.2	226	132.31±0.05	1.587	0.018±0.001	21.2±0.0;133.4±0.3		
1SWASPJ125433.12-304458.7	194	210.3±0.8	54.162	0.061±0.011	25.7±0.0		
1SWASPJ132340.37+071245.5	136	139.921±0.003	8.951	0.01±0.002			
1SWASPJ135339.14-440532.0	188	126.96±0.04	2.036	0.0079±0.0005	124.1±0.3		
1SWASPJ135811.20-421543.5	193	142.2±0.5	3.155	0.014±0.001	155.5±0.8;274.3±1.8;143.8±0.7	ASAS135813-4215.1	146.01
1SWASPJ140512.13-433713.0	199	63.2±0.3	1.713	0.025±0.001	62.8±0.1		
1SWASPJ141931.16-385129.1	243	168.2±0.5	12.007	0.009±0.002			

Table 5.1 (cont.)

SWASP id	N	P_{PDM} [d]	sin χ^2	A_{sin} [d]	P_{BL} [d]	Skarka name	P_{Skarka} [d]
1SWASPJ142305.58+015401.0	168	52.8±0.2	11.947	0.035±0.001	44.9±0.1;51.7±0.1	V551 Vir	48
1SWASPJ142706.37-182023.0	256	71.209±0.001	3.883	0.012±0.001	71.2±0.2		
1SWASPJ143025.38-360435.1	181	200.2±1.7	10.388	0.0232±0.0009	200.4±1.0		
1SWASPJ143051.06-351502.1	145	171.3±0.8	4.609	0.016±0.001			
1SWASPJ143333.21+314516.6	180	127.48±0.04	10.597	0.0063±0.0004		RS Boo	41.3; 62.5; 532
1SWASPJ143735.46-215929.4	259	164.98±0.05	2.305	0.016±0.001	243.2±1.2		
1SWASPJ143927.36-032736.7	124	152±11.3	16.268	0.014±0.002	92.4±0.4	V585 Vir	93.8
1SWASPJ144421.24+403907.5	147	190.4±0.5	3.937	0.01048±0.0006	40.1±0.0;354.7±0.2		
1SWASPJ145729.11-432450.8	132	88.04±0.09	2.590	0.02205±0.0009			
1SWASPJ145945.79-145816.9	221	46.59±0.03	2.985	0.048±0.001	45.5±0.1		
1SWASPJ145950.99-124501.4	149	79.9±0.5	1.322	0.025±0.001	79.3±0.1		
1SWASPJ150612.76+025457.2	211	175.8±0.7	133.213	0.017±0.003			
1SWASPJ150646.11+212616.8	152	201.49±0.03	6.309	0.012±0.001			
1SWASPJ150652.19+030621.3	90	130.1±0.03	8.479	0.05±0.005	131.8±0.4		
1SWASPJ150923.77-431937.1	138	42.897±0.0008	19.535	0.038±0.002	42.7±0.1	FU Lup	42.81
1SWASPJ151113.33+342615.7	116	190.2±0.04	3.426	0.0098±0.0009			
1SWASPJ151120.07+392037.0	116	59.877±0.003	5.941	0.026±0.002	49.4±0.0;257.0±1.6		
1SWASPJ151516.34-380734.6	159	156.01±0.05	5.089	0.018±0.002	273.3±1.9		
1SWASPJ152304.26-385153.6	209	99.86±0.04	7.480	0.05±0.003	99.5±0.3		
1SWASPJ152329.33+025026.1	152	41.8±0.3	1.909	0.019±0.001			
1SWASPJ152333.63-385714.2	117	171.1±4.2	1.618	0.025±0.003			
1SWASPJ153505.76-280842.0	160	100.9±0.1	4.699	0.025±0.002	102.2±0.3		
1SWASPJ153746.85-064303.8	192	119.9±0.5	8.138	0.0178±0.001	90.6±0.4;121.8±0.4		
1SWASPJ154224.08-081106.9	171	124.9±0.5	2.382	0.01±0.002			
1SWASPJ154250.87-285004.9	102	205.6±0.9	3.082	0.027±0.003	81.1±0.1		
1SWASPJ155224.92-071153.1	110	106.5±0.8	1.000	0.01942±0.0009	95.3±0.2		
1SWASPJ155428.14+152122.0	241	63.792±0.001	25.142	0.024±0.002	39.3±0.0;76.9±0.0		
1SWASPJ155637.93-185049.7	227	164.5±0.4	3.647	0.012±0.001	81.3±0.1		
1SWASPJ160045.89+262548.5	86	193.4±0.6	2.140	0.035±0.002			

Table 5.1 (cont.)

SWASP id	N	P_{PDM} [d]	$\sin \chi^2$	A_{sin} [d]	P_{BL} [d]	Skarka name	P_{Skarka} [d]
1SWASPJ161657.40+160954.8	226	201.2±0.1	6.715	0.027±0.006			
1SWASPJ162400.46-112101.6	71	91±114.7	1.924	0.014±0.003	41.2±0.0		
1SWASPJ162640.02+012001.2	252	72.3±0.2	1.306	0.0087±0.0005	319.8±2.2		
1SWASPJ163531.60+575023.1	136	82.9±0.2	160.613	0.005±0.002		RW Dra	41.42; 72.6
1SWASPJ163818.04+374804.8	368	45.92±0.01	45.239	0.028±0.002		GY Her	49.6
1SWASPJ165149.34+410744.9	260	209.4±1	8.826	0.025±0.002	70.7±0.1;68.8±0.2;390.8±5.4;58.5±0.1		
1SWASPJ170656.91+502054.2	258	160.51±0.03	3.074	0.012±0.002	50.9±0.1;110.0±0.3		
1SWASPJ172135.75+374319.4	497	264.5±0.1	24.553	0.039±0.002	115.0±0.4;143.5±0.3;235.4±1.1		
1SWASPJ174424.78+551029.8	164	191.16±0.04	1.024	0.01±0.001	14.8±0.0		
1SWASPJ175818.67+382054.8	90	190.7±0.8	1.000	0.02016±0.0008			
1SWASPJ175944.23+515301.7	194	141.22±0.04	1.791	0.0084±0.0006		AV Dra	96
1SWASPJ180217.68+275327.3	186	190.42±0.05	6.982	0.046±0.002			
1SWASPJ180638.75+195444.3	55	91±171	2.552	0.028±0.003			
1SWASPJ180820.56+335713.7	163	78.9±0.3	1.074	0.02±0.001	79.6±0.2		
1SWASPJ181254.44+333534.2	215	212.1±5.2	3.663	0.015±0.002	10.2±0.0		
1SWASPJ181437.46+423037.1	246	70±0.2	3.506	0.021±0.002	108.7±0.1;83.4±0.1;70.0±0.1;83.4±0.1		
1SWASPJ183905.41+422113.0	209	193.9±7	1.000	0.0109±0.0007			
1SWASPJ185922.79+454428.9	130	211.004±0.004	1.130	0.017±0.001			
1SWASPJ191719.71-431624.2	141	167.4±0.5	3.426	0.035±0.002	346.1±5.7;276.8±2.2		
1SWASPJ192818.86-415115.7	164	45.1±0.1	4.839	0.028±0.001			
1SWASPJ192919.64-331444.5	91	217.74±0.05	5.837	0.022±0.002	214.9±0.7;344.4±2.6		
1SWASPJ195005.68-682229.4	195	150.64±0.05	10.866	0.008±0.001			
1SWASPJ195348.19-335546.2	167	201.4±0.5	1.792	0.01347±0.0009	57.4±0.0		
1SWASPJ200227.86-370016.8	139	211.9±1.1	1.440	0.019±0.001	210.6±1.8		
1SWASPJ200832.32-602916.6	185	108.634±0.001	4.421	0.036±0.002	105.5±0.3	GV Pav	109.42
1SWASPJ200925.36-205824.3	151	133±0.04	4.391	0.005±0.003	81.8±0.1		
1SWASPJ201311.95-335639.3	138	160.1±0.1	3.612	0.019±0.003	290.9±3.5;200.5±1.6		
1SWASPJ202340.08-573343.5	115	142.8±0.5	1.000	0.018±0.001	156.6±1.0		
1SWASPJ202812.31-423607.4	377	183.4±0.1	6.205	0.0138±0.0008		V2281 Sgr	179.72

Table 5.1 (cont.)

SWASP id	N	P_{PDM} [d]	$\sin \chi^2$	A_{sin} [d]	P_{BL} [d]	Skarka name	P_{Skarka} [d]
1SWASPJ203041.85-235720.2	100	152.2±0.6	6.799	0.046±0.004		J203041.85-235720.2	...
1SWASPJ203047.35-600017.0	192	116.417±0.004	1.865	0.0141±0.0006	117.8±0.5		
1SWASPJ204545.61-183411.9	104	171.4±0.03	1.768	0.026±0.003			
1SWASPJ204723.03-145818.3	209	144.1±0.7	2.886	0.018±0.001			
1SWASPJ204802.04-222604.7	150	198.4±0.6	7.469	0.025±0.002	38.6±0.0		
1SWASPJ210006.62-403410.6	347	95.9±0.5	4.367	0.0131±0.0005	97.6±0.3		
1SWASPJ211527.38-090942.6	137	222.7±0.5	7.381	0.12±0.01			
1SWASPJ212749.95+133039.7	215	176±0.5	8.285	0.027±0.003	342.2±0.3;137.5±0.1		
1SWASPJ213653.21+015847.0	153	101.3±5.4	4.259	0.023±0.002	102.9±0.4		
1SWASPJ214913.01+043029.3	166	159.893±0.004	1.000	0.0103±0.0006			
1SWASPJ214943.41+031148.4	168	47.1±0.2	4.384	0.032±0.002			
1SWASPJ214947.24+210838.1	192	118.1±0.7	5.125	0.013±0.002		CY Peg	464
1SWASPJ220323.56+004946.7	178	83.9±0.6	3.399	0.024±0.001			
1SWASPJ220444.40-083142.7	190	152.584±0.035	8.322	0.018±0.002	263.4±2.5		
1SWASPJ220453.96-663456.7	242	206.4±0.5	24.904	0.021±0.002	45.7±0.1;138.4±0.5		
1SWASPJ220703.97-444926.6	220	94.9±0.3	2.713	0.025±0.002	96.8±0.1		
1SWASPJ221003.82-423834.2	235	51.918±0.003	3.880	0.037±0.001	52.9±0.1		
1SWASPJ221203.02-084545.6	137	78.2±0.6	2.788	0.016±0.001			
1SWASPJ222000.85-182240.2	106	210.4±0.6	1.000	0.02±0.002			
1SWASPJ222220.80-343007.9	155	162.899±0.005	4.564	0.02±0.002			
1SWASPJ222341.36+040614.4	177	168.4±0.1	9.930	0.019±0.002	159.3±0.5;283.9±2.4		
1SWASPJ222907.30+210340.2	90	193.2±0.5	1.452	0.03±0.004			
1SWASPJ222938.21+272422.9	127	172.62±0.05	12.682	0.069±0.006	365.3±1.6;81.1±0.2		
1SWASPJ223726.07-182217.8	177	199.8±0.6	2.548	0.014±0.001	124.4±0.4		

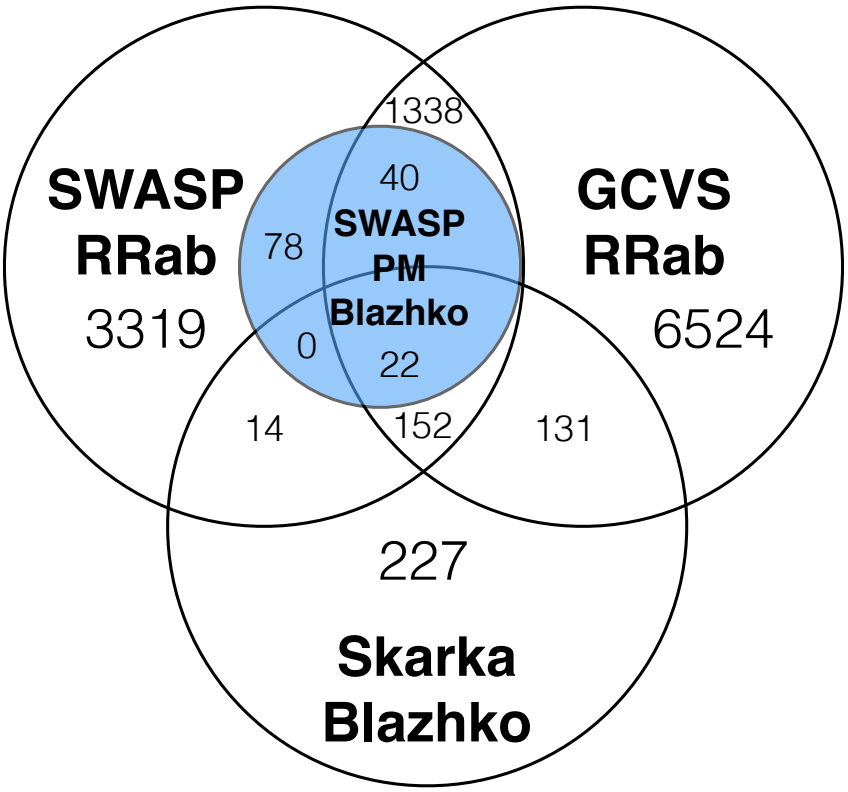

Figure 5.5: Venn diagram showing the number of PM Blazhko objects in relation to known Blazhko objects in Skarka's database, and known RRab objects in GCVS.

5.3.3 Analysis of PDM results

The analysis of the phase–folded O–C diagrams commences with checking the amplitude of the sine fits and the goodness of fits against the number of points, before comparing the goodness of fit for different sets of Blazhko objects. Then the modulation periods of the Blazhko candidates are compared.

The difference in sine fit amplitudes between Blazhko and non–Blazhko candidates is shown in Fig. 5.6. The lower amplitudes for the non–Blazhko objects implies that the folded residuals were not generally over–fitted by sine fitting routine, which would have resulted in very large amplitudes, and, instead, non–periodic O–C diagrams produced a lower amplitude, flatter sine fit. The visually selected objects have a mean amplitude of 0.024 d.

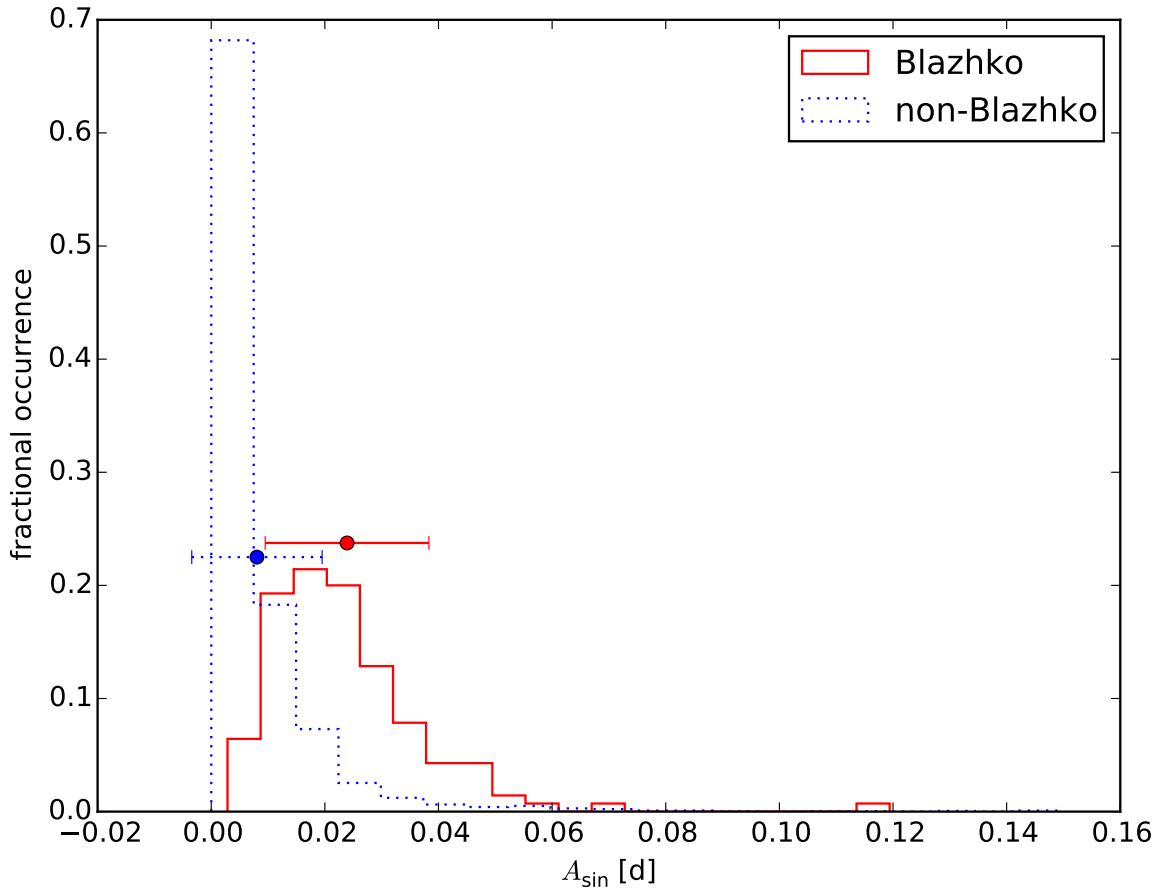

Figure 5.6: Comparison of sine fit amplitudes for PM and non–PM objects.

The goodness of fit of the sine wave to the residuals phase–folded by the candidate Blazhko period does not appear to be dependent on the number of residuals left after the clipping stage, as shown in Fig. 5.7.

One of the aims of the analysis of the fitting of models to phase–folded O–C residuals

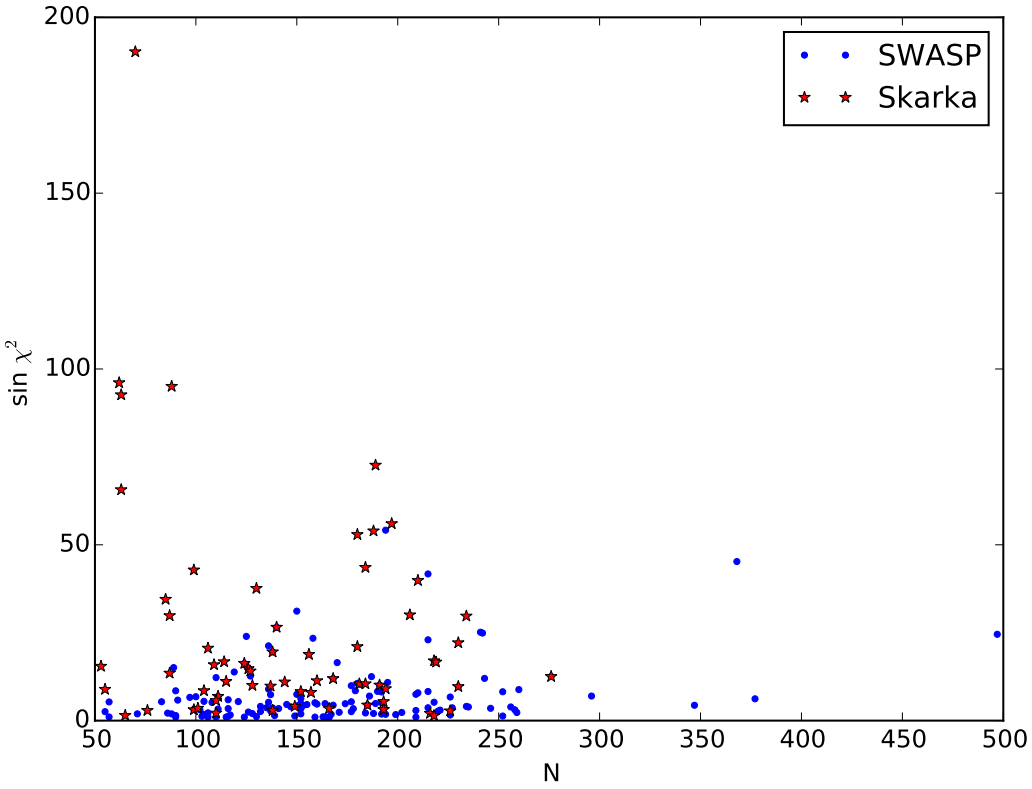

Figure 5.7: Relationship between sine χ^2 and the number of residuals after clipping. The goodness of fit of the sine wave to the phase–folded residuals does not appear to be correlated to the number of residuals.

was to investigate if the visual inspection stage could be automated by finding a threshold χ^2 value, below which Blazhko candidates could be automatically recognised after the phase–folding stage. The sine χ^2 values of the 140 visually identified Blazhko candidates were therefore compared to linear and quadratic fits, and to the remaining objects' χ^2 values. The mean and standard deviation of χ^2 values for the visually identified Blazhko candidates and the rejected objects are represented by the horizontal error bars in Fig. 5.8 which shows the distributions of χ^2 below 50 for these two populations. The average sine χ^2 value for the visually identified Blazhko candidates is 7.3, whereas the average linear and quadratic χ^2 values for these objects are 9.4 and 14.8, respectively. Those visual Blazhko objects that also have a SuperWASP Blazhko period (87 objects) have a similar sine χ^2 value of 7.6. The lower χ^2 value for the sinusoidal fit implies that those particular objects are indeed sinusoidal. However, the average sine χ^2 of the non–periodic objects is only 5.4, and the mean linear and quadratic χ^2 values for the non–Blazhko candidates are also lower at 6.0 and 5.4. The consistently lower χ^2 values for all three types of fit for the non–Blazhko candidates suggests

this is due to a combination of large uncertainties and how a badly folded curve will produce a constant, flat O–C curve with large scatter in each bin. This flat, noisy O–C diagram will be fitted best by a linear fit, as suggested by the large difference between the linear fit χ^2 values for sinusoidal and non–sinusoidal objects. The similarity in χ^2 values for all 3 fits for non–sinusoidal objects shows that all models are tending to resemble the flat linear model. The higher sinusoidal χ^2 average for actual sinusoidal phase–folded O–C curves is most likely due to how outliers can be far from the model which raises the χ^2 value.

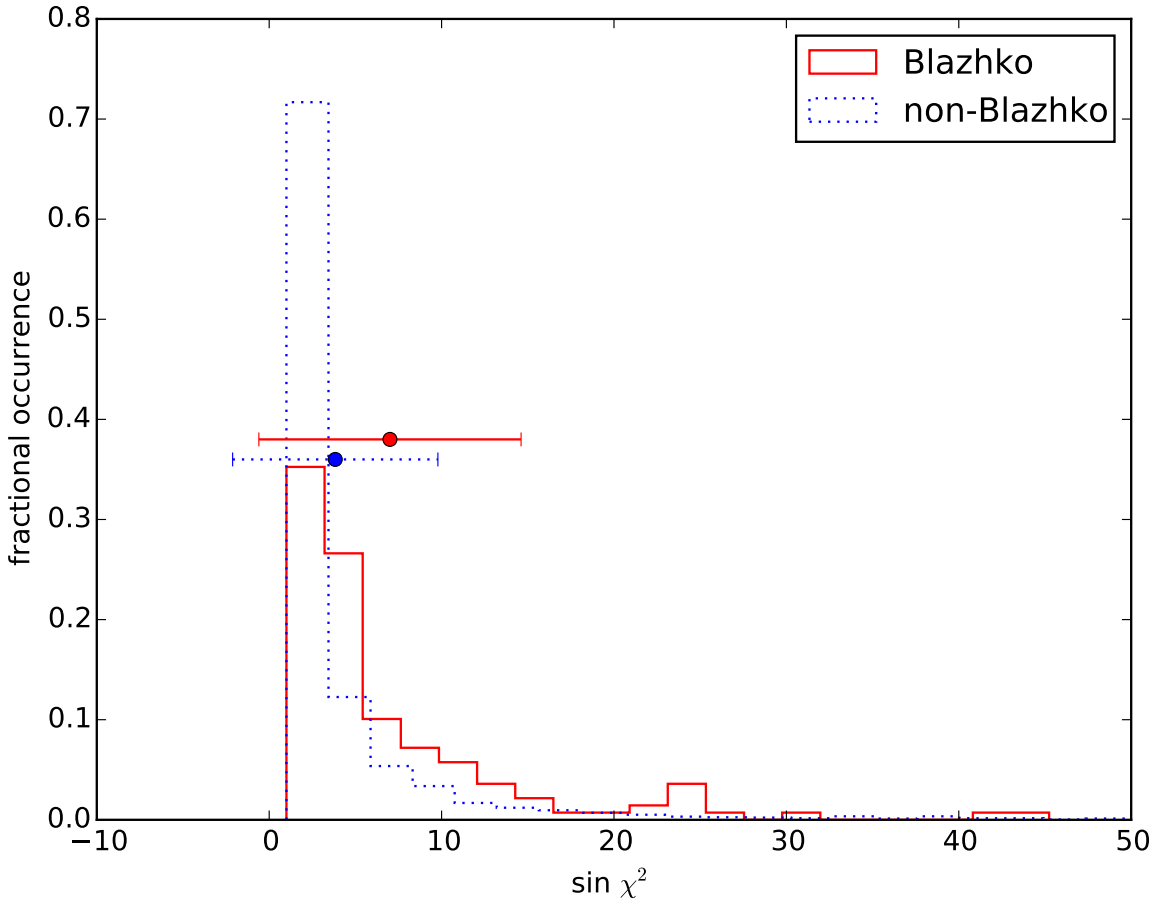

Figure 5.8: Comparison of sine χ^2 values for PDM folded O–C residuals visually identified as Blazhko candidates, against the remaining objects. Populations have been normalised for easier comparison and only objects with $\chi^2 < 50$ are shown.

Figure 5.9 compares the distributions of sine χ^2 values of PM Blazhko candidates and Blazhko objects from the Fourier analysis stage. Firstly, Fig. 5.9 shows that existing Blazhko candidates have relatively good quality fits of sinusoidal models to the data, so the fitting of sinusoidal models to phase–folded O–C diagrams appears to be valid. Secondly, the similarity between the Fourier candidates and the visually selected PM candidates implies that the visual inspection process is as robust as the Fourier process from the previous chapter.

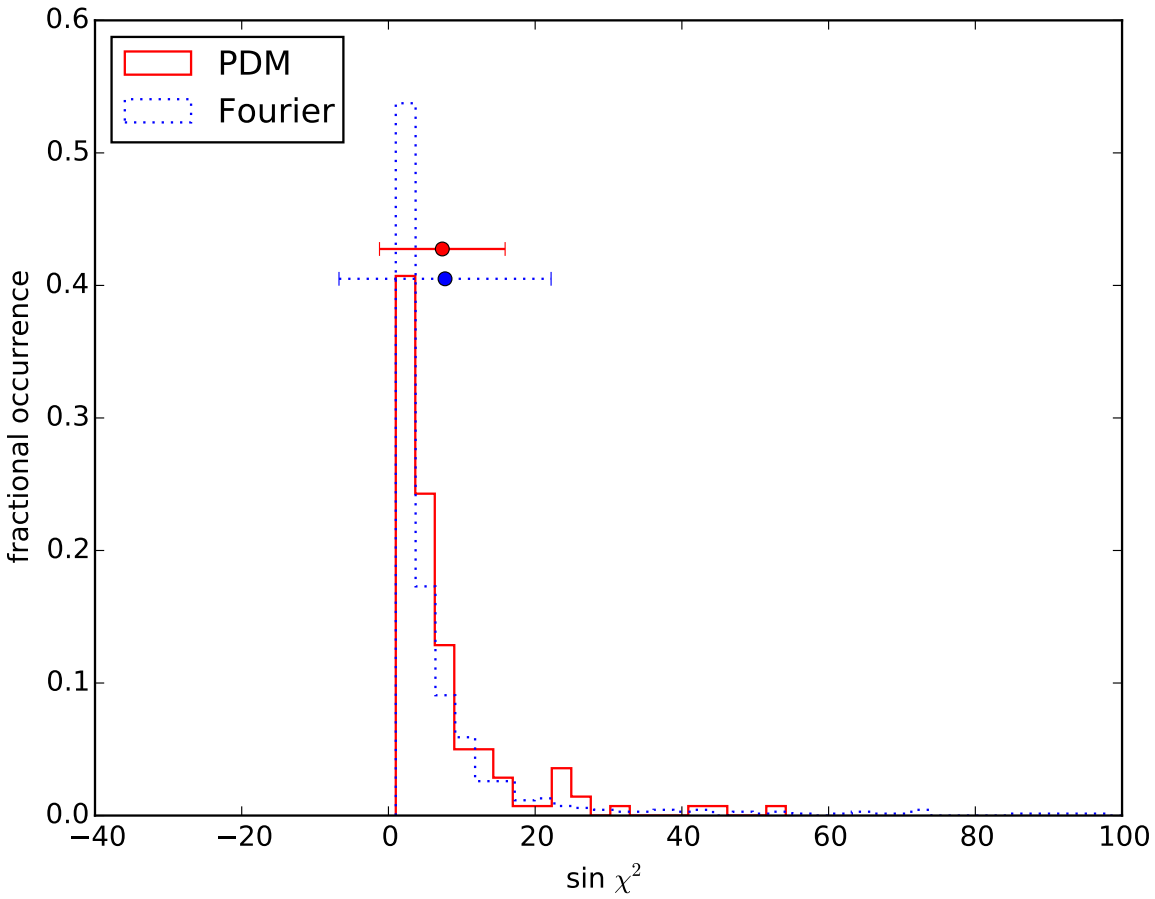

Figure 5.9: Comparison of the distributions of sine χ^2 values of candidate PM Blazhko objects against the sine χ^2 values of the Blazhko objects defined using Fourier analysis, showing the strong similarity in the ranges of their distributions.

The sine χ^2 values of non–Blazhko candidates was contrasted against known Blazhko objects from Skarka's online database as shown in Fig. 5.10, in order to find a lower threshold value below which an object is likely to be a Blazhko candidate. The large overlap in the standard deviations of these two distributions shows that no such threshold exists. Fig. 5.10 also shows that there would not have been any benefit in using the Skarka objects as a training dataset to select potential PM objects from the SuperWASP dataset based on χ^2 values, instead of relying on visual inspection.

As Fig. 5.8 showed, the range of sine χ^2 values for the visually selected PM candidates means that there is no clear delineation between them and the non–PM objects, therefore a selection threshold based on sine χ^2 value alone is not possible. However, in an analogy to the relative scatter parameter from the time domain light curve analysis, the sine χ^2 can be divided by the linear fit's χ^2 to produce a χ^2 ratio, as shown in Fig. 5.11. The difference in the ratio of χ^2 values is most likely as a result of the amplification in a high sine χ^2 by a low linear χ^2 in the case of the non–PM objects helping to distinguish them from the sine

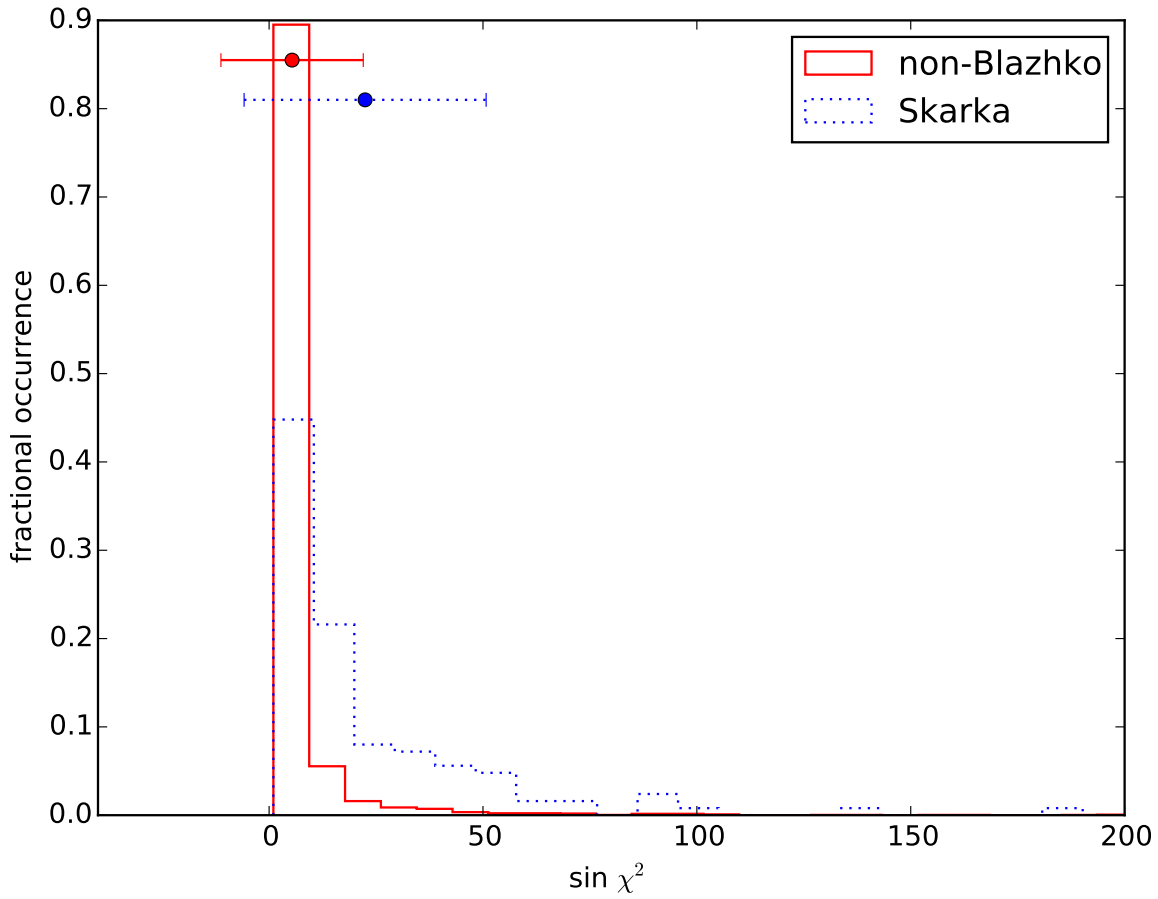

Figure 5.10: Comparison of the distributions of sine χ^2 values of visually identified non–PM objects against the sine χ^2 values of the Skarka dataset objects, showing the similarity in the ranges of their distributions.

fits of the PM objects. Fig. 5.11 therefore suggests that objects with a χ^2 ratio below 0.8 are potential PM objects (as they are beyond 1σ of the mean of the non–visual objects but within 1σ of the mean of the visually selected objects) but require visual verification. Objects with a χ^2 ratio below 0.5 are highly likely to be PM objects as they are approximately 2σ from the mean of the non–visual objects and are near the mean of the visually selected objects.

The Blazhko periods of the candidate objects were compared against non–Blazhko objects, the extreme AM objects (EAM) from Chapter 3, and the periods of the Blazhko candidates from the Fourier analysis process of Chapter 4. Figure 5.12 shows that the only difference between the Blazhko periods (P_{BL}) for those objects visually selected as candidates and those that were not appears to be a slightly narrower range of values for the periods of the objects that were not selected (labelled as non–vis in the figure).

Figure 5.13 shows that the candidate Blazhko periods calculated by the PDM process mostly agree with the known Blazhko periods for those objects. Objects 1SWASPJ1329-22.47-055259.2 (V476 Vir), 1SWASPJ123811.99-442231.8 (ASAS123812-4422.5), and

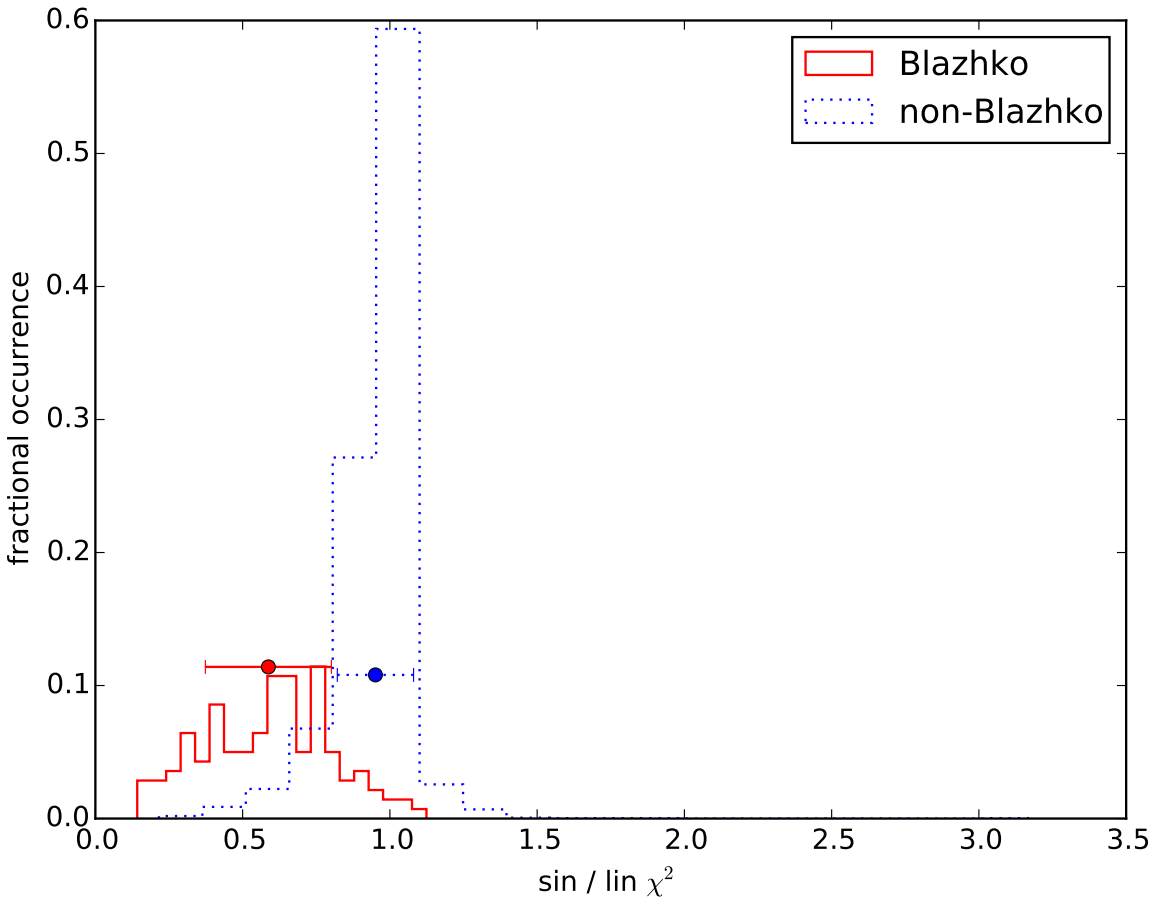

Figure 5.11: Sine to linear χ^2 ratios for visually identified PM and non–PM objects. The error bars indicate the 1σ deviations for each population.

1SWASPJ202044.47-410705.9 (V1645 Sgr) have published Blazhko periods of 1398.99 d, 1307.7 d, and 1302 d respectively, and have been removed from plots including Skarka's Blazhko period in order to improve clarity amongst the shorter period objects. The three objects that do not match the folded O–C period are 1SWASPJ040010.75-194936.9 (PM period of 168.9±0.83 d vs a known $P_{\rm BL}$ of 123.5 d), 1SWASPJ143927.36-032736.7 (152±0 d vs 93.8 d), and, to a lesser extent, 1SWASPJ142305.58+015401.0 (52.8±0 d vs 48 d). The former two candidates have noisy phase–folded O–C diagrams, but the diagram for 1SWASPJ142305.58+015401.0 has very little noise and is a well–defined sinusoidal PM curve as shown in Fig. 5.15. The Blazhko periods for this object calculated during the frequency domain investigation in Chapter 4 are 44.9±0.1 d and 51.7±0.1 d, suggesting a Blazhko period around 52 d based on the two closest periods from both the PM and FM techniques. The SuperWASP Blazhko periods for 1SWASPJ040010.75-194936.9 are 78.4±0.1 d and 127.0±0.3 d, which agree more closely with the known Blazhko period than the period found here using PM. Likewise, the SuperWASP Blazhko period for 1SWASPJ143927.36-

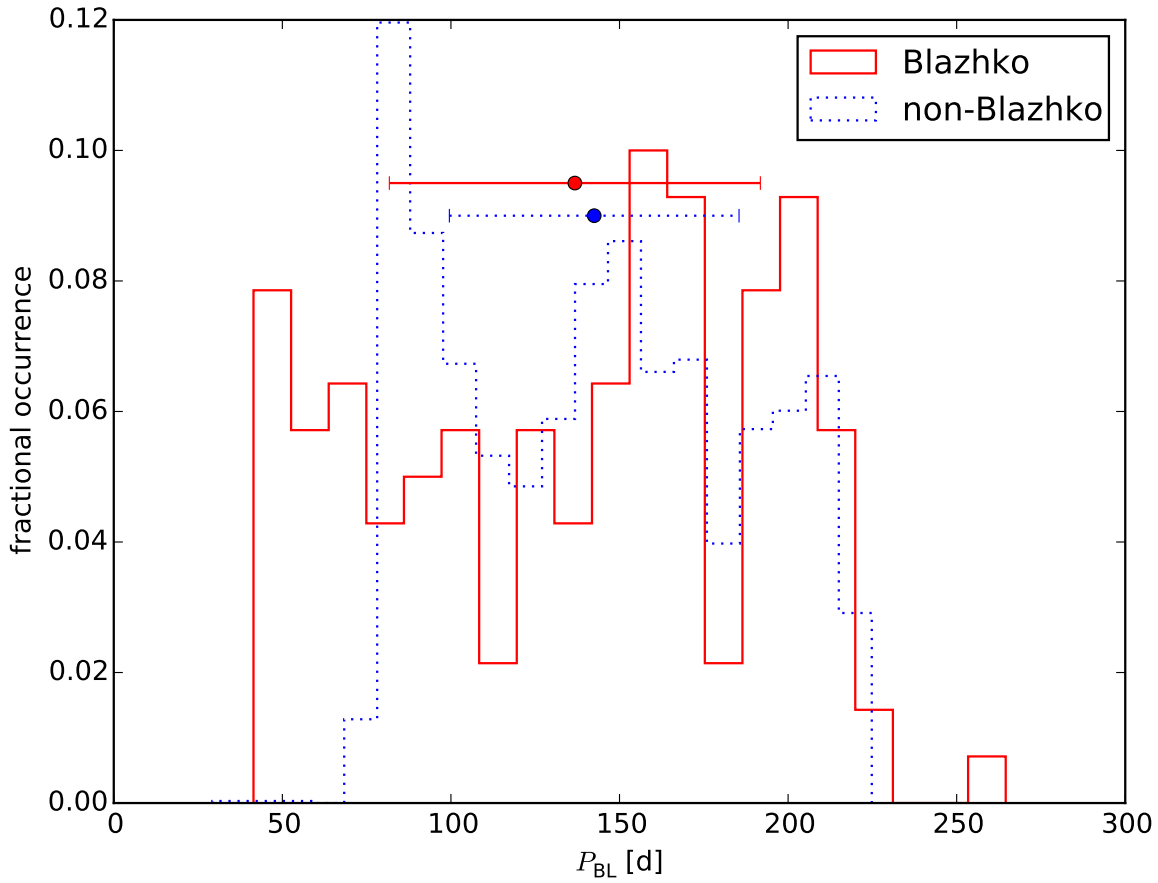

Figure 5.12: Comparison of PM periods for PDM folded O–C residuals visually identified as Blazhko candidates, against those not showing any periodicity. Populations have again been normalised for easier comparison.

032736.7 is 92.4±0.4 d, which is far closer to the known period than the period found here using PDM.

Figure 5.14 shows that there is some agreement between periods found using Fourier analysis in the previous chapter and using O–C diagrams in this chapter. However, there appears to be a large discrepancy around the 140 – 210 d range. Only a handful of these periods appear at small integer multiples of the other Blazhko period, the rest do not appear to form any correlation or pattern so it is unclear why there is such little correlation in this range. The minimum of the initial search range in the phase–folding of their O–C diagrams was 10 d, so this cannot be used to explain why some low Fourier analysis periods could have such large PM periods.

Object 1SWASPJ004757.06+114223.5 (FR Psc) is a known Blazhko object with a Blazhko period of 55.0 d. The PDM method produces a Blazhko period of 51.4 d which is within 10% of the published Blazhko period. This object was also detected as Blazhko using the Fourier analysis techniques described in the previous chapter, resulting in a candidate Blazhko period

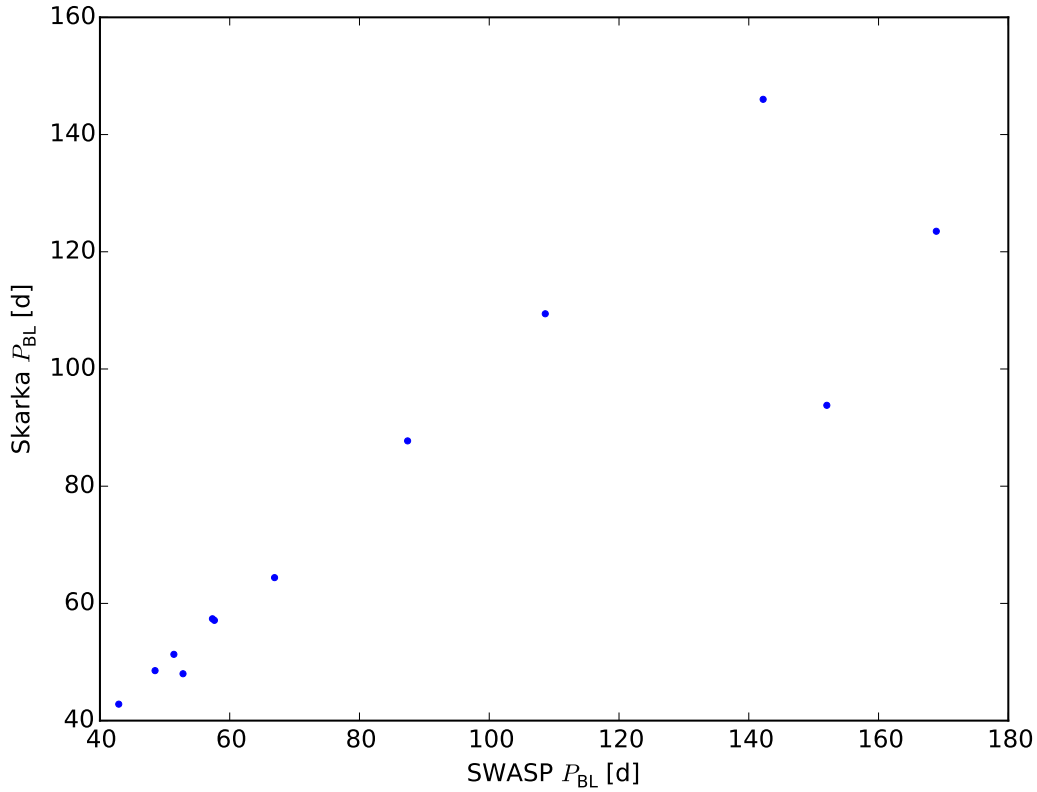

Figure 5.13: Known Blazhko periods plotted against Blazhko periods calculated by the PDM method.

of 50.9 ± 0.1 d which is within 0.5 d of the PDM derived value.

In the time domain PM causes the horizontal shifting of the pulsation in light curves phase–folded by the pulsation period. It is therefore interesting to investigate if PM had an adverse effect on the relative scatter parameter from the time domain chapter. Inspection of Fig. 5.16 shows there is no clear correlation or anti–correlation between these two variables, which is verified by their Spearman correlation coefficient of 0.24. This implies that the relative scatter parameter is not hampered by PM.

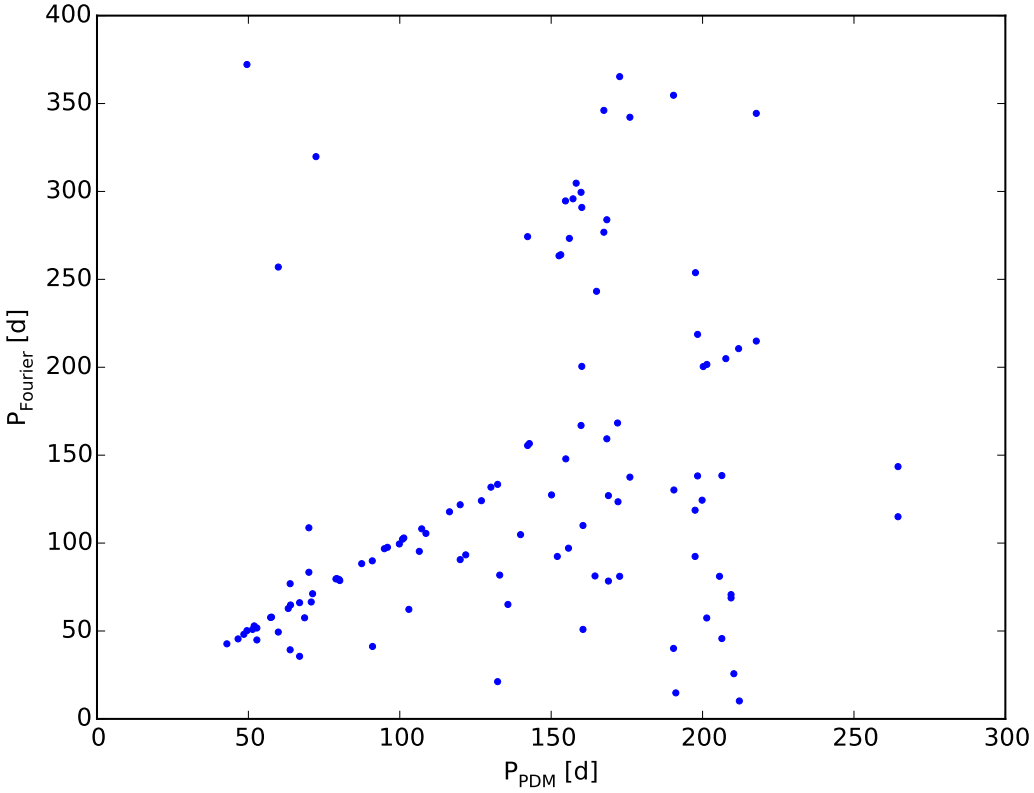

Figure 5.14: Blazhko periods from the Fourier analysis stage plotted against those calculated by the PDM method.

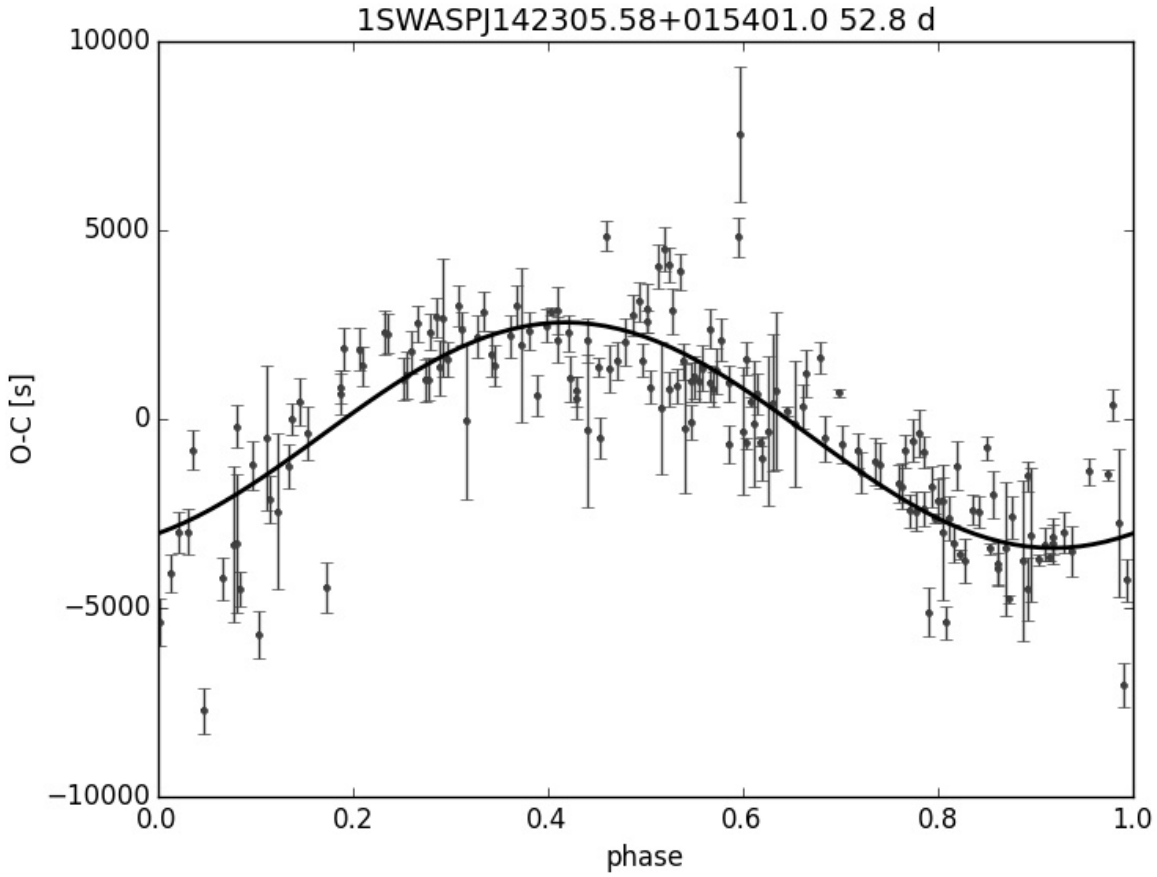

Figure 5.15: The O–C residuals of objects 1SWASPJ142305.58+015401.0 phase–folded by the candidate Blazhko period of 52.8 d showing a well–defined sinusoidal PM effect.

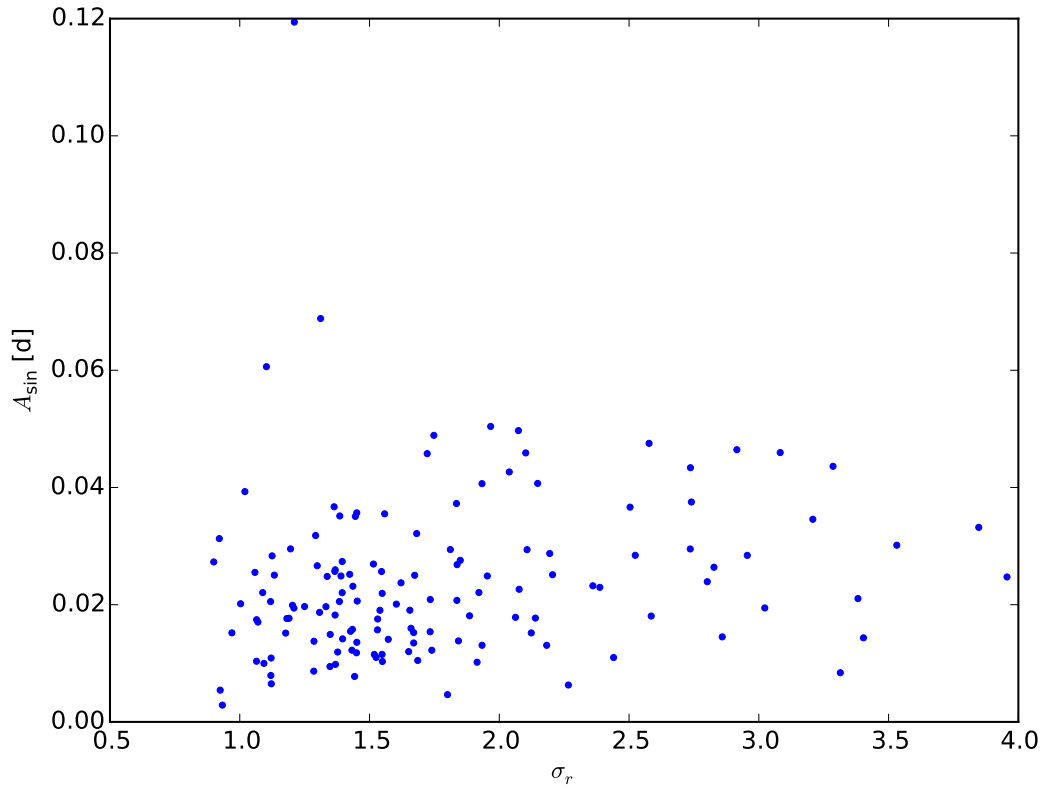

Figure 5.16: Relative scatter parameter against PM amplitude for the 140 objects selected as having PM. No correlation, or anti–correlation can be seen between these 2 parameters.

5.3.4 Comparing Blazhko periods with EAM objects

Another useful comparison is between Blazhko periods of the extreme amplitude modulated objects (EAM) and the visually selected PM objects, as both sets used PDM to find their periods. Figure 5.17 shows that there is good correlation between the Blazhko periods of the 9 objects in both sets, apart from 1SWASPJ095515.90+034532.3 (284.5 d from AM versus 158.3 d from PM) and 1SWASPJ123811.99-442231.8 (122.7 d from AM versus 172.1 d from PM), with a Spearman correlation coefficient of 0.97 (p–value = 2.1×10^{-5}). Unlike the Fourier analysis Blazhko periods which could be derived from corresponding frequency peaks caused by either FM or AM, the EAM periods are derived solely from AM. Although this is a small dataset, the strong correlation shows that both the AM and PM aspects of the Blazhko effect have the same period. Comparing the quality of the light curve folded by the period calculated from extracting the envelope function against the folded O–C residuals for object 1SWASPJ123811.99-442231.8 (Fig. 5.18), the EAM $P_{\rm BL}$ of 122.7 d looks like the correct Blazhko period. Fig. 5.18 is reminiscent of the envelope function of 1SWASPJ120447.27-274043.2, where part of the folded envelope function was well defined and another part was noisy, hinting at a variable Blazhko period. In this case however, it is more likely that the O–C Blazhko period of 172.1 d is a small integer ratio, i.e. 5:7, of the true 122.7 d Blazhko period. Interestingly, object 1SWASPJ120447.27-274043.2 itself is missing from the list of PM based Blazhko candidates as its phase–folded O–C diagram shows a large variance in residuals but failed to be folded into a sinusoidal shape.

The folded O–C residuals for object 1SWASPJ095515.90+034532.3 (Fig. 5.19) form a well defined sine wave, with some slightly noisier residuals in the first half of the diagram. It is harder in this case to conclude which candidate Blazhko period is the correct one. The large difference of 126.2 d between the two techniques suggests that the O–C derived candidate period is almost half of the true 284.5 d period.

This and the previous section have focused on phase–folding O–C diagrams to find relatively short period modulations. However, long timescale patterns and trends can be identified in the unfolded O–C diagrams, such as light travel time effects (LTTE) from the RR Lyrae star orbiting a common centre of mass in a binary system. The next section concentrates on the search for these objects within the SuperWASP RRab dataset.

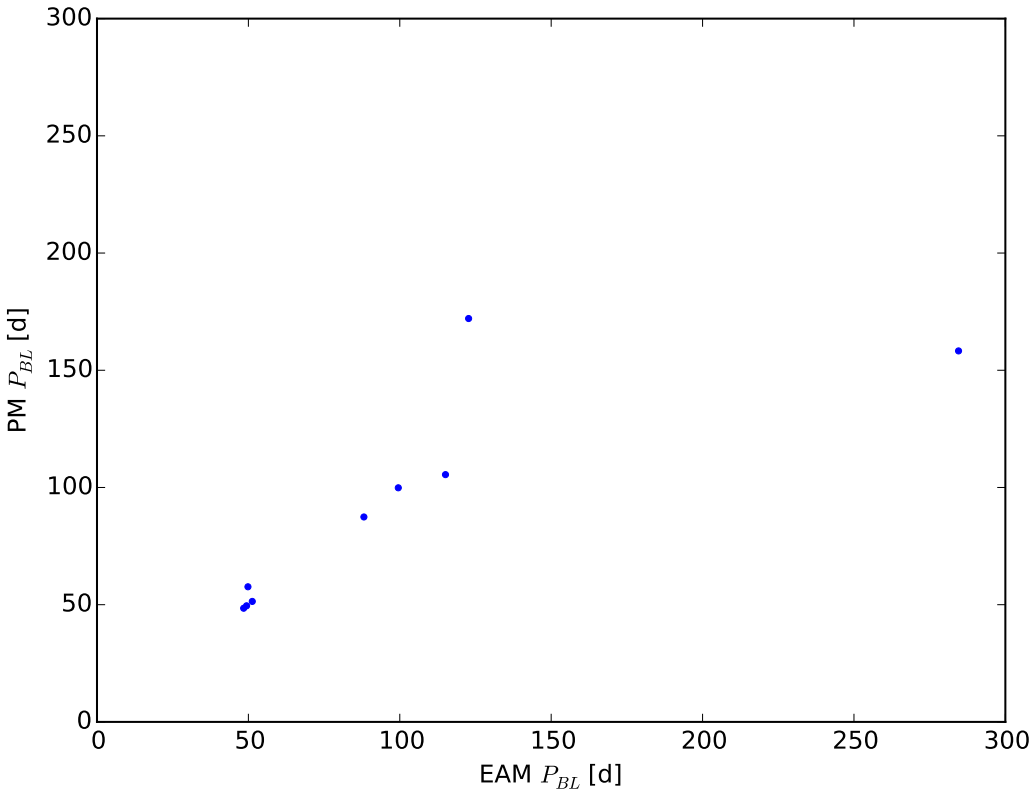

Figure 5.17: Comparison of candidate Blazhko periods for EAM and PM objects. There is a strong correlation between the 2 data sets apart from the very long period objects.

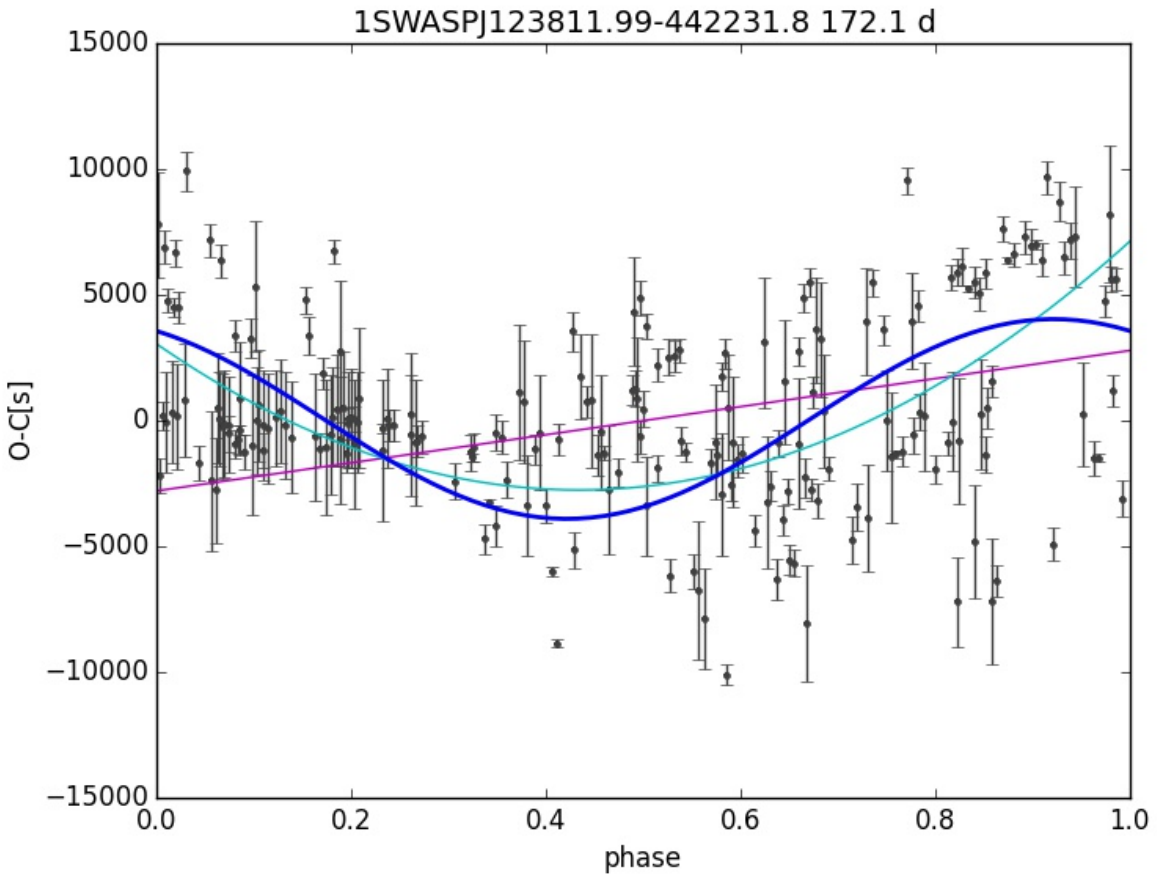

Figure 5.18: O–C residuals for 1SWASPJ123811.99-442231.8 folded at a candidate Blazhko period of 172.1 d showing some variability in the PM. A linear model is shown in magenta, and a quadratic model is in light blue for comparison.

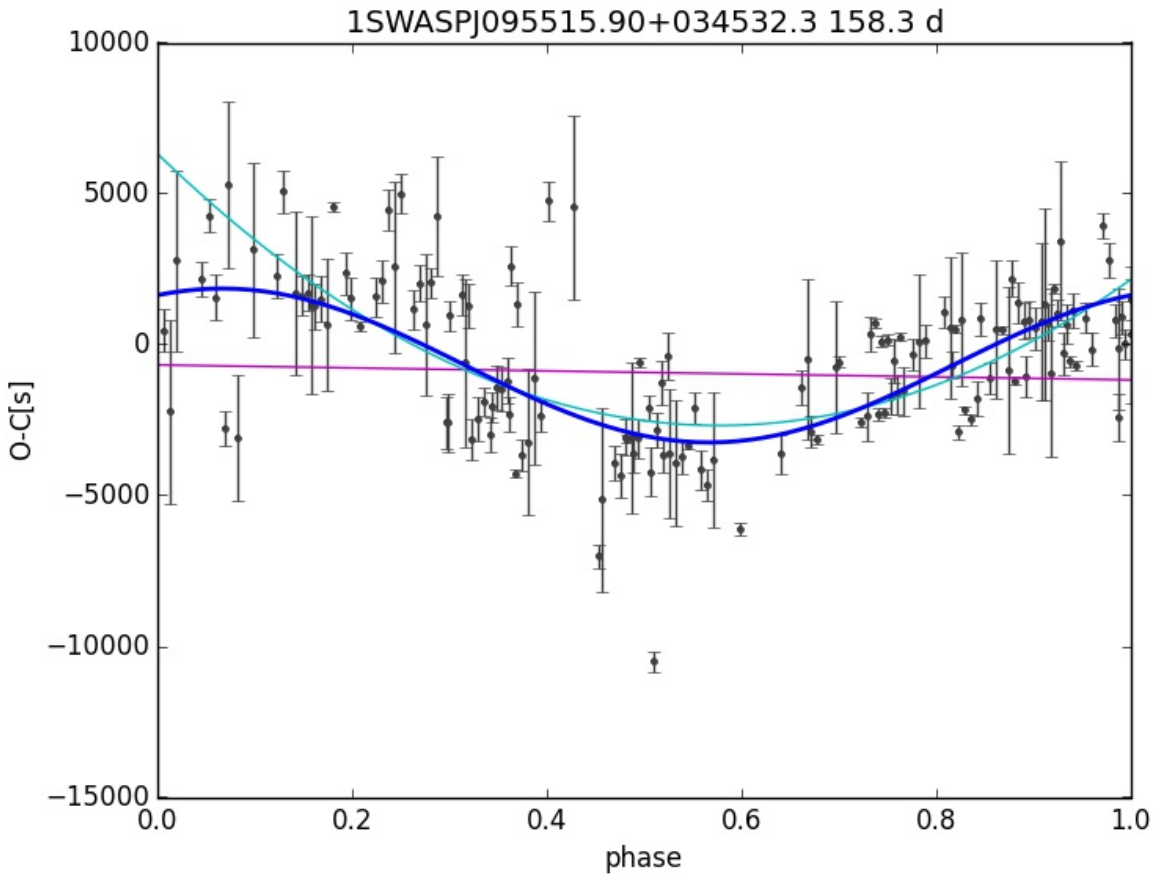

Figure 5.19: O–C residuals for 1SWASPJ095515.90+034532.3 folded at a candidate Blazhko period of 284.5 d. Again, a linear model is shown in magenta, and a quadratic model is in light blue.

5.4 Searching for PM caused by LTTE

The same 4891 objects were available after the template fitting stage for light travel time effect (LTTE) analysis as for the Blazhko analysis. Short term periodic trends were dealt with in the previous section, as they are due to PM. In contrast, this section deals with fitting linear, quadratic and sinusoidal models to the un–folded O–C diagrams to find any long term trends which may be caused by the pulsator orbiting a common centre of mass in a binary system. LTTE is caused by the lengthening and shortening distance to the pulsator as its orbit causes it to move away and then closer to us. The pulsations appear to quicken and slow down due this extrinsic Doppler effect. The pulsating object can therefore be used to identify binary systems where only one component of the system is observed.

5.4.1 Sinusoidal O–C trends

Unlike the previous section where the O–C diagrams were phase–folded, fitting models to the unfolded O–C curves did not require the binning of residuals. Therefore, the minimum number of residuals needed was reduced to 5 residuals, 1 more than the minimum required by a sinusoidal model. 202 objects failed to have a successful linear, quadratic or sinusoidal fit, due to having fewer than 5 points, leaving 4689 objects for analysis of their quadratic fits. A further 35 had successful linear and quadratic fits but failed to have a successful sinusoidal fit, leaving a final 4617 objects for sinusoidal analysis. Of these, 846 had their sine χ^2 rescaled to unity as it was less than 1.0, by rescaling the residuals and recalculating χ^2 values for all three models.

Blazhko effect objects cannot be considered for LTTE candidacy as the Blazhko effect may contain a long–period PM component which could be mistaken for LTTE PM. Also, the AM component of the Blazhko effect may affect the shape of the light curve, affecting the quality and reliability of the template fitting, even if a vertical offset between nights is accounted for. Blazhko objects tended to have a large scatter of O–C values within each season, making the sine fits more visually convincing than they actually were, e.g. objects 1SWASPJ065128.70-424201.3, 1SWASPJ090241.26-001334.8 and 1SWASPJ093023.90 -124916.4 shown in Fig. 5.20.

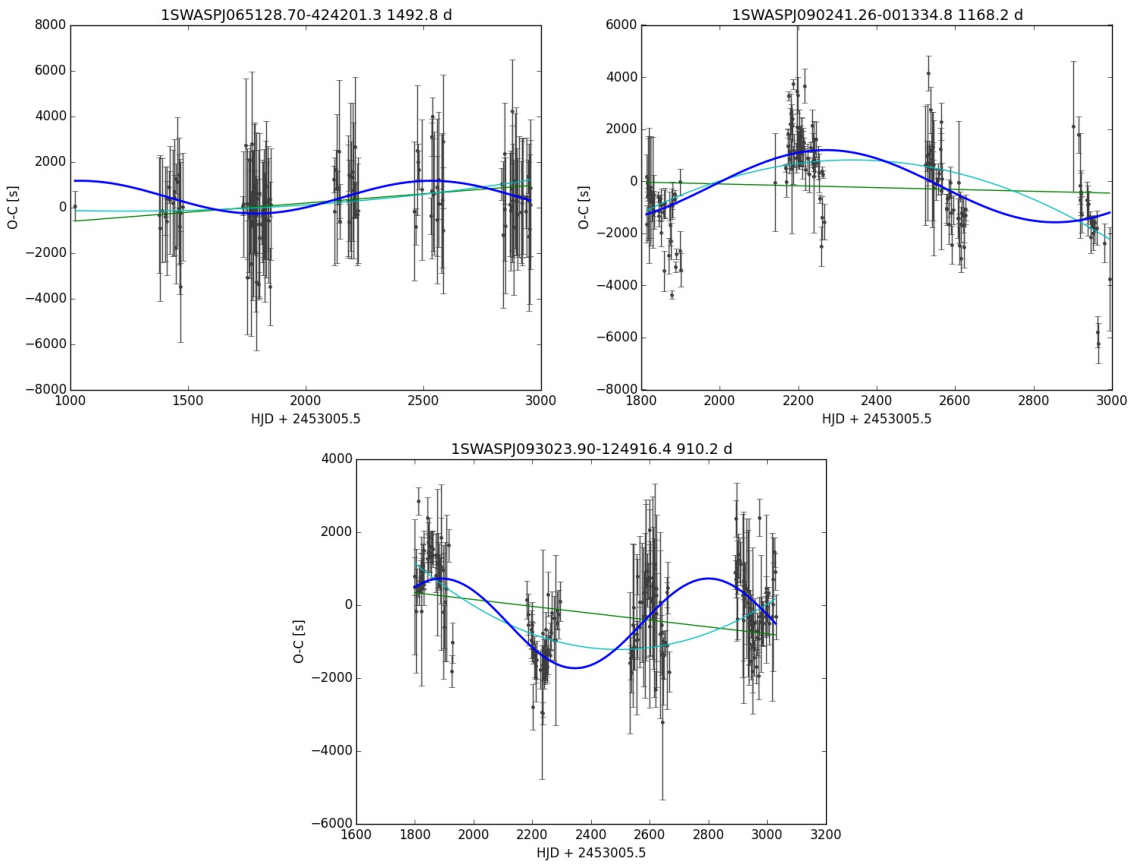

Figure 5.20: Examples of O–C diagrams with high levels of scatter within each season.

A second round of visual inspection focused on how well the sine curve fitted points within each season for these 66 objects. Their sinusoidal fits were compared to their respective quadratic fits. Objects where the quadratic fit was no worse than the sinusoidal fit were removed from the LTTE candidate list and added to the quadratic (long term LTTE) list. In some of these cases there was negligible difference between sine and quadratic χ^2 values. Likewise, sine fits that used a large amplitude in order to fit seasons on either side of a large gap were excluded where these could be fitted just as well with a quadratic model. Objects were also removed from the list of 66 potential candidates where all seasons could be joined just as well by a linear fit, and no real quadratic or sinusoidal fit could be clearly seen, due to large uncertainties in the residuals. In these cases there was only a small difference between the χ^2 value of the linear fit and the other two fits. On the other hand, objects were selected as either quadratic or sinusoidal in diagrams where quadratic or sinusoidal trends could be visually discerned even if the linear fit passed through all error bars. In these cases the χ^2 value of the linear fit tended to be higher than the other two fits.

After visual inspection 18 objects were denoted as sinusoidal. Care was taken to check if the sine model was over–fitting the data, such as creating a large amplitude sinusoidal to fit

seasons with a large gap between them, or where a quadratic fit was visually just as good a fit. Examples from this initial set of 18 are shown in Fig. 5.21. Although no Blazhko objects from the SuperWASP Blazhko catalogue were included in this list of 18 sinusoidal objects, when these 18 objects were then compared to the new list of Blazhko candidates found by phase–folding their O–C residuals (see Sect. 5.3.1) one object, 1SWASPJ021952.30+091648.0, shown in the first panel of Fig. 5.21, was found in both lists. Its LTTE period was 508 d which was approximately double the PDM period of 225 d. Its un–folded O–C diagram seemed to show a good fit to the 508 d period over the 3 seasons of observations. This object was therefore re–folded on a range centred on 510 d which resulted in a PDM period of 492 d and a well–folded O–C diagram. If this longer period was the correct one, folding at half of the period would result in a badly–folded O–C diagram. However, since this object can be folded equally well on the shorter 225 d it is more likely that 1SWASPJ021952.30+091648.0 is a Blazhko candidate and not an LTTE candidate, since the period is less than 500 d. It was therefore removed from the LTTE candidate list leaving 17 objects, shown in Table 5.2.

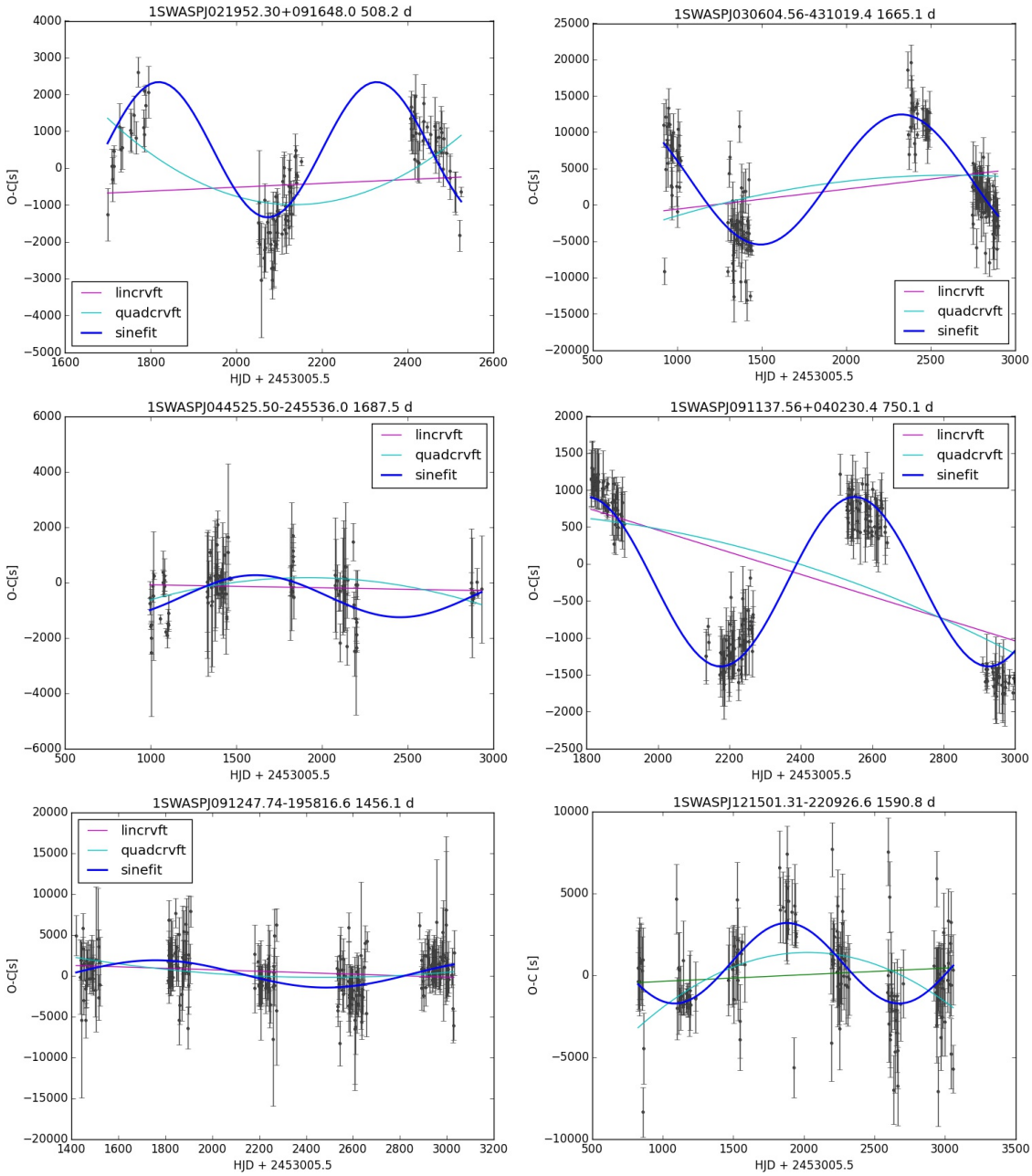

Figure 5.21: Examples of O–C diagrams that have a good fit to sinusoidal models. The vertical axis is in seconds and the residuals have been fitted with a sinusoidal model. The candidate LTTE periods for each objects are shown in the plot title after the SuperWASP identifier.

Table 5.2: List of LTTE candidates

SWASP id	N	ΔT [d]	$P_{\rm sin}$ [d]	linχ^2	quadχ^2	sinχ^2
1SWASPJ030604.56-431019.4	200	1978	1670±14	33.827	33.555	4.232
1SWASPJ030811.32-384525.9	153	1962	1400±7	119.476	6.031	2.462
1SWASPJ044525.50-245536.0	122	1935	1690±63	11.159	9.200	6.299
1SWASPJ054235.00-322603.3	146	1955	1900±171	4.703	4.692	4.044
1SWASPJ091137.56+040230.4	205	1187	750±10	42.364	41.722	3.600
1SWASPJ091247.74-195816.6	232	1610	1460±78	1.496	1.447	1.250
1SWASPJ112321.73-210849.6	106	1455	1600±109	4.328	1.239	1.000
1SWASPJ112322.47+063805.1	143	1122	1300±161	5.328	4.774	4.331
1SWASPJ114401.11+012639.9	109	1839	930±21	11.608	11.594	2.091
1SWASPJ121501.31-220926.6	167	2233	1590±45	4.245	3.155	1.714
1SWASPJ124006.35-341532.6	205	2231	1360±14	18.319	16.552	5.533
1SWASPJ144050.73-265449.3	199	2243	1760±24	4.604	3.780	1.185
1SWASPJ144057.53-223323.9	164	2243	1320±55	1.333	1.332	1.132
1SWASPJ150740.25-142437.6	155	1472	1320±24	12.020	4.180	1.000
1SWASPJ152017.19-371238.0	152	2244	1920±85	6.063	5.992	4.778
1SWASPJ153554.49-181536.1	167	2244	1470±47	2.115	2.115	1.267
1SWASPJ192447.12-185815.5	33	2182	1700±36	1.263	1.262	1.000

The headings above refer to the following: SWASP id is the unique SuperWASP identifier; N is the number of nights in the O–C diagram; ΔT is the duration of observations taken as the difference between the first night and the last night; $P_{\rm sin}$ is the candidate LTTE period found from the sinusoidal fit to the data; linχ^2, quadχ^2 and sinχ^2 refer to the goodness of fit values for the linear, quadratic and sinusoidal fits, respectively.

5.4.2 Analysis of sinusoidal results

The sinusoidal periods listed above are candidate LTTE periods. They range from 750 d (2.05 yr) to 1924 d (5.27 yr), with a mean value of 1476 d (4.04 yr). Of the total 4981 O–C objects, 20 are in the Liska database of RR Lyrae binary candidates Liška et al. (2016) (available at http://rrlyrbincan.physics.muni.cz). Their minimum periods are 794 d for FN Lyr and 1676 d for TU Com. The other periods are all longer than 23 yr, taking them well beyond the maximum period for the LTTE candidates found in this work. None of the 17 sinusoidal LTTE candidates are among the 20 Liska objects so their periods cannot be compared. Figure 5.22 shows that the sine period uncertainty, σ_s, and goodness of fit values are not correlated. There is quite a large range of sine χ^2 values for these visually selected objects. It is unclear from Fig. 5.22 whether either the period uncertainty or the goodness of fit can be used to filter out non–LTTE objects. Figure 5.23 shows that the goodness of fit is not affected by the length of the period of the sine model. Conversely, long LTTE period objects are fitted just as well as those with short periods. Figure 5.24 shows that there is no correlation between the number of points and the quality of the sine fit, as measured with a χ^2 fit, for the visually sinusoidal objects that did not include candidate Blazhko objects from previous chapters.

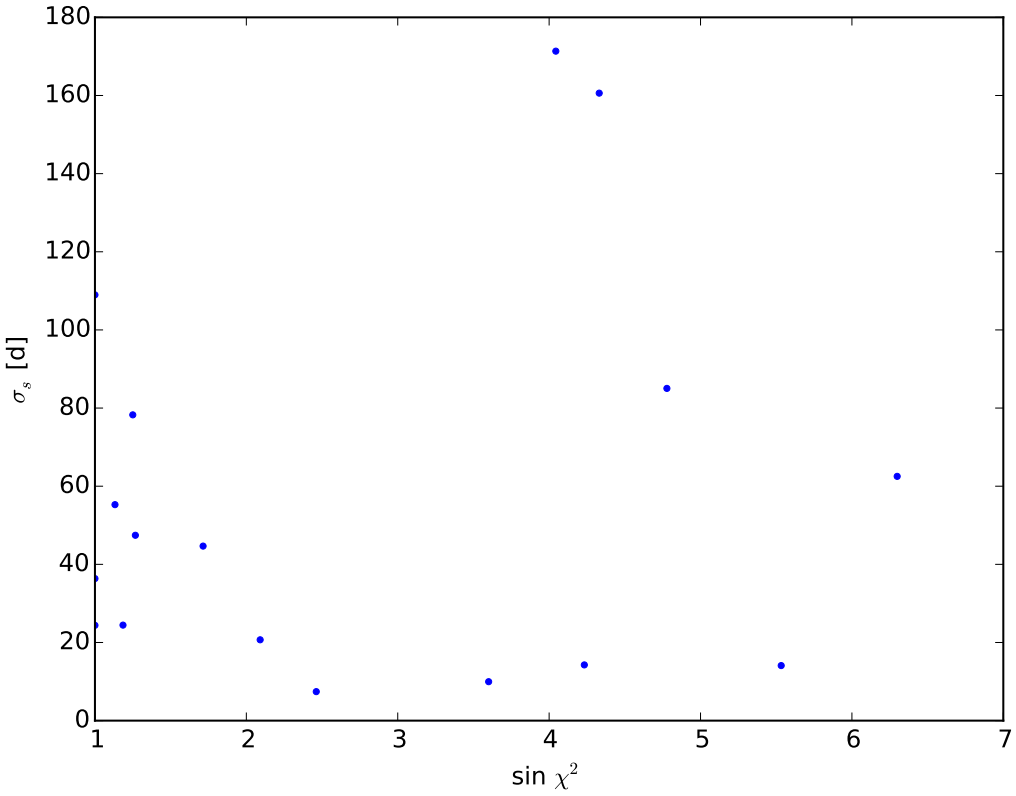

Figure 5.22: Sine period uncertainty vs goodness of fit measurements for visually sinusoidal objects. No correlation can be seen between these two variables. The sin χ^2 values cover a wide range considering they all belong to O–C diagrams that were selected as good fits.

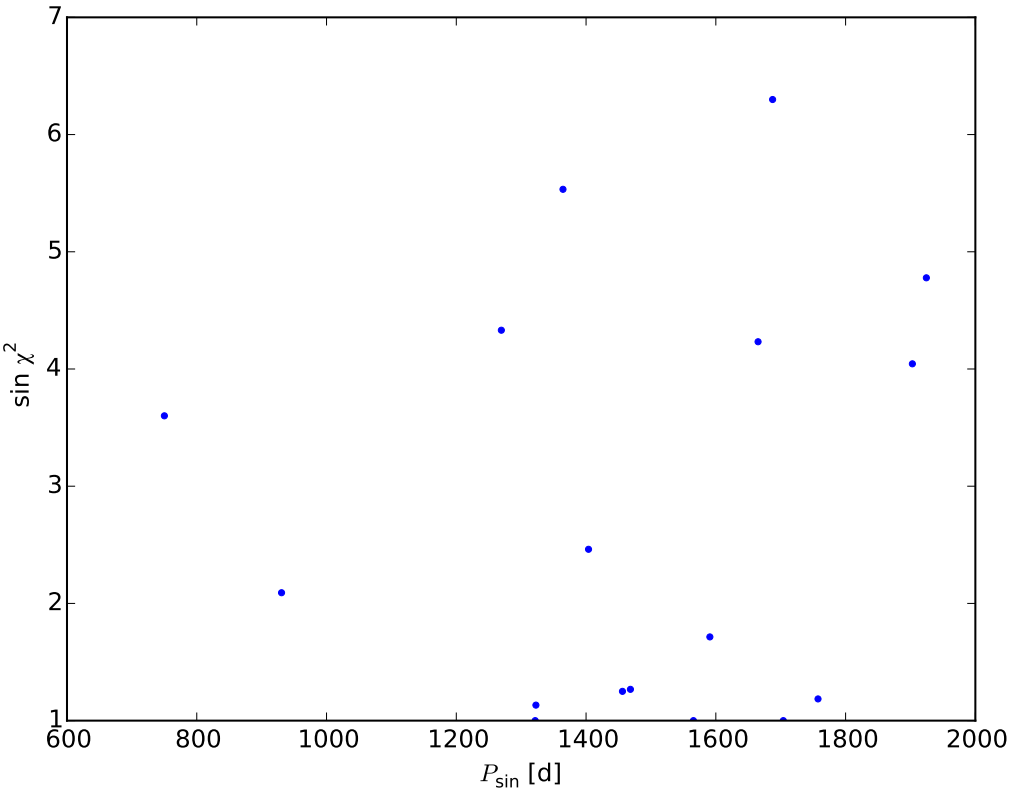

Figure 5.23: Comparison of sine model period against sine χ^2 for visually selected LTTE candidates. No correlation can be seen between the length of the period and the goodness of fit of the sine model.

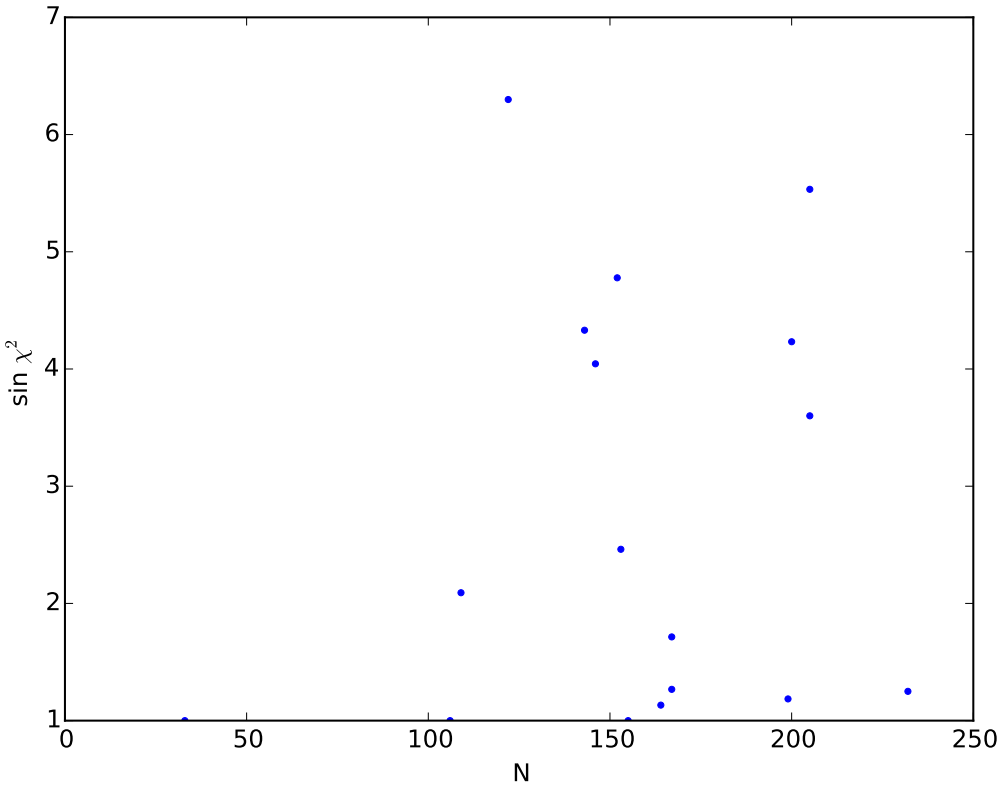

Figure 5.24: Goodness of fit measurement sin χ^2 vs number of residual after clipping, N, showing how the goodness of the sinusoidal fit does not appear to be correlated to the number of points.

To achieve any automation of the detection of LTTE in SuperWASP data, it is necessary to identify clear thresholds in the attributes of the data that can be used to create distinct populations of objects. The range of values of each of the χ^2 goodness of fit measures means that on their own they are unable to produce clear thresholds as shown in Fig. 5.25.

However, a plot of sine χ^2 against linear χ^2 for visually identified sinusoidal O–C residuals (Fig. 5.26) shows many of the objects not selected as LTTE candidates as having lower sine χ^2 than linear χ^2, suggesting that a comparison between these two parameters is not sufficient to automatically distinguish good LTTE candidates. When the ratio of the sine and linear χ^2 values is calculated, as shown in Fig. 5.27, it confirms that there is no threshold value below which LTTE candidates can be automatically selected.

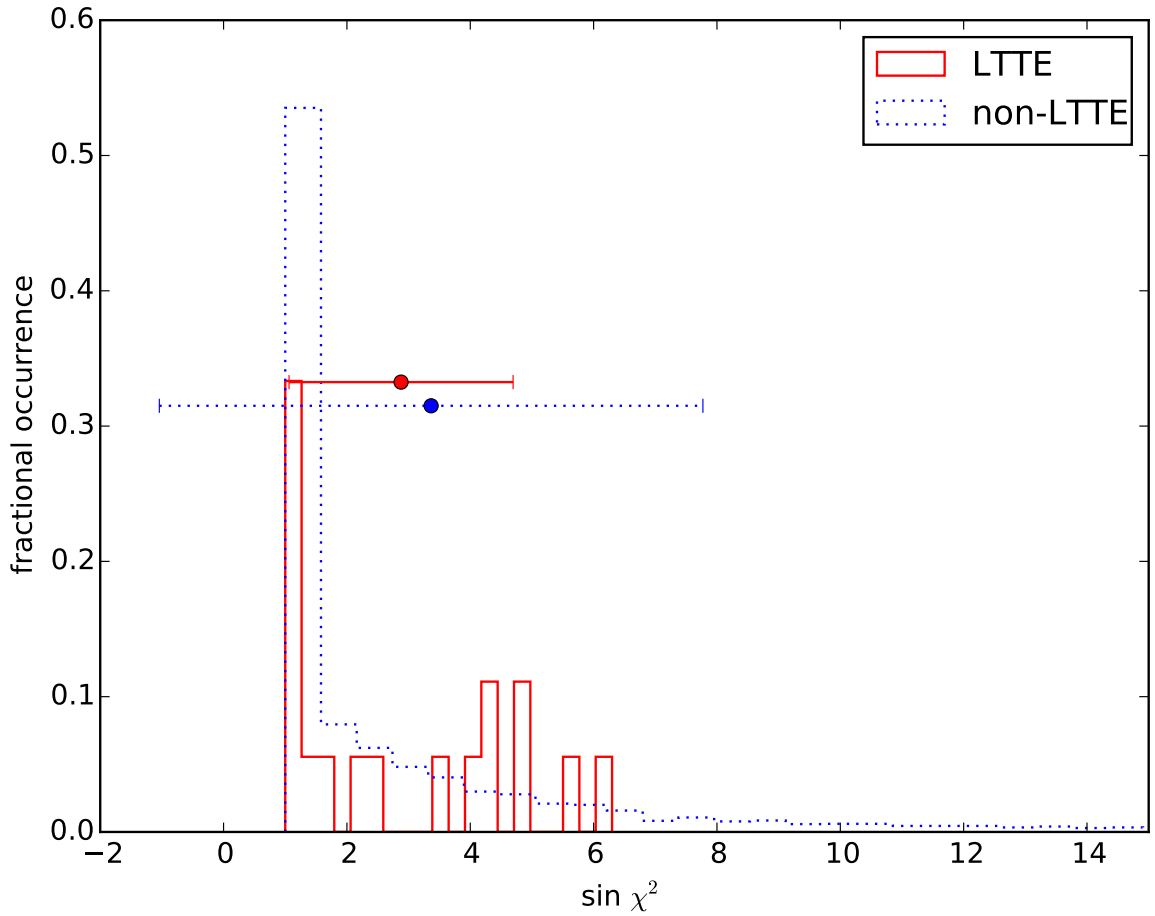

Figure 5.25: Distribution of χ^2 values for sinusoidal O–C diagrams compared to those rejected during visual inspection. There is an upper limit to the visually selected objects, but the standard deviation of the rejected objects overlaps this range of values as shown by the error bars.

Figure 5.28 shows that there is a large difference between the periods found using the PDM and unfolded LTTE sine fitting techniques for the larger datasets of all non–Blazhko LTTE candidates and the PDM candidates, but that these two groups are not entirely mutually

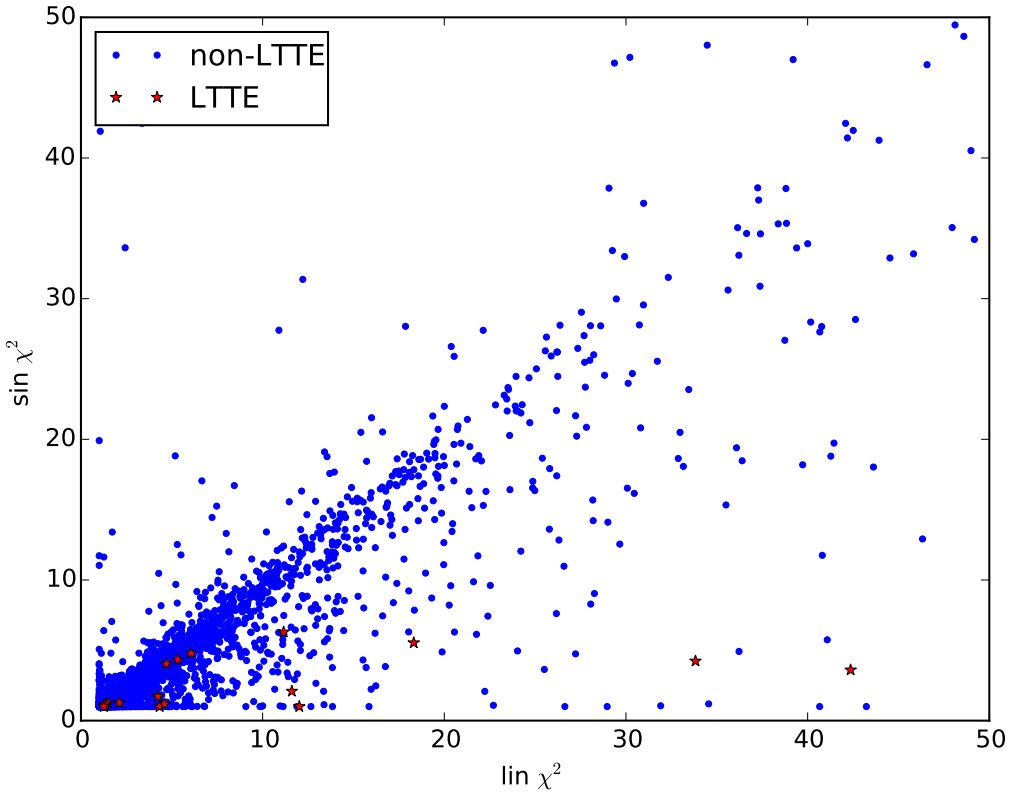

Figure 5.26: Goodness of fit values for visually selected and rejected objects, truncated to χ^2 values below 50. Many of the objects not selected as LTTE candidates have lower sine χ^2 than linear χ^2.

exclusive. This implies that some sinusoidal O–C objects could be Blazhko objects, based on the length of period alone. This figure demonstrates the limit in the range of periods searched over by the PDM routine, but it also shows that the mean LTTE period of 1473 d and the 1σ range of both groups is mutually exclusive. However, the limited range of periods that could be productively searched over by the PDM program, and the fact that some Blazhko objects appear to have very long components, as shown in Fig. 5.28, means that it is unreasonable to use the period as a threshold to distinguish between the Blazhko effect and LTTE, despite the differences in the periods shown here.

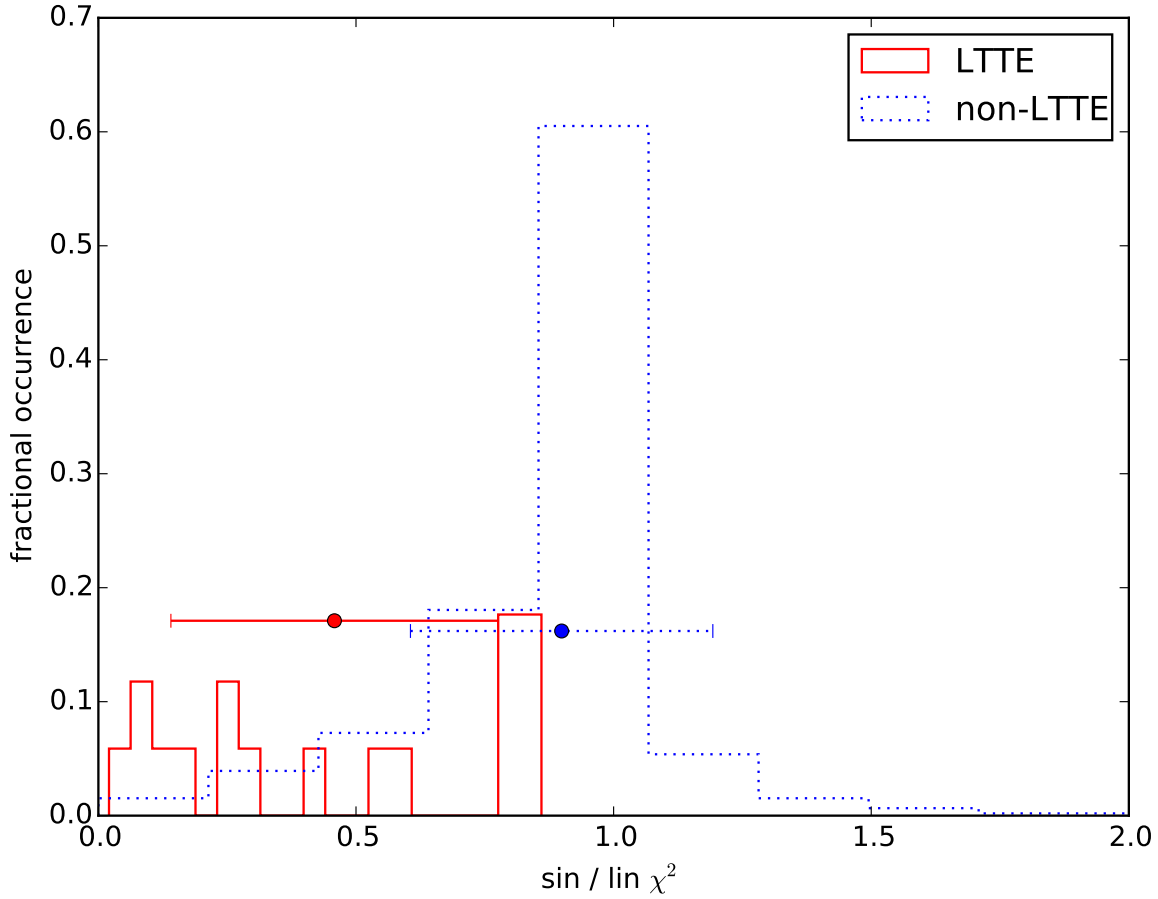

Figure 5.27: Ratio of sinusoidal to linear χ^2 values for visually identified and non–identified objects. Unlike the PDM Blazhko case, there is no clear delineation between the two groups. Ratio values have been limited to less than 5.0 in the non–LTTE dataset for clarity.

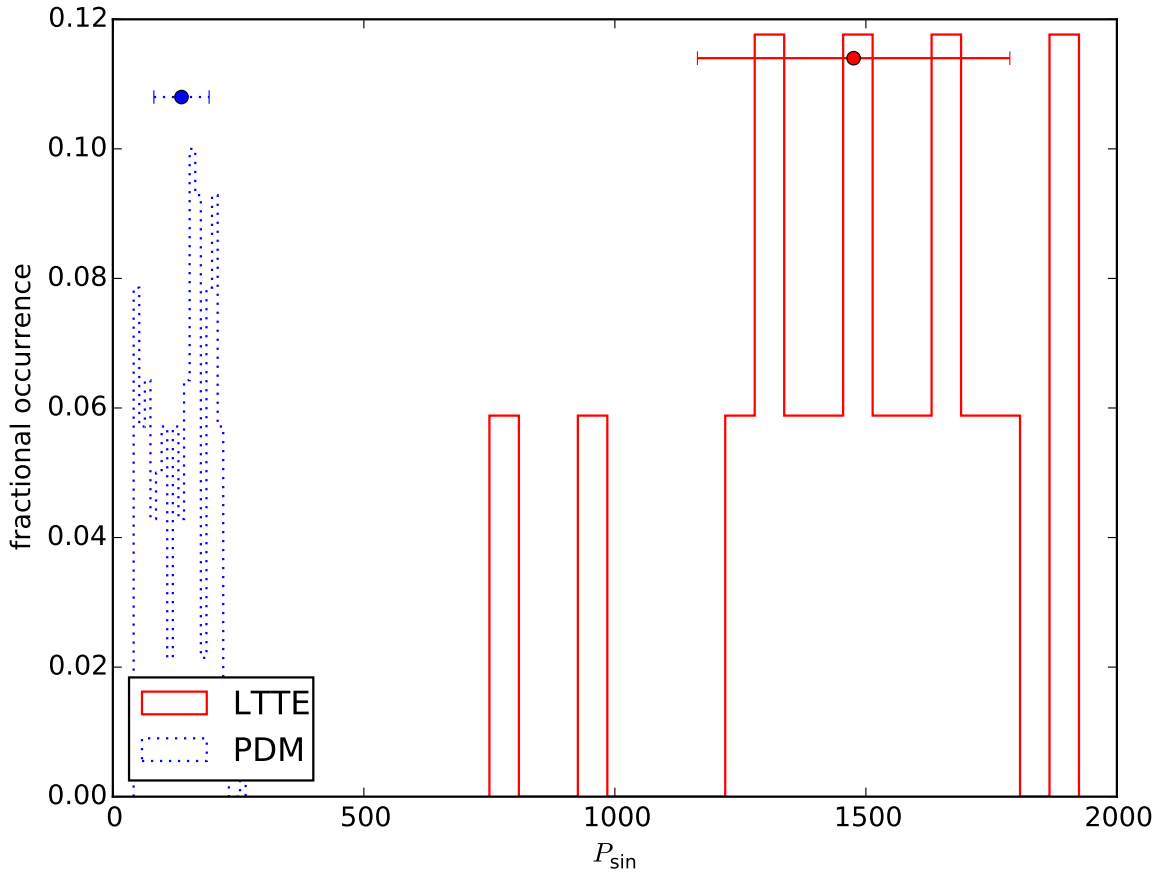

Figure 5.28: Comparison of the ranges of candidate Blazhko and LTTE periods showing the difference in the period ranges.

5.4.3 Quadratic O–C trends

Some changes in the pulsations of RR Lyrae take place over time–scales far longer than the duration of even the longest ground–based surveys. These can be due to evolutionary changes as the star continues to burn helium in its core. Such long term changes in pulsation period will become integrated over time when observed using O–C diagrams, changing a linear change in period into a quadratic curve in the O–C diagram. They can also be due to LTTE where the pulsator is in a binary system with a long orbital period where, over the course of SuperWASP observations, the O–C diagram only captures part of a very long term sinusoidal trend. In order to identify these quadratic occurrences, another visual inspection of the O–C diagrams was made, which led to the identification of 73 objects showing quadratic trends, listed in Table 5.3. None of these objects are included in Liska's dataset of RR Lyrae binary candidates. A sample off these quadratic fits are shown in Fig. 5.29 below. In the case of 1SWASPJ103846.50-343844.0, the quadratic fit matches the sine fit so well that the light blue quadratic fit line is hidden by the dark blue sine fit line.

Table 5.3 includes the rate of period change dP/dt, derived by doubling the quadratic coefficient of the quadratic model. The linear, quadratic and sinusoidal χ^2 values are included for comparison. As in Table 5.2, the other headings refer to the following: SWASP id refers to the unique SuperWASP identifier; N is the number of nights in the O–C diagram; ΔT is the duration of observations taken as the difference between the first night and the last night; linχ^2, quadχ^2 and sinχ^2 refer to the goodness of fit values for the linear, quadratic and sinusoidal fits, respectively.

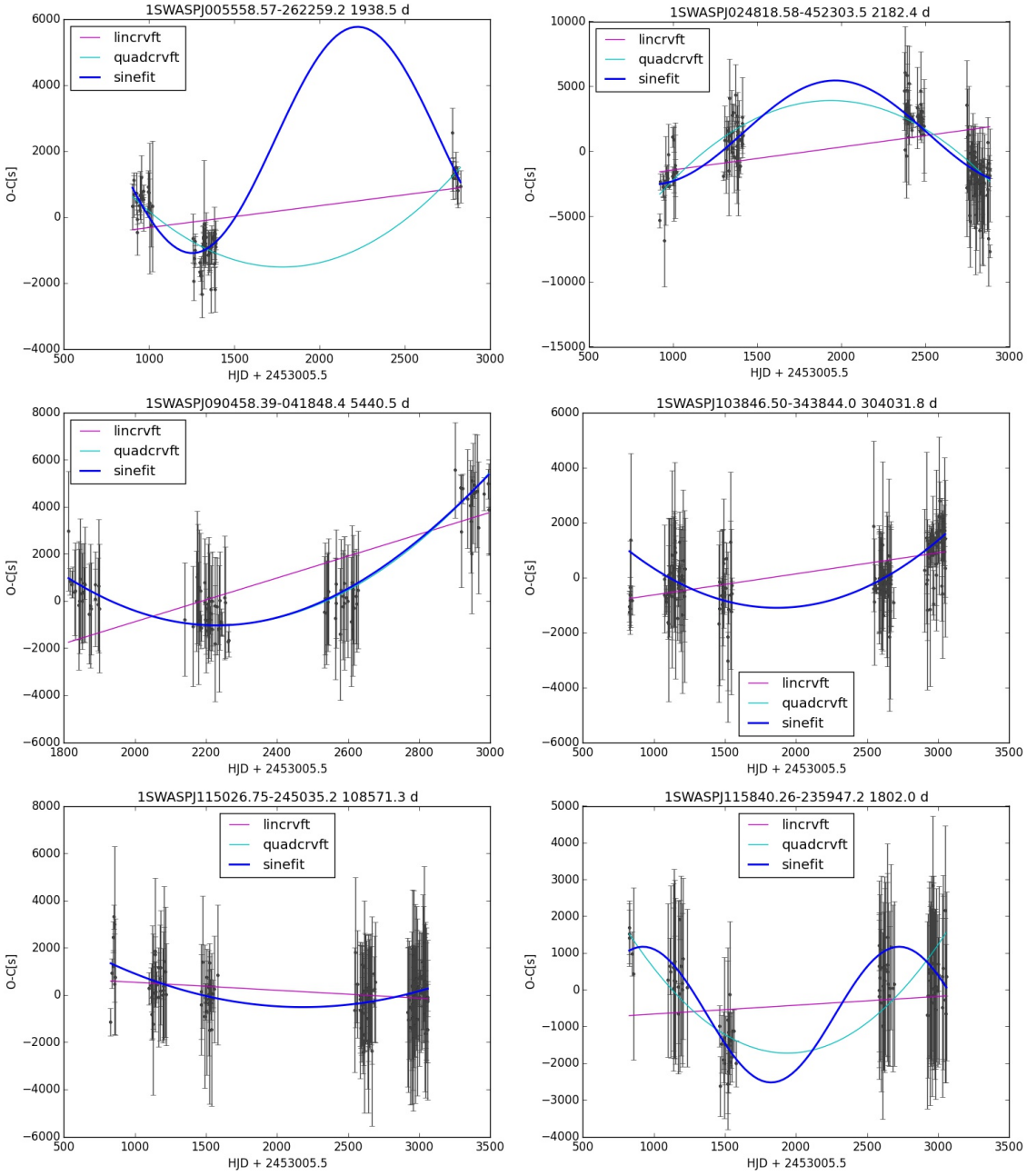

Figure 5.29: Examples of O–C diagrams with good quadratic fits to their residuals. The quadratic fits are shown in light blue. In the 3rd, 4th and 5th panels the dark blue sinusoidal fit matches the quadratic fit, implying that even the addition of another degree of freedom did little to improve the underlying quadratic fit.

Table 5.3: Quadratic O–C trending objects

SWASP id	N	ΔT [d]	$P_{\rm BL}$	dP/dt [d d^{-1} $\times$ 10^{-4}]	lin χ^2	quad χ^2	sin χ^2
1SWASPJ005558.57-262259.2	82	1922		55±3	13.357	2.671	2.084
1SWASPJ010823.34+133821.3	105	2596		-13±2	1.361	1.004	1.000
1SWASPJ021450.56-122147.0	99	839	76.5±0.4	380±35	2.244	1.000	1.017
1SWASPJ024818.58-452303.5	175	1963		-139±6	12.935	2.896	2.654
1SWASPJ030534.19-081410.0	187	875		300±12	4.249	1.000	1.193
1SWASPJ040010.75-194936.9	140	1927	78.4±0.1;127.0±0.3	-133±8	40.808	12.658	11.752
1SWASPJ041115.24-445028.3	218	1953	110.4±0.6	88±7	10.884	6.210	6.268
1SWASPJ050548.92-441806.3	203	1945	25.6±0.0	111±6	8.605	2.831	2.639
1SWASPJ062837.50-314145.3	195	1891	78.5±0.2;39.4±0.0	42±4	2.813	1.904	1.924
1SWASPJ063357.00-401542.0	82	1869		-40±33	1.824	1.784	1.513
1SWASPJ090458.39-041848.4	102	1182		223±7	9.942	1.000	1.018
1SWASPJ102438.07-184643.4	211	1250		-84±3	9.853	2.291	1.000
1SWASPJ103846.50-343844.0	199	2220		38±2	4.148	1.782	1.801
1SWASPJ115026.75-245035.2	165	2230		20±3	1.219	1.000	1.012
1SWASPJ115840.26-235947.2	105	2231		53±5	4.515	2.002	1.000
1SWASPJ120621.96+020000.9	153	1844		-500±10	83.503	4.982	3.115
1SWASPJ121812.02+055941.0	109	1800	94.0±0.2;126.9±0.4	210±14	5.342	1.722	1.755
1SWASPJ123200.16-235418.1	181	2244	224.9±0.7	27±6	11.803	10.706	10.827
1SWASPJ125047.70-390333.3	192	2233		-17±7	1.034	1.000	1.009
1SWASPJ125121.92-450115.5	163	2232		-18±7	1.038	1.000	1.013
1SWASPJ130614.35-295708.2	141	2232		50±7	2.104	1.570	1.591
1SWASPJ132316.35-231859.3	191	2246		5±2	1.109	1.074	1.086
1SWASPJ133204.26-383632.3	175	2246	96.3±0.1	-98±6	7.813	2.971	1.771
1SWASPJ133951.71-265217.3	163	1944		-25±3	8.227	6.113	6.190
1SWASPJ134301.34-454726.2	166	2229	24.3±0.0	62±4	2.417	1.034	1.047
1SWASPJ134948.28+012317.9	157	1125	79.5±0.3	-170±18	3.715	2.278	2.181
1SWASPJ135601.81+045647.5	137	1115		380±21	3.463	1.038	1.053

Table 5.3 (cont.)

SWASP id	N	ΔT [d]	$P_{\rm BL}$	dP/dt [d d^{-1} $\times$ 10^{-4}]	lin χ^2	quad χ^2	sin χ^2
1SWASPJ135653.18-123320.2	75	1024		-220±48	4.528	3.536	3.636
1SWASPJ140105.09-405231.6	191	2244	77.7±0.2;51.9±0.1	-70±6	9.554	5.685	5.507
1SWASPJ140324.07-362420.1	144	1588		89±7	20.354	9.453	9.589
1SWASPJ143634.00-451253.4	118	2231		18±1	2.275	1.000	1.018
1SWASPJ144017.54-241127.7	164	2244		-30±6	1.175	1.002	1.000
1SWASPJ144407.36-283124.6	116	2233		31±4	1.581	1.000	1.018
1SWASPJ145315.45-143556.4	210	1482	35.6±0.0;49.9±0.1;42.1±0.0	220±27	27.286	20.491	20.223
1SWASPJ145427.29-251148.2	117	1879		33±3	2.037	1.000	1.004
1SWASPJ150340.77-292049.4	172	1947		-95±6	4.135	1.714	1.249
1SWASPJ150637.63-180552.1	110	2244	170.8±0.8;125.9±0.4	-59±3	4.063	1.000	1.006
1SWASPJ151542.10-283620.0	159	1947		50±33	4.501	4.439	4.365
1SWASPJ151855.15-164048.4	146	1482		206±7	6.402	1.000	1.014
1SWASPJ153118.79-173055.6	297	2233	22.9±0.0	-10±1	2.343	1.923	1.918
1SWASPJ153720.74-285924.4	158	2243	40.9±0.1	65±3	11.348	3.345	3.389
1SWASPJ154149.49-230324.0	89	2244		-44±6	1.621	1.000	1.083
1SWASPJ154203.23-275054.9	147	2243		-19±2	2.036	1.255	1.273
1SWASPJ154258.42-064922.9	225	1548	353.5±4.2;68.5±0.1	-114±7	14.461	6.456	6.400
1SWASPJ154330.77-292201.5	180	2244	28.9±0.0;108.3±0.2	-200±10	59.528	18.339	18.547
1SWASPJ155637.93-185049.7	227	1554	81.3±0.1	-61±7	5.124	3.756	3.789
1SWASPJ162007.21-173714.9	164	1546	40.2±0.0	-165±9	18.037	6.229	6.307
1SWASPJ185646.00-444010.6	146	2244	120.9±0.5	-48±6	4.442	3.140	3.184
1SWASPJ190707.07-320830.3	97	2243		62±7	1.883	1.070	1.000
1SWASPJ191045.84-453306.9	107	2232		-80±13	3.725	2.744	2.689
1SWASPJ193304.05-263235.9	139	2182		-77±4	3.436	1.079	1.078
1SWASPJ194006.38-292440.5	158	2241	41.3±0.0	111±8	11.053	4.916	4.425
1SWASPJ195005.68-682229.4	195	1484		84±4	7.717	2.437	2.111
1SWASPJ195013.90-335254.7	145	2243		92±9	5.515	3.111	3.155

Table 5.3 (cont.)

SWASP id	N	ΔT [d]	$P_{\rm BL}$	dP/dt [d d^{-1} $\times$ 10^{-4}]	lin χ^2	quad χ^2	sin χ^2
1SWASPJ195015.69-650256.0	180	1484		-89±7	2.450	1.229	1.000
1SWASPJ200026.89+485937.7	188	1207		54±4	10.305	4.858	4.765
1SWASPJ200914.89-293321.8	115	2226		-16±3	7.308	5.608	5.709
1SWASPJ201311.95-335639.3	138	2243	290.9±3.5;200.5±1.6	111±6	4.549	1.267	1.286
1SWASPJ201757.52-603656.0	215	1483	213.4±1.2	150±11	9.613	5.181	5.231
1SWASPJ202044.47-410705.9	170	2239	286.8±1.7	-120±6	90.817	24.838	25.138
1SWASPJ202812.31-423607.4	377	2234		38±2	11.108	5.426	5.412
1SWASPJ203158.38-184825.7	112	2220		-110±11	13.406	7.468	7.399
1SWASPJ211037.39-085345.0	192	1943		-30±2	5.600	2.885	1.000
1SWASPJ211437.86+073728.1	304	3343	54.1±0.0;79.9±0.0	-17±1	15.568	7.958	8.011
1SWASPJ211527.38-090942.6	137	1923		500±27	10.666	2.945	2.232
1SWASPJ211530.40+071513.6	194	3306	320.5±0.4	68±4	8.360	2.802	2.832
1SWASPJ211615.69-681458.0	215	1483		-131±9	2.281	1.186	1.000
1SWASPJ213530.97-390630.5	84	2212		44±5	1.828	1.000	1.025
1SWASPJ213621.04-695719.2	234	1484		-260±15	9.815	4.052	3.806
1SWASPJ214805.26-504931.2	176	1469	283.2±2.4;83.3±0.3	130±11	1.850	1.000	1.012
1SWASPJ214934.98-494730.1	282	1484		-80±3	5.742	1.511	1.522
1SWASPJ220453.96-663456.7	242	1484	45.7±0.1;138.4±0.5	207±7	24.031	5.482	4.955
1SWASPJ223321.57-233707.3	90	2197	35.9±0.0	-88±9	3.598	1.781	1.708

5.4.4 Analysis of quadratic results

Thirty visually parabolic diagrams identified during this visual inspection stage belonged to Blazhko effect objects. Figure 5.30 shows that quadratic models have similar qualities of fit for both Blazhko and non–Blazhko populations, below a χ^2 value of 10. This is contradicts the subjective impression that Blazhko objects can be identified due to the larger scatter in their O–C residuals. This also means that Blazhko effect objects cannot be excluded based on their quadratic χ^2 values alone.

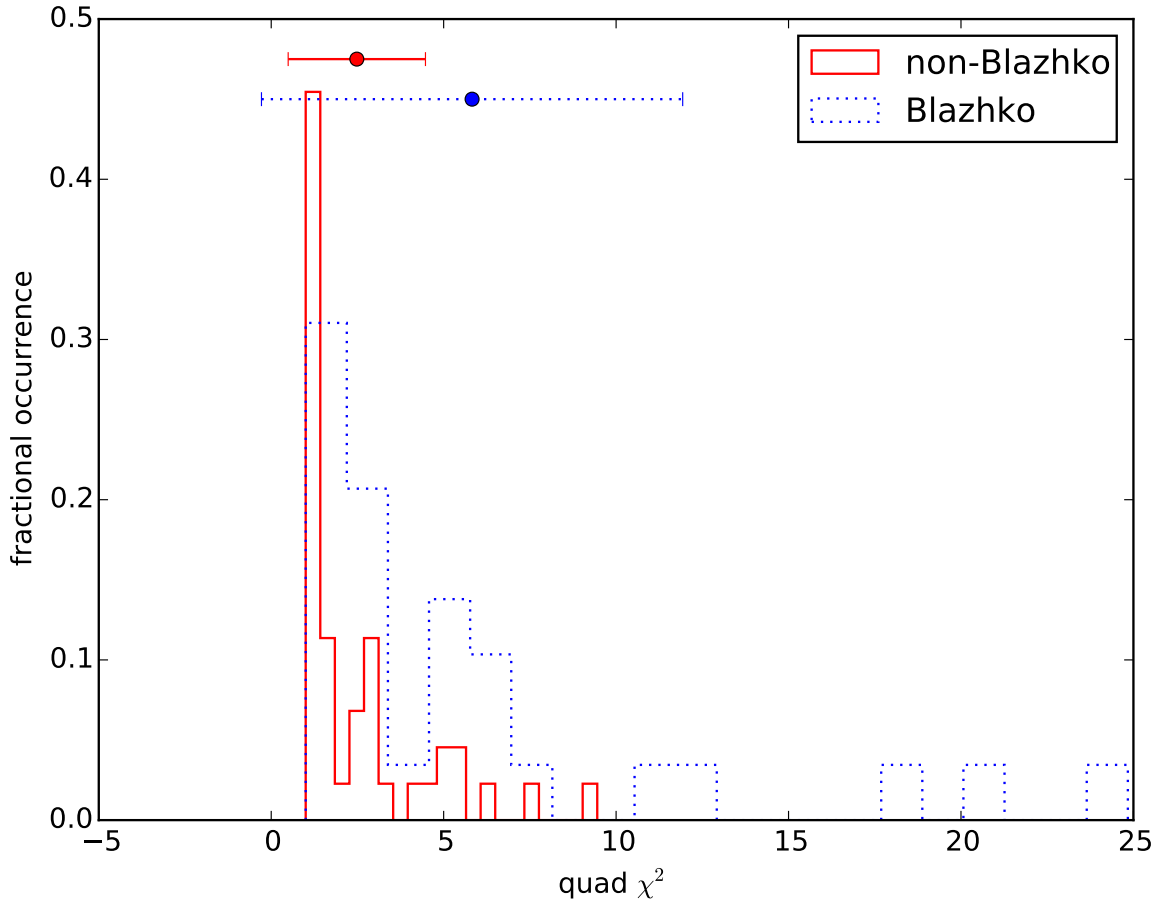

Figure 5.30: Comparison of goodness of fit values for Blazhko and non–Blazhko objects visually selected as having a parabolic trend.

The levels of curvature of all the visually selected quatratic objects are at least 2 orders of magnitude higher than the $\sim 10^{-6}$ d d^{-1} figures given in Li and Qian (2014) for the linear period change in their LTTE examples. It is therefore unlikely that the selected quadratic curves are part of an evolutionary period change. Table 5.3 shows, however, that some visual quadratic fits have lower sine χ^2 than quadratic χ^2 values. This is due to the extra degree of freedom of the sine fit, which can lead to overfitting in some cases. In the case of 1SWASPJ05558.57 for example, the last season of observation appears to be better fitted by

the sine model at the expense of an extremely large amplitude sinusoidal fit. The quadratic fit appears more accurate given the three seasons of data available for this object.

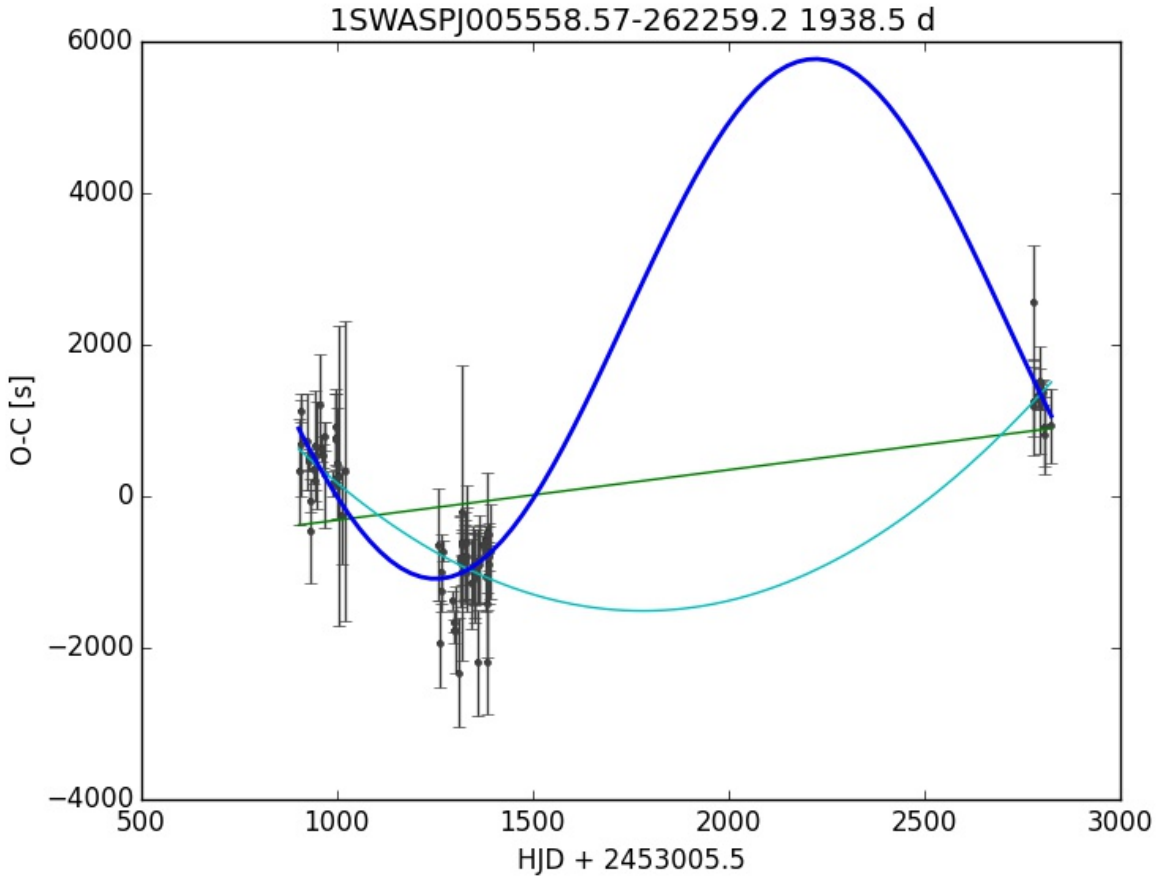

Figure 5.31: Linear, quadratic and sinusoidal fits to the O–C diagram of object 1SWASPJ005558.57-262259.2. The sinusoidal fit has a lower χ^2 value but an extremely large amplitude. The plot title includes the period in days, based on the sinusoidal fit.

Figure 5.32 shows that there is no correlation between the quality of the quadratic fit and the level of curvature. It also shows that there is no difference between objects defined as Blazhko using Fourier analysis and non–Blazhko objects in this regard.

Figure 5.33 shows that the amount of curvature in these cases does not appear to be dependent on the duration of observations (after outliers were removed). In particular, higher levels of curvature are not identified for objects observed over shorter durations implying that the curvature is not limited by the duration of observations. Similarly, Fig. 5.34 shows that the quality of fit for non–Blazhko parabolic O–C diagrams is also not dependent on the duration of observations. This figure also demonstrates that there is no bias towards positive or negative curvature in the O–C diagrams.

Figure 5.35 confirms that both Blazhko and non–Blazhko objects that were visually selected as parabolic have higher linear χ^2 values than quadratic χ^2 values, which implies that

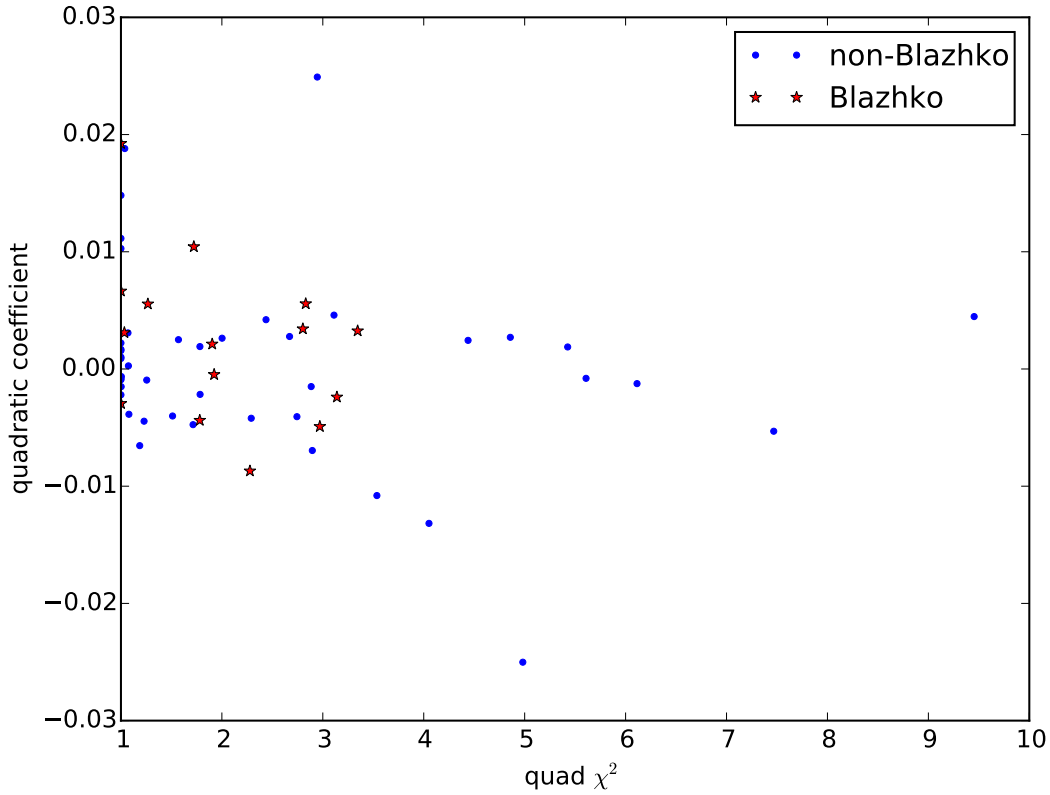

Figure 5.32: Curvature of the parabolic fit against its goodness of fit for visually parabolic O–C objects. There is no noticeable difference between Blazhko and non–Blazhko objects.

there is some merit to the visual identification of parabolic fits to O–C diagrams.

Figure 5.36 shows that an automated method of identifying quadratic SuperWASP O–C diagrams may exist by taking the ratio of the quadratic to linear χ^2 values for each object, at the 1σ limit: the upper 1σ limit for visually identified objects is 0.744, and the lower 1σ limit for the visually non–quadratic objects is 0.745. This result can be compared with the attempt at finding a threshold value using the sinusoidal to linear ratio for visually sinusoidal objects where there was too large an overlap between visually and non–visually identified objects. There are 56 more (over 4 times as many) quadratic than sinusoidal objects, so the sinusoidal χ^2 ratio may improve with more objects. The results of using a ratio of χ^2 values for the quadratic objects appears to have a similar confidence level (1σ) as the visually identified Blazhko objects. However, the distribution of the ratio for visually quadratic objects ranges from below 0.2 to almost 1.0 and appears more uniform than unimodal. It is therefore not possible to say that an object will definitely not have a quadratic trend above the 1σ limit, rather that an object with a ratio of χ^2 values below 0.74 is unlikely to be non–quadratic, with 68% confidence.

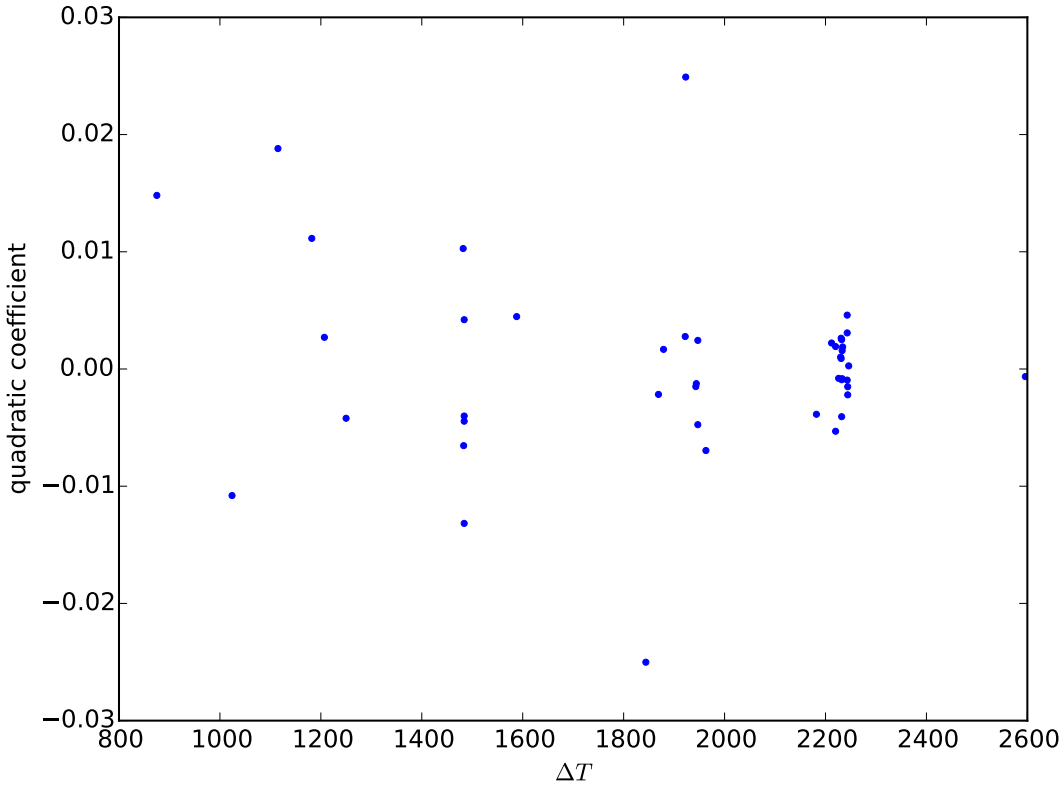

Figure 5.33: Quadratic coefficient of parabolic fits against duration of observations. There does not appear to be any limitation in the curvature of the O–C diagram caused by the duration of SuperWASP observations.

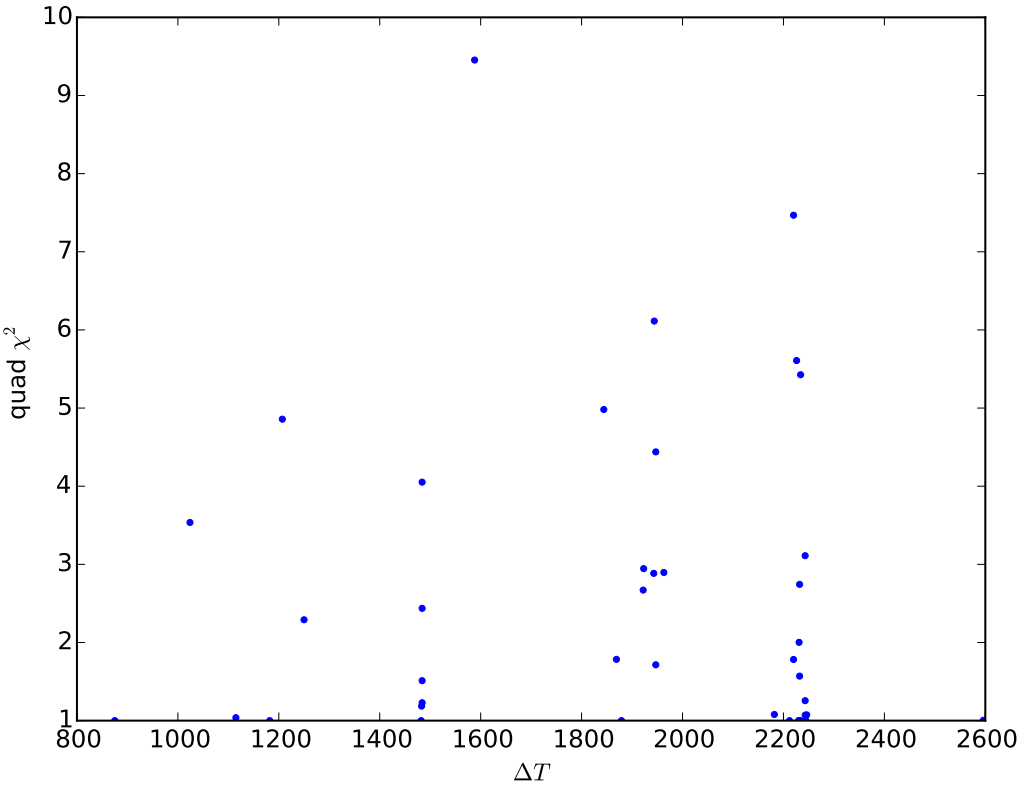

Figure 5.34: Quality of parabolic fits, measured by their χ^2 fit, against duration of observations. There does not appear to be any limitation in the quality of the fits to the O–C residuals caused by limitations in the duration of SuperWASP observations.

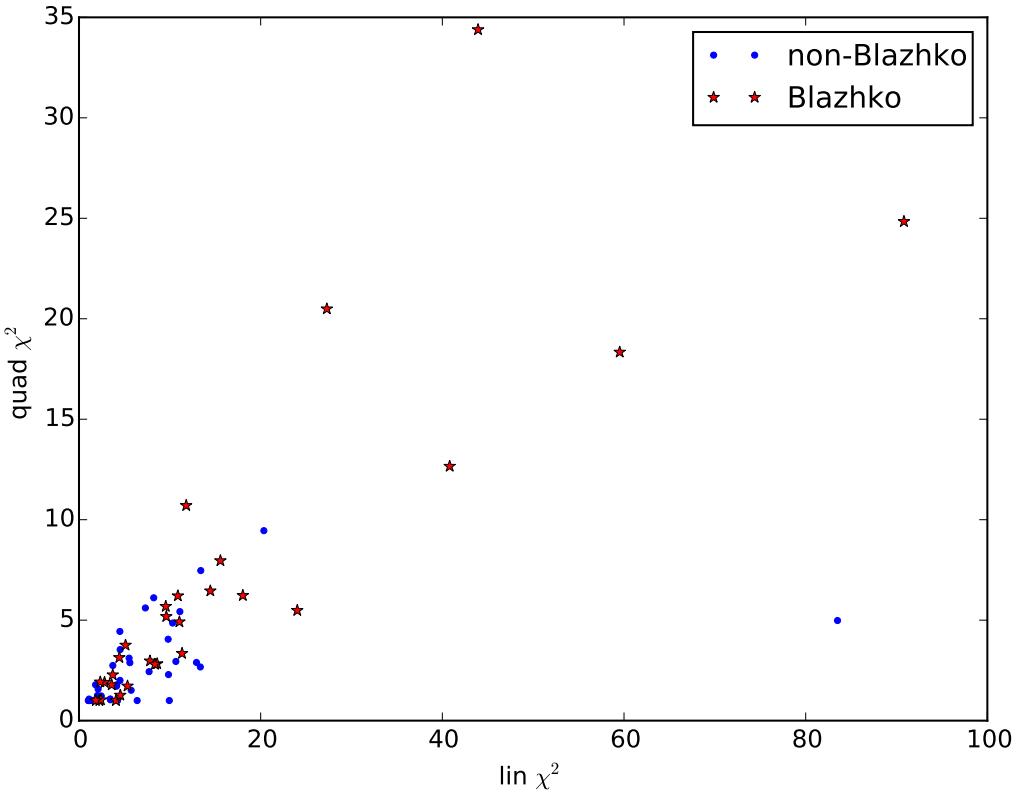

Figure 5.35: Comparison of linear and quadratic χ^2 values for the visually parabolic O–C objects. Blazhko effect candidates have a larger range of χ^2 values, symptomatic of the short timescale variability caused by the Blazhko PM.

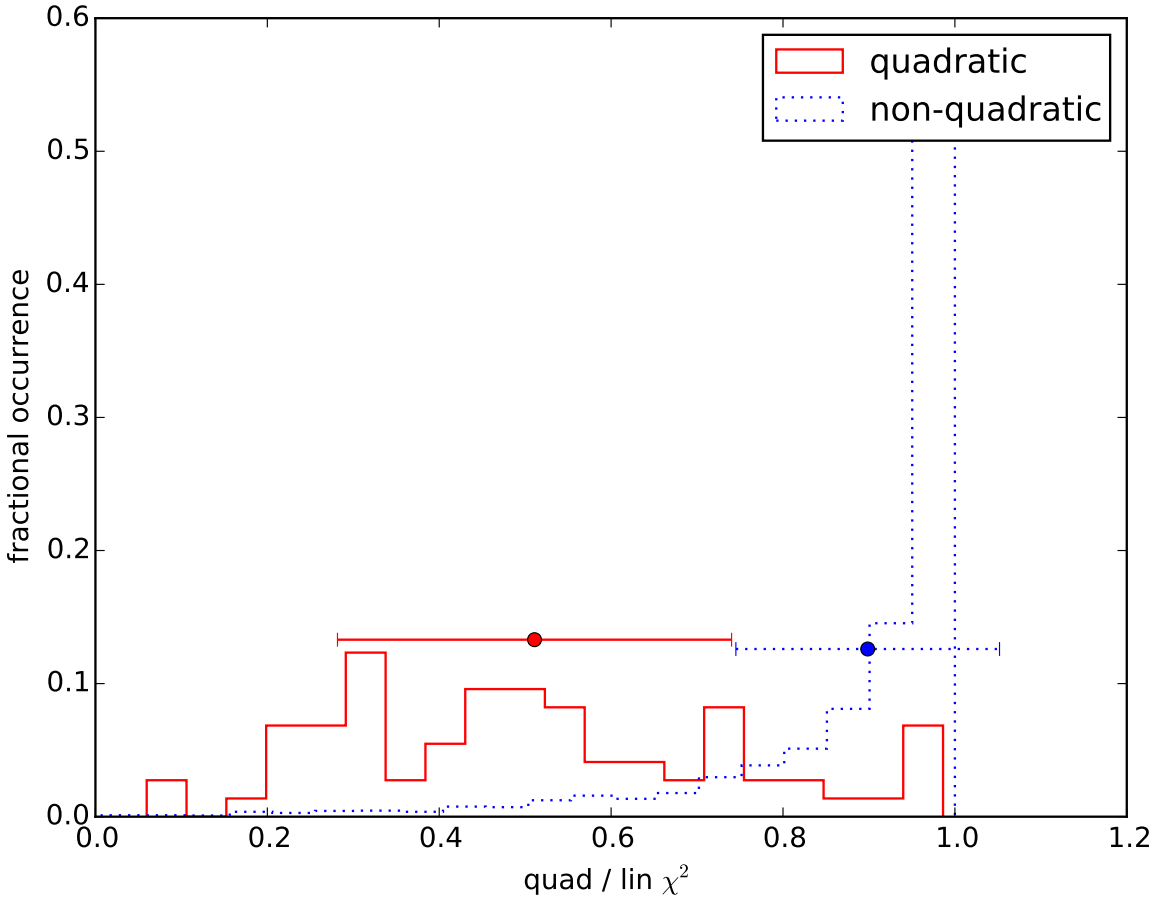

Figure 5.36: Comparison of quadratic to linear χ^2 ratios for the visually quadratic O–C objects against those deemed not to be quadratic. The 1σ uncertainties in the mean are shown by the error bars for each population. There does not appear to be an overlap of the two populations at this 1σ uncertainty.

5.5 Discussion

There is a level of subjectivity required for the acceptance of a phase–folded O–C diagram as being well folded, but since the curves are roughly sinusoidal in shape their identification is not overly difficult. Visual inspection of the CLEAN power spectra for the 53 new Blazhko candidates shows that they failed to be found using Fourier analysis for two main reasons. In 26 of the 44 objects, there were both sidebands and low frequency peaks in their CLEANed spectra. In 8 cases there were only sidepeaks, and in 7 cases there were only low frequency peaks. Therefore, the majority of these 53 objects were not selected as Blazhko candidates due to the sidepeaks and low frequency peaks not having coincident modulation frequencies. Based on the high number of Blazhko candidates that were successfully detected during the processes described in Chapter 4, it is unlikely that the peak–finding process failed to detect so many strong signal peaks. However, it is then unclear without an in–depth study of these particular objects why they would have modulation peaks that were not coincident at all. It is more likely that the peaks that are above the signal to noise thresholds in the frequency spectra are a mixture of some modulation peaks (which were successfully detected through the PM process) and some systematic aliases remaining after the CLEANing process.

12 of the 53 objects had neither sidepeaks nor low frequency peaks that were above the threshold signal to noise ratio required for automatic Blazhko detection. Only in these 12 cases (23%) can we definitely say that O–C based techniques were better than Fourier analysis techniques, since no modulation was detected in their frequency spectra. It should also be remembered that the PM method only detected a total of 140 objects compared to the CLEAN inspection method which detected 983 Blazhko candidates. Where objects appear in both FM and PM Blazhko datasets, but have a large discrepancy in their periods, it is possible that the visually selected PM objects have the correct period and that the automatically detected frequency peaks of the FM objects are actually systematic aliases of the true Blazhko period.

The same visual inspection showed that a further 7 of the 44 objects missing from the original SuperWASP Blazhko catalogue would have been excluded due to having noisy power spectra. A total of 9 extreme amplitude modulated objects were found using the O–C folding process. This suggests that the O–C based method is better than the Fourier analysis techniques in cases where the high level of amplitude modulation results in frequency spectra that are unsuitable for automatic detection of the Blazhko effect.

Regarding the 896 objects in the earlier SuperWASP Blazhko catalogue that were not detected by the O–C diagram folding technique, this appears to be due to a failure of the PDM routine to correctly phase–fold the O–C residuals. Their phase–folded O–C diagrams all show variability but no coherent pattern appears. In many cases, the uncertainties in the residuals are not excessively large, so the quality of the fitting stage does not appear to be a factor in the failure to find a modulation period.

The amplitude of the PM has been compared to the AM amplitude calculated using the relative peak scatter parameter from 3.3.1, but no correlation was found. It may be more useful to compare it against the upper envelope function from later in the same chapter.

In terms of automatically detecting Blazhko and LTTE objects in large datasets, two potential thresholds have been identified. The Blazhko effect may be identified by phase–folding the O–C diagrams, fitting sinusoidal and linear models to the data and then calculating the ratio of sinusoidal to linear χ^2 values from the models. However, the same ratio of sinusoidal to linear χ^2 values did not produce a threshold for unfolded O–C diagrams used to identify LTTE candidates. The final set of visually identified fits, the objects with quadratic trends in their residuals, produced the second threshold for systematic identification. This threshold was defined by calculating the ratio of χ^2 values of quadratic to linear models.

As in the folded O–C diagram process discussed so far, there are several factors to include when discussing the subjectivity of the visual inspection stage of the LTTE candidates. Visual inspection of unfolded O–C diagrams is more likely to miss a trend within each season due to noise, whereas the curve and sine fitting routines take errors into account and find the good points within each season before using these to produce a more rigorously fitted model to the data. However, the drawback of the curve fitting routines is that they tend to over–fit: they are more susceptible to points where the errors have been underestimated, or they include individual points near the start or end of observations which may be less reliable compared to an entire season of observations. The template fitting stage which calculated the O–C residuals included a vertical shifting of the template which should make the calculations more robust to vertical offsets between seasons.

Work by Li and Qian (2014) resulted in 2 binary systems containing RR Lyrae objects being identified from 21 non–Blazhko Kepler objects. Their binary systems represent a proportion of 9.5% from a small sample, which is far higher than the 0.3% identified in this

work, with 17 binaries identified from within an original catalogue of 4963 RRab objects. The minimum candidate LTTE period listed in Table 5.2 of 1122 d (3.07 yr) for object 1SWASPJ112322.47+063805.1 is within 10% of the smaller period found for V894 Cyg by Li and Qian (1046.0±11.8 d), and well above their suggested minimum period for binaries containing RR Lyrae of 500 d. The minimum period found in this study is 89% of the minimum period found by Hajdu et al. (2015) of 1255 d (3.5 yr) for OGLE-BLG-RRLYR-07640. Being near the Galactic bulge, this object is not included in the SuperWASP RRab catalogue.

5.6 Conclusions

This chapter has concentrated on the use of O–C diagrams to measure and look for periodicity in the PM of RR Lyrae objects in the SuperWASP RRab catalogue. Phase folding of O–C diagrams has led to the visual identification of 140 Blazhko candidates. 44 of these 140 objects were previously unidentified as Blazhko objects in either the Skarka database or the previous Fourier analysis in this work. A potential method has been found for automatically detecting Blazhko candidates using the ratio of their sinusoidal and linear goodness of fit measurements. A second method of identifying the Blazhko effect would be to perform Fourier analysis on the residuals. This would require another CLEANing process to remove the artefacts due to the SuperWASP observing schedule. The non–linear fitting method used to detect LTTE is similar to the method employed by the Period04 software, so there would be little benefit to using the software on the frequency spectra derived from the O–C residuals.

Visual identification of un–folded O–C diagrams has identified 17 binary candidates due to their sinusoidal shapes. The periods of the cyclic changes of the objects selected for having sinusoidal O–C diagrams are the same order of magnitude as the two binary candidates given in Li and Qian (2014). All binary candidates require confirmation through radial velocity measurements.

Another round of visual searching of the un–folded O–C diagrams for parabolic trends led to the identification of 45 objects with long term period change. These are potential binary objects with periods longer than the duration of observation, since their periods would be far longer than Blazhko periods, yet their curvature is too high for evolutionary effect. Us-

ing the ratio of their quadratic and linear goodness of fit measurements is a potential method of automatically identifying quadratic O–C candidates in large populations of objects.

Blazhko objects have been excluded while identifying LTTE, but visually identified sinusoidal and parabolic O–C diagrams of Blazhko objects could be useful. The short–term Blazhko effect components could be isolated using the Fourier analysis method, and removed, leaving the long–term component which can be investigated in order to further our knowledge of the Blazhko effect itself. Alternatively, with enough examples (which is a strength of large–scale robotic ground–based surveys), it may be possible to determine additional effects, in the same way that a long term evolutionary effect can be removed from LTTE curves.

Chapter 6

Conclusions and Future Work

This research has investigated the Blazhko effect of RR Lyrae stars using a large sample of objects from the SuperWASP archive. The SuperWASP observations have facilitated the fitting of templates to individual pulsations on the timescales of a few hours, and the identification of long–term changes in the frequency of pulsations on the timescales of up to a year. These have been made possible thanks to SuperWASP's combination of high cadence and wide–field coverage allowing the same objects to be observed many times a night for several weeks over the course of several years. The archive contains millions of objects so the results of the machine learning classification by S. Payne were used as a starting dataset of a manageable size. The initial stage of this study, the identification of RRab class RR Lyrae objects, resulted in a dataset of 4963 objects. Throughout this study, systematic methods have been developed to automate the processing such a large dataset of astronomical data. These methods have included automating the CLEAN algorithm to run on batches of 100 objects at a time; combining the phase–folding techniques and template fitting programs to create O–C residuals that can be phase–folded to find their Blazhko periods; adapting the scatter measuring program to identify and extract the pulsation peak to be further analysed for symptoms of AM.

The common feature throughout this research has been the identification of common properties, trends and correlations in RR Lyrae objects, in particular those identified as being modulated by the Blazhko effect. For instance, a new technique of calculating the relative levels of scatter at the peak of the phase–folded light curves was devised after observing the same characteristic feature in a large proportion of known Blazhko objects. During this

stage the pulsation characteristics (period, amplitude and median light curve brightness) were measured. The initial catalogue of 8556 RRab candidates were refined through inspection of their phase–folded light curves leading to the creation of a SuperWASP RRab catalogue containing 4963 RRab candidates. Fourier spectra was used in order to isolate the power and period of the Blazhko effect in order to look for trends in Blazhko properties. This led to a novel approach to identifying Blazhko in power spectra of SuperWASP RRab objects utilizing the high cadence and long duration of SuperWASP observations. Identification of low frequency peak due to the change in average brightness, and equidistant sidebands during the CLEAN process has resulted in the identification of the of 983 Blazhko objects. The search for correlations was then expanded to include Blazhko effect properties, such as Blazhko period and amplitude, and compare them to the pulsation properties from the RRab catalogue. The results and analysis of the Fourier and AM investigation have been published in the Astronomy and Astrophysics journal.

A second approach to measuring the Blazhko period in candidate objects was developed by looking for trends in O–C residuals, resulting in 140 Blazhko candidates, 44 of which were previously unidentified in Skarka dataset or the previous Fourier analysis stage. This O–C analysis also led to the identification of 17 candidate binary objects due to their sinusoidal O–C curves. Such objects containing a horizontal branch pulsator are extremely rare. 73 objects had quadratic O–C curves, which are suggestive of binary candidates with periods longer than the duration of SuperWASP observations, as the curvature of the O–C diagrams is too high to be due to changes as the stars evolve in the horizontal branch. Preliminary results from this work are due to be published in the Proceedings of the Polish Astronomical Society.

In conclusion, these results show a lack of correlation between characteristics of the Blazhko effect. There does appear to be a lack of Blazhko effect RR Lyrae with long pulsation periods. Despite this, the Blazhko period is independent of other aspects of the pulsation mechanism. This apparent lack of correlation between any Blazhko characteristics and also between the Blazhko and pulsation characteristics raises some questions about these results.

If the lack of correlations was due to a lack of precision in SuperWASP data, this would create more scatter around the correlating trends in the properties analysis, but the trends would still be apparent.

The method of calculating the Blazhko amplitude relies of the asymmetrical modulation of light curve maxima and minima. Even if this only captures a proportion of the true Blazhko amplitude it should still express the relative AM power between objects and thereby allow a comparison of Blazhko properties between objects.

If the wrong objects had been classified as Blazhko, these would appear as outliers in a sample as large as the SuperWASP archive data. The analysis stage also shows that the lack of correlations are clearly not due to a lack of candidate objects.

Putting the results of this study alongside other photometric studies, the simple explanation is that the Blazhko effect does not provide any correlations in photometric observations in the visible waveband, despite the evidence of the variation in brightness of the photosphere being affected by modulations. This is disappointing as a statistically significant correlation would have been useful to the hydrodynamical models of Kallath et al.. Perhaps another variable such as metallicity needs to be removed in order to see the true correlations between the Blazhko and pulsation attributes.

The intriguing feature of period doubling has not been independently investigated within this study as it is expected to be too subtle for SuperWASP's detectors. The range of pulsation periods in the SuperWASP RRab objects means however that there are plenty of RRab objects with pulsation periods long and short enough to allow ground–based observations of this anomaly, should they have the sensitivity.

The identification of the of the Blazhko objects was made more convoluted due SuperWASP's irregular sampling creating a complex window function, and large levels of scatter compared to space–based observations. Also, differences in average brightness between seasons due to different seasonal fields of view, and objects being observed simultaneously with multiple cameras may have occurred. Both of these systematic effects may result in higher levels of scatter in flux values, but not in the timings of observations.

6.1 Future Work

This section describes what research could be continued in the future, based on the results of the study so far. Firstly, the visual selection of RRab objects can be made more systematic in the future by calculating the ratio of harmonics in the Fourier spectra, rather than visual

inspection of their phase–folded light curves.

Further investigations could be made into making the process robust enough that the extreme AM objects could be automatically detected as Blazhko objects. However, individual CLEAN parameters may be required for such objects. It would also be productive in performing more in–depth analysis of individual objects or small data sets of a handful of objects, for example, those Blazhko candidates in multiple SuperWASP catalogues but with different Blazhko periods, or objects such as 1SWASPJ120447.27-274043.2 (IK Hya) with varying or anomalous Blazhko periods.

Due to the additional stage of using Period04, the only Blazhko amplitude is that of the low frequency peak, i.e. the change in average brightness over the course of a Blazhko cycle. This will result in the correct Blazhko period, but it may only represent a fraction of the true amplitude of the Blazhko effect. An alternative method of using the height of the corresponding sidepeak in the CLEANed spectra to represent the Blazhko amplitude is that the power of the modulation signal will be spread across all harmonics and the proportion will not be consistent. Investigation of the scatter at the peak of the light curve compared to an unaffected region has had mixed results. This does not appear to be due to the PM aspect of the Blazhko effect, as previously thought. An alternative measure of the Blazhko amplitude could be based on the amplitude of the envelope function isolated from the peak of the phase–folded light curve. This upper envelope would give a larger estimate of the amplitude than the change in mean brightness, but there is still no guarantee that there would be any correlation between this and other aspects of the Blazhko effect, even if this amplified the effects of the modulation. Distance and reddening affect brightness, but the location and distance of the stars should not make any difference to analysis of the pulsation amplitude or period. Obtaining the distance to the SuperWASP RR Lyrae objects, through Gaia observations for example, would allow the calculation of the absolute luminosity of these objects. It would be interesting to look for new correlations between Blazhko characteristics and this intrinsic property.

There does not appear to be a threshold level of scatter at the peak of the phase–folded light curve that indicates the Blazhko effect. However, potential thresholds were found for automatically indicating Blazhko objects based on the ratio of quality of sinusoidal to linear fits to their phase–folded O–C diagrams. However, there was not a corresponding threshold

for detecting binary candidates via LTTE. There is also a method of automatically indicating quadratic O–C diagrams in large samples by taking the ratio of their quadratic and linear goodness of fit measurements.

The catalogues produced in this work all contain what have been deemed ‘candidates’. This term has been used judiciously as the final classification of all these objects, whether as ‘RRab’, ‘Blazhko’ or ‘binary’ requires a second method of analysis. The discovery of several binary systems containing pulsators in particular is worthy of further work, where spectroscopic analysis would be required to confirm if the visible pulsators are indeed orbiting a common centre of mass. Despite this requirement for analysis using different methods, there are still several objects within the SuperWASP archive, highlighted in this work, that could provide more information on the Blazhko effect, given individual, in–depth analysis. The SuperWASP archive can be a source of interesting research for years to come. The methods, analysis and results developed during work with SuperWASP data will continue to be useful for the next generation of surveys, such as the LSST and PLATO.

The main RRab catalogue provides a new dataset of standard candles. The distances to these objects has been calculated in this work using a single known absolute magnitude, and these distances can be compared with those presented in future Gaia data releases for objects in both datasets. By identifying differences in distance, and therefore absolute magnitude, this comparison can thereby contribute to the improvement of calibrations of period–luminosity–metallicity relationships.

This work provides several points which contribute to future research into the physical explanation of the Blazhko effect. Any models of the Blazhko effect need to be able to reproduce the number of multiple periods per object discovered in this work (261/983=27%). They also need to be able to reproduce the large levels of AM with very little PM shown in examples from the EAM section of this work. These models should not produce any correlations between the parameters, in particular the model should not rely on a relation between the Blazhko period and amplitude. It should also not rely on correlations with the pulsation period and amplitude. An interesting feature that physical models should not rule out is variable modulation periods, such as with IK Hya whose variable Blazhko period has been confirmed in this work. They should also reproduce the large range of scatter at the peaks of the light curve, replicating the early findings of this study. Finally this work

has shown that ground-based surveys can still contribute to variable object research, and, given high enough cadence combined with long enough observing timescales, they can even identify very long term variability such as LTTE for objects in wide orbits.

6.2 Reflections

The need to create workflows and pipelines in order to work efficiently and productively with large data has been an interesting aspect to this study. The total number of objects was not excessive, but an individual light curve can have hundreds of nights with nearly a hundred points per night, so a systematic approach to repeating the analysis for each object was needed. Often the process was automated to the extent that the workload could be spread across fifty independent nodes on the university cluster server, often saving weeks of computation time. The SuperWASP FITS files were converted to ASCII text files containing only the timing, flux and error fields, as these were needed by the CLEAN routine. However, these text files were then used as the input files throughout the rest of this study because the clipping of outliers had been included during this stage. The analysis stage of each chapter would be improved over several iterations and therefore would become a separate stage in the pipeline. The plotting and table production stages of each chapter were also written into a separate program, allowing results to be reproduced efficiently after each iteration.

Appendices

Appendix A

This appendix, available in electronic format, contains the full SuperWASP catalogue of 4963 RRab class RR Lyrae objects. The headings are as follows: SWASP id: unique SuperWASP object identifier; P_{Pulse} : pulsation period in days; A_{LC}: pulsation amplitude in magnitudes; $\tilde{m}_{LC}$: median light curve brightness in magnitudes; d[kpc]: distance in kiloparsecs; GCVS name: name of coincident object from the General Catalogue of Variable Stars; CRTS name: name of coincident object from the Catalina Real–Time Transit Surveys.

Appendix B

This appendix shows the yearly then weekly light curves for each object given in Table 3.7. For each object, the unfolded light curves are also presented for a year exhibiting strong AM, along with the entire light curve for the same object phase folded at the candidate Blazhko period found by the PDM routine described in Chapter 3. At the timescales of both the year–long segments and the phase folded light curves, individual pulsations are compressed horizontally to the point where they appear as vertical stripes of points in both light curves.

a) 1SWASPJ004757.06+114223.5

The year–long light curves for 1SWASPJ004757.06+114223.5 folded by the pulsation period (Fig. B.1) show a clear distinction between the low and high amplitude phases of the modulation cycle. The lower amplitude phases can be seen in weeks 399, 400, and 401 of Fig. B.2.

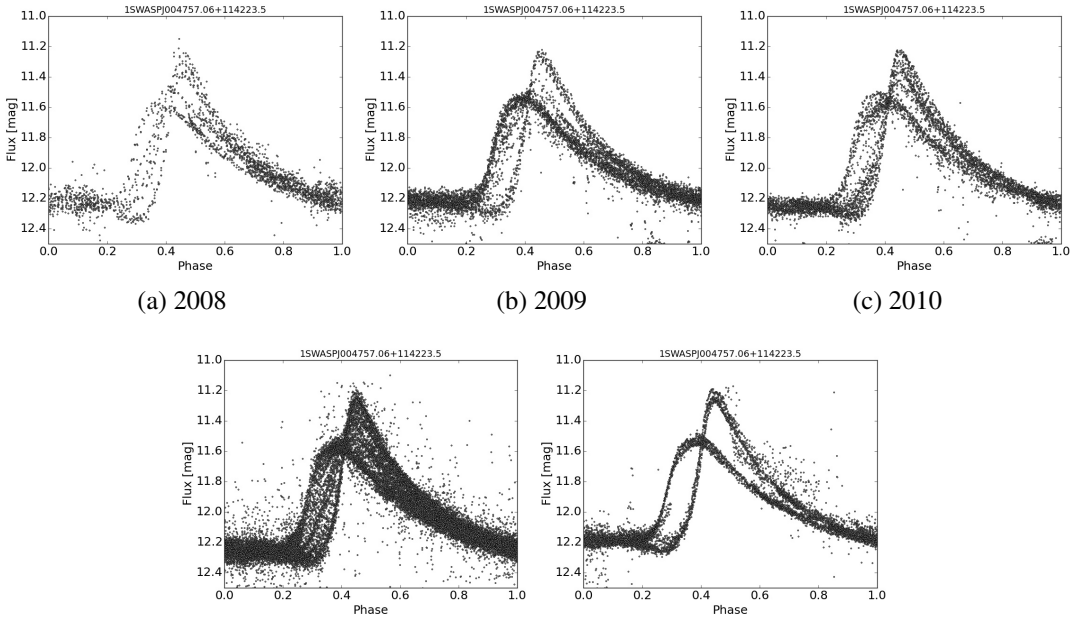

(a) 2008 (b) 2009 (c) 2010

(d) 2011 (e) 2012

Figure B.1: Yearly light curves of 1SWASPJ004757.06+114223.5 from 2008 to 2012 showing how each year contains both a high and low pulsation amplitude. Flux levels are in mag to show the flux consistently for each year.

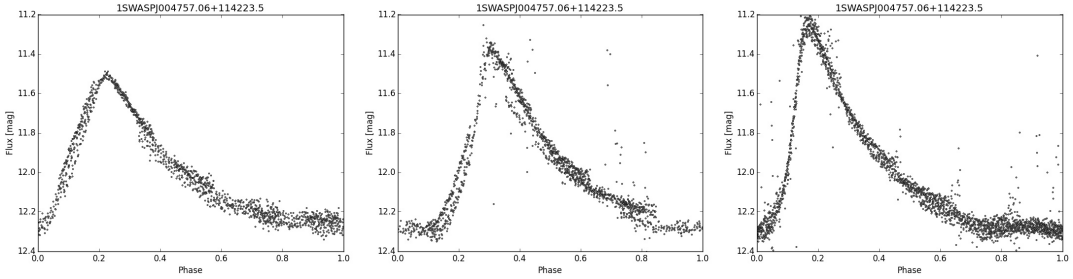

(a) 394

(b) 395

(c) 396

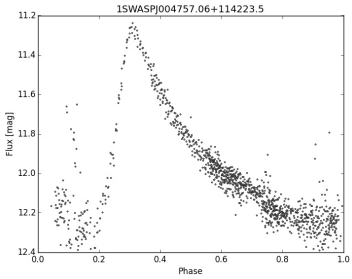

(d) 397

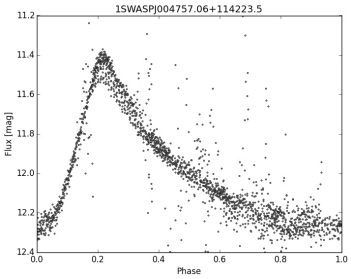

(e) 398

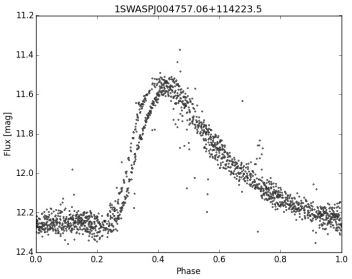

(f) 399

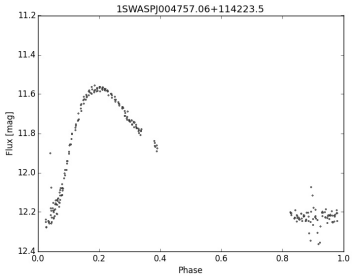

(g) 400

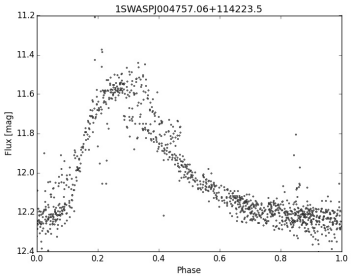

(h) 401

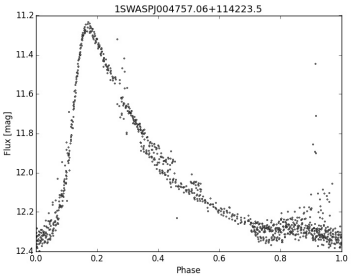

(i) 403

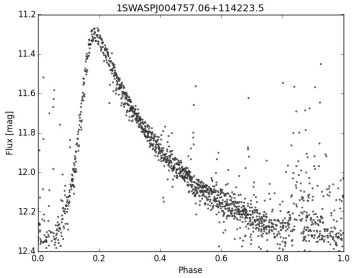

(j) 404

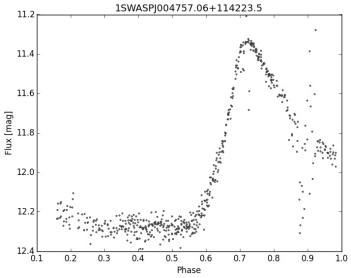

(k) 405

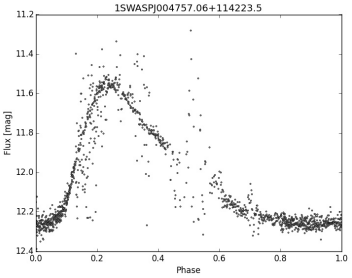

(l) 406

Figure B.2: Weekly sections from 2011 of the light curve of 1SWASPJ004757.06+114223.5 for the weeks with enough data for light curve plotting. The week number from the start of the light curve is given under each plot and flux is in magnitudes. All weekly sections of the light curve are folded on the same pulsation period of 0.65029929 days with no change in the phase offset.

The unfolded light curve for 1SWASPJ004757.06+114223.5 from 2011 spanning 120 d (Fig. B.3) shows a clear envelope function with approximately 2 cycles within those 120 d. The PDM program found a candidate Blazhko period of 51.3 d (Fig. B.4). The lower envelope in this case is very subtle, with only a small change in the minima of the pulsations.

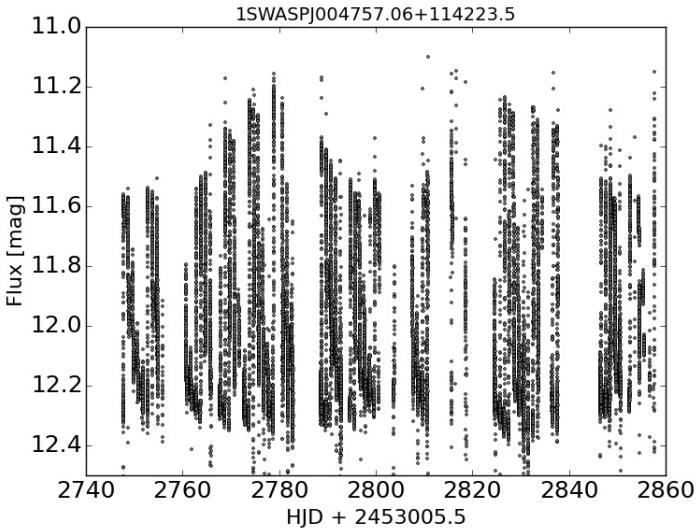

Figure B.3: Unfolded light curve from observations made during 2011 of 1SWASPJ004757.06+114223.5 showing a modulation period of roughly 60 d.

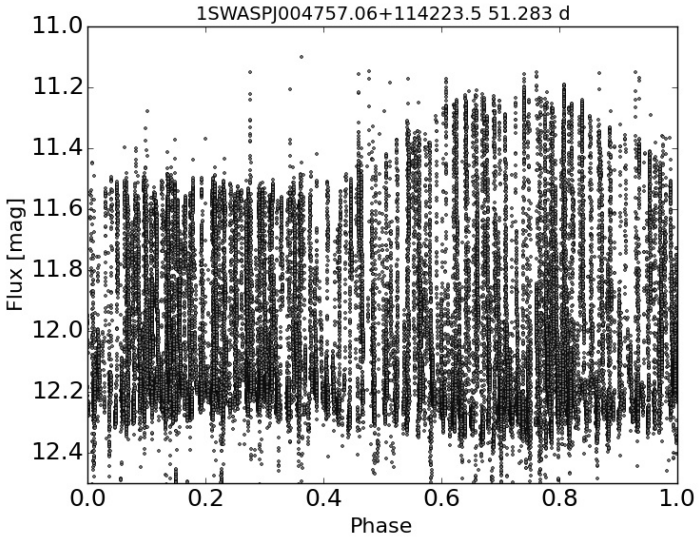

Figure B.4: Light curve for 1SWASPJ004757.06+114223.5 phase folded by a candidate Blazhko period of 51.3 d showing an accurately folded envelope function.

b) 1SWASPJ010510.70+341306.2

The light curves of these extreme AM objects can be misconstrued as the object pulsating simultaneously in two modes, which does actually occur in the case of RRd (double mode) class objects. However, in the case of RRd objects, the light curves do not show two clearly defined curves but a spread of points, as both modes in RRd have different periods. In the extreme AM examples given here, one of these 'modes' appears more dominant than the other due to the difference in the density of the flux data points in each of the light curve pulsation shapes, such as the final two years of 1SWASPJ010510.70+341306.2 (Fig. B.5). The unfolded light curve, used to highlight the envelope function, explains that this density is related purely to the timing of the observations, since it is due to the number of points captured during the Blazhko phase with larger or smaller amplitudes. In the case of 1SWASPJ010510.70+341306.2 in 2013 (Fig. B.5e), more observations were made during the low amplitude phase of the Blazhko effect when the pulsation amplitude was reduced, making the smaller pulsation shape appear more 'dominant', i.e. the density is not due to the duration of the high or low amplitude phases of the Blazhko effect. The weekly folded light curves for 1SWASPJ010510.70+341306.2 (Fig. B.6) show the AM reaching a maximum at week 498, and the pulsation peaks in the other weeks are more rounded.

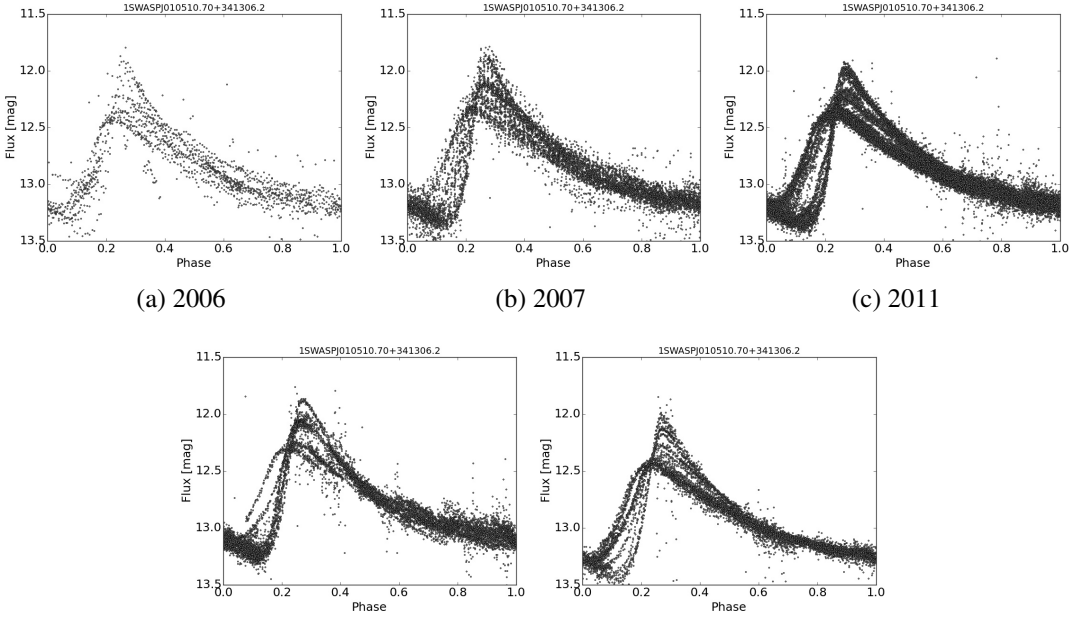

(a) 2006 (b) 2007 (c) 2011

(d) 2012 (e) 2013

Figure B.5: Yearly light curves of 1SWASPJ010510.70+341306.2 in 2006, 2007, 2011, 2012 and 2013 showing some small but clear signs of AM as each year contains at least one light curve pulsation shape. Flux levels are in mag to show the flux consistently for each year.

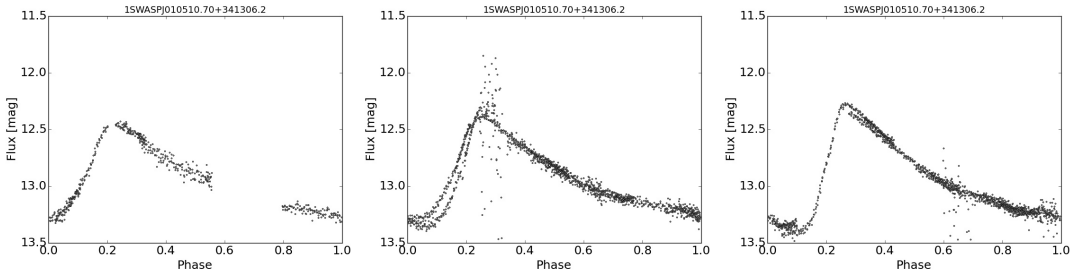

(a) 495 (b) 496 (c) 497

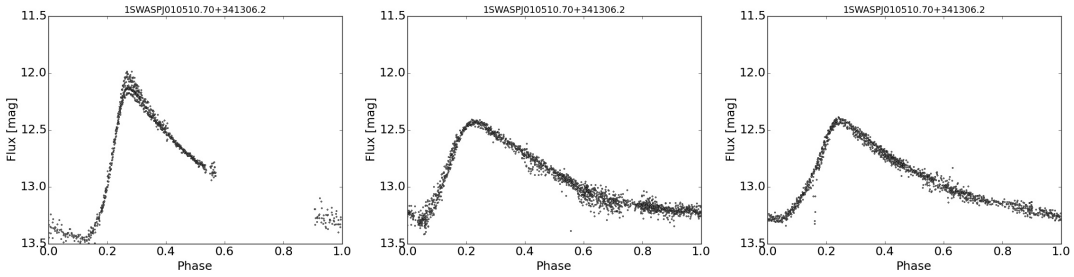

(d) 498 (e) 502 (f) 504

Figure B.6: Weekly sections of the light curve of 1SWASPJ010510.70+341306.2 for the weeks 495 to 504. The week number from the start of the light curve is given under each plot and flux is in magnitudes.

The timings of the observations of 1SWASPJ010510.70+341306.2 in 2013 (Fig. B.7) means more data points were recorded during low amplitude phases of the Blazhko effect. This led to the lower amplitude pulsations appearing to be more ‘dominant’ in that year. The PDM routine identified a candidate Blazhko period of 49.9 d and Fig. B.8 shows the light curve folded at this period.

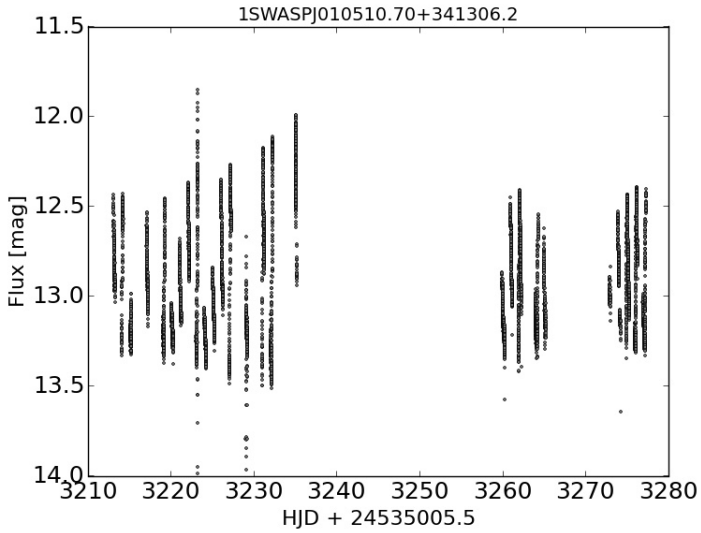

Figure B.7: Unfolded light curve from observations made during 2013 of 1SWASPJ010510.70+341306.2. Part of the envelope function due to AM can be clearly seen as a change in the amplitude of the pulsations.

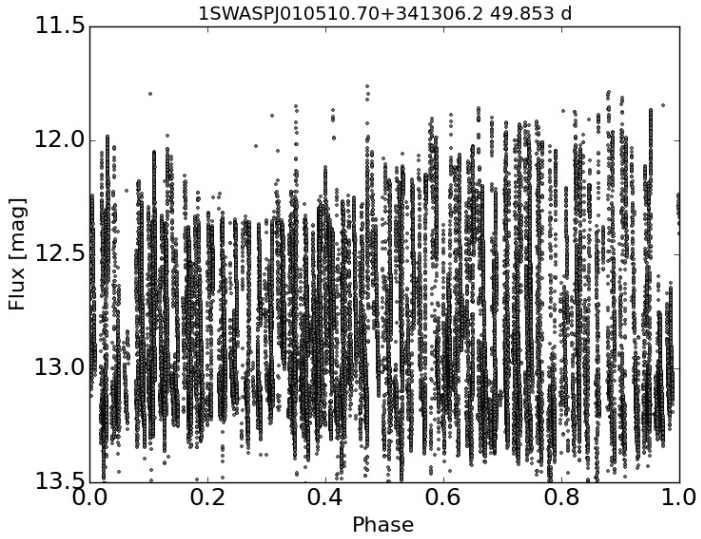

Figure B.8: Light curve for 1SWASPJ010510.70+341306.2 phase folded by a candidate Blazhko period of 49.9 d showing a clear envelope function.

c) 1SWASPJ091348.80-091908.8

The pulsations in the year long phase folded light curves for 1SWASPJ091348.80-091908.8 (Fig. B.9) show very little change in phase, helping to express the effects of AM. The extreme AM can be seen in the difference between the amplitude of weeks 366 and 368 and the opposite change is seen between weeks 375 and 377 (Fig. B.10), thereby capturing the entire candidate Blazhko period.

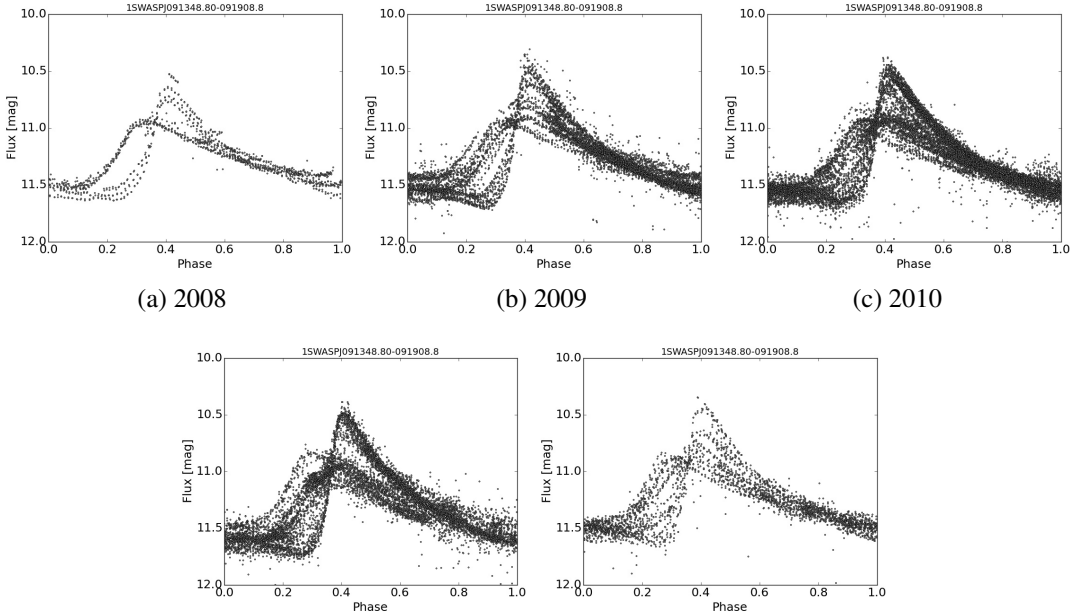

(a) 2008 (b) 2009 (c) 2010

(d) 2011 (e) 2012

Figure B.9: Yearly light curves of 1SWASPJ091348.80-091908.8 from 2008 to 2012.

Figure B.11 for 1SWASPJ091348.80-091908.8 in 2011 shows a strong AM period of approximately 30 d. The PDM program finds the candidate Blazhko period at 26.3 d (Fig. B.12) using the entire light curve for 1SWASPJ091348.80-091908.8.

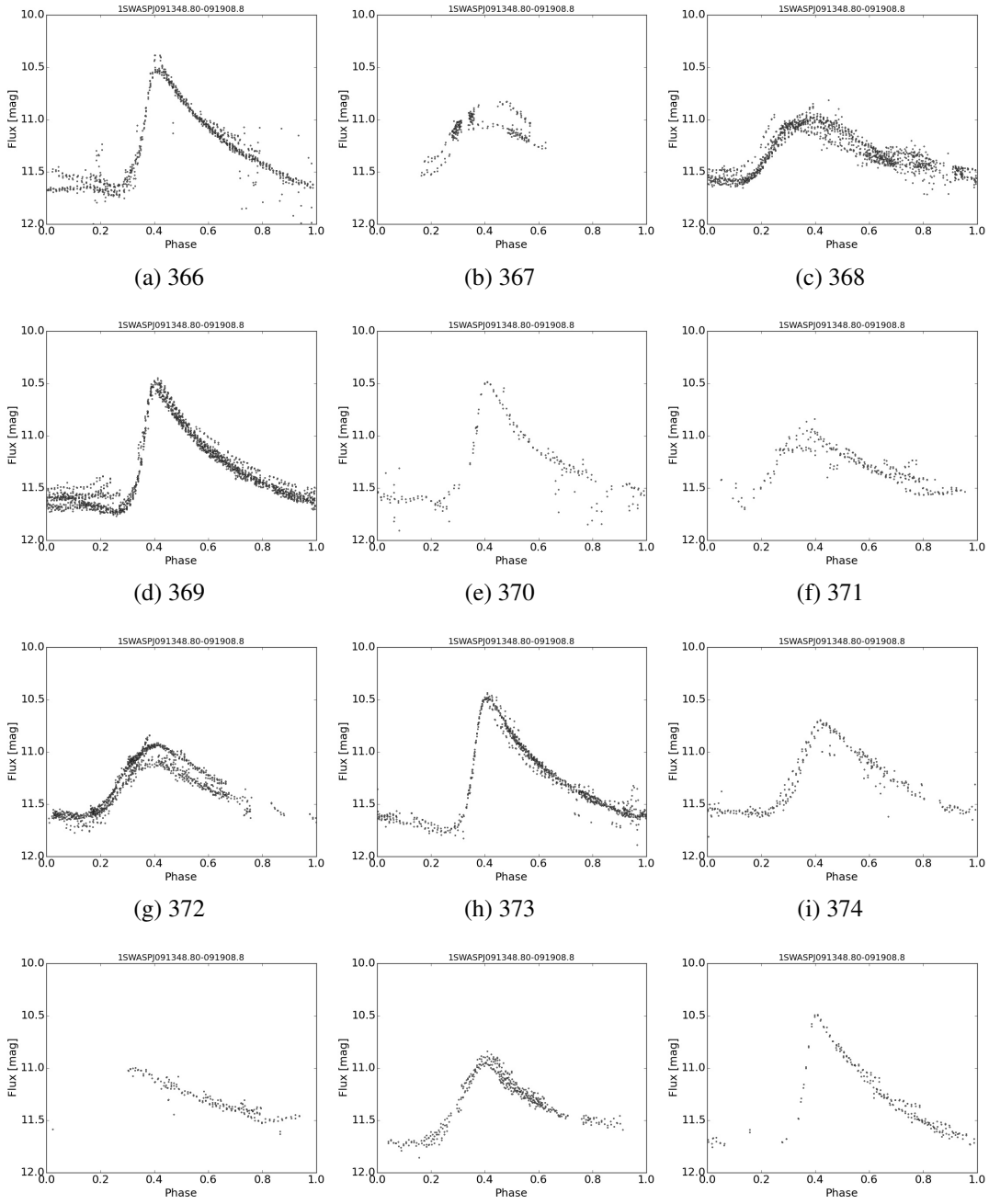

(a) 366 (b) 367 (c) 368

(d) 369 (e) 370 (f) 371

(g) 372 (h) 373 (i) 374

(j) 375 (k) 376 (l) 377

Figure B.10: Weekly sections of the light curve of 1SWASPJ091348.80-091908.8 for 12 consecutive weeks 366 to 377. The week number from the start of the light curve is given under each plot and flux is in magnitudes.

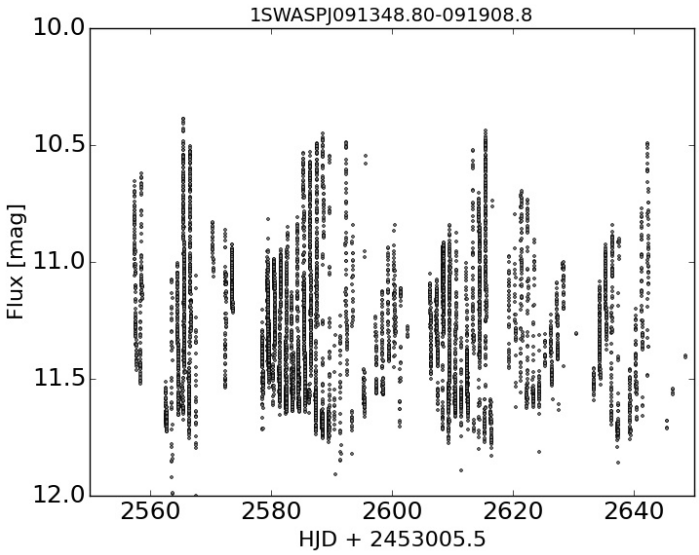

Figure B.11: Unfolded light curve from 2011 of 1SWASPJ091348.80-091908.8.

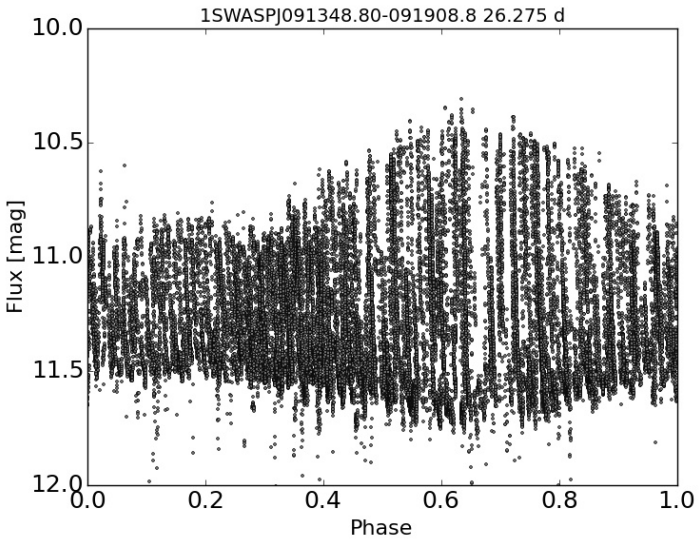

Figure B.12: Light curve for 1SWASPJ091348.80-091908.8 phase folded by a candidate Blazhko period of 26.3 d.

d) 1SWASPJ091809.74-193718.4

Being a ground–based survey, SuperWASP's daily observing schedule suffers from being roughly twice the pulsation period of most RR Lyrae stars. This can mean that the part of the pulsation being observed can change slowly over the course of an observing season which can look like amplitude modulation if the light curve is not folded. An example of this is object 1SWASPJ091809.74-193718.4 whose unfolded 2011 light curve (Fig. B.13) shows periodic decreases in brightness more obviously than any modulation effect. However,

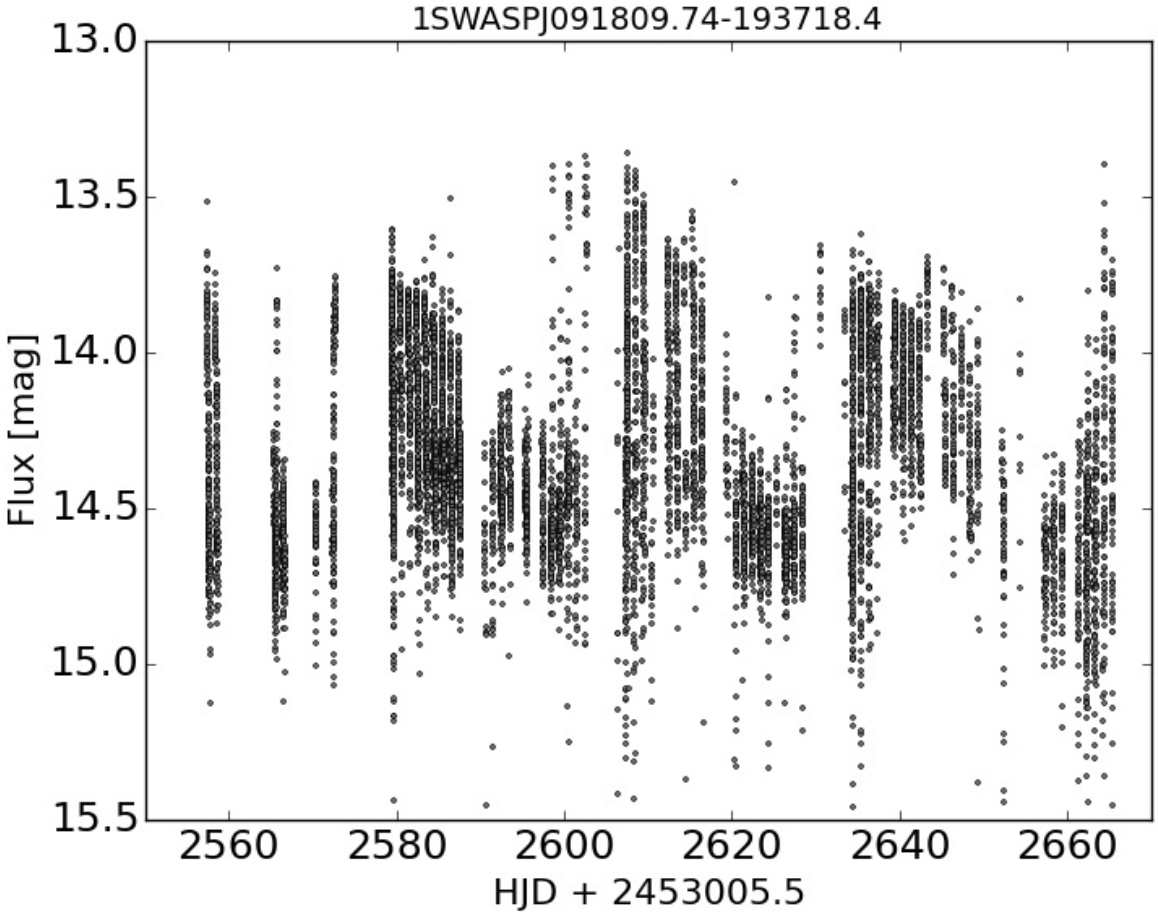

Figure B.13: The unfolded light curve of 1SWASPJ091809.74-193718.4 from 2011 showing regular decreases in median pulsation brightness due to a slight phase difference between observations and pulsations.

inspection of the weekly sections of light curve (Fig. B.14) show that this is not caused by systematic changes during the observing schedule, but by different segments of the pulsation being observed during each week.

Instead, the AM is clearly visible when the yearly light curve is folded (Fig. B.15). The pulsation amplitude changes with no clear change in vertical offset caused by an instrumental effect for instance. The change in horizontal position of the pulsation in the phase folded light

curve could be due to monotonic period change (i.e. the pulsation period derived from PDM could be slightly wrong) or it could be an indication of phase modulation. In the former case, further observations from other years would show a continuation in this phase shift. In the latter case, the phase shift would increase and decrease periodically as the light curve undergoes positive and negative phase changes. This change in phase is taken up in more detail in the later chapter on the Blazhko effect in the phase domain, but the combination of both amplitude and phase modulation is a common symptom of the Blazhko effect in the time domain.

The unfolded 2011 light curve for 1SWASPJ091809.74-193718.4 was previously shown in Fig. B.13, where the declining average light curve brightness was commented on. Figure B.16 shows that the PDM program finds the candidate Blazhko period of 49.4 d. As in the case of objects 1SWASPJ004757.06+114223.5 and 1SWASPJ091348.80-091908.8, the upper envelope function appears to remain almost constant for part of the Blazhko cycle, rather than continue in a sinusoidal shape.

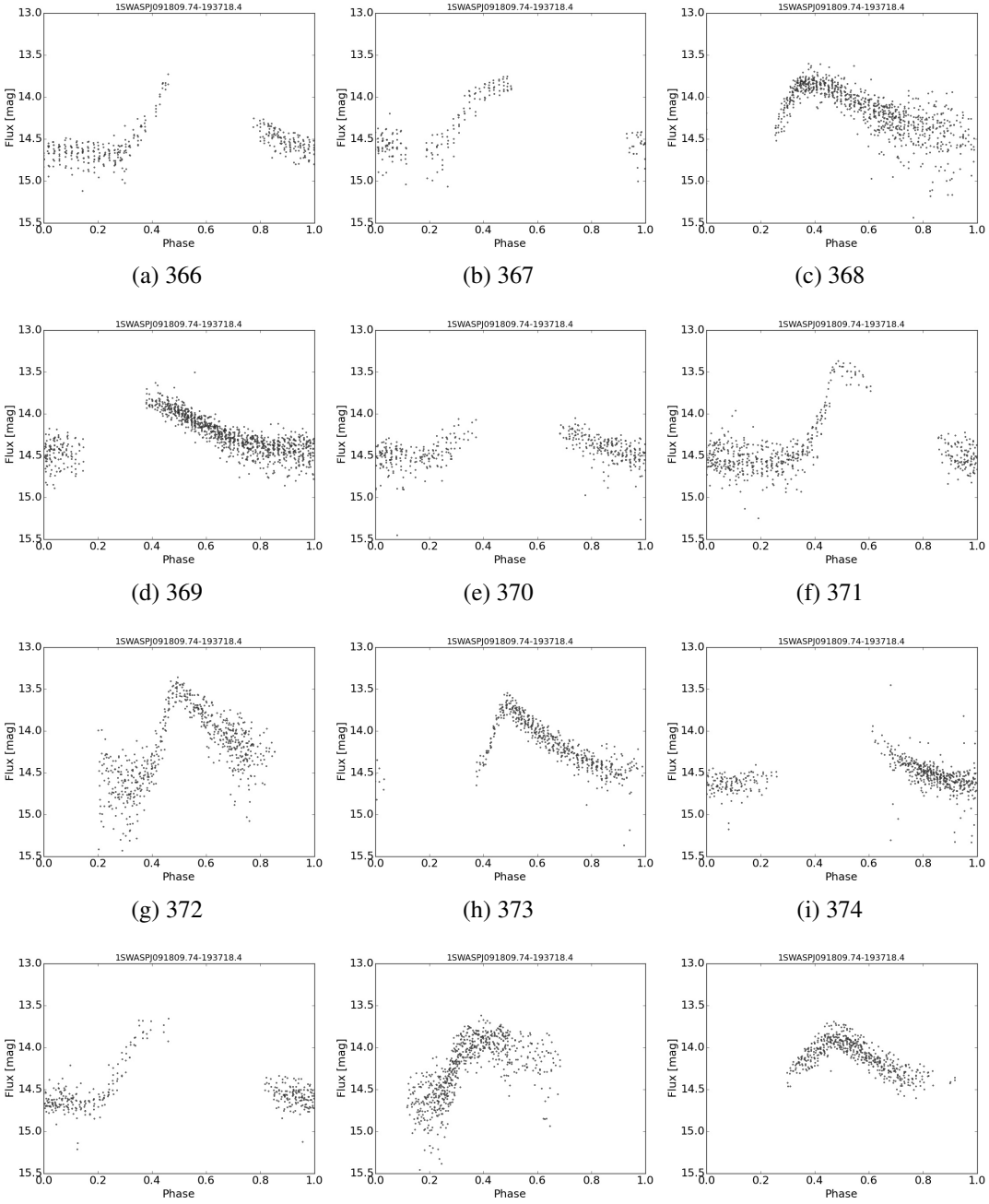

(a) 366 (b) 367 (c) 368

(d) 369 (e) 370 (f) 371

(g) 372 (h) 373 (i) 374

(j) 375 (k) 376 (l) 377

Figure B.14: Weekly phase–folded sections of the light curve from 2011 of 1SWASPJ091809.74-193718.4 that happen to be the same weeks as used for 1SWASPJ091348.80-091908.8. The week number from the start of the light curve is given under each plot and flux is in magnitudes. All weekly sections of the light curve are folded on the same pulsation period of 0.49108422 days with no change in the phase offset.

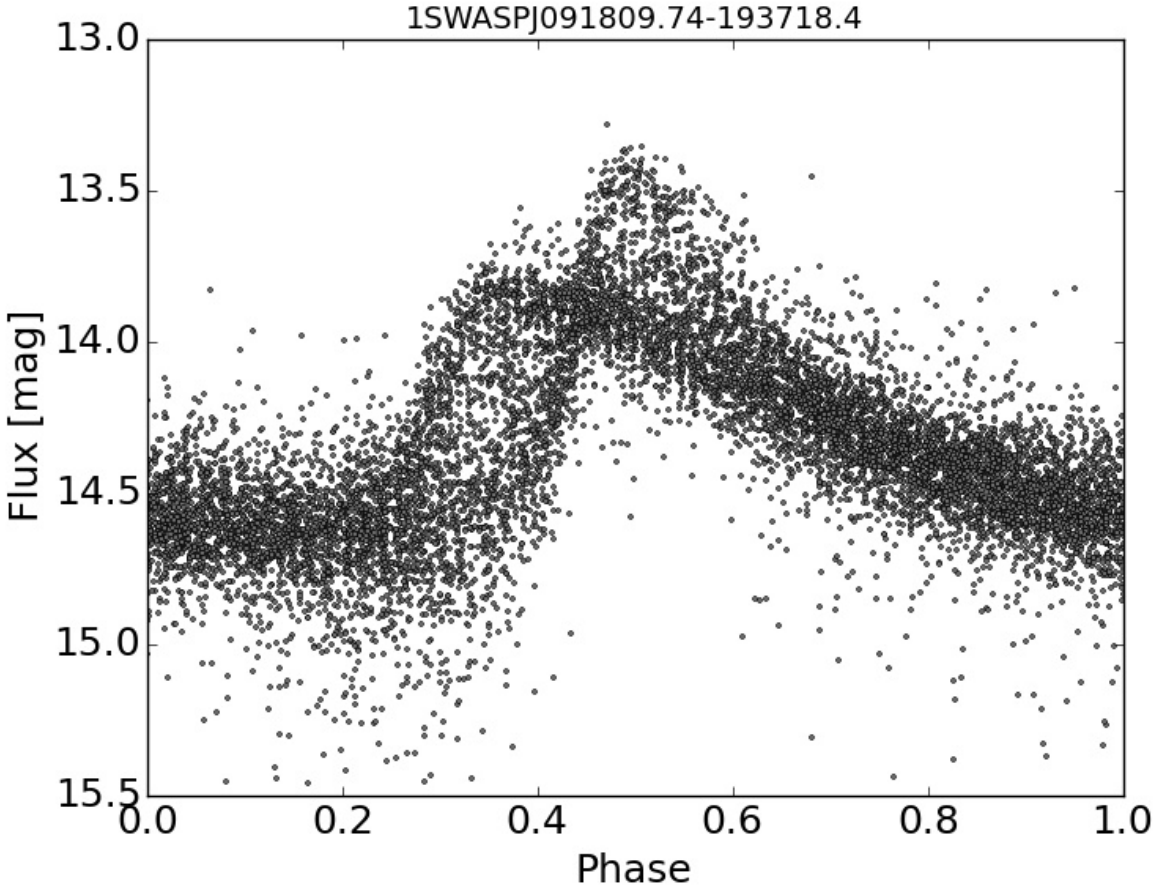

Figure B.15: Phase folded light curve of 1SWASPJ091809.74-193718.4 covering an entire year of observations during 2011. The amplitude modulation can be seen more clearly over this timescale as well as some change in the pulsation phase, the combination of both being indicative of the Blazhko effect.

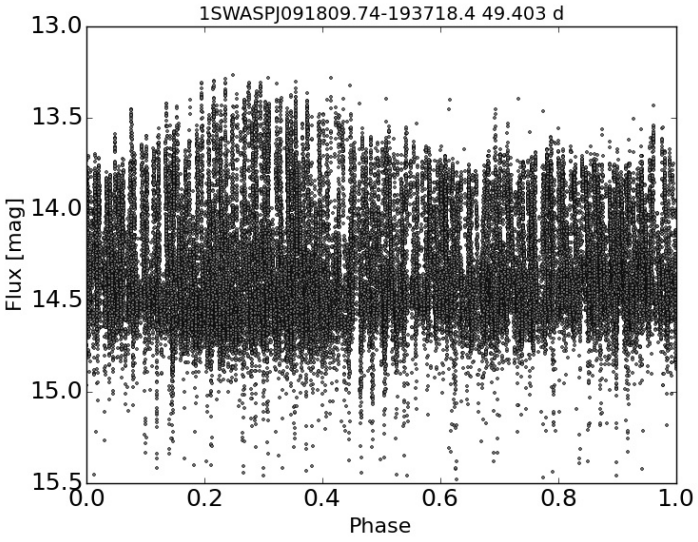

Figure B.16: Light curve for 1SWASPJ091809.74-193718.4 phase folded by a candidate Blazhko period of 49.4 d.

e) 1SWASPJ093731.34-181612.9

The year long phase folded light curves for 1SWASPJ093731.34-181612.9 show higher levels of scatter around the minimum as the object becomes fainter (Fig. B.17). The weekly phase folded light curves are correspondingly faint (Fig. B.18) with a difference in amplitude visible in the 3 week gap between week 365 and 368.

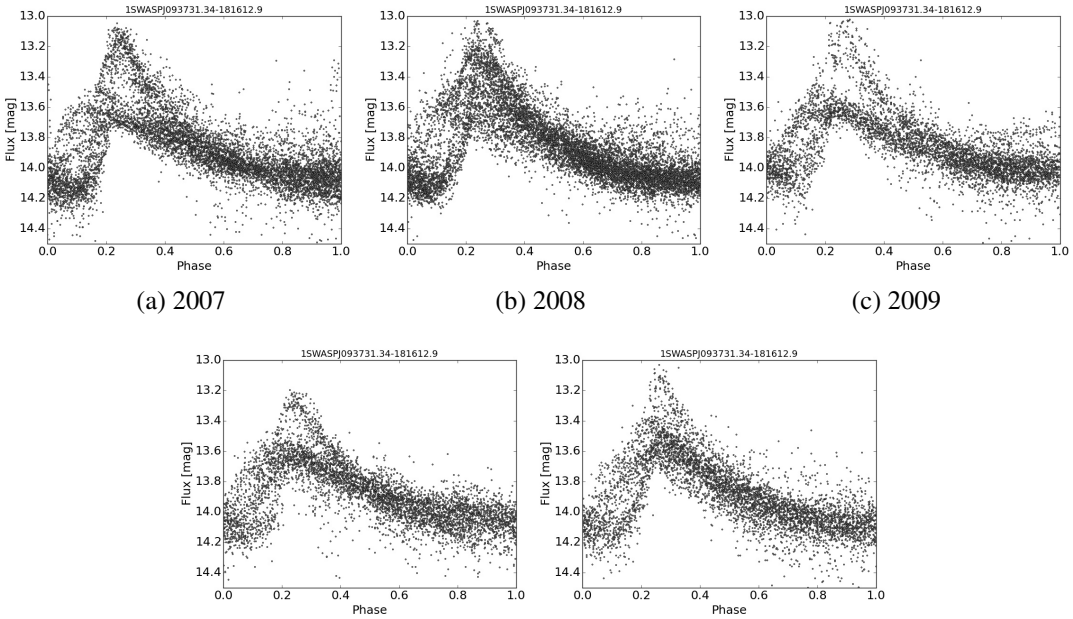

(a) 2007 (b) 2008 (c) 2009

(d) 2010 (e) 2011

Figure B.17: Yearly light curves of 1SWASPJ093731.34-181612.9 from 2008 to 2012.

The unfolded light curve for 1SWASPJ093731.34-181612.9 in 2011 (Fig. B.19) shows a possible Blazhko period of approximately 100 d. The PDM routine finds a candidate Blazhko period of 88.1 d, as shown in Fig. B.20 where a clearly defined envelope function are formed by both the upper and lower extremes of the pulsations.

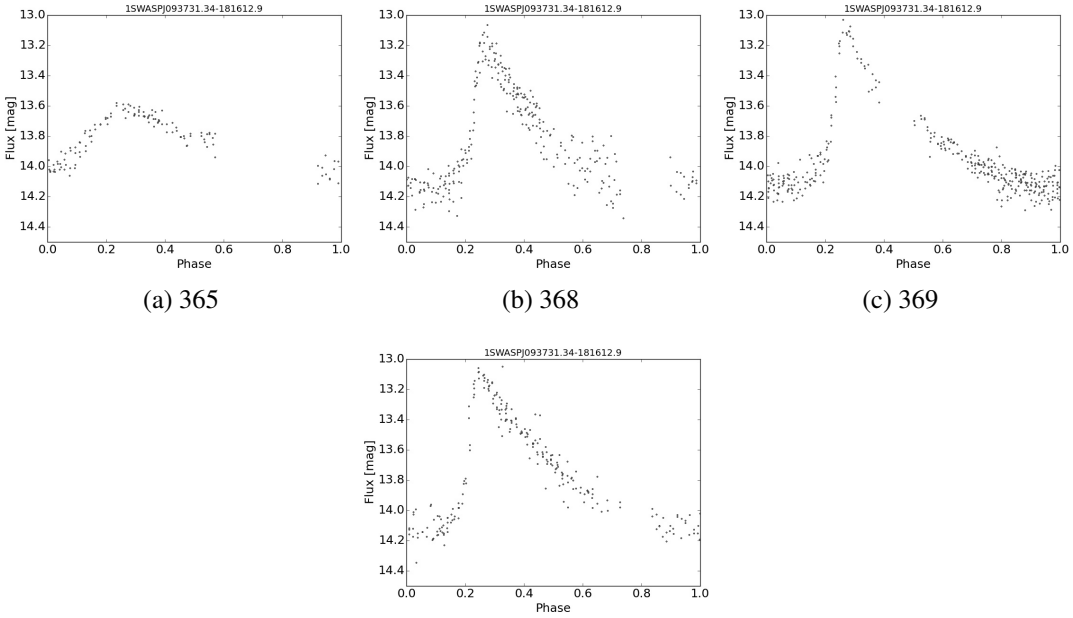

(a) 365 (b) 368 (c) 369

(d) 370

Figure B.18: Weekly sections of the light curve of 1SWASPJ093731.34-181612.9 for 4 weeks 365 to 370.

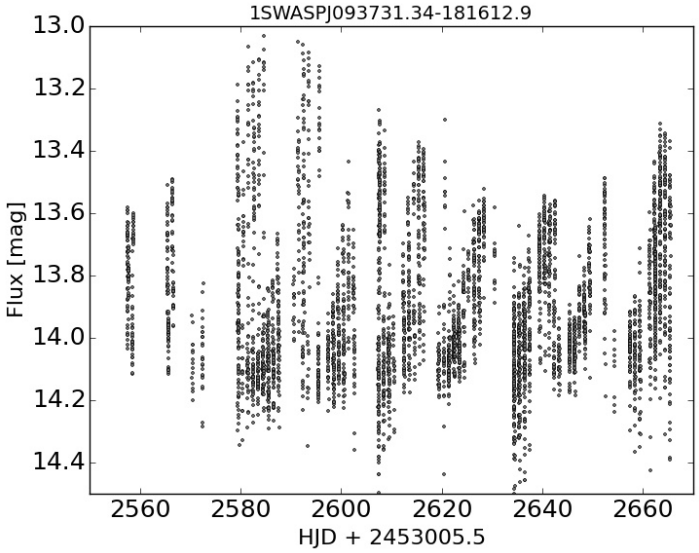

Figure B.19: Unfolded light curve from 2011 of 1SWASPJ093731.34-181612.9.

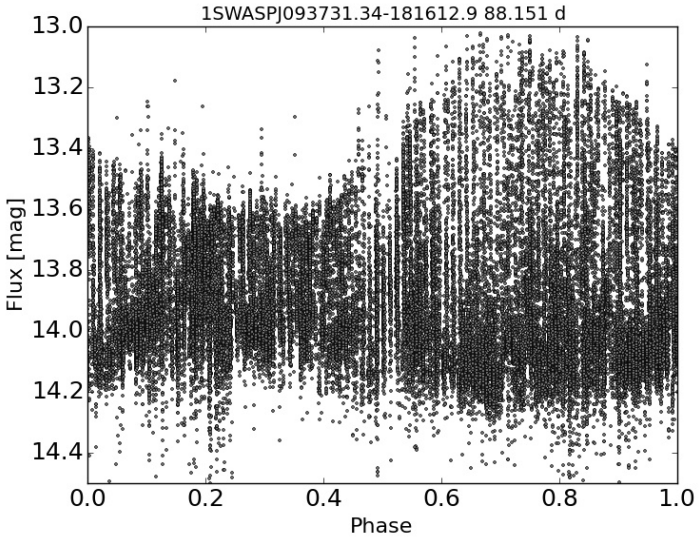

Figure B.20: Light curve for 1SWASPJ093731.34-181612.9 phase folded by a candidate Blazhko period of 88.2 d.

f) 1SWASPJ095515.90+034532.3

The effects of AM can be clearly seen in the light curves for 1SWASPJ095515.90+034532.3 from 2008 to 2010 (Fig. B.21). These effects are more subtle when using the week long sections of the light curve from a single year (Fig. B.22), where the shape of the pulsation light curve remains similar. This suggests that the modulation period is over a year long.

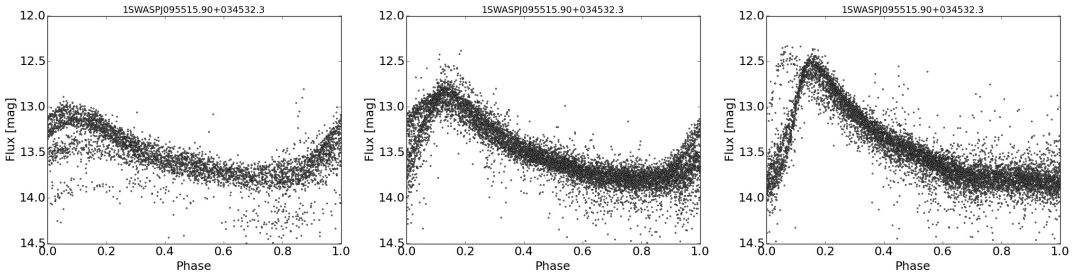

(a) 2008 (b) 2009 (c) 2010

Figure B.21: Yearly light curves of 1SWASPJ095515.90+034532.3 from 2008 to 2012.

The entire unfolded light curve for 1SWASPJ095515.90+034532.3 is shown in Fig. B.23 as it appears to show a modulation period longer than 1 year, perhaps even one twice as long as the duration of observations. The PDM program finds a candidate Blazhko period of 284.5 d (Fig. B.24). However, this envelope function is not as continuous as in previous cases, casting some doubt in the reliability of this period.

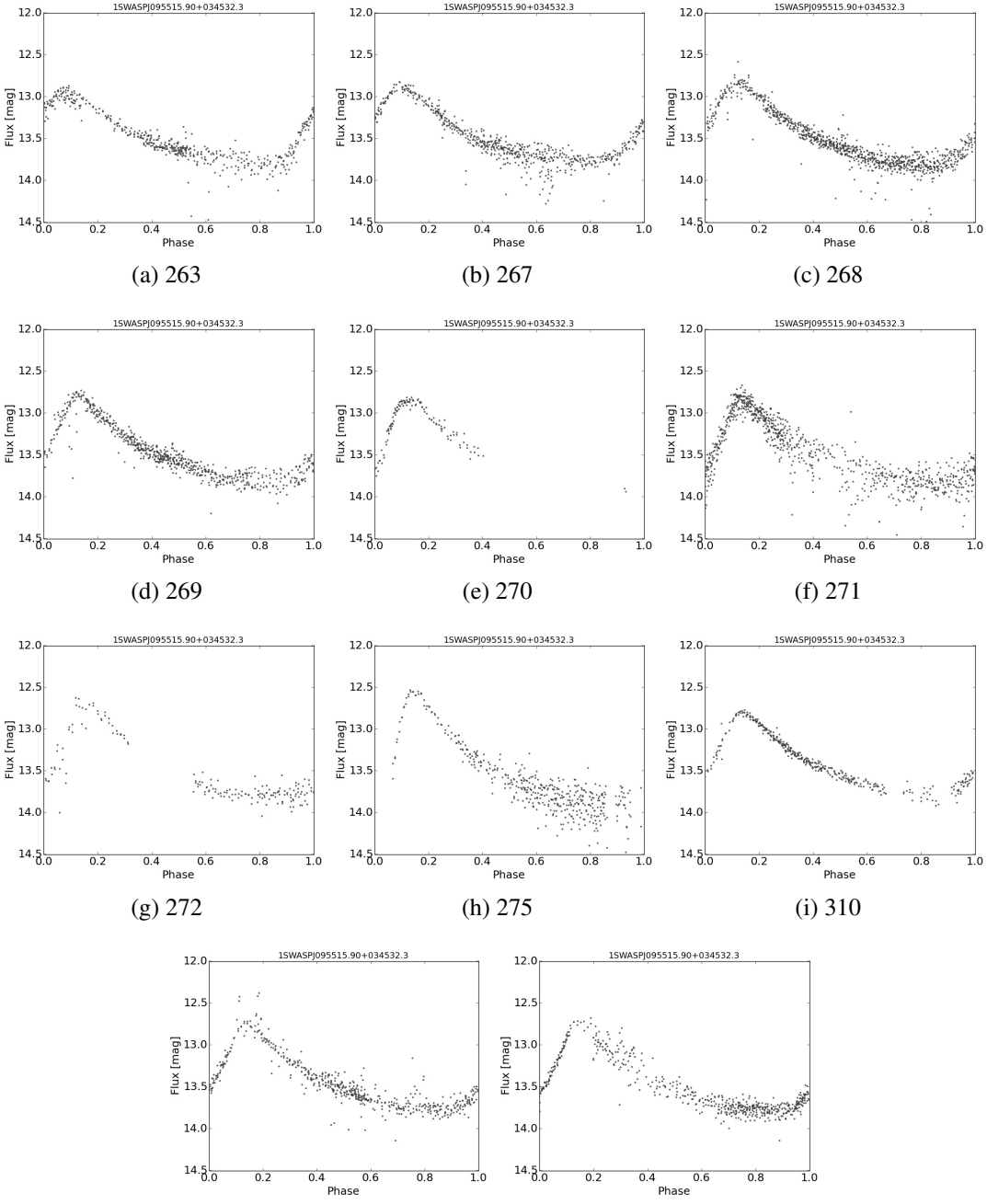

(a) 263 (b) 267 (c) 268

(d) 269 (e) 270 (f) 271

(g) 272 (h) 275 (i) 310

(j) 311 (k) 312

Figure B.22: 10 weekly sections of the light curve of 1SWASPJ093731.34-181612.9.

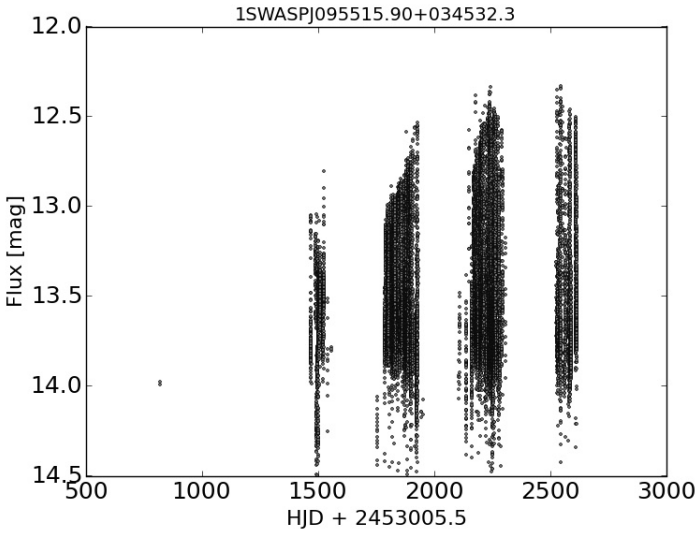

Figure B.23: Unfolded entire light curve of 1SWASPJ095515.90+034532.3. The entire light curve is shown as the modulation period appears longer than 1 year.

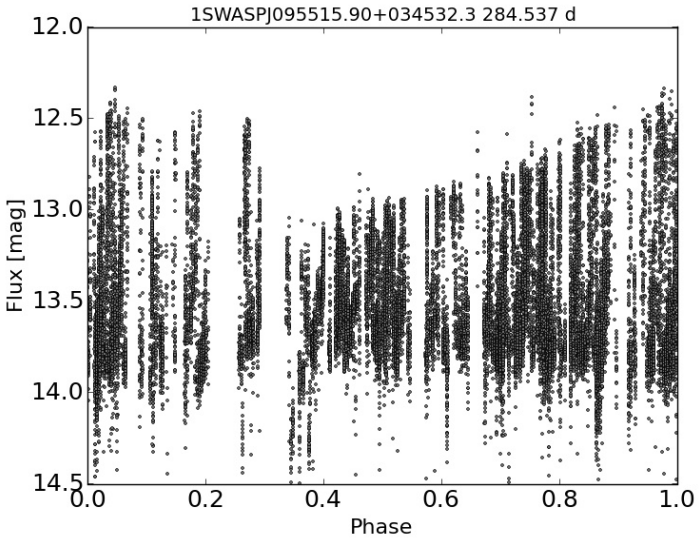

Figure B.24: Light curve for 1SWASPJ095515.90+034532.3 phase folded by a candidate Blazhko period of 284.5 d showing an envelope function with a possible discontinuity at phase 0.3.

g) 1SWASPJ120447.27-274043.2

Object 1SWASPJ120447.27-274043.2 is one of the most extreme examples of AM in the SuperWASP catalogue as shown in particular in years 2007 and 2008 in Fig. B.25. The AM is so clear that a candidate Blazhko effect period of approximately 70 d can be estimated from week–long segments of the light curve from weeks 209 to 225 shown in Fig. B.25.

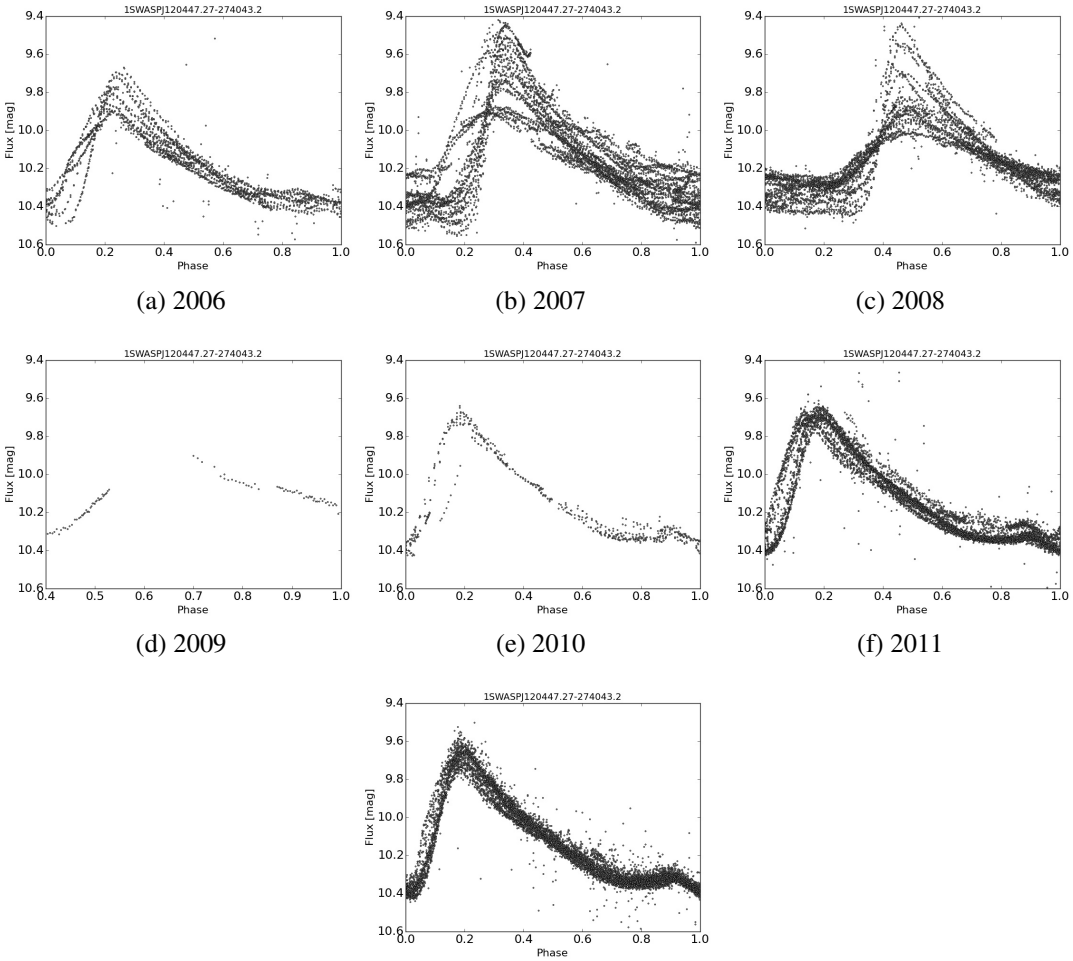

(a) 2006 (b) 2007 (c) 2008

(d) 2009 (e) 2010 (f) 2011

(g) 2012

Figure B.25: Yearly light curves of 1SWASPJ120447.27-274043.2 from 2006 to 2012 showing how the amplitude of the light curve decreased from 2006 to 2008 and increased again to 2010. Flux levels are scaled in each case to the peak flux.

1SWASPJ120447.27-274043.2 (IK Hya) showed a clear AM envelope function for individual years, such as in 2008, shown in Fig. B.27, when the light curve was not phase folded. However, the pulsation maxima only, phase folded by the candidate Blazhko period of 151 d, shown in Fig. B.28 shows a varying envelope function, implying a varying Blazhko effect. The full light curve folded by this candidate Blazhko period suggests the true modulation period is about half this length, which corresponds with the first 71 – 75 d period provided by Skarka's online database, whereas the triple line segment between phase 0.1 and 0.5 of the cycle suggests a longer period of approximately 450 d. Fig. B.29 shows the light curve folded at the shorter candidate Blazhko period of 75.7 d resulting in a single peak to the envelope function. IK Hya appears to be an example of a pulsating variable object with a varying variability.

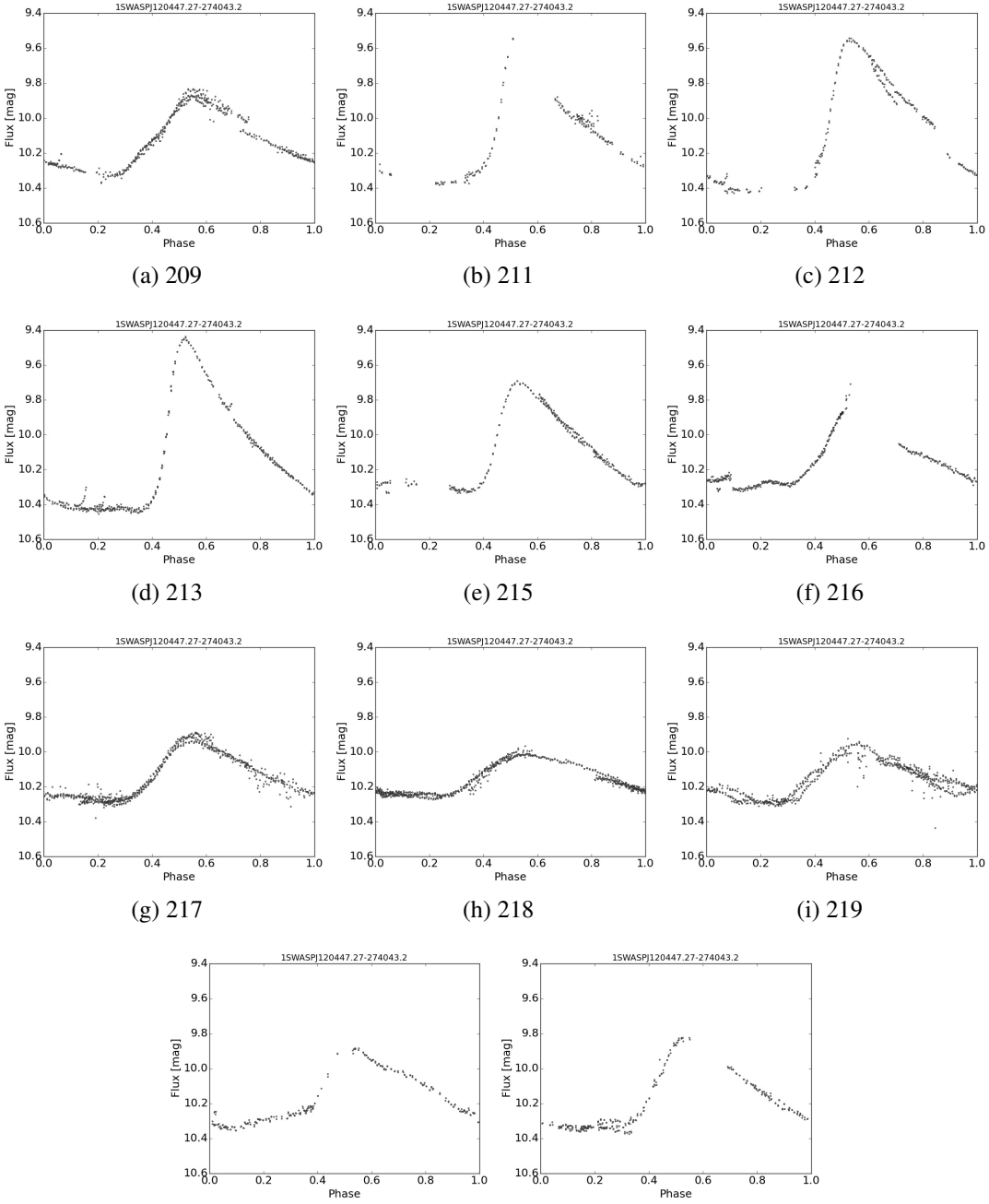

(a) 209 (b) 211 (c) 212

(d) 213 (e) 215 (f) 216

(g) 217 (h) 218 (i) 219

(j) 220 (k) 221

Figure B.26: Weekly sections from 2008 of the light curve of 1SWASPJ120447.27-274043.2 for the weeks with enough data for light curve plotting. The week number from the start of the light curve is given under each plot and flux is in magnitudes. All weekly sections of the light curve are folded on the same pulsation period of 0.65029929 days with no change in the phase offset.

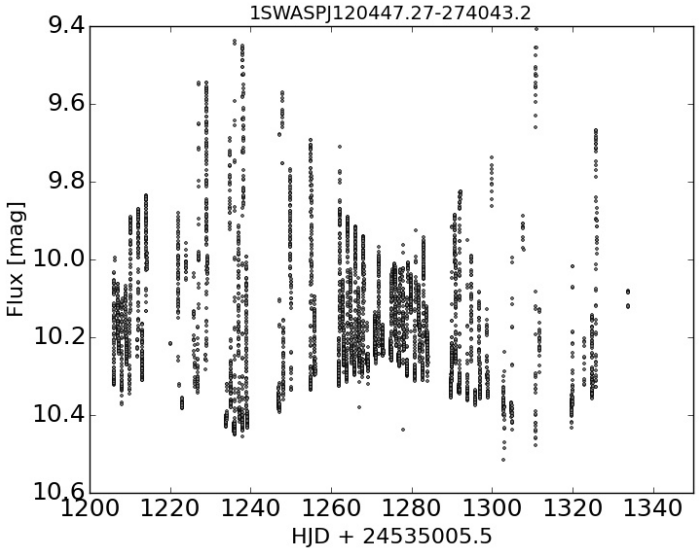

Figure B.27: Unfolded light curve from observations made during 2008 of 1SWASPJ120447.27-274043.2. The envelope function can be clearly seen as the large increase and decrease in pulsation amplitude.

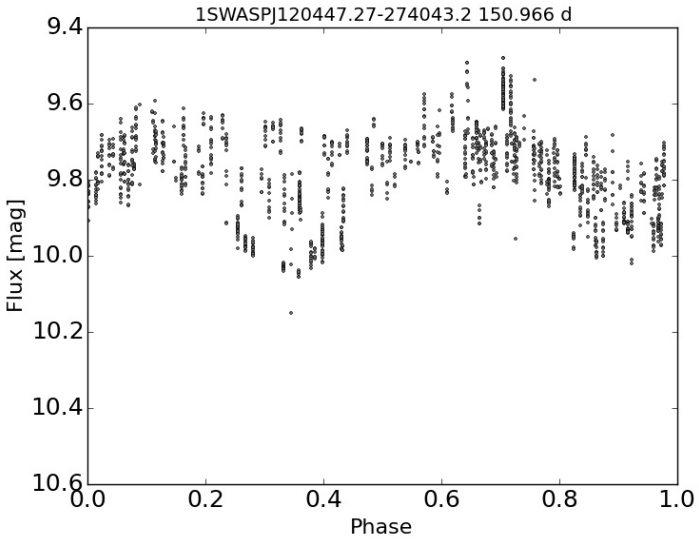

Figure B.28: Light curve maxima only for 1SWASPJ120447.27-274043.2 phase folded by a candidate Blazhko period of 151.0 d where the variation in the envelope function can be seen in the left half of the diagram.

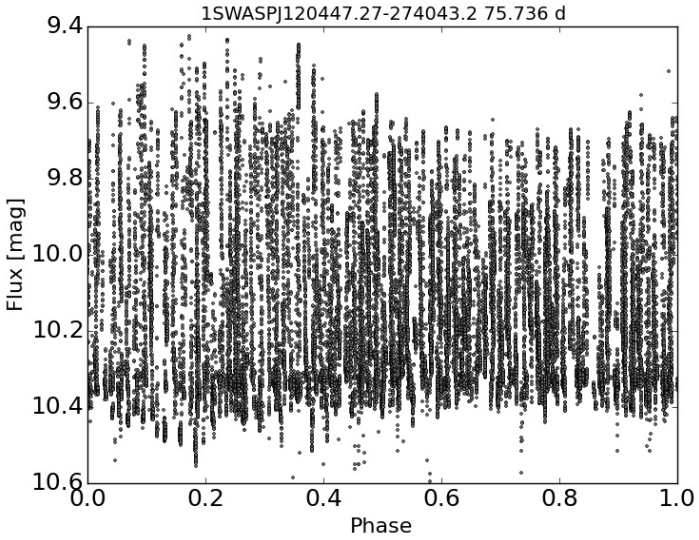

Figure B.29: Light curve for 1SWASPJ120447.27-274043.2 phase folded by a candidate Blazhko period of 75.7 d showing a well defined envelope function.

h) 1SWASPJ121206.15-261248.0

The year long sections of light curve for 1SWASPJ121206.15-261248.0 show the pulsation shape changing from the low to high amplitude phases of modulation (Fig. B.30). The effects of AM on the pulsation can be seen more clearly over the course of 19 consecutive weeks as shown in Fig. B.31.

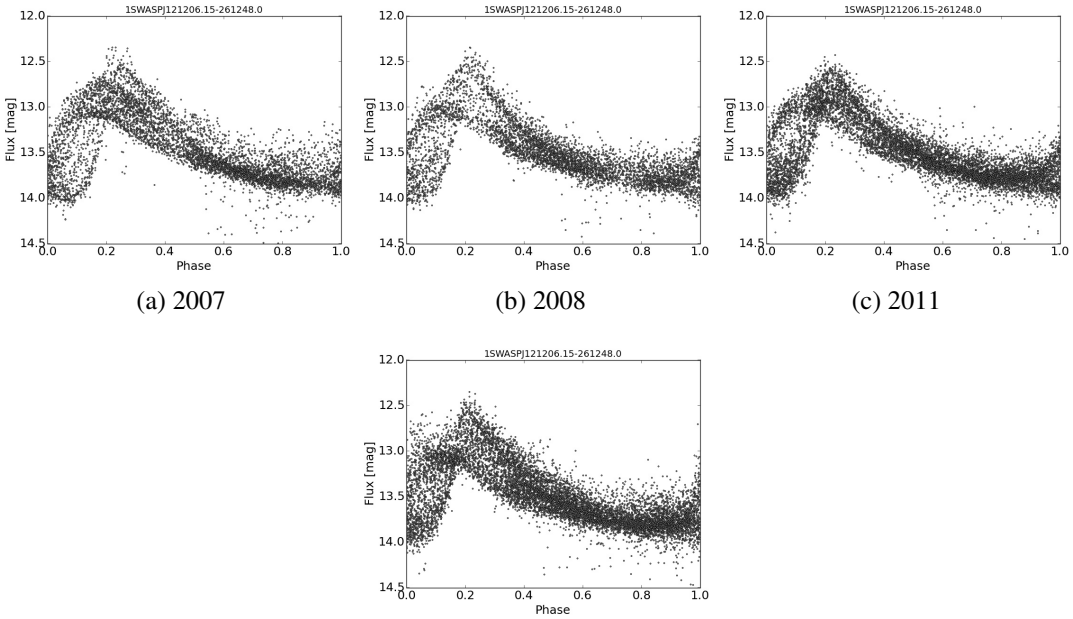

(a) 2007 (b) 2008 (c) 2011

(d) 2012

Figure B.30: Yearly light curves of 1SWASPJ121206.15-261248.0 from 2008 to 2012.

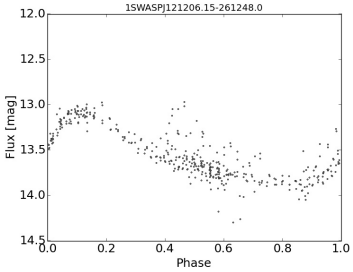

(a) 419

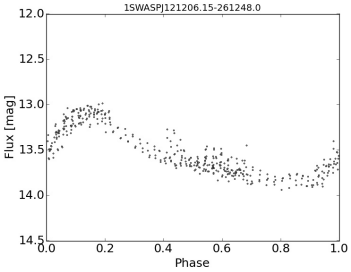

(b) 420

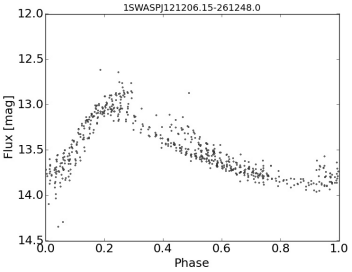

(c) 421

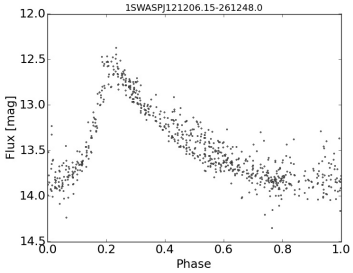

(d) 422

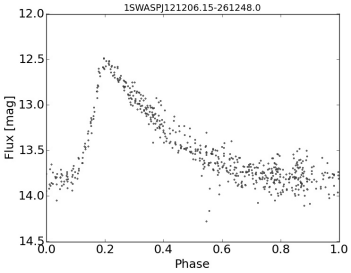

(e) 423

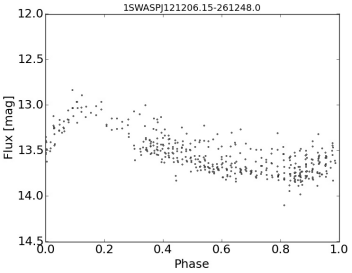

(f) 434

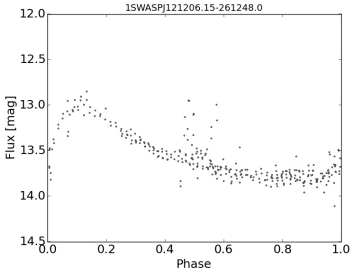

(g) 425

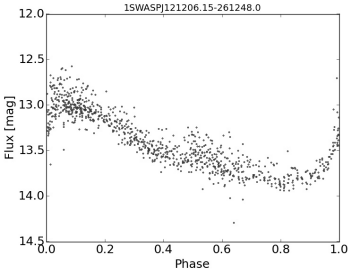

(h) 426

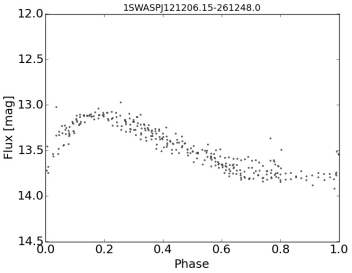

(i) 427

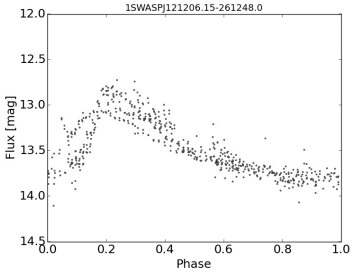

(j) 428

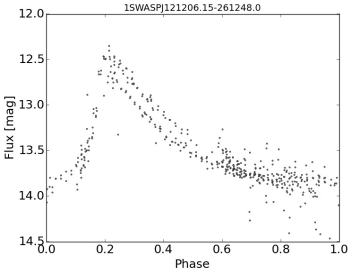

(k) 429

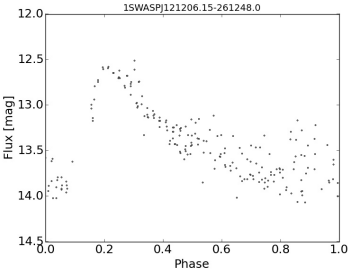

(l) 430

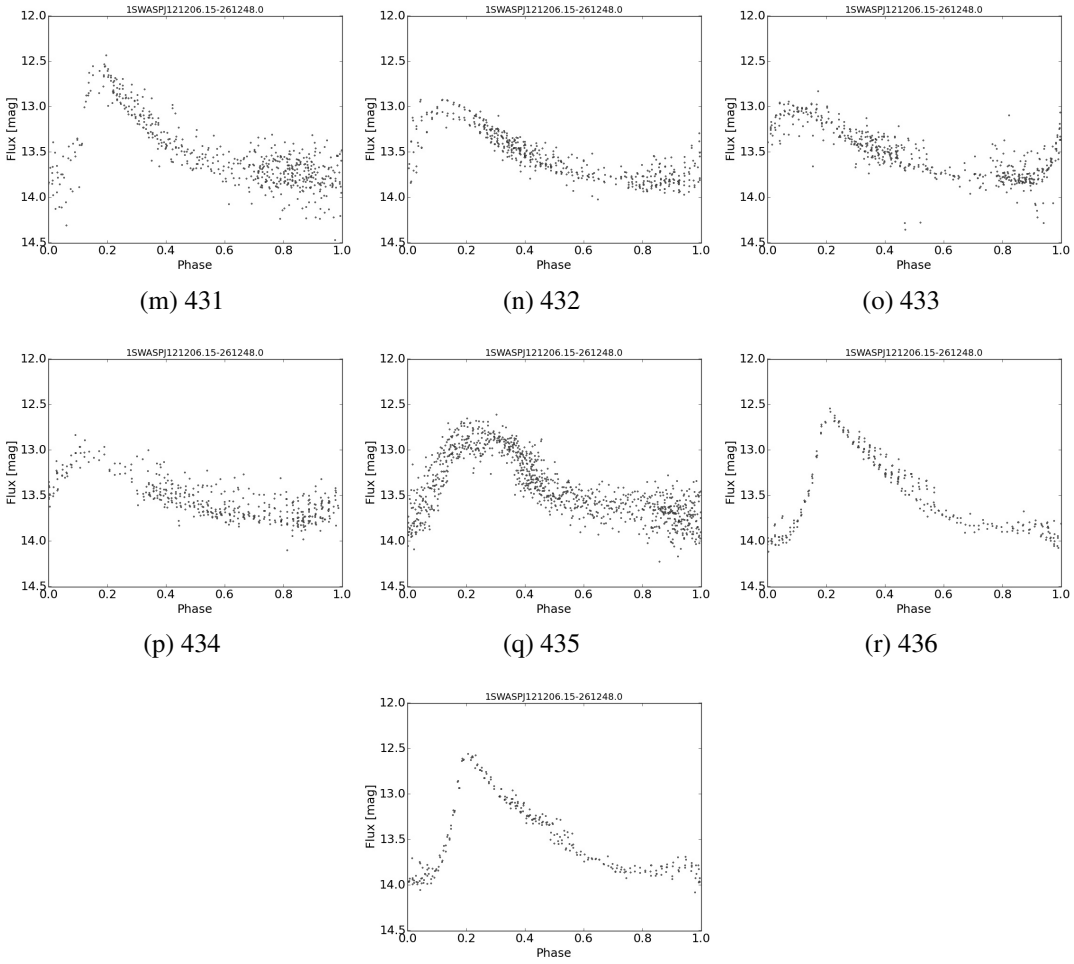

(m) 431 (n) 432 (o) 433

(p) 434 (q) 435 (r) 436

(s) 437

Figure B.31: 19 consecutive weekly sections of the light curve of 1SWASPJ121206.15-261248.0.

The unfolded light curve for 1SWASPJ121206.15-261248.0 (Fig. B.32) shows 3 modulation cycles of approximately 50 – 60 d. Figure. B.33 shows the light curve folded by the candidate Blazhko period of 48.4 d. The period was found after the PDM routine produced a double peaked envelope function with an initial trial period range centred on 120 d.

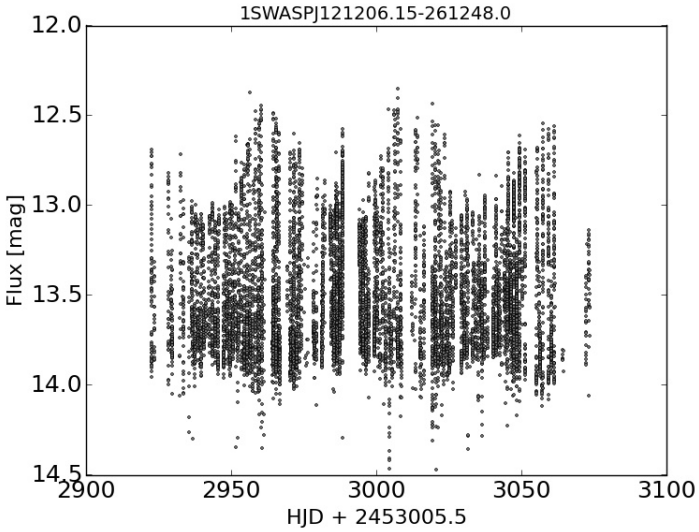

Figure B.32: Unfolded light curve from observations of 1SWASPJ121206.15-261248.0 taken during 2012.

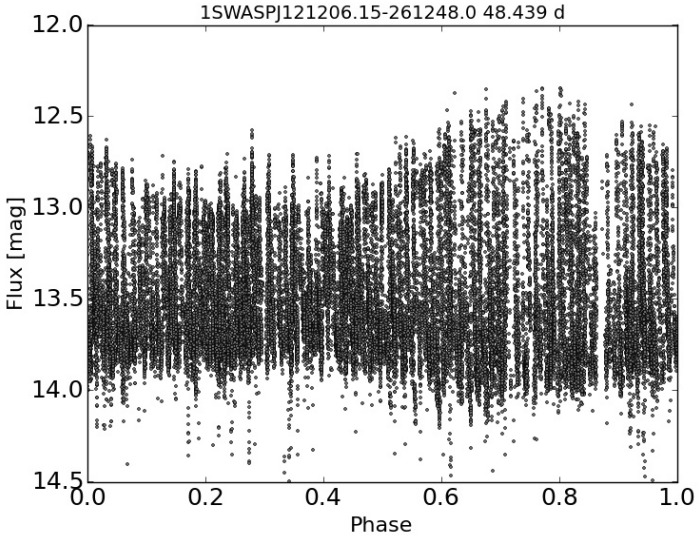

Figure B.33: Light curve for 1SWASPJ121206.15-261248.0 phase folded by a candidate Blazhko period of 48.4 d showing a well defined envelope function.

i) 1SWASPJ123810.96+385027.9

There is a marked difference between 2011 and 2012 in Fig. B.34 , where the large amplitude phase is completely missing from 2012. On their own, these 2 light curves could imply that this was a blended object. However, the weekly decomposition of 2011 (Fig. B.35) shows that 1SWASPJ123810.96+385027.9 shows signs of strong AM where a light curve similar to that of 2012 can be seen in weeks 378 and 381.

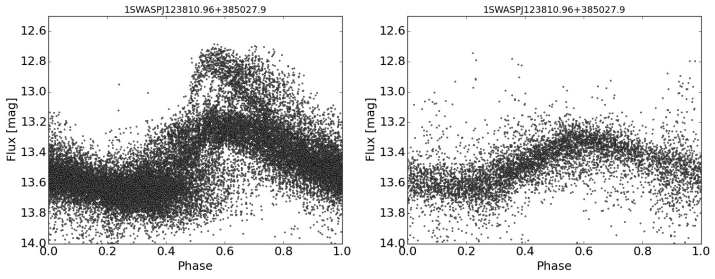

(a) 2011 (b) 2012

Figure B.34: Yearly light curves of 1SWASPJ123810.96+385027.9 from 2011 and 2012.

Phase folding the light curve of 1SWASPJ123810.96+385027.9 based on the envelope function from 2011's section of the light curve (Fig. B.36) results in a candidate Blazhko period of 115.1 d (Fig. B.37). However, the envelope function is not as clearly defined as in other cases, probably due to the high level of noise present throughout the light curve as shown in Fig. B.38.

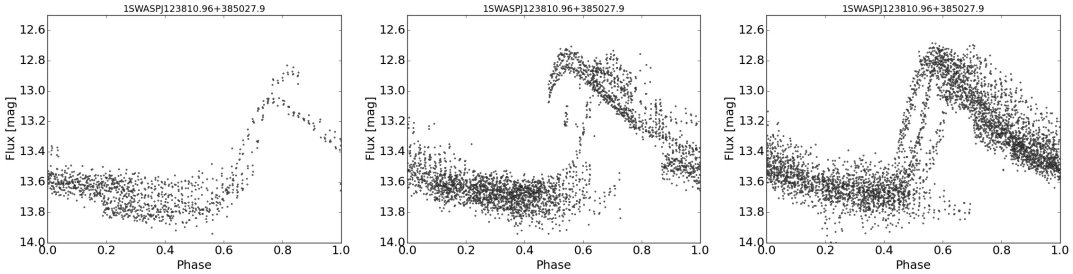

(a) 373 (b) 374 (c) 375

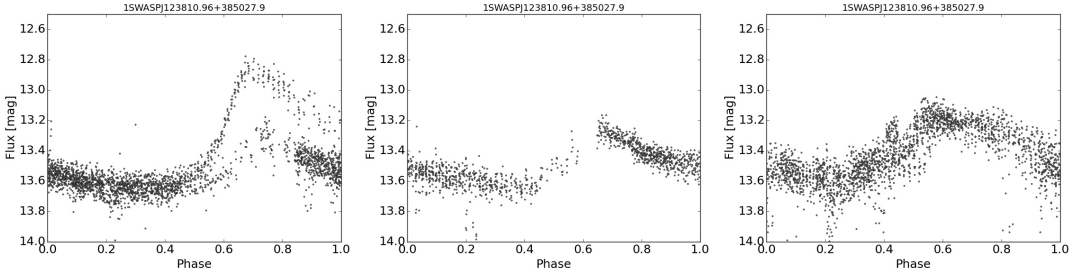

(d) 377 (e) 378 (f) 379

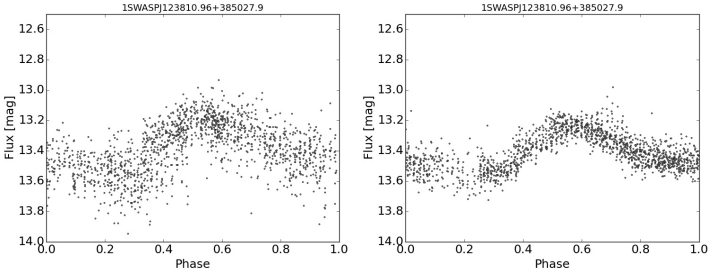

(g) 380 (h) 381

Figure B.35: 8 weekly sections of the light curve of 1SWASPJ123810.96+385027.9.

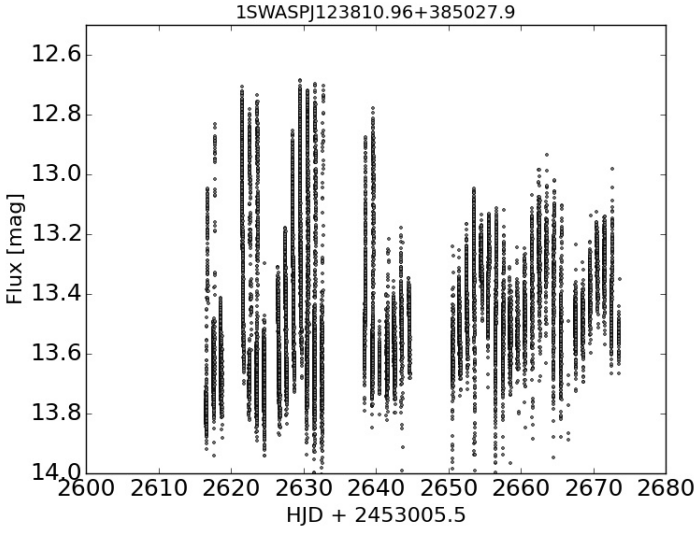

Figure B.36: Unfolded light curve from observations of 1SWASPJ123810.96+385027.9 taken during 2011.

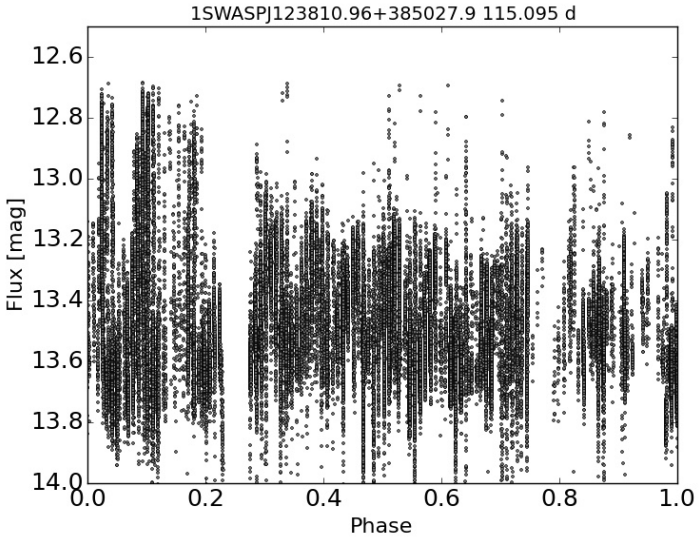

Figure B.37: Light curve for 1SWASPJ123810.96+385027.9 phase folded by a candidate Blazhko period of 115.1 d, showing how both upper and lower envelope functions are not well defined.

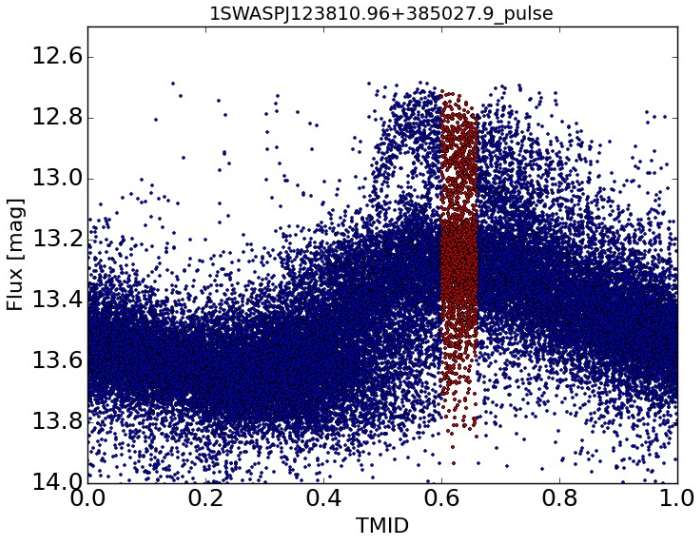

Figure B.38: Light curve for object 1SWASPJ123810.96+385027.9 phase folded by the pulsation period showing large levels of noise throughout the pulsation. The data defined as maxima are highlighted in red.

j) 1SWASPJ123811.99-442231.8

Two of the year long light curves for 1SWASPJ123811.99-442231.8 in Fig. B.39 only show the high amplitude phase of the potential Blazhko period. This may be due to the timing of observations. The weekly light curves (Fig. B.40) suggest a Blazhko period of 15 – 16 weeks.

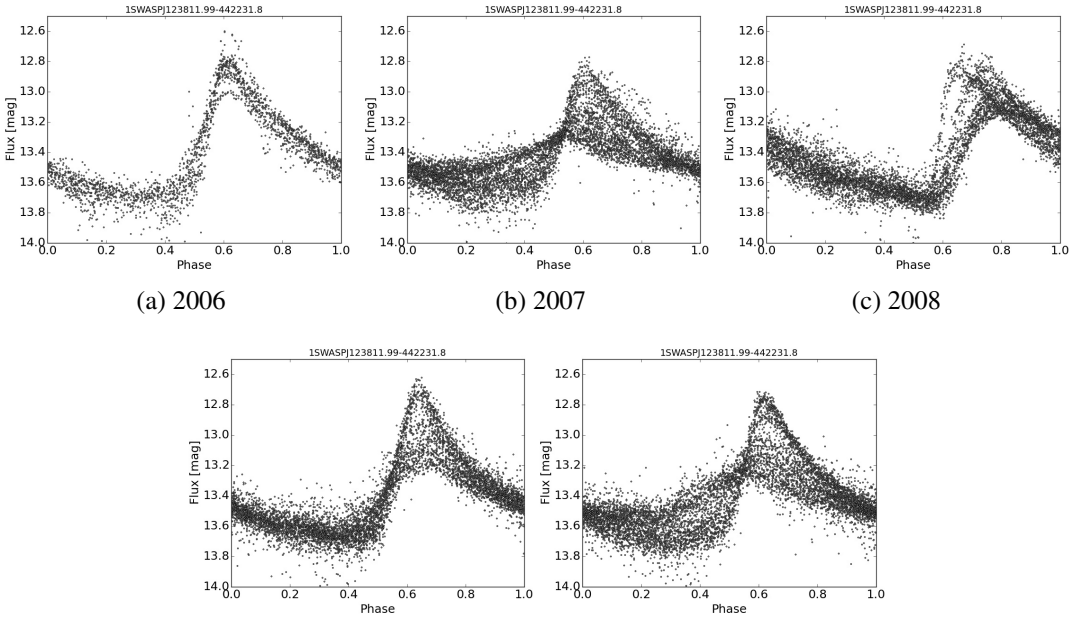

(a) 2006 (b) 2007 (c) 2008

(d) 2011 (e) 2012

Figure B.39: Yearly light curves of 1SWASPJ123811.99-442231.8 from 2008 to 2012.

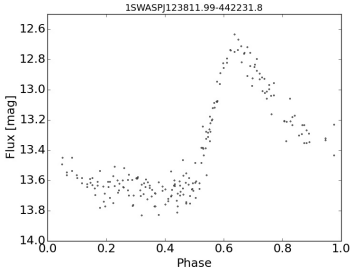

(a) 368

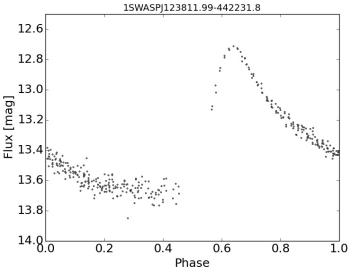

(b) 369

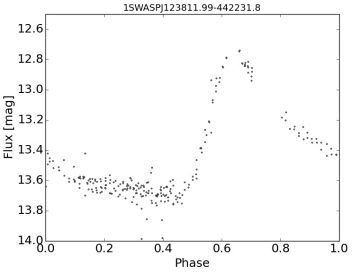

(c) 370

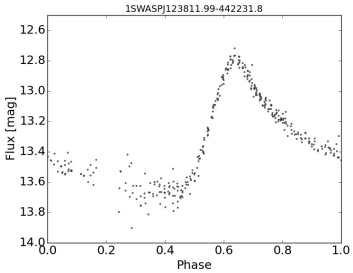

(d) 371

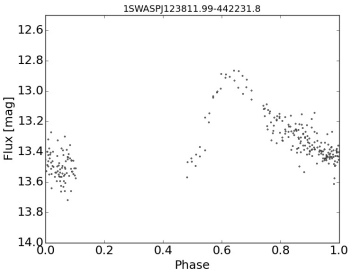

(e) 372

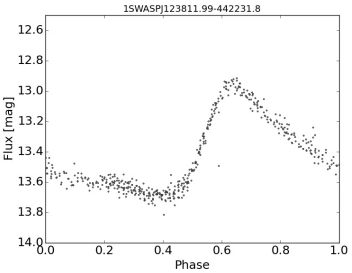

(f) 373

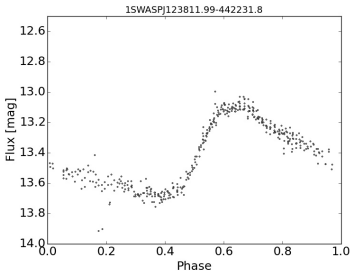

(g) 374

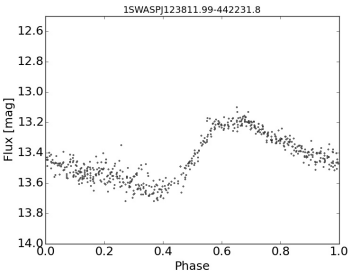

(h) 377

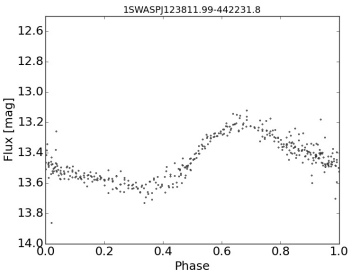

(i) 378

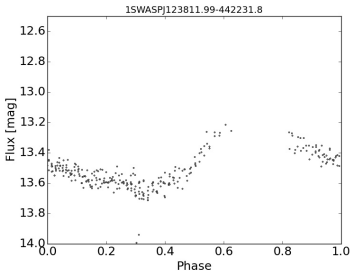

(j) 379

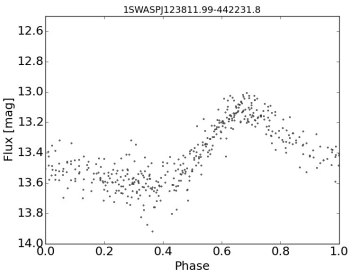

(k) 380

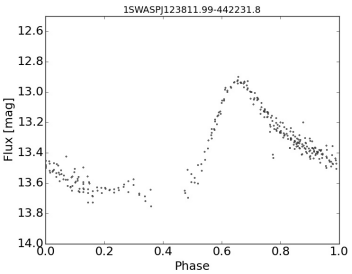

(l) 383

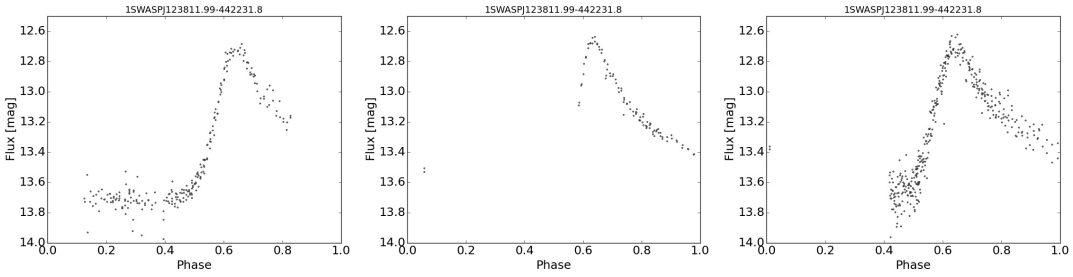

(m) 385 (n) 386 (o) 388

Figure B.40: 15 consecutive weekly sections of the light curve of 1SWASPJ123811.99-442231.8.

Figure B.41 shows a large amount of AM during 2011 for 1SWASPJ123811.99-442231.8. The phase folding routine successfully finds a very sinusoidal envelope function at 122.7 d, as shown in (Fig. B.42).

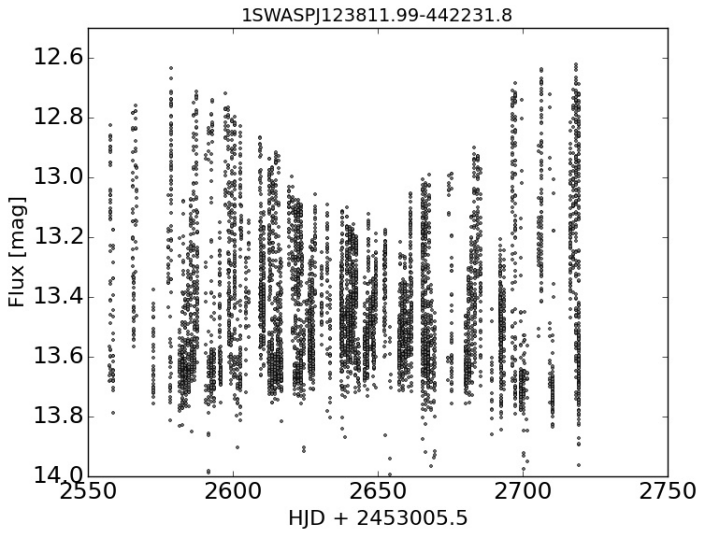

Figure B.41: Unfolded light curve from observations of 1SWASPJ123811.99-442231.8 taken during 2011.

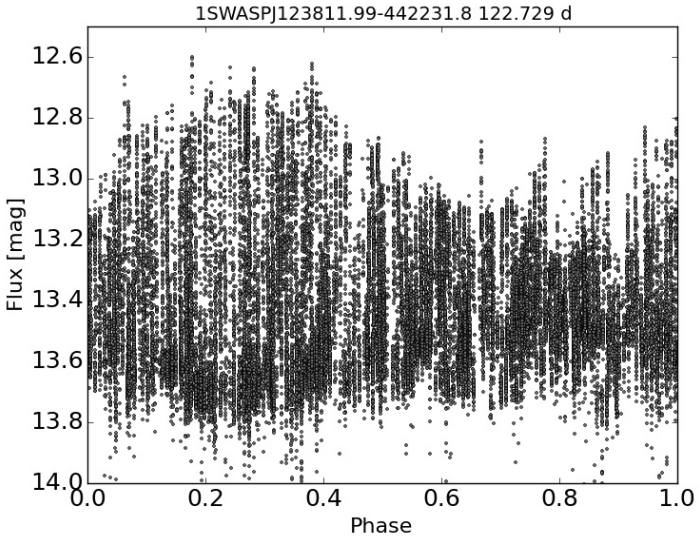

Figure B.42: Light curve for 1SWASPJ123811.99-442231.8 phase folded by a candidate Blazhko period of 122.7 d showing an overlapping envelope function.

k) 1SWASPJ132922.47-055259.2

The light curve for the 2008 observations of 1SWASPJ132922.47-055259.2 (Fig. B.43) clearly shows the changing pulsation amplitude due to the Blazhko effect. The weekly light curves (Fig. B.44) suggest a potential Blazhko period of just over 11 weeks.

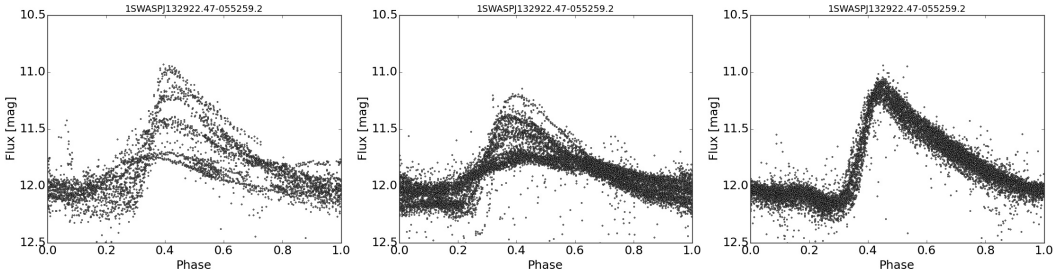

(a) 2008 (b) 2009 (c) 2010

Figure B.43: Yearly light curves of 1SWASPJ132922.47-055259.2 from 2008 to 2010.

Figure B.45 shows a long modulation period extending over the entire SuperWASP light curve for 1SWASPJ132922.47-055259.2. The same light curve folded by the candidate Blazhko period of 676.2 d shows a large seasonal gap but also the single cycle of the AM envelope function over this period.

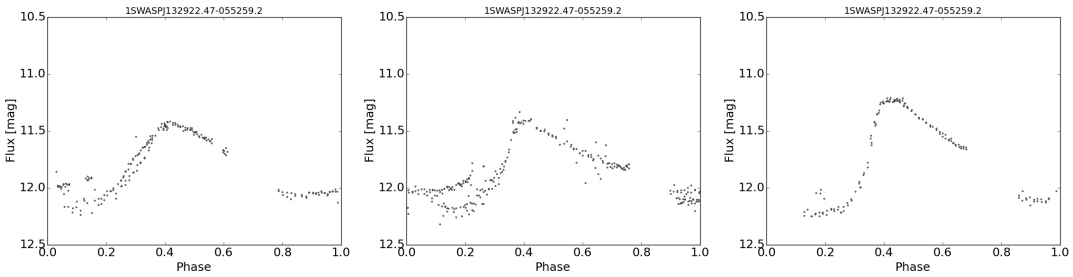

(a) 214 (b) 215 (c) 217

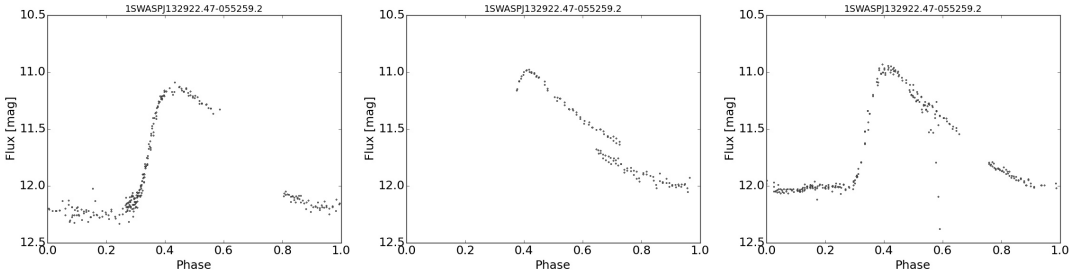

(d) 219 (e) 220 (f) 221

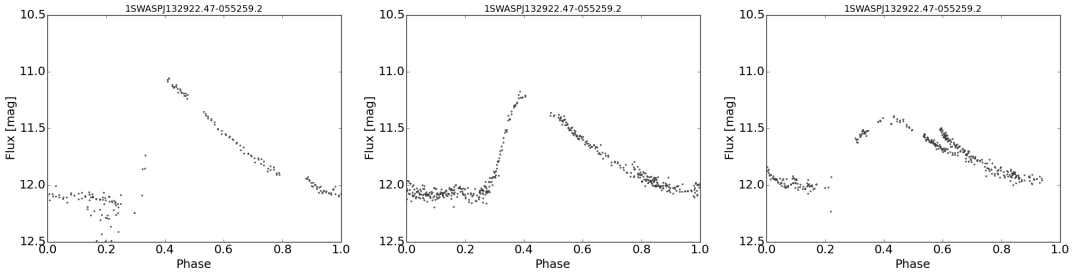

(g) 222 (h) 223 (i) 225

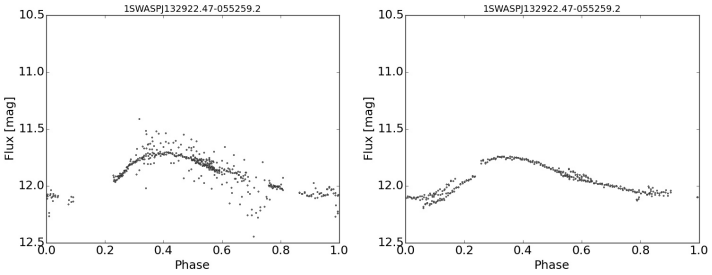

(j) 227 (k) 229

Figure B.44: 11 week long segments of the light curve of 1SWASPJ132922.47-055259.2.

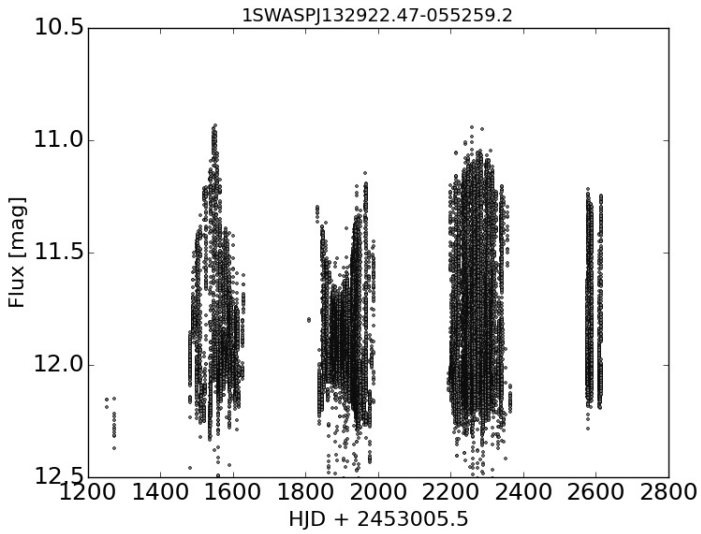

Figure B.45: Entire unfolded light curve from of 1SWASPJ132922.47-055259.2.

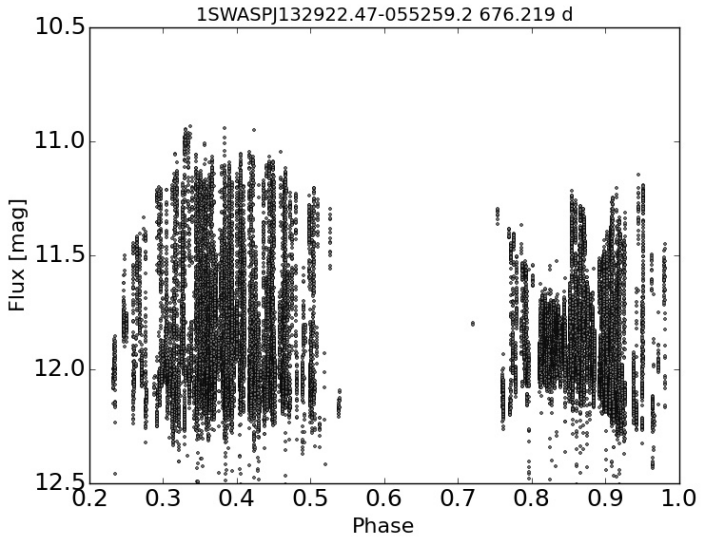

Figure B.46: Light curve for 1SWASPJ132922.47-055259.2 phase folded by a long candidate Blazhko period of 676.2 d.

l) 1SWASPJ134815.94+395403.0

Part of the low amplitude phase of the light curve for 1SWASPJ134815.94+395403.0 (Fig. B.47) in 2007 resembles an RRc light curve with quite a rounded pulsation shape. However, this pulsation shape only appears in week 23 of Fig. B.48, showing this is not a separate pulsation mode, but merely a highly amplitude modulated pulsation.

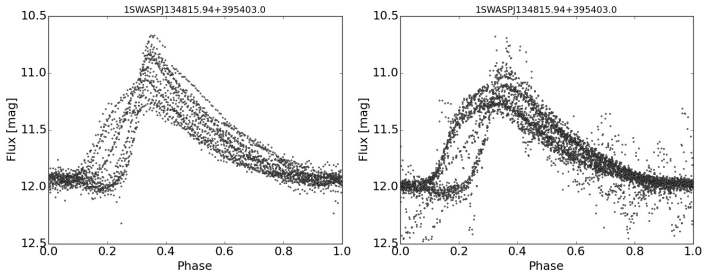

(a) 2004 (b) 2007

Figure B.47: 2 yearly light curves of 1SWASPJ134815.94+395403.0.

The unfolded light curve for 1SWASPJ134815.94+395403.0 (Fig. B.49) shows well defined variation in both maxima and minima of the object's pulsations over a period of roughly 120 d. Figure B.50 shows that this estimation is close to the candidate Blazhko period of 130.1 d derived from using the entire light curve.

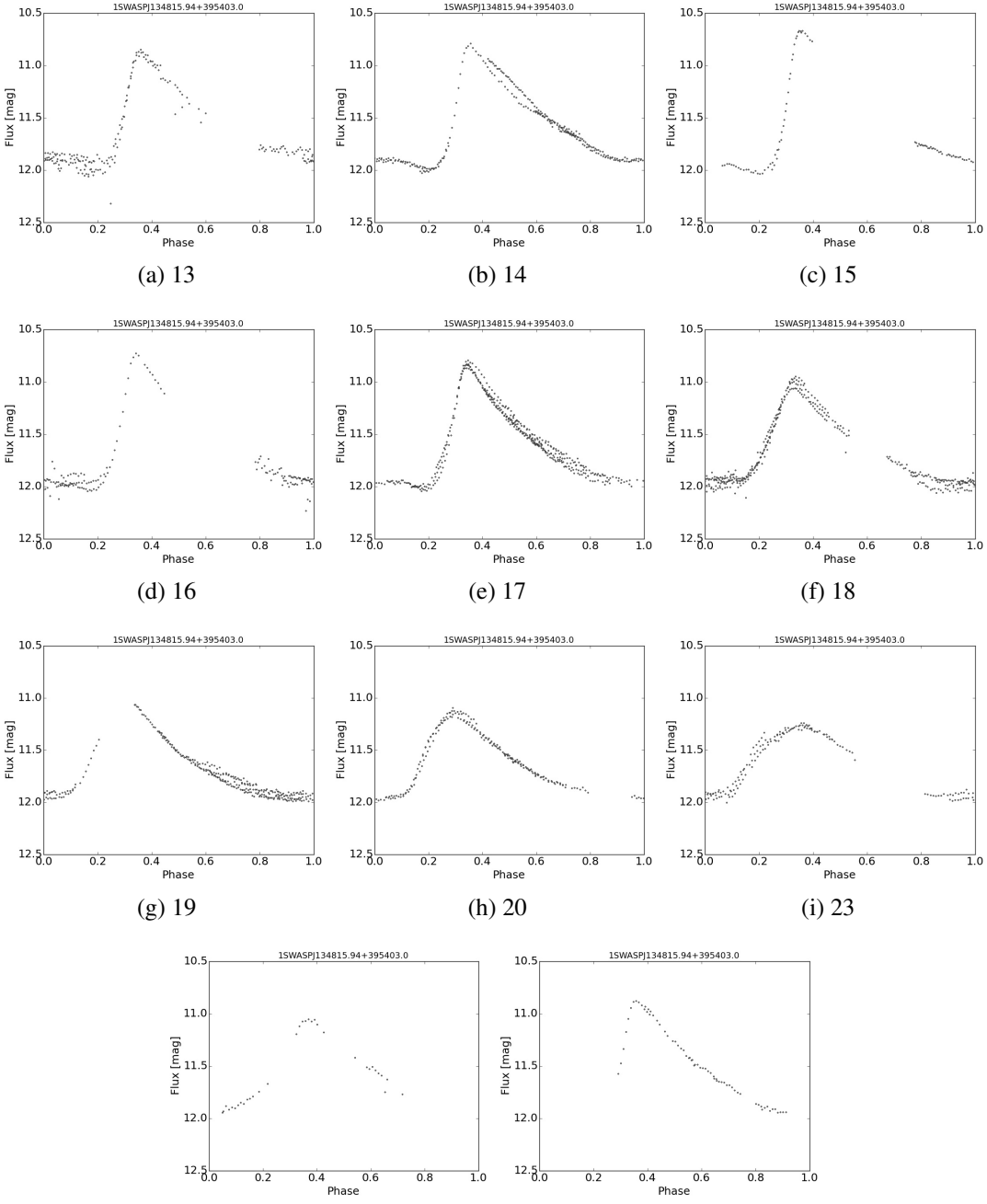

(a) 13 (b) 14 (c) 15

(d) 16 (e) 17 (f) 18

(g) 19 (h) 20 (i) 23

(j) 25 (k) 27

Figure B.48: 11 week long segments of the light curve of 1SWASPJ134815.94+395403.0.

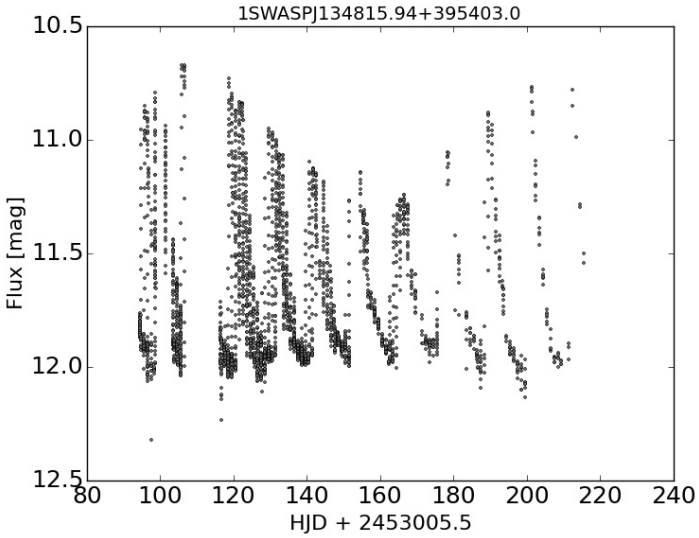

Figure B.49: Unfolded light curve from observations of 1SWASPJ134815.94+395403.0 taken during 2004.

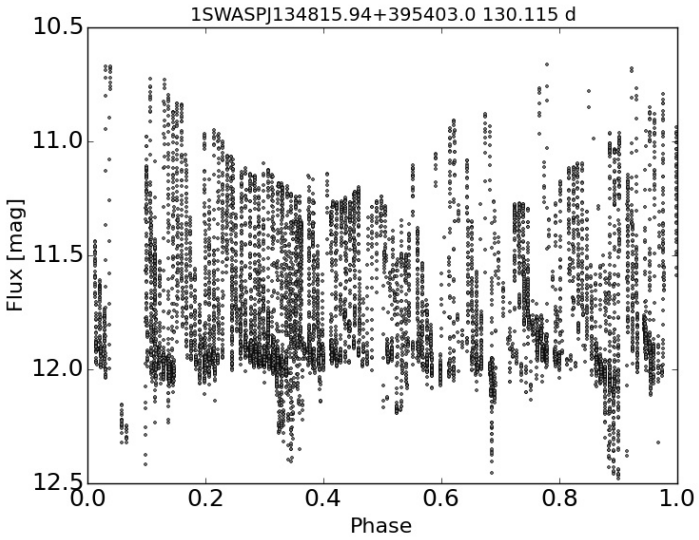

Figure B.50: Light curve for 1SWASPJ134815.94+395403.0 phase folded by a candidate Blazhko period of 130.1 d showing a very well defined envelope function.

m) 1SWASPJ141345.50-225441.8

The effects of AM can be clearly seen in all 3 years of Fig. B.51 for 1SWASPJ141345.50-225441.8. The weekly light curves in Fig. B.52 show this subtle but consistent change in amplitude over the course of 6 weeks.

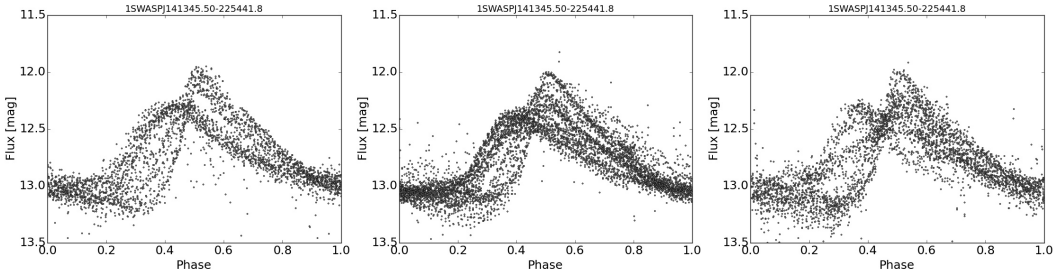

(a) 2006 (b) 2007 (c) 2008

Figure B.51: 2 yearly light curves of 1SWASPJ141345.50-225441.8.

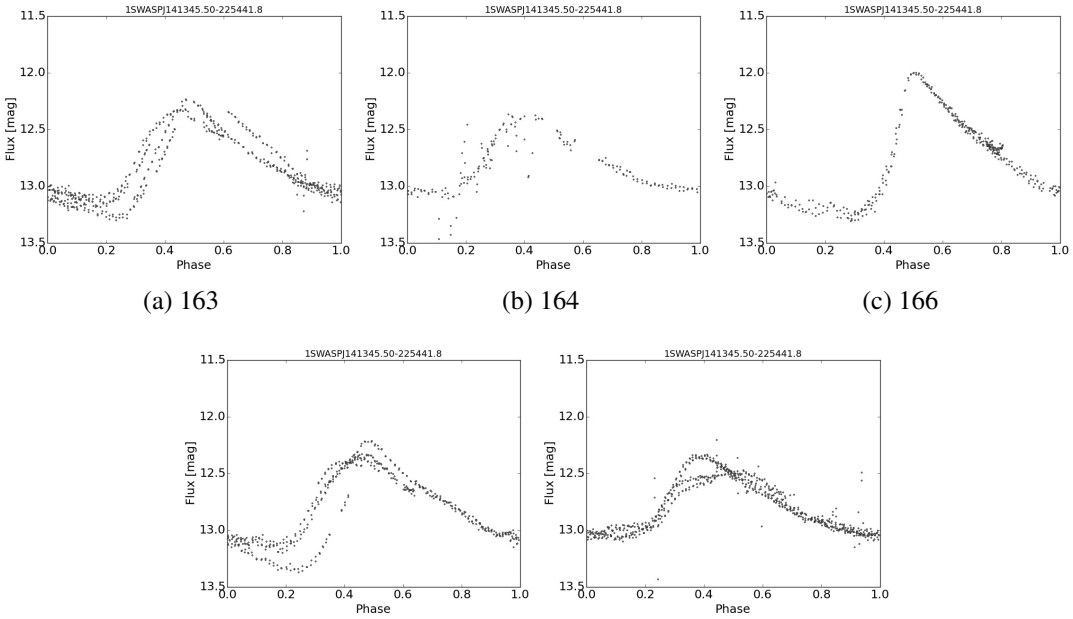

(a) 163 (b) 164 (c) 166

(d) 167 (e) 168

Figure B.52: 5 week long segments of the light curve of 1SWASPJ141345.50-225441.8.

The light curve for 1SWASPJ141345.50-225441.8 in 2007 (Fig. B.53) suggests a modulation period of around 30 d. When the entire light curve is folded by 26.5 d a clear envelope function is produced. (Fig. B.54).

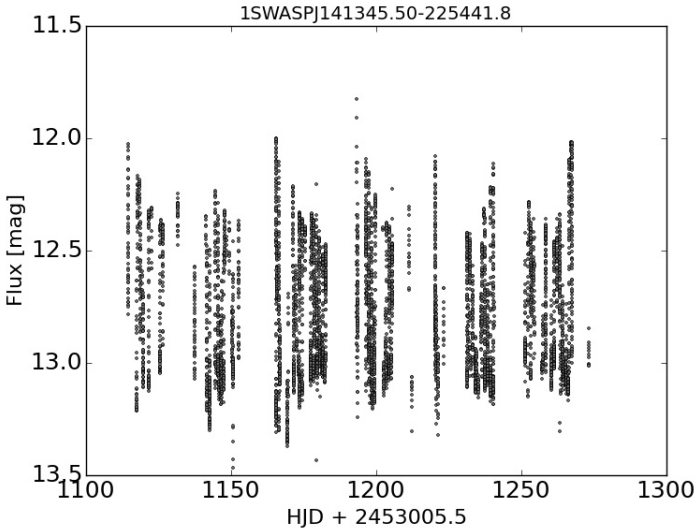

Figure B.53: Unfolded light curve from observations of 1SWASPJ141345.50-225441.8 taken during 2007.

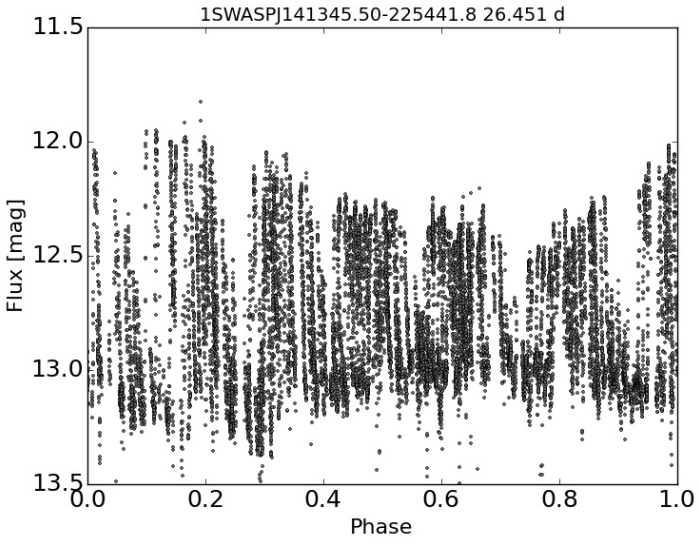

Figure B.54: Light curve for 1SWASPJ141345.50-225441.8 phase folded by a candidate Blazhko period of 26.5 d.

n) 1SWASPJ145315.45-143556.4

An extensive amount of AM can be seen in each year of the light curves of 1SWASPJ145315.45-143556.4 (Fig. B.55). This is reiterated in its weekly light curves (Fig. B.56), which also suggest quite a short Blazhko period.

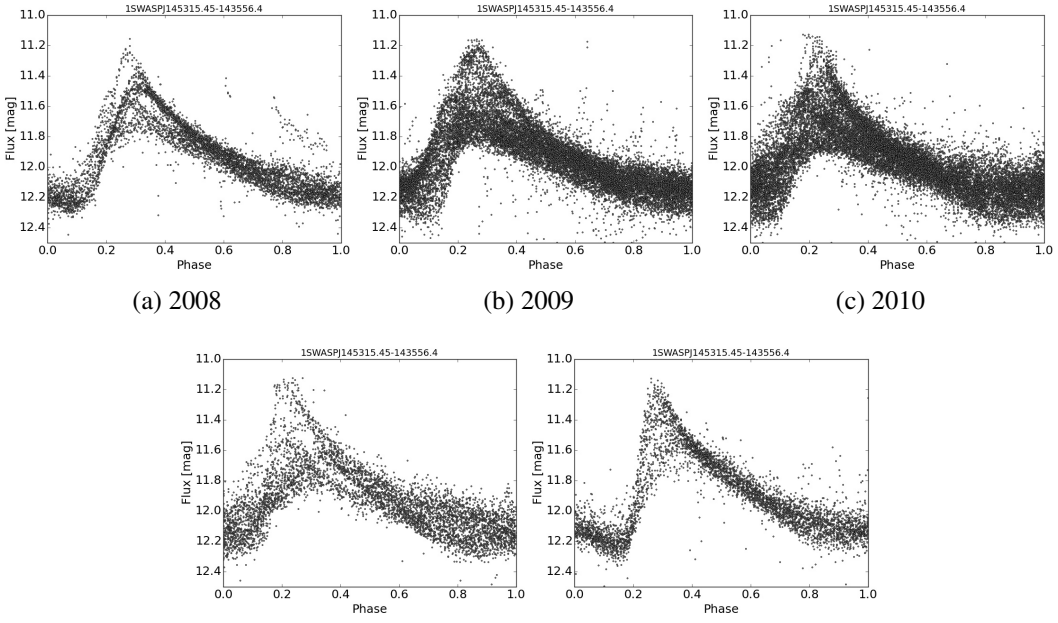

(a) 2008 (b) 2009 (c) 2010

(d) 2011 (e) 2012

Figure B.55: 5 consecutive yearly light curves of 1SWASPJ145315.45-143556.4.

The unfolded light curve for 1SWASPJ145315.45-143556.4 shown in Fig. B.57 for 2011 suggests a Blazhko period of just under 50 d. However, the Blazhko period of 84.0 d found by the phase folding program (Fig. B.58), even after setting the initial trial period to 35 d, shows 2 cycles, implying the actual Blazhko period is closer to 42 d.

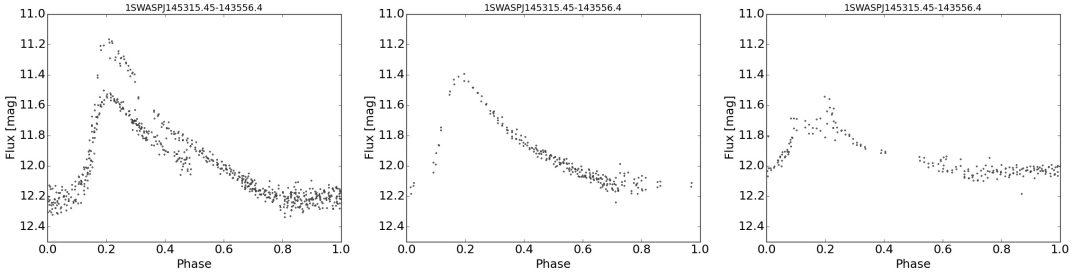

(a) 373 (b) 374 (c) 375

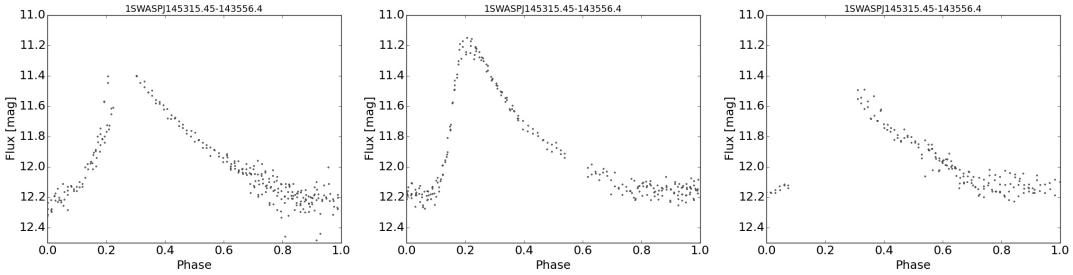

(d) 378 (e) 379 (f) 380

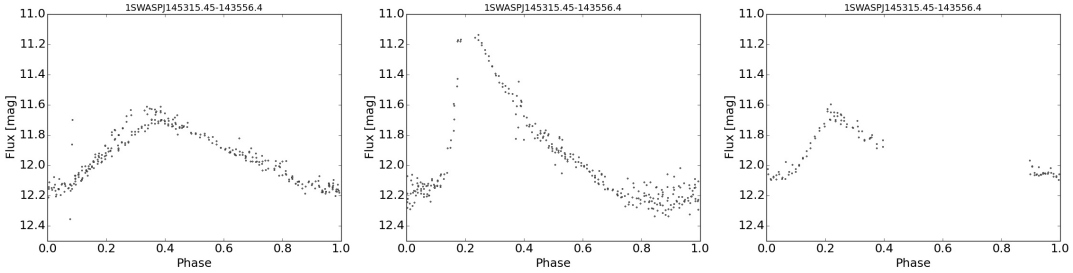

(g) 383 (h) 385 (i) 387

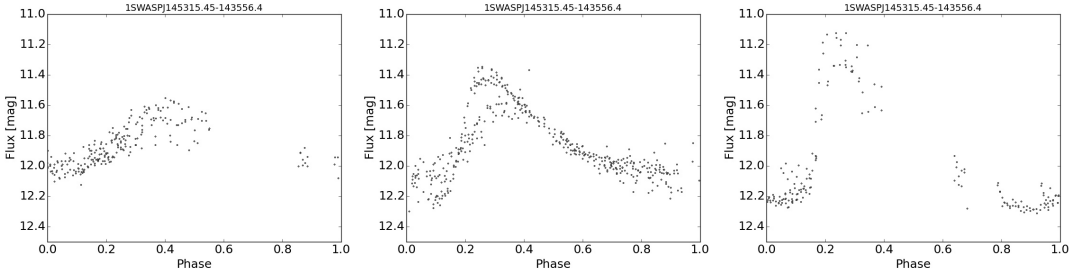

(j) 388 (k) 389 (l) 390

Figure B.56: 12 weekly light curves of 1SWASPJ145315.45-143556.4.

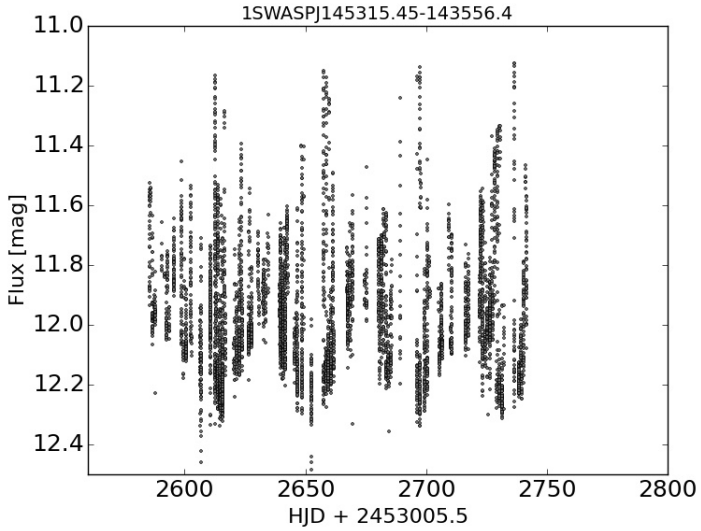

Figure B.57: Unfolded light curve from observations of 1SWASPJ145315.45-143556.4 taken during 2011.

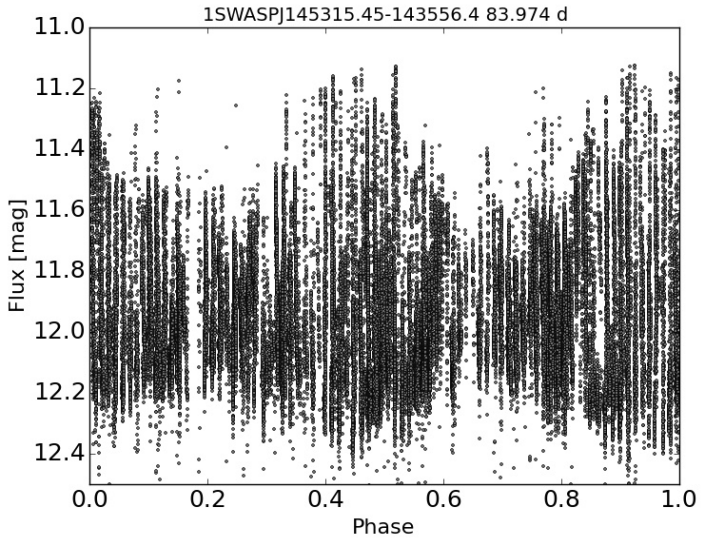

Figure B.58: Light curve for 1SWASPJ145315.45-143556.4 phase folded by a candidate Blazhko period of 84.0 d showing 2 Blazhko cycles.

o) 1SWASPJ152304.26-385153.6

Two pulsation shapes can be clearly seen the in the year–long light curves of 1SWASPJ152304.26-385153.6 (Fig. B.59). The weekly light curves (Fig. B.60) show how much the pulsation amplitude is reduced, particularly weeks 168 and 171.

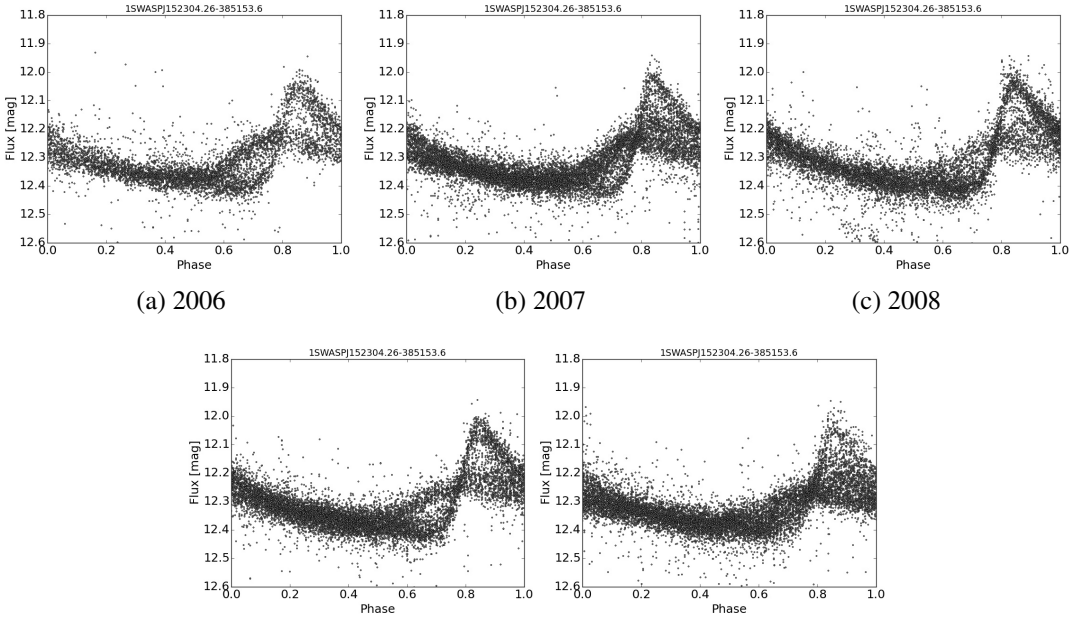

(a) 2006 (b) 2007 (c) 2008

(d) 2011 (e) 2012

Figure B.59: Yearly light curves of 1SWASPJ152304.26-385153.6 from 2008 to 2012.

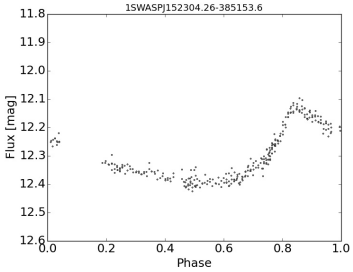

(a) 159

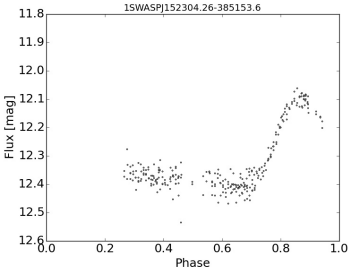

(b) 160

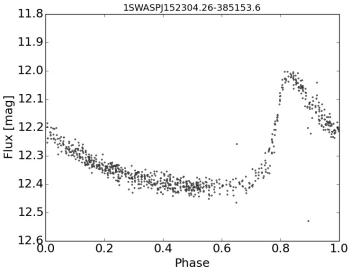

(c) 163

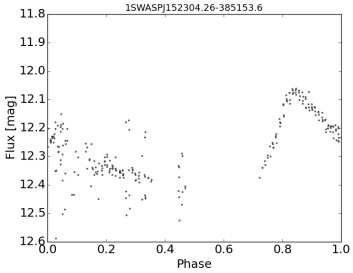

(d) 164

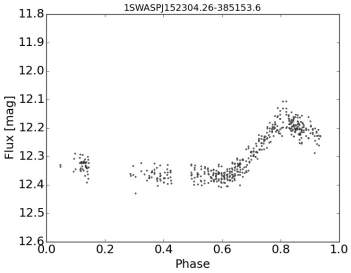

(e) 166

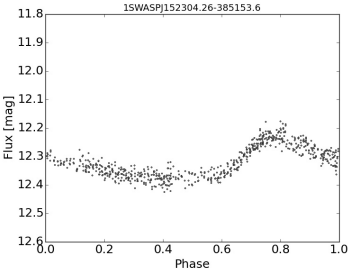

(f) 167

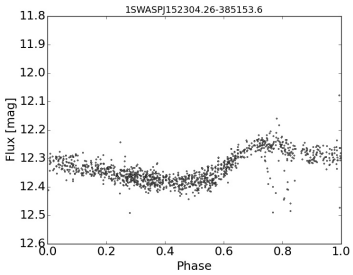

(g) 168

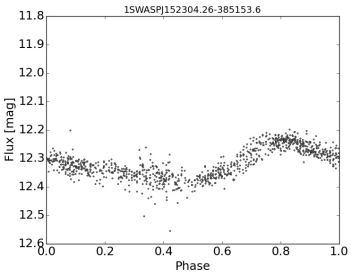

(h) 171

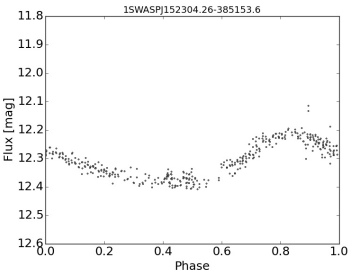

(i) 172

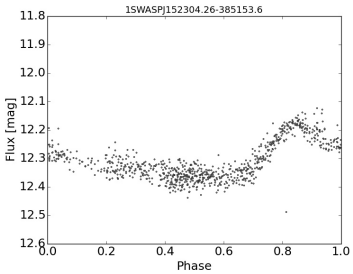

(j) 173

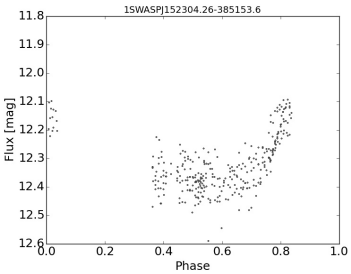

(k) 174

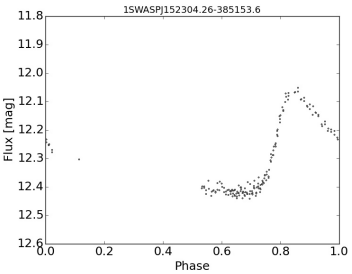

(l) 175

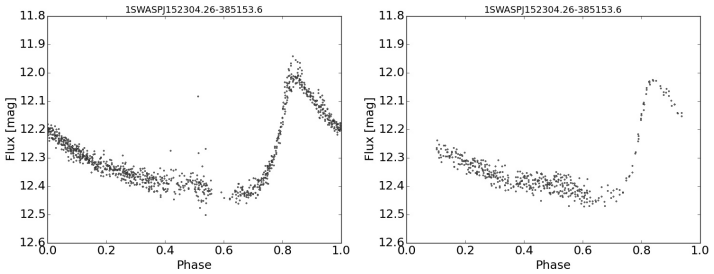

(m) 176 (n) 177

Figure B.60: 14 consecutive weekly sections of the light curve of 1SWASPJ152304.26-385153.6.

Figure B.61 shows a very clear envelope function for 1SWASPJ152304.26-385153.6 in 2007. The PDM routine discovers a period of 99.5 d (Fig. B.62) with a well defined envelope function where the pulsation doubles in amplitude over the course of each cycle.

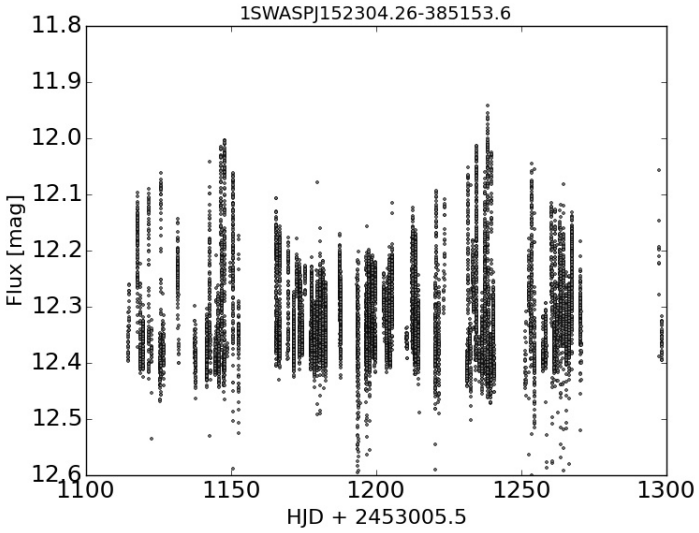

Figure B.61: Unfolded light curve from observations of 1SWASPJ152304.26-385153.6 taken during 2007.

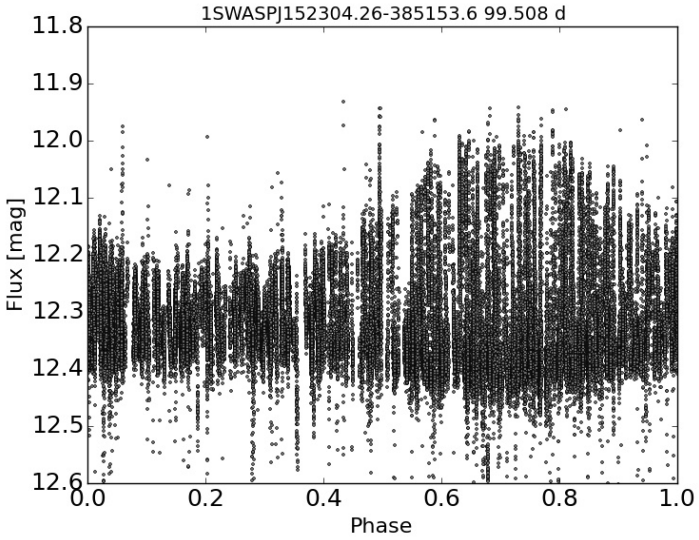

Figure B.62: Light curve for 1SWASPJ152304.26-385153.6 phase folded by a candidate Blazhko period of 99.5 d showing a very well defined envelope function.

p) 1SWASPJ153911.88+035524.6

Both the year (Fig. B.63) and week (Fig. B.64) long light curves for 1SWASPJ153911.88+035524.6 show that it maintains quite a large pulsation amplitude despite AM which is most apparent in 2008.

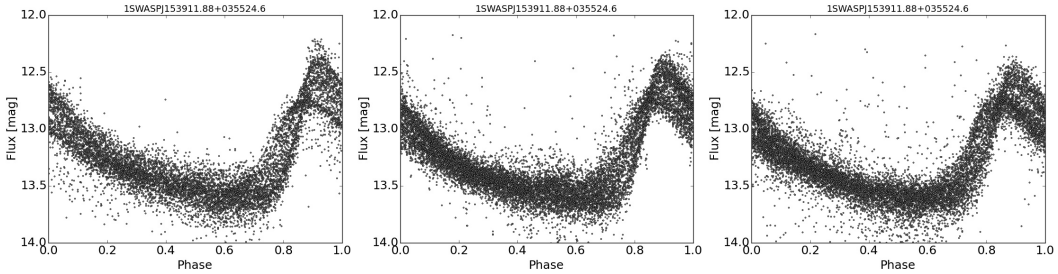

(a) 2008 (b) 2009 (c) 2010

Figure B.63: 3 consecutive yearly light curves of 1SWASPJ153911.88+035524.6.

The unfolded light curve for 1SWASPJ153911.88+035524.6 in 2013 (Fig. B.65) shows very little AM, despite showing consistent AM when the 3 light curves in Fig. B.63, each lasting a year, were phase folded by the pulsation period. The folded light curve (Fig. B.66) does, however, show AM, with a short candidate Blazhko period of 22.7 d.

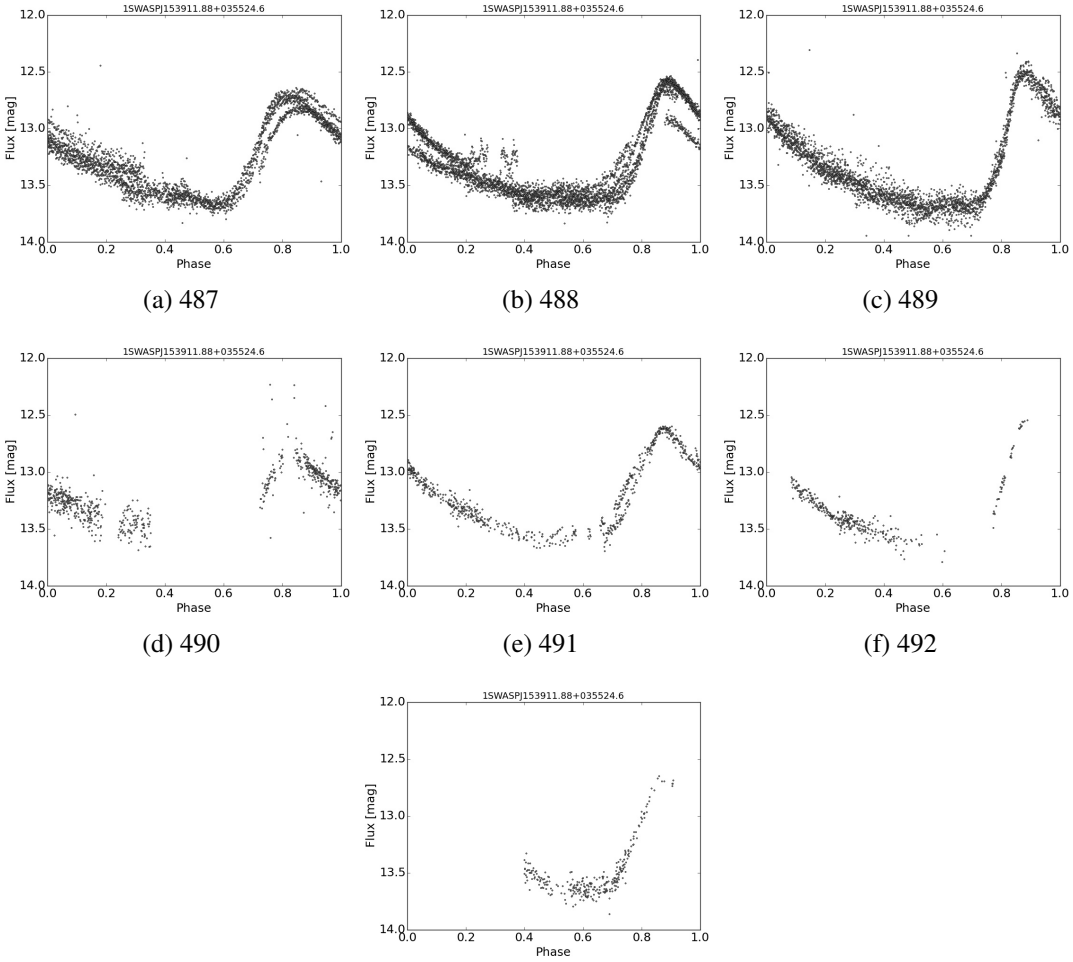

(a) 487 (b) 488 (c) 489

(d) 490 (e) 491 (f) 492

(g) 493

Figure B.64: 7 consecutive weekly light curves of 1SWASPJ153911.88+035524.6.

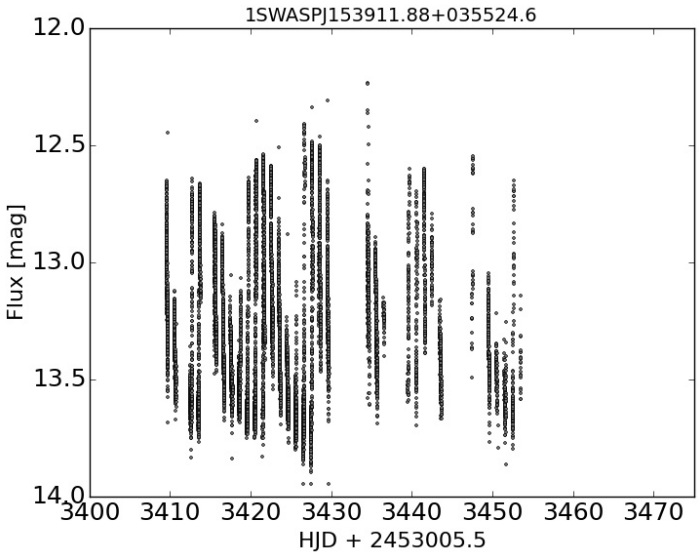

Figure B.65: Unfolded light curve from observations of 1SWASPJ153911.88+035524.6 taken during 2013.

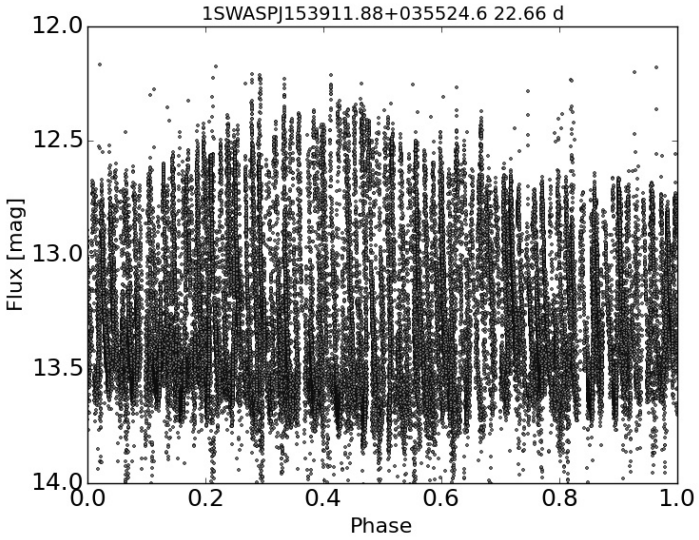

Figure B.66: Light curve for 1SWASPJ153911.88+035524.6 phase folded by a candidate Blazhko period of 22.7 d.

q) 1SWASPJ161255.64-082727.6

1SWASPJ161255.64-082727.6 shows extreme levels of AM in each year (Fig. B.67). Its weekly light curves (Fig. B.68) show an interesting bump feature around the minimum of each pulsation.

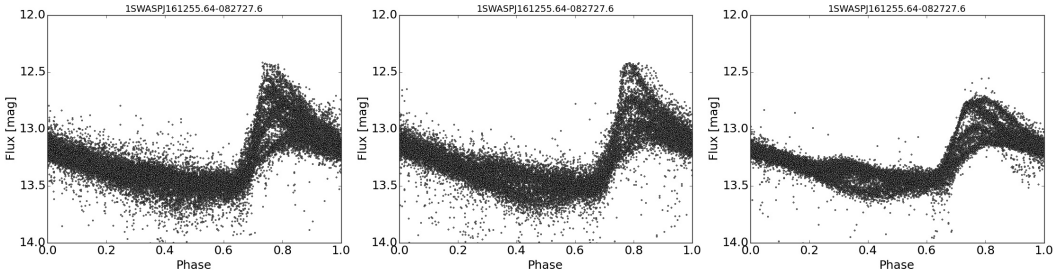

(a) 2009 (b) 2010 (c) 2013

Figure B.67: 3 yearly light curves of 1SWASPJ161255.64-082727.6.

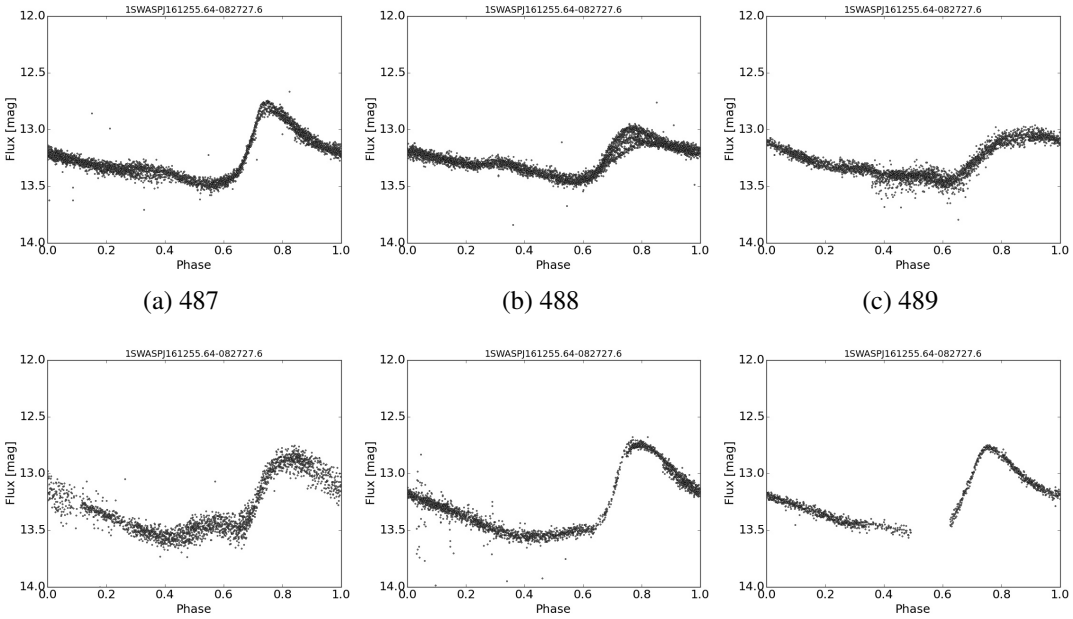

(a) 487 (b) 488 (c) 489

(d) 490 (e) 491 (f) 492

Figure B.68: 6 consecutive weekly light curves of 1SWASPJ161255.64-082727.6.

The unfolded light curve for 1SWASPJ161255.64-082727.6 in 2013 shows very clear AM (Fig. B.69). The phase folding program finds a candidate Blazhko period of 39.2 d that gives a very clear envelope function as shown in Fig. B.70.

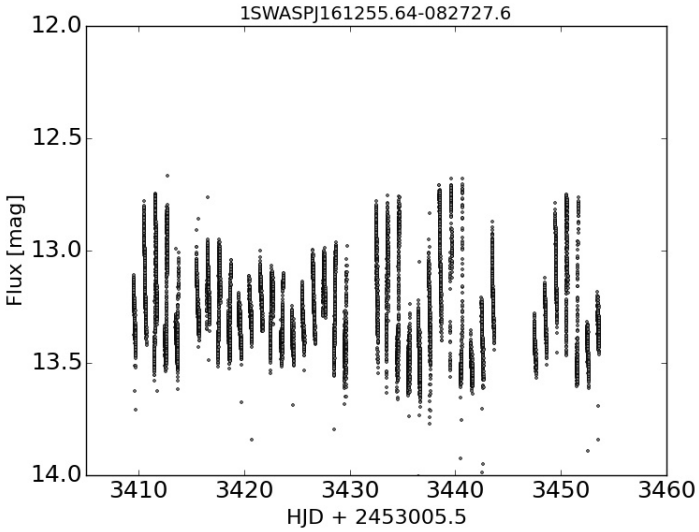

Figure B.69: Unfolded light curve from observations of 1SWASPJ161255.64-082727.6 taken during 2013.

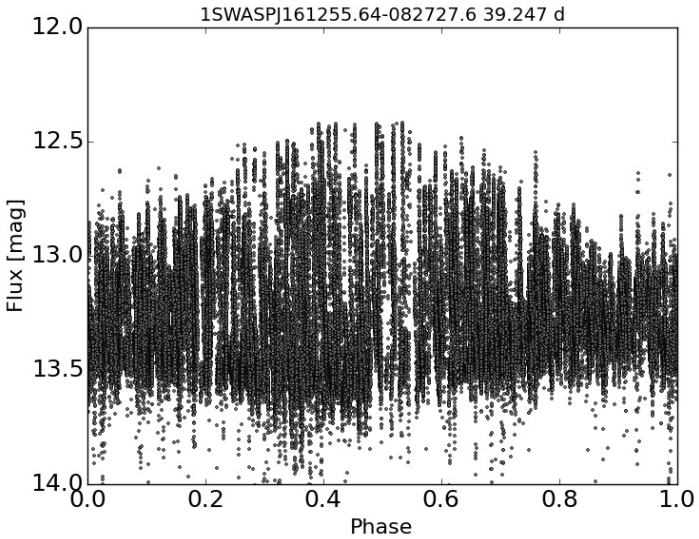

Figure B.70: Light curve for 1SWASPJ161255.64-082727.6 phase folded by a candidate Blazhko period of 39.2 d showing a well defined envelope function.

r) 1SWASPJ195926.63-340015.6

1SWASPJ195926.63-340015.6 is another example of extreme AM where the pulsation amplitude is greatly reduced (Fig. B.71). This is most apparent when comparing weeks 178 and 181 in Fig. B.72, which are only 3 weeks apart, suggesting a short Blazhko period.

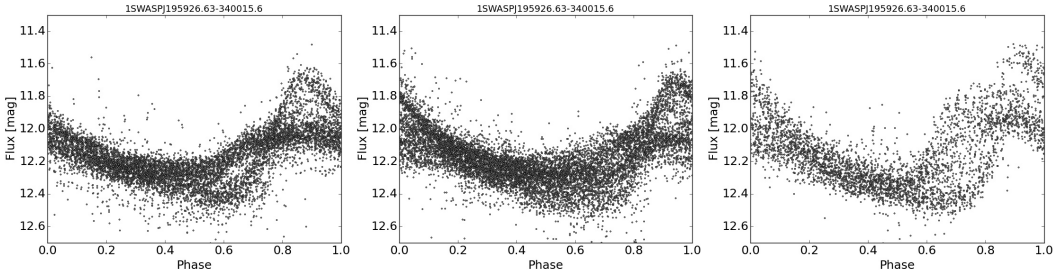

(a) 2006 (b) 2007 (c) 2011

Figure B.71: 3 yearly light curves of 1SWASPJ195926.63-340015.6.

1SWASPJ195926.63-340015.6 shows high levels of AM during 2007 (Fig. B.73) but also has large gaps in the light curve. The PDM program finds a candidate Blazhko period of 44.6 d (Fig. B.74). However, the envelope function is not as well defined in the second half of the cycle.

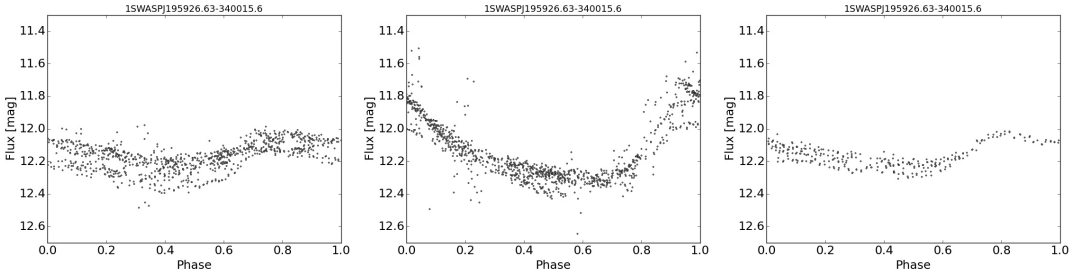

(a) 171 (b) 173 (c) 177

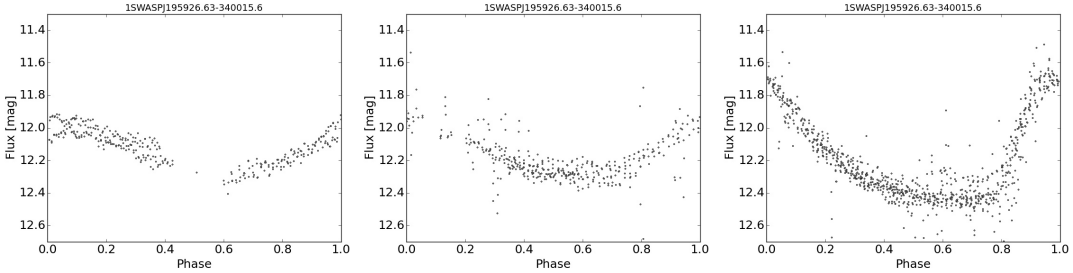

(d) 178 (e) 179 (f) 180

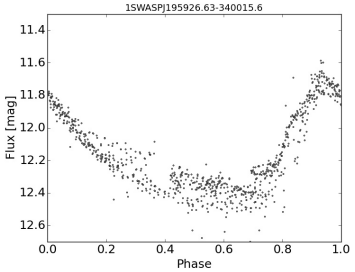

(g) 181

Figure B.72: 7 weekly light curves of 1SWASPJ195926.63-340015.6.

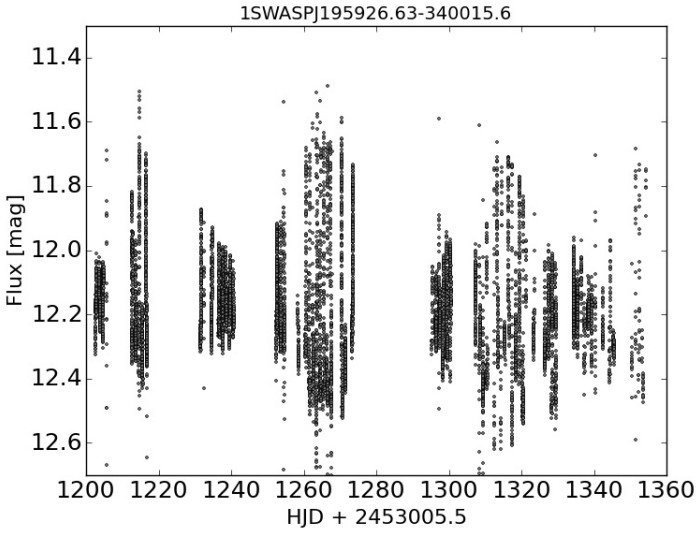

Figure B.73: Unfolded light curve from observations of 1SWASPJ195926.63-340015.6 taken during 2007.

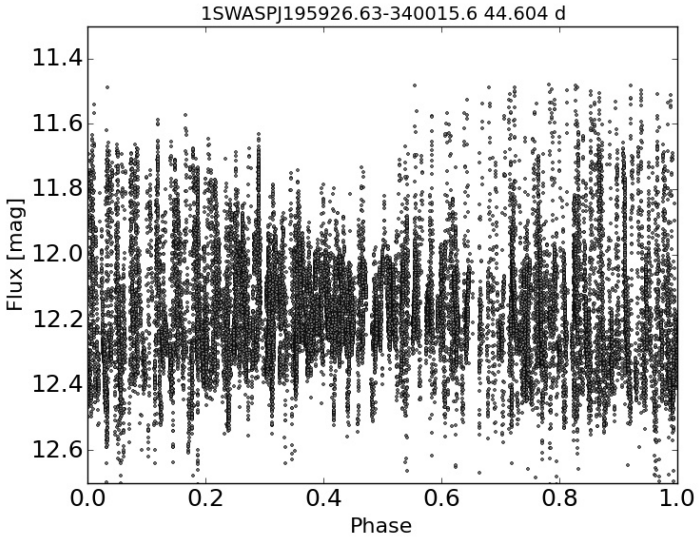

Figure B.74: Light curve for 1SWASPJ195926.63-340015.6 phase folded by a candidate Blazhko period of 44.6 d.

s) 1SWASPJ204432.08-342404.6

The high quality of both year and week long light curves for 1SWASPJ204432.08-342404.6 are shown in Fig. B.75 and Fig. B.76, where the pulsation amplitude can be seen to be changing in the order of 16 weeks.

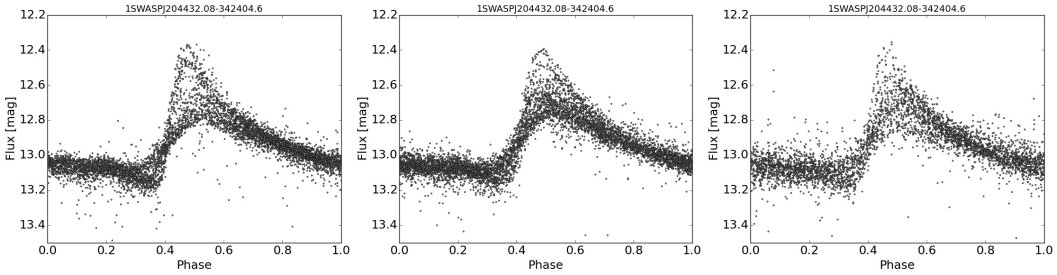

(a) 2006 (b) 2007 (c) 2011

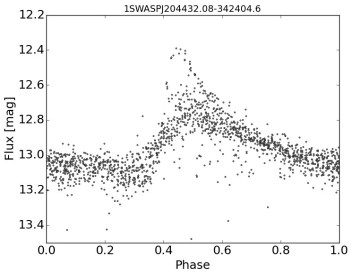

(d) 2012

Figure B.75: 4 yearly light curves of 1SWASPJ204432.08-342404.6.

1SWASPJ204432.08-342404.6 shows a very clear envelope function in the unfolded light curve for 2006 (Fig. B.77). The phase folded light curve (Fig. B.78) is able to reproduce this strong AM when folding the entire light curve by a candidate Blazhko period of 53.7 d.

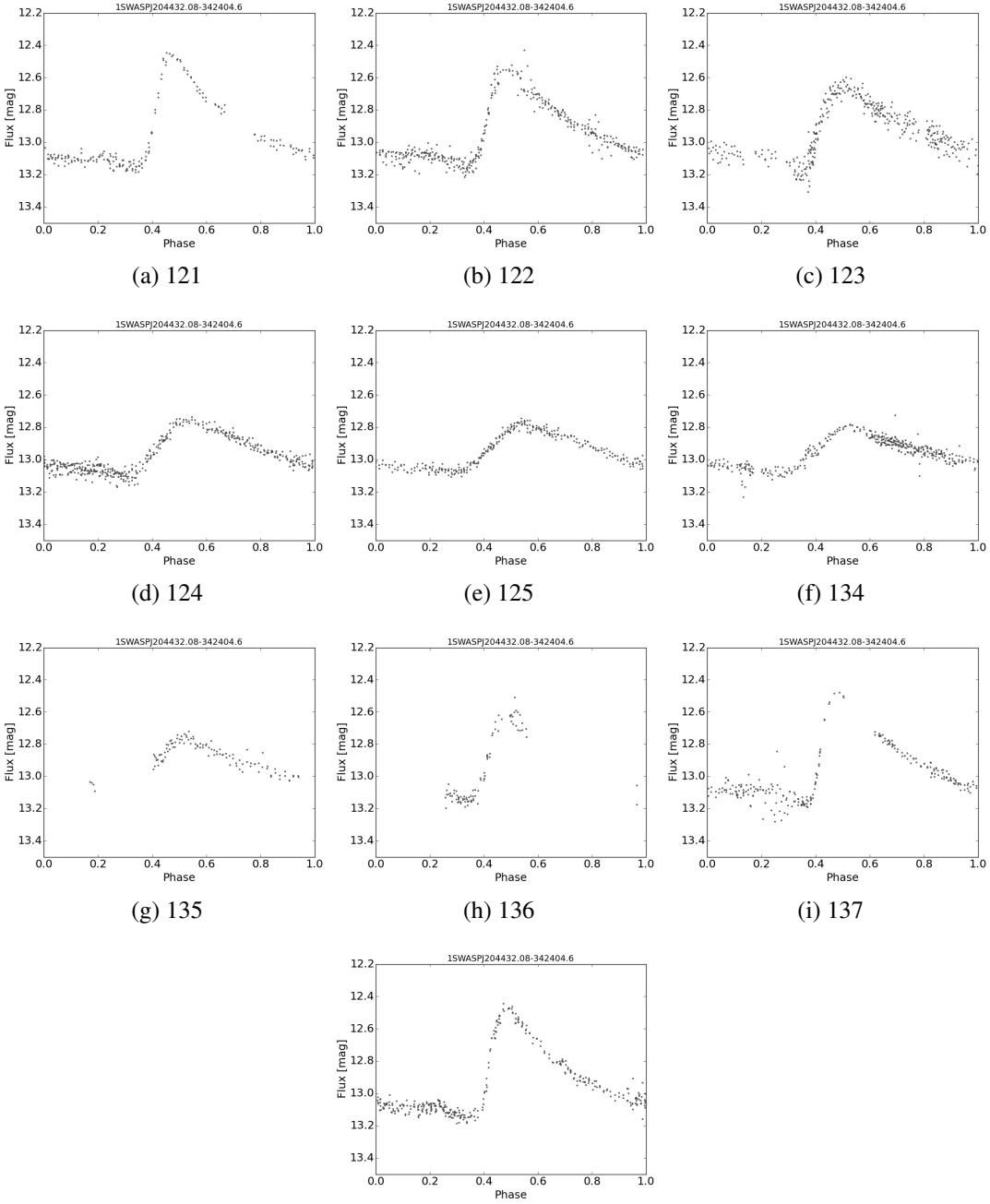

(a) 121 (b) 122 (c) 123

(d) 124 (e) 125 (f) 134

(g) 135 (h) 136 (i) 137

(j) 138

Figure B.76: 10 weekly light curves of 1SWASPJ204432.08-342404.6.

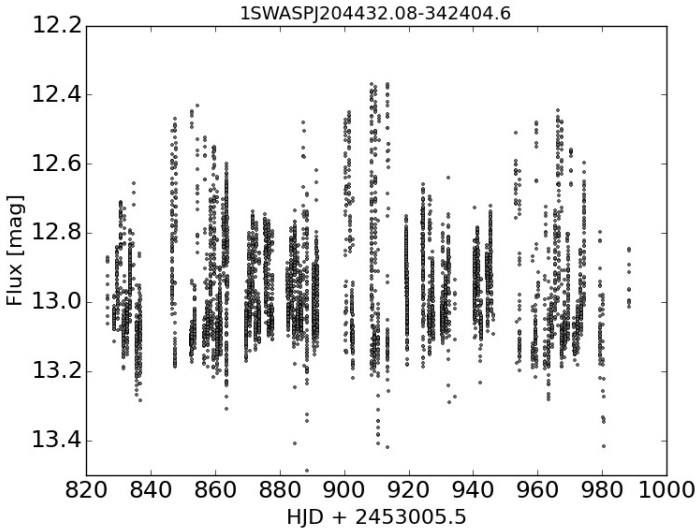

Figure B.77: Unfolded light curve from observations of 1SWASPJ204432.08-342404.6 taken during 2006.

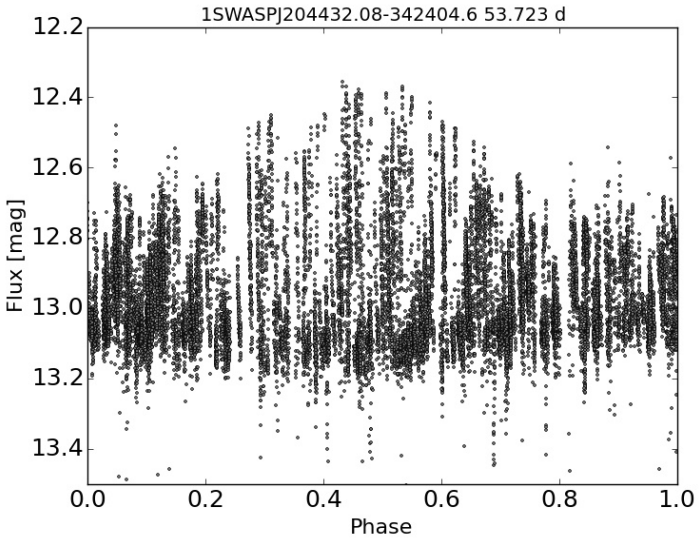

Figure B.78: Light curve for 1SWASPJ204432.08-342404.6 phase folded by a candidate Blazhko period of 53.7 d.

t) 1SWASPJ225247.51-244213.2

Despite only having 2 years of well defined light curves (Fig. B.79), 1SWASPJ225247.51-244213.2 shows both high and low phases of AM over the course of each year. The week long light curves in Fig. B.80 show a marked reduction in pulsation amplitudes from week 390 to week 404 of observations, implying that the potential Blazhko period is at least twice the timescale of 14 weeks.

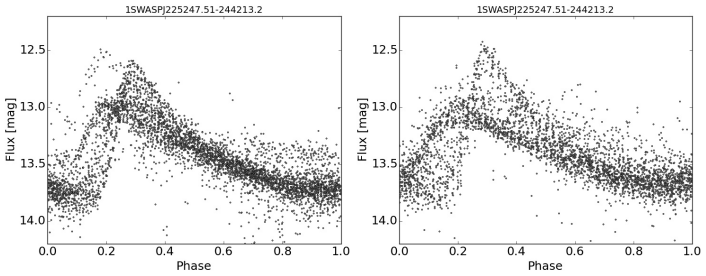

(a) 2007 (b) 2011

Figure B.79: 2 year long segments of the light curve of 1SWASPJ225247.51-244213.2.

The entire light curve for 1SWASPJ225247.51-244213.2 phase folded on a period of 180.8 d follows the shape of the envelope function for the individual 2006 season (Fig. B.81), which had initially indicated a trial period range centred on 200 d for the PDM folding routine.

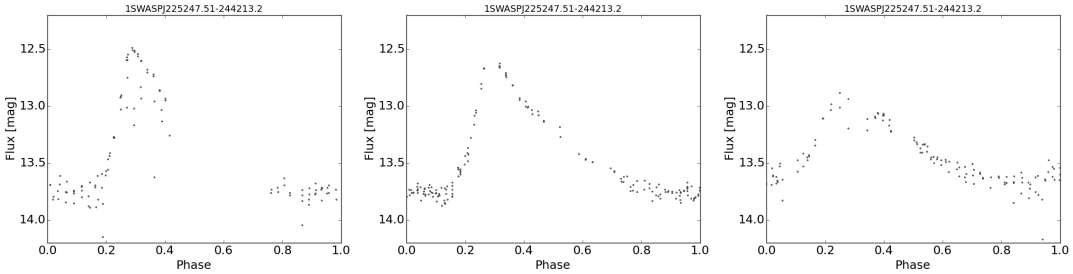

(a) 390 (b) 391 (c) 394

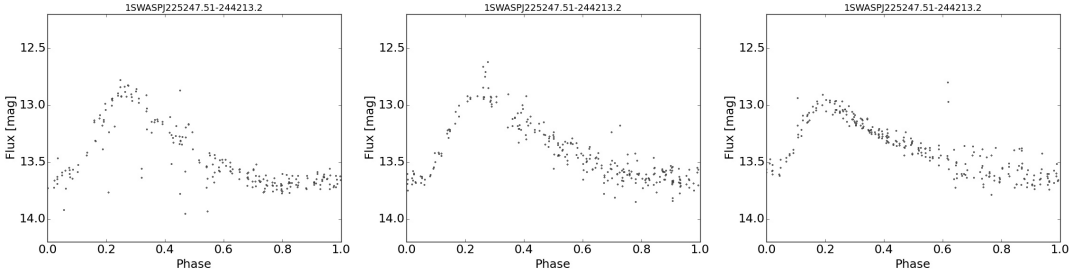

(d) 395 (e) 396 (f) 398

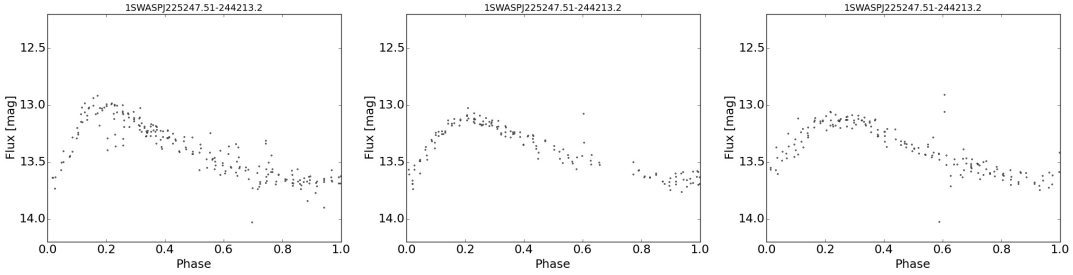

(g) 400 (h) 403 (i) 404

Figure B.80: 9 weekly light curves of 1SWASPJ225247.51-244213.2.

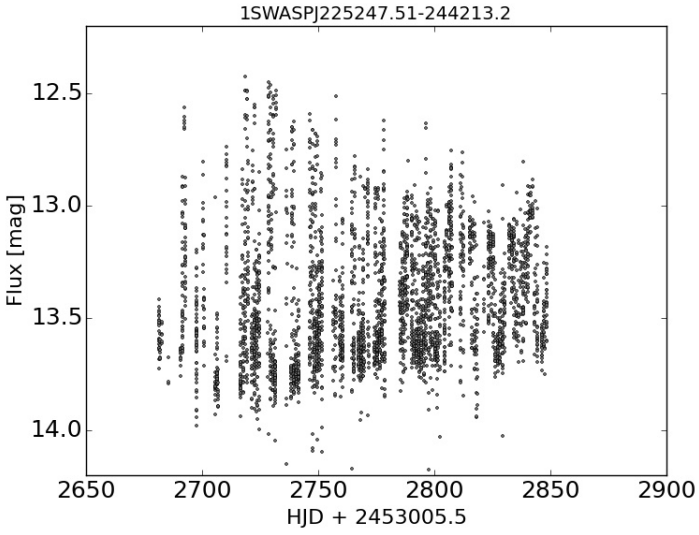

Figure B.81: Unfolded light curve from observations of 1SWASPJ204432.08-342404.6 taken during 2006.

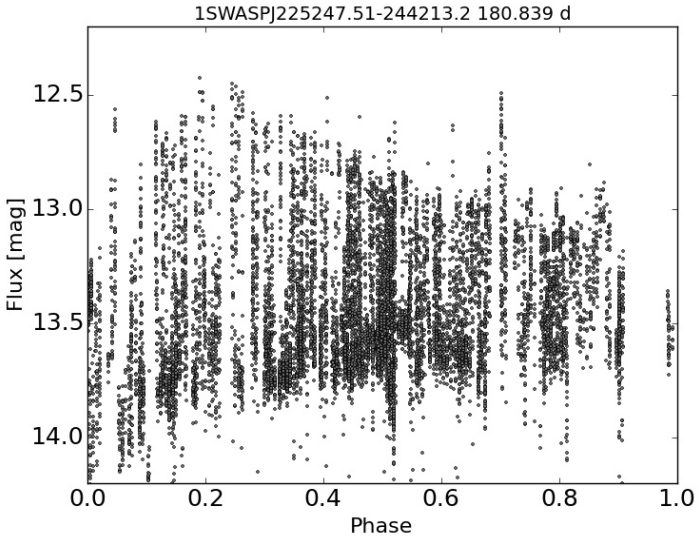

Figure B.82: Light curve for 1SWASPJ225247.51-244213.2 phase folded by a candidate Blazhko period of 180.8 d showing a reasonably well defined envelope function.

Appendix C

This appendix, available in electronic format, contains the full SuperWASP catalogue of 983 Blazhko effect objects along with coincident objects from the Skarka online database 'Known Blazhko stars in Galactic field'. The headings are as follows: SWASP id: unique SuperWASP object identifier; P_{Pulse} : pulsation period in days; A_{LC}: pulsation amplitude in magnitudes; P_{BL}: Blazhko period in days; A_{BL}: Blazhko amplitude in millimagnitudes; Skarka name: name of the coincident object in the online Skarka database; Skarka P_{BL}: Blazhko period in days as listed, if known, in the Skarka database.

Appendix D

This appendix, available in electronic format,contains the full SuperWASP catalogue of 983 Blazhko effect objects along with coincident CRTS objects. The headings are as follows: SWASP id: unique SuperWASP object identifier; $P_{\rm Pulse}$: pulsation period in days; $A_{\rm LC}$: pulsation amplitude in magnitudes; $P_{\rm BL}$: Blazhko period in days; $A_{\rm BL}$: Blazhko amplitude in millimagnitudes; CRTS name: name of the coincident object in the CRTS catalogues; CRTS Blazhko: denotes objects as a Blazhko object in the CRTS catalogues.

Bibliography

Akerlof, C., Amrose, S., Balsano, R., Bloch, J., Casperson, D., Fletcher, S., Gisler, G., Hills, J., Kehoe, R., Lee, B., Marshall, S., McKay, T., Pawl, A., Schaefer, J., Szymanski, J., and Wren, J.: 2000, *AJ* **119**, 1901

Alton, K. B.: 2014, *Journal of the American Association of Variable Star Observers (JAAVSO)* **42**, 66

Bailey, S. I.: 1902, *Annals of Harvard College Observatory* **38**, 1

Benedict, G. F., McArthur, B. E., Feast, M. W., Barnes, T. G., Harrison, T. E., Bean, J. L., Menzies, J. W., Chaboyer, B., Fossati, L., Nesvacil, N., Smith, H. A., Kolenberg, K., Laney, C. D., Kochukhov, O., Nelan, E. P., Shulyak, D. V., Taylor, D., and Freedman, W. L.: 2011, *AJ* **142**, 187

Benkő, J. M., Kolenberg, K., Szabó, R., Kurtz, D. W., Bryson, S., Bregman, J., Still, M., Smolec, R., Nuspl, J., Nemec, J. M., Moskalik, P., Kopacki, G., Kolláth, Z., Guggenberger, E., di Criscienzo, M., Christensen-Dalsgaard, J., Kjeldsen, H., Borucki, W. J., Koch, D., Jenkins, J. M., and van Cleve, J. E.: 2010, *MNRAS* **409**, 1585

Benkő, J. M. and Szabó, R.: 2014, in *CoRoT Symposium, Kepler KASC-7 Joint Meeting 2014: The Space Photometry Revolution*, Vol. 1411, p. 1914, EDP Sciences

Benkő, J. M., Szabó, R., and Paparó, M.: 2011, *MNRAS* **417**, 974

Bertin, E. and Arnouts, S.: 1996, *AAPS* **117**, 393

Blažko, S.: 1907, *Astronomische Nachrichten* **175(20)**, 325

Boch, T. and Fernique, P.: 2014, in N. Manset and P. Forshay (eds.), *Astronomical Data*

Analysis Software and Systems XXIII, Vol. 485 of *Astronomical Society of the Pacific Conference Series*, p. 277

Bonnarel, F., Fernique, P., Bienaymé, O., Egret, D., Genova, F., Louys, M., Ochsenbein, F., Wenger, M., and Bartlett, J. G.: 2000, *AAPS* **143**, 33

Bono, G., Caputo, F., Castellani, V., and Marconi, M.: 1997, *AAPS* **121**, 327

Braga, V. F., Dall'Ora, M., Bono, G., Stetson, P. B., Ferraro, I., Iannicola, G., Marengo, M., Neeley, J., Persson, S. E., Buonanno, R., Coppola, G., Freedman, W., Madore, B. F., Marconi, M., Matsunaga, N., Monson, A., Rich, J., Scowcroft, V., and Seibert, M.: 2015, *ApJ* **799**, 165

Bryant, P. H.: 2014, *ApJL* **783**, L15

Bryant, P. H.: 2015, *ApJ* **802**, 52

Caputo, F.: 1998, *A&AR* **9(1-2)**, 33

Caputo, F.: 2012, *Astrophysics and Space Science* **341**, 77

Catelan, Márcio and Smith, Horace A.: 2014, *Pulsating Stars*, John Wiley & Sons, Incorporated, Weinheim

Chadid, M., Benkő, J. M., Szabó, R., Paparó, M., Chapellier, E., Kolenberg, K., Poretti, E., Bono, G., Le Borgne, J.-F., Trinquet, H., Artemenko, S., Auvergne, M., Baglin, A., Debosscher, J., Grankin, K. N., Guggenberger, E., and Weiss, W. W.: 2010, *AAP* **510**, A39

Chadid, M., Perini, C., Bono, G., Auvergne, M., Baglin, A., Weiss, W. W., and Deboscher, J.: 2011, *A&A* **527**, A146

Cunha, M. S., Aerts, C., Christensen-Dalsgaard, J., Baglin, A., Bigot, L., Brown, T. M., Catala, C., Creevey, O. L., Domiciano de Souza, A., Eggenberger, P., Garcia, P. J. V., Grundahl, F., Kervella, P., Kurtz, D. W., Mathias, P., Miglio, A., Monteiro, M. J. P. F. G., Perrin, G., Pijpers, F. P., Pourbaix, D., Quirrenbach, A., Rousselet-Perraut, K., Teixeira, T. C., Thévenin, F., and Thompson, M. J.: 2007, *The Astronomy and Astrophysics Review* **14**, 217

Damasso, M., Bernagozzi, A., Bertolini, E., Calcidese, P., Carbognani, A., Cenadelli, D., Christille, J. M., Giacibbe, P., Lanteri, L., Lattanzi, M. G., Smart, R., and Sozzetti, A.: 2014, *The Journal of the American Association of Variable Star Observers* 42

Davies, S. R.: 1990, *MNRAS* **244**, 93

Drake, A. J., Catelan, M., Djorgovski, S. G., Torrealba, G., Graham, M. J., Belokurov, V., Koposov, S. E., Mahabal, A., Prieto, J. L., Donalek, C., Williams, R., Larson, S., Christensen, E., and Beshore, E.: 2013a, *ApJ* **763**, 32

Drake, A. J., Catelan, M., Djorgovski, S. G., Torrealba, G., Graham, M. J., Mahabal, A., Prieto, J. L., Donalek, C., Williams, R., Larson, S., Christensen, E., and Beshore, E.: 2013b, *ApJ* **765**, 154

Drake, A. J., Djorgovski, S. G., Catelan, M., Graham, M. J., Mahabal, A. A., Larson, S., Christensen, E., Torrealba, G., Beshore, E., McNaught, R. H., Garradd, G., Belokurov, V., and Koposov, S. E.: 2017, *MNRAS* **469**, 3688

Drake, A. J., Djorgovski, S. G., Mahabal, A., Beshore, E., Larson, S., Graham, M. J., Williams, R., Christensen, E., Catelan, M., Boattini, A., Gibbs, A., Hill, R., and Kowałski, R.: 2009, *ApJ* **696**, 870

Drake, A. J., Graham, M. J., Djorgovski, S. G., Catelan, M., Mahabal, A. A., Torrealba, G., García-Álvarez, D., Donalek, C., Prieto, J. L., Williams, R., Larson, S., Christen sen, E., Belokurov, V., Koposov, S. E., Beshore, E., Boattini, A., Gibbs, A., Hill, R., Kowalski, R., Johnson, J., and Shelly, F.: 2014, *ApJ* **213**, 9

Drake, A. J., Williams, R., Graham, M. J., Mahabal, A., Djorgovski, S. G., White, R. R., Vestrand, W. T., and Bloom, J.: 2007, in *American Astronomical Society Meeting Abstracts*, Vol. 39 of *Bulletin of the American Astronomical Society*, p. 805

Evans, N. R., Szabó, R., Derekas, A., Szabados, L., Cameron, C., Matthews, J. M., Sasselov, D., Kuschnig, R., Rowe, J. F., Guenther, D. B., Moffat, A. F. J., Rucinski, S. M., and Weiss, W. W.: 2015, *MNRAS* **446**, 4008

Feast, M., Laney, C., Kinman, T., van Leeuwen, F., and Whitelock, P.: 2008, *MNRAS* **386(4)**, 2115

Fiorentino, G., Contreras Ramos, R., Tolstoy, E., Clementini, G., and Saha, A.: 2012, *A&A* **539**, A138

Fossati, L., Kolenberg, K., Shulyak, D. V., Elmasli, A., Tsymbal, V., Barnes, T. G., Guggenberger, E., and Kochukhov, O.: 2014, *MNRAS* **445**, 4094

Gallart, C., Zoccali, M., and Aparicio, A.: 2005, *ARA&A* **43**, 387

García, R. A., Jiménez, A., Mathur, S., Ballot, J., Eff-Darwich, A., Jiménez-Reyes, S. J., Pallé, P. L., Provost, J., and Turck-Chièze, S.: 2008, *Astronomische Nachrichten* **329**, 476

Gavrilchenko, T., Klein, C. R., Bloom, J. S., and Richards, J. W.: 2014, *MNRAS* **441**, 715

Gillet, D.: 2013, *A&A* **554**, A46

Gillet, D. and Fokin, A. B.: 2014, *A&A* **565**, A73

Gilliland, R. L., Brown, T. M., Christensen-Dalsgaard, J., Kjeldsen, H., Aerts, C., Appourchaux, T., Basu, S., Bedding, T. R., Chaplin, W. J., Cunha, M. S., De Cat, P., De Ridder, J., Guzik, J. A., Handler, G., Kawaler, S., Kiss, L., Kolenberg, K., Kurtz, D. W., Metcalfe, T. S., Monteiro, M. J. P. F. G., Szabó, R., Arentoft, T., Balona, L., Debosscher, J., Elsworth, Y. P., Quirion, P.-O., Stello, D., Suárez, J. C., Borucki, W. J., Jenkins, J. M., Koch, D., Kondo, Y., Latham, D. W., Rowe, J. F., and Steffen, J. H.: 2010, *PASP* **122**, 131

Gratton, R. G., Fusi Pecci, F., Carretta, E., Clementini, G., Corsi, C. E., and Lattanzi, M.: 1997, *ApJ* **491**, 749

Greer, P. A., Payne, S. G., Norton, A. J., Maxted, P. F. L., Smalley, B., West, R. G., Wheatley, P. J., and Kolb, U. C.: 2017, *A&A* **607**, A11

Groebel, R.: 2013, *eprint arXiv:1307.6454*

Hajdu, G., Catelan, M., Jurcsik, J., Dékány, I., Drake, A., and Marquette, J.-B.: 2015, *MNRAS* **449**, L113

Hernitschek, N., Schlafly, E. F., Sesar, B., Rix, H.-W., Hogg, D. W., Ivezić, Z., Grebel, E. K., Bell, E. F., Martin, N. F., Burgett, W. S., Flewelling, H., Hodapp, K. W., Kaiser, N., Magnier, E. A., Metcalfe, N., Wainscoat, R. J., and Waters, C.: 2016, *ApJ* **817**, 73

Holdsworth, D. L., Smalley, B., Gillon, M., Clubb, K. I., Southworth, J., Maxted, P. F. L., Anderson, D. R., Barros, S. C. C., Cameron, A. C., Delrez, L., Faedi, F., Haswell, C. A., Hellier, C., Horne, K., Jehin, E., Norton, A. J., Pollacco, D., Skillen, I., Smith, A. M. S., West, R. G., and Wheatley, P. J.: 2014, *MNRAS* **439(2)**, 2078

Högbom, J. A.: 1974, *A&AS* **15**, 417

Jurcsik, J., Smitola, P., Hajdu, G., and Nuspl, J.: 2014, *ApJ* **797**, L3

Jurcsik, J., Smitola, P., Hajdu, G., Pilachowski, C., Kolenberg, K., Sódor, Á., Fürész, G., Moór, A., Kun, E., Saha, A., Prakash, P., Blum, P., and Tóth, I.: 2013, *ApJ* **778(2)**, L27

Jurcsik, J., Sódor, A., Szeidl, B., Hurta, Z., Varadi, M., Posztobanyi, K., Vida, K., Hajdu, G., Kovari, Z., Nagy, I., Molnár, L., and Belucz, B.: 2009, *MNRAS* **400(2)**, 1006

Kaiser, N., Burgett, W., Chambers, K., Denneau, L., Heasley, J., Jedicke, R., Magnier, E., Morgan, J., Onaka, P., and Tonry, J.: 2010, in *Ground-based and Airborne Telescopes III*, Vol. 7733 of *Proceedings of SPIE*, p. 77330E

Kolenberg, K.: 2011, in A. McWilliam (ed.), *RR Lyrae Stars, Metal-Poor Stars, and the Galaxy*, Vol. 5, p. 100

Kolenberg, K., Bryson, S., Szabó, R., Kurtz, D. W., Smolec, R., Nemec, J. M., Guggenberger, E., Moskalik, P., Benkő, J. M., Chadid, M., Jeon, Y. B., Kiss, L. L., Kopacki, G., Nuspl, J., Still, M., Christensen-Dalsgaard, J., Kjeldsen, H., Borucki, W. J., Caldwell, D. A., Jenkins, J. M., and Koch, D.: 2010a, *MNRAS* **411(2)**, 878

Kolenberg, K., Fossati, L., Shulyak, D., Pikall, H., Barnes, T. G., Kochukhov, O., and Tsymbal, V.: 2010b, *A&A* **519**, A64

Kolenberg, K., Kurucz, R. L., Stellingwerf, R., Nemec, J. M., Moskalik, P., Fossati, L., Barnes, T. G., Guzik, J. A., Chaplin, W. J., Handler, G., and Pigulski, A.: 2014, in *IAU Symposium*, Vol. 301, pp 257–260

Kolláth, Z., Molnár, L., and Szabó, R.: 2011, *MNRAS* **414**, 1111

Kurtz, D. W.: 2006, in C. Aerts and C. Sterken (eds.), *Astrophysics of Variable Stars*, Vol. 349, p. 101

Le Borgne, J. F., Poretti, E., Klotz, A., Denoux, E., Smith, H. A., Kolenberg, K., Szabo, R., Bryson, S., Audejean, M., Buil, C., Caron, J., Conseil, E., Corp, L., Drillaud, C., de France, T., Graham, K., Hirosawa, K., Klotz, A. N., Kugel, F., Loughney, D., Menzies, K., Rodriguez, M., and Ruscitti, P. M.: 2014, *MNRAS* **441(2)**, 1435

Lehto, H. J.: 1997, in D. Maoz, A. Sternberg, and E. M. Leibowitz (eds.), *Astronomical Time Series*, Vol. 218, p. 269

Lenz, P. and Breger, M.: 2005, *Communications in Asteroseismology* **146**, 53

Li, L.-J. and Qian, S.-B.: 2014, *MNRAS* **444(1)**, 600

Liška, J., Skarka, M., Zejda, M., Mikulášek, Z., and de Villiers, S. N.: 2016, *MNRAS* **459**, 4360

Lohr, M. E., Norton, A. J., Kolb, U. C., Anderson, D. R., Faedi, F., and West, R. G.: 2012, *A&A* **542**, A124

Lohr, M. E., Norton, A. J., Kolb, U. C., Maxted, P. F. L., Todd, I., and West, R. G.: 2013, *A&A* **549**, A86

Maxted, P. F. L., Norton, A. J., West, R. G., Copperwheat, C., and Marsh, T. R.: 2008, in U. Heber, C. S. Jeffery, and R. Napiwotzki (eds.), *Hot Subdwarf Stars and Related Objects*, Vol. 392 of *Astronomical Society of the Pacific Conference Series*, p. 179

Molnár, L., Benkő, J. M., Szabó, R., Kolláth, Z., Guzik, J. A., Chaplin, W. J., Handler, G., and Pigulski, A.: 2014, in *IAU Symposium*, Vol. 301, pp 459–460

Monet, D. G., Levine, S. E., Canzian, B., Ables, H. D., Bird, A. R., Dahn, C. C., Guetter, H. H., Harris, H. C., Henden, A. A., Leggett, S. K., Levison, H. F., Luginbuhl, C. B., Martini, J., Monet, A. K. B., Munn, J. A., Pier, J. R., Rhodes, A. R., Riepe, B., Sell, S., Stone, R. C., Vrba, F. J., Walker, R. L., Westerhout, G., Brucato, R. J., Reid, I. N., Schoening, W., Hartley, M., Read, M. A., and Tritton, S. B.: 2003, *AJ* **125**, 984

Moskalik, P., Smolec, R., Kolenberg, K., Molnár, L., Kurtz, D. W., Szabó, R., Benkő, J. M., Nemec, J. M., Chadid, M., Guggenberger, E., Ngeow, C.-C., Jeon, Y.-B., Kopacki, G., and Kanbur, S. M.: 2015, *MNRAS* **447**, 2348

Murphy, S. J., Bedding, T. R., Shibahashi, H., Kurtz, D. W., and Kjeldsen, H.: 2014, *MNRAS* **441(3)**, 2515

Nemec, J. M., Cohen, J. G., Ripepi, V., Derekas, A., Moskalik, P., Sesar, B., Chadid, M., and Bruntt, H.: 2013, *ApJ* **773(2)**, 181

Nemec, J. M., Smolec, R., Benkő, J. M., Moskalik, P., Kolenberg, K., Szabó, R., Kurtz, D. W., Bryson, S., Guggenberger, E., Chadid, M., Jeon, Y. B., Kunder, A., Layden, A. C., Kinemuchi, K., Kiss, L. L., Poretti, E., Christensen-Dalsgaard, J., Kjeldsen, H., Caldwell, D., Ripepi, V., Derekas, A., Nuspl, J., Mullally, F., Thompson, S. E., and Borucki, W. J.: 2011, *MNRAS* **417(2)**, 1022

Netzel, H., Smolec, R., and Moskalik, P.: 2015, *MNRAS* **447**, 1173

Ngeow, C.-C., Gieren, W., and Klein, C.: 2013, *Proceedings of the International Astronomical Union* **9(S301)**, 123

Norton, A. J., Payne, S. G., Evans, T., West, R. G., Wheatley, P. J., Anderson, D. R., Barros, S. C. C., Butters, O. W., Collier Cameron, A., Christian, D. J., Enoch, B., Faedi, F., Haswell, C. A., Hellier, C., Holmes, S., Horne, K. D., Kane, S. R., Lister, T. A., Maxted, P. F. L., Parley, N., Pollacco, D., Simpson, E. K., Skillen, I., Smalley, B., Southworth, J., and Street, R. A.: 2011, *AAP* **528**, A90

Norton, A. J., Wheatley, P. J., West, R. G., Haswell, C. A., Street, R. A., Collier Cameron, A., Christian, D. J., Clarkson, W. I., Enoch, B., Gallaway, M., Hellier, C., Horne, K., Irwin, J., Kane, S. R., Lister, T. A., Nicholas, J. P., Parley, N., Pollacco, D., Ryans, R., Skillen, I., and Wilson, D. M.: 2007, *A&A* **467**, 785

Paczyński, B.: 1997, in R. Ferlet, J.-P. Maillard, and B. Raban (eds.), *Variables Stars and the Astrophysical Returns of the Microlensing Surveys*, p. 357

Paczyński, B.: 2000, *The Publications of the Astronomical Society of the Pacific* **112**, 1281

Payne, S.: 2013, *Ph.D. thesis*, The Open University, Milton Keynes

Percy, J. R.: 2007, *Understanding Variable Stars*, Cambridge University Press, Cambridge

Pigulski, A.: 2013, *Proceedings of the International Astronomical Union* **9(S301)**, 31

Pojmanski, G.: 1997, *Acta Astron.* **47**, 467

Pojmanski, G.: 2000, *Acta Astron.* **50**, 177

Pojmanski, G.: 2010, *ASAS Gallery - Statistics*

Pollacco, D. L., Skillen, I., Cameron, A. C., Christian, D. J., Hellier, C., Irwin, J., Lister, T. A., Street, R. A., West, R. G., Anderson, D., Clarkson, W. I., Deeg, H., Enoch, B., Evans, A., Fitzsimmons, A., Haswell, C. A., Hodgkin, S., Horne, K., Kane, S. R., Keenan, F. P., Maxted, P. F. L., Norton, A. J., Osborne, J., Parley, N. R., Ryans, R. S. I., Smalley, B., Wheatley, P. J., and Wilson, D. M.: 2006, *Publications of the Astronomical Society of the Pacific* **118(848)**, 1407

Prudil, Z. and Skarka, M.: 2017, *MNRAS* **466**, 2602

Riess, A. G., Macri, L. M., Hoffmann, S. L., Scolnic, D., Casertano, S., Filippenko, A. V., Tucker, B. E., Reid, M. J., Jones, D. O., Silverman, J. M., Chornock, R., Challis, P., Yuan, W., Brown, P. J., and Foley, R. J.: 2016, *ApJ* **826**, 56

Rob Ratkowski / PS1SC: 2015, *PS1 sunrise*

Roberts, D. H., Lehar, J., and Dreher, J. W.: 1987, *AJ* **93**, 968

Samus, N. N., Durlevich, O. V., and et al.: 2009, *VizieR Online Data Catalog* 1

Sandage, A.: 1993, *AJ* **106**, 687

Sariya, D. P., Lata, S., and Yadav, R. K. S.: 2014, *New Astronomy* **27**, 56

Scargle, J.: 1982, *ApJ* **263**, 835

Sesar, B., Hernitschek, N., Mitrović, S., Ivezić, Z., Rix, H.-W., Cohen, J. G., Bernard, E. J., Grebel, E. K., Martin, N. F., Schlafly, E. F., Burgett, W. S., Draper, P. W., Flewelling, H., Kaiser, N., Kudritzki, R. P., Magnier, E. A., Metcalfe, N., Tonry, J. L., and Waters, C.: 2017, *AJ* **153**, 204

Skarka, M.: 2013, *Proceedings of the International Astronomical Union* **9(S301)**, 485

Skarka, M.: 2014a, *A&A* **562**, A90

Skarka, M.: 2014b, *MNRAS* **445**, 1584

Smalley, B.: 2013, in *IAUS 301: Precision asteroseismology*, Vol. Wroclaw, Poland

Smalley, B., Kurtz, D. W., Smith, A. M. S., Fossati, L., Anderson, D. R., Barros, S. C. C., Butters, O. W., Collier Cameron, A., Christian, D. J., Enoch, B., Faedi, F., Haswell, C. A., Hellier, C., Holmes, S., Horne, K., Kane, S. R., Lister, T. A., Maxted, P. F. L., Norton, A. J., Parley, N., Pollacco, D., Simpson, E. K., Skillen, I., Southworth, J., Street, R. A., West, R. G., Wheatley, P. J., and Wood, P. L.: 2011, *AAP* **535**, A3

Smith, A. M. S., Collier Cameron, A., Christian, D. J., Clarkson, W. I., Enoch, B., Evans, A., Haswell, C. A., Hellier, C., Horne, K., Irwin, J., Kane, S. R., Lister, T. A., Norton, A. J., Parley, N., Pollacco, D. L., Ryans, R., Skillen, I., Street, R. A., Triaud, A. H. M. J., West, R. G., Wheatley, P. J., and Wilson, D. M.: 2006, *MNRAS* **373**, 1151

Smith, H. A., Catelan, M., and Clementini, G.: 2009, in J. A. Guzik and P. A. Bradley (eds.), *American Institute of Physics Conference Series*, Vol. 1170, pp 179–187

Smith, H. A., Catelan, M., and Kuehn, C.: 2011, *Carnegie Observatories Astrophysics Series* 5

Smolec, R., Soszyński, I., Udalski, A., Szymanski, M. K., Pietrukowicz, P., Skowron, J., Kozłowski, S., Poleski, R., Moskalik, P., Skowron, D., Pietrzynski, G., Wyrzykowski, Ł., Ulaczyk, K., and Mr'oz, P.: 2015a, *MNRAS* **447**, 3873

Smolec, R., Soszyński, I., Udalski, A., Szymański, M. K., Pietrukowicz, P., Skowron, J., Kozłowski, S., Poleski, R., Skowron, D., Pietrzynski, G., Wyrzykowski, Ł., Ulaczyk, K., and Mróz, P.: 2015b, *MNRAS* **447**, 3756

Soszyński, I., Dziembowski, W. A., Udalski, A., Poleski, R., Szymański, M. K., Kubiak, M., Pietrzyński, G., Wyrzykowski, Ł., Ulaczyk, K., Kozłowski, S., and Pietrukowicz, P.: 2011, *Acta Astron* **61**, 1

Soszyński, I., Udalski, A., Szymański, M. K., Kubiak, J., Pietrzyński, G., Wyrzykowski, Ł., Ulaczyk, K., and Poleski, R.: 2010, *Acta Astron* **60**, 165

Soszyński, I., Udalski, A., Szymański, M. K., Kubiak, M., Pietrzyński, G., Wyrzykowski, Ł., Szewczyk, O., Ulaczyk, K., and Poleski, R.: 2009, *Acta Astron* **59**, 1

Soszyński, I., Udalski, A., Szymański, M. K., Pietrukowicz, P., Mróz, P., Skowron, J., Kozłowski, S., Poleski, R., Skowron, D., Pietrzynski, G., Wyrzykowski, Ł., Ulaczyk, K., and Kubiak, M.: 2014, *Acta Astronomica* **64**, 177

Stellingwerf, R. F.: 1984, *ApJ* **277**, 322

Stellingwerf, R. F., Nemec, J. M., and Moskalik, P.: 2013, *eprint arXiv:1310.0543*

Stothers, R. B.: 2006, *ApJ* **652(1)**, 643

Strugnell, P., Reid, N., and Murray, C. A.: 1986, *MNRAS* **220**, 413

Szabó, R.: 2014, in J. A. Guzik, W. J. Chaplin, G. Handler, and A. Pigulski (eds.), *Precision Asteroseismology*, Vol. 301 of *IAU Symposium*, pp 241–248

Szabó, R., Benkő, J. M., Paparó, M., Chapellier, E., Poretti, E., Baglin, A., Weiss, W. W., Kolenberg, K., Guggenberger, E., and Le Borgne, J. F.: 2014, *A&A* **570**, A100

Szabó, R., Kolláth, Z., and Buchler, J. R.: 2004, *A&A* **425**, 627

Szabó, R., Kolláth, Z., Molnár, L., Kolenberg, K., Kurtz, D. W., Bryson, S. T., Benkő, J. M., Christensen-Dalsgaard, J., Kjeldsen, H., Borucki, W. J., Koch, D., Twicken, J. D., Chadid, M., di Criscienzo, M., Jeon, Y.-B., Moskalik, P., Nemec, J. M., and Nuspl, J.: 2010, *MNRAS* **409**, 1244

Szczygieł, D. M., Pojmański, G., and Pilecki, B.: 2009, *Acta Astron.* **59**, 137

Tamuz, O., Mazeh, T., and Zucker, S.: 2005, *MNRAS* **356(4)**, 1466

The University of Arizona: 2008, *CSS Telescopes*

Torrealba, G., Catelan, M., Drake, A. J., Djorgovski, S. G., McNaught, R. H., Belokurov, V., Koposov, S., Graham, M. J., Mahabal, A., Larson, S., and Christensen, E.: 2015, *MNRAS* **446**, 2251

Turner, O., Anderson, D. R., Maxted, P. L. F., and Hellier, C.: 2015, *European Planetary Science Congress 2015, held 27 September - 2 October, 2015 in Nantes, France, Online at http://meetingorganizer.copernicus.org/EPSC2015, id.EPSC2015-718* **10**, EPSC2015

Udalski, A., Szymanski, M., Kaluzny, J., Kubiak, M., and Mateo, M.: 1992, *Acta Astron.* **42**, 253

Udalski, A., Szymański, M. K., and Szymański, G.: 2015, *Acta Astron.* **65**, 1

VanderPlas, J. T.: 2017, *ArXiv e-prints*

Voges, W., Aschenbach, B., Boller, T., Bräuninger, H., Briel, U., Burkert, W., Dennerl, K., Englhauser, J., Gruber, R., Haberl, F., Hartner, G., Hasinger, G., Kürster, M., Pfeffermann, E., Pietsch, W., Predehl, P., Rosso, C., Schmitt, J. H. M. M., Trümper, J., and Zimmermann, H. U.: 1999, *aap* **349**, 389

Watson, C. L.: 2006, *Society for Astronomical Sciences Annual Symposium* **25**, 47